

# **Carbon Nitride Nanotube-based Photocatalysts for Solar to Chemical Energy Conversion**

By

Yuxiang Zhu

A THESIS SUBMITTED TO MACQUARIE UNIVERSITY

FOR THE DEGREE OF

DOCTOR OF PHILOSOPHY

SCHOOL OF ENGINEERING

October 2018



**MACQUARIE**  
University



I certify that the work in this thesis has not previously been submitted for a degree nor has it been submitted as part of requirements for a degree to any other university or institution other than Macquarie University.

---

Yuxiang Zhu 16-Oct-2018

Copyright © 2018 Yuxiang Zhu

All Rights Reserved

## **Acknowledgements**

I would like to express my deepest gratitude to my principal supervisor, Dr Yijiao Jiang, for having me as her first PhD student at Macquarie University (MQ). I appreciate her tireless supervision, continuous encouragement, support and advice for the PhD project, both as mentor and friend. I am thankful to my co-supervisor, Professor Candace Lang, who has been the source of continuous inspirations during the past three years of my candidature.

Financial support by the ARC Discovery Early Career Researcher Award, ARC Discovery Project and China Scholarship Council scholarship is gratefully acknowledged. I would like to acknowledge the HDR budget funding support of the School of Engineering at MQ throughout my PhD projects. I also acknowledge the Postgraduate Research Fund from MQ to attend an international conference and three laboratory visits in USA.

Completion of the project would not have been possible without technical support from Sue Lindsay and Dr. Chao Shen at MQ Microscopy Unit on SEM and TEM characterisation, Russell Field and Tony Wang on XRD and HPLC analysis. I would also like to thank Walther Adendorff in Macquarie Engineering & Technical Services.

I am especially thankful to A/Prof. Dewei Chu and Tao Wan from UNSW, Dr Xiaoming Wen from the Swinburne University of Technology and A/Prof. Jun Huang from the University of Sydney. All my group members and lab colleagues at MQ are greatly acknowledged, especially Dedong He, Aleksei Marianov, Haimei Xu, Wenwen Zhang, Xiaoxia Yang, Shengsheng Gu and Amanj Kheradmand, all of whom have helped me in many ways. I would acknowledge Keith Imrie from School of Engineering for proofreading of my papers and thesis. Besides, I also received a lot of support from my project collaborators in the Department of Physics at MQ.

I would like to present my special gratitude to my dearest parents. Thank you for their endless love and encouragement all the time.

Last but not least, I express my sincere gratitude to the examiners for reviewing my thesis and for their valuable comments.

## List of publications

### Journal publications included in the thesis

- [1] **Yuxiang Zhu**, Tao Wan, Xiaoming Wen, Dewei Chu and Yijiao Jiang. Tunable Type I and II heterojunction of CoO<sub>x</sub> nanoparticles confined in g-C<sub>3</sub>N<sub>4</sub> nanotubes for photocatalytic hydrogen production, *Applied Catalysis B-Environmental*. Under Review. (Chapter 4)
- [2] **Yuxiang Zhu**, Xianlin Zheng, Amanj Kheradmand, Zhenxu Bai, Yiqing Lu, Yijiao Jiang. NIR-responsive ammonia synthesis over NaYF<sub>4</sub>:Yb,Tm nanoparticle assembled C<sub>3</sub>N<sub>4</sub> NTs with nitrogen vacancies, *Journal of Material Chemistry A*. Submitted. (Chapter 6)
- [3] **Yuxiang Zhu**, Aleksei Marianov, Haimei Xu, Candace Lang and Yijiao Jiang. Bimetallic Ag-Cu supported on graphitic carbon nitride nanotubes for improved visible-light photocatalytic hydrogen production, *ACS Applied Materials & Interfaces*. 10 (2018) 9468-9477. (Chapter 3)

### Other publications

- [1] Yibin Wei, **Yuxiang Zhu** and Yijiao Jiang. Photocatalytic self-cleaning carbon nitride nanotube intercalated reduced graphene oxide membranes for enhanced water purification, *Chemical Engineering Journal*. 356 (2019) 915-925.
- [2] Wenwen Zhang, **Yuxiang Zhu**, Haimei Xu, Marianne Gaborieau, Jun Huang and Yijiao Jiang. Glucose conversion to 5-hydroxymethylfurfural on zirconia: Tuning surface sites by calcination temperatures, *Catalysis Today*. Accepted on 02/10/2018.
- [3] Xiaoxia Yang, Sicong Tian, Tao Kan, **Yuxiang Zhu**, Honghui Xu, Vladimir Strezov, Peter Nelson and Yijiao Jiang. Sorption-enhanced thermochemical conversion of sewage sludge to syngas with intensified carbon utilisation, *Applied Energy*. Under review

### Conference presentations

- [1] **Yuxiang Zhu** and Yijiao Jiang. NIR-responsive photocatalytic H<sub>2</sub> generation over UCNPs/C<sub>3</sub>N<sub>4</sub> NTs. Nanoworld Conference, San Francisco, USA, Apr. 23-25, 2018, **Oral Presentation**
- [2] **Yuxiang Zhu** and Yijiao Jiang. NIR-Responsive nitrogen photofixation over NaYF<sub>4</sub>:Yb,Tm/NV-C<sub>3</sub>N<sub>4</sub> NTs. The 47<sup>th</sup> Chemeca 2018, Queenstown, New Zealand, Sep. 30-Oct. 3, 2018, **Oral Presentation**
- [3] **Yuxiang Zhu** and Yijiao Jiang. Tunable Type I and II heterojunction of CoO<sub>x</sub> nanoparticles confined in g-C<sub>3</sub>N<sub>4</sub> nanotubes for photocatalytic hydrogen production. The 3<sup>rd</sup> International Symposium on Renewable Energy Technology, Gold Coast, Australia, July 19-22, 2018, **Best Oral Presentation Award**
- [4] **Yuxiang Zhu** and Yijiao Jiang. Carbon nitride nanotube based nanocomposites for solar fuel production. Inaugural School of Engineering HDR conference, Macquarie University, Australia, June 7, 2018, **Best Poster Presentation Award**
- [5] **Yuxiang Zhu** and Yijiao Jiang. NIR-responsive nitrogen photofixation over NaYF<sub>4</sub>:Yb,Tm/NV-C<sub>3</sub>N<sub>4</sub> NTs. International Symposium on Relations between Homogeneous and Heterogeneous Catalysis, Sydney, Australia, July 22-25, 2018, **Poster Presentation**
- [6] **Yuxiang Zhu**, Candace Lang and Yijiao Jiang. Visible-light photocatalytic hydrogen generation over metal-supported graphitic carbon nitride nanotubes. The 9<sup>th</sup> International Conference on Environmental Catalysis, Newcastle, Australia, July 10-13, 2016, **Poster Presentation**



## Abstract

Solar-to-chemical energy conversion via photocatalysis has attracted tremendous attention as a potential solution to the worldwide energy shortage and environmental issues. In this thesis, a range of graphitic carbon nitride nanotube ( $C_3N_4$  NT)-based photocatalysts were developed and fabricated via the facile methods. The work started with visible-light active bare  $C_3N_4$  NTs for photocatalytic hydrogen ( $H_2$ ) generation, even in the absence of any co-catalyst. Upon good dispersion of the non-noble co-catalysts, Ag-Cu nanoparticles (NPs) on the bare  $C_3N_4$  NTs, it exhibited twice the  $H_2$  evolution rate of the bare  $C_3N_4$  NTs and about 1.5 times higher than that of the Pt/ $C_3N_4$  NTs. The improved activity is attributed to its unique tubular nanostructure, strong metal-support interaction, and efficient photo-induced electron-hole separation compared to their bare and monometallic counterparts, evidenced by complementary characterisation techniques. It reveals that the  $H_2$  production rates correlate well with the oxidation potentials of the sacrificial reagents used. Triethylamine (TEA) outperforms other sacrificial reagents including triethanolamine (TEOA) and methanol (MeOH). Mechanistic studies on the role of various sacrificial reagents in photocatalytic  $H_2$  generation demonstrate that irreversible photodegradation of TEA into diethylamine and acetaldehyde *via* monoelectronic oxidation contributes to the improved hydrogen yield. Similarly, TEOA is oxidised to diethanolamine and glycolaldehyde, while MeOH is unable to quickly capture the photo-induced holes and remains intact due to the high oxidation potential.

Tunable heterojunction architectures of cobalt oxide ( $CoO_x$ ) nanoparticles were confined on well-arrayed  $C_3N_4$  NTs by using a facile one-pot method but under different annealing atmospheres. A Type II heterojunction of cobalt monoxide nanoparticles ( $CoO$  NPs)/ $C_3N_4$  NTs was obtained after annealing under vacuum, and fine  $CoO$  NPs less than 8 nm in size were homogeneously anchored on the surface of  $C_3N_4$  NTs. A Type I heterojunction of tricobalt tetraoxide ( $Co_3O_4$ )/ $C_3N_4$  NTs were formed under air condition, and  $Co_3O_4$  NPs in the size range

of 10 to 50 nm were aggregated on the surface. The photocatalytic activities of these two heterojunctions were evaluated with H<sub>2</sub> production from water. The strategically developed CoO/C<sub>3</sub>N<sub>4</sub> NTs with 7 wt. % CoO shows the highest H<sub>2</sub> yield under visible light irradiation and the best stability among the photocatalysts studied in this work. Comprehensive characterisation results reveal that the superior catalytic performance of CoO/C<sub>3</sub>N<sub>4</sub> NTs may be attributed to the uniformly distributed smaller nanoparticles on the well-arrayed nanotubes, the longer lifetime of excited electrons, the faster charge transfer and the stronger electronic interaction between the heterojunctions. The Kelvin probe force microscopy results verify that the CoO/C<sub>3</sub>N<sub>4</sub> NT and Co<sub>3</sub>O<sub>4</sub>/C<sub>3</sub>N<sub>4</sub> NT nanocomposites form a Type II and Type I heterojunction, respectively, and charge transfer pathways and reaction mechanisms are therefore established.

To further extend the light absorption of C<sub>3</sub>N<sub>4</sub> NTs toward near-infrared (NIR) light, upconversion nanoparticles (UCNPs), NaYF<sub>4</sub>:Yb,Tm,Gd (NYFG) and NaYF<sub>4</sub>:Yb,Tm (NYF) were decorated on C<sub>3</sub>N<sub>4</sub> NTs separately by a facile technique to construct heterojunction structures. It is found that, with a loading content of 15 wt. %, NYFG/C<sub>3</sub>N<sub>4</sub> NTs exhibited the highest H<sub>2</sub> generation with an apparent quantum efficiency (AQE) of 0.80 %, about 1.4 times higher than that of NYF/C<sub>3</sub>N<sub>4</sub> NTs under 980 nm laser irradiation. This enhanced photocatalytic activity is attributed to the synergistic effect, stronger interaction, higher emission intensity, and faster charge transfer between the two nanocomposites. The energy transfer between NYFG NPs and C<sub>3</sub>N<sub>4</sub> NTs was investigated by the steady-state and dynamic fluorescence spectroscopy. The emitted photons were absorbed by C<sub>3</sub>N<sub>4</sub> NTs via a fluorescence resonance energy transfer process, leading to a high photocatalytic activities. This work highlights the potential of developing near-infrared (NIR) responsive catalysts for energy and environmental applications.

The last part of the thesis works on the photocatalytic fixation of  $\text{N}_2$  to  $\text{NH}_3$  under NIR light irradiation over UCNPs decorated  $\text{C}_3\text{N}_4$  NTs with nitrogen vacancies (NV- $\text{C}_3\text{N}_4$  NTs). NYF/NV- $\text{C}_3\text{N}_4$  NTs with a mass ratio of 15 % exhibited a higher ammonia synthesis rate of  $0.80 \text{ mmol L}^{-1} \text{ g}_{\text{cat}}^{-1}$  (0.99 % for AQE), which is higher than the other catalysts reported so far under NIR light irradiation. This catalyst also provided about three times higher activity than the bare  $\text{C}_3\text{N}_4$  NTs under UV-filtered solar light. Characterisation results reveal that the abundant NVs play an important role in increasing the active sites, light absorption and energy migration. NYF NPs endow the nanostructure with NIR light response. Moreover, the mechanism of the energy transfer pathway was investigated. This work paves the way towards the development of NIR responsive heterogeneous photocatalysts for solar to chemical energy conversion.

## Table of Contents

Acknowledgements.....	iii
List of publications .....	v
Abstract.....	vii
Table of Contents.....	x
Chapter 1 Introduction .....	1
1.1    Background .....	1
1.2    Scope and objectives .....	4
References .....	5
Chapter 2 Literature review .....	8
2.1    Photocatalysis.....	8
2.1.1    The mechanism of the photocatalytic process .....	8
2.1.2    Photocatalytic hydrogen generation.....	10
2.1.3    Photocatalytic ammonia synthesis .....	11
2.2    C <sub>3</sub> N <sub>4</sub> -based semiconductors .....	13
2.2.1    Introduction of C <sub>3</sub> N <sub>4</sub> .....	13
2.2.2    Properties of C <sub>3</sub> N <sub>4</sub> NTs .....	15
2.2.3    Synthesis of C <sub>3</sub> N <sub>4</sub> NTs.....	17
2.2.4    Modification of C <sub>3</sub> N <sub>4</sub> NTs .....	20
2.3    Summary .....	31
References .....	31
Chapter 3 Bimetallic Ag-Cu supported on C <sub>3</sub> N <sub>4</sub> NTs for improved visible-light photocatalytic hydrogen production .....	43
3.1    Introduction .....	43
3.2    Experimental section .....	45

3.2.1	Catalyst fabrication .....	45
3.2.2	Structural characterisation .....	46
3.2.3	Photocatalytic performance .....	47
3.2.4	Mechanistic studies on the role of sacrificial reagents .....	47
3.3	Results and discussion.....	48
3.3.1	Photocatalytic hydrogen production .....	48
3.3.2	Textural and structural properties .....	53
3.3.3	Charge separation studies .....	58
3.3.4	Degradation mechanism of sacrificial reagents .....	59
3.4	Conclusion.....	63
	References .....	64
Chapter 4 Tunable Type I and II heterojunction of CoO <sub>x</sub> nanoparticles confined in C <sub>3</sub> N <sub>4</sub> NTs		
	for photocatalytic H <sub>2</sub> production.....	68
4.1	Introduction .....	68
4.2	Experimental section .....	71
4.2.1	Catalyst fabrication .....	71
4.2.2	Characterisation .....	71
4.2.3	Photocatalytic hydrogen production .....	73
4.3	Results and discussion.....	73
4.3.1	Photocatalytic performance .....	73
4.3.2	Structure characterisation.....	75
4.3.3	Interpretation of charge transfer and reaction pathways .....	86
4.4	Conclusion.....	89
	References .....	90

Chapter 5 NIR-driven photocatalytic H <sub>2</sub> production over upconversion nanoparticle engineered C <sub>3</sub> N <sub>4</sub> NTs.....	93
5.1 Introduction .....	93
5.2 Experimental section .....	95
5.2.1 Catalyst synthesis.....	95
5.2.2 Characterisation .....	96
5.2.3 Photocatalytic H <sub>2</sub> generation.....	96
5.3 Results and discussion.....	97
5.3.1 Photocatalytic performance .....	97
5.3.2 Characterisation of the photocatalysts .....	100
5.3.3 Photocatalytic mechanism .....	109
5.4 Conclusions .....	110
References .....	111
Chapter 6 NIR-responsive ammonia synthesis over NaYF <sub>4</sub> :Yb,Tm nanoparticle assembled C <sub>3</sub> N <sub>4</sub> NTs with nitrogen vacancies .....	115
6.1 Introduction .....	115
6.2 Experimental section.....	117
6.2.1 Catalyst synthesis.....	117
6.2.2 Characterisation .....	118
6.2.3 Photocatalytic ammonia synthesis .....	119
6.3 Results and discussion.....	119
6.3.1 Photocatalytic performance .....	119
6.3.2 Structure characterisation.....	122
6.3.3 Interpretation of charge transfer and reaction pathways.....	134
6.4 Conclusion.....	136

References .....	136
Chapter 7 Conclusions and future work.....	141
7.1 Conclusions .....	141
7.2 Future work .....	143
References .....	144
Appendix .....	145

# Chapter 1 Introduction

## 1.1 Background

The energy shortage and environmental pollution have become topics of global concern. Although the traditional fossil fuels, such as oil, coal and natural gas, are still our major energy sources, it is urgent to develop pollution-free technologies for the long-term development of human society [1, 2]. Among numerous green-earth projects underway, photocatalysis has emerged as one of the most promising technologies, since it operates under ambient conditions, utilising the natural sunlight as the driving force and semiconductors as catalysts with earth-abundant elements [3]. Solar energy has the advantages of inexhaustibility, non-pollution, high safety and wide distribution, etc. Thus, harvesting and conversion of solar energy into renewable energy form is highly desirable. In the early 1970s, Fujishima and Honda, the pioneers of semiconductor photocatalysis, discovered the photoelectrochemical water splitting over the  $\text{TiO}_2$  electrode to produce hydrogen ( $\text{H}_2$ ) [4]. Since then, photocatalysis has attracted tremendous attention in the fields of environment, materials, energy, chemical industry and many others [5, 6].

$\text{H}_2$  energy is clean, non-polluting, renewable and has a high energy density (122 kJ/g, about three times that of gasoline) [7]. It has been considered to be one of the most promising energy carriers.  $\text{H}_2$  has been used in the chemical industries on a massive scale, ranging from ammonia synthesis to MeOH production [8]. However,  $\text{H}_2$  is mainly produced on a large scale from fossil fuels such as natural gas, resulting in emitting carbon dioxide ( $\text{CO}_2$ ) gas which causes the greenhouse effect [9]. There are several alternative clean approaches to  $\text{H}_2$  production *via* direct water splitting to generate oxygen ( $\text{O}_2$ ) and  $\text{H}_2$ , including thermochemical water splitting, water electrolysis, photocatalytic water splitting and water bio-photolysis [10]. Among these



techniques, H<sub>2</sub> produced from water splitting using renewable energy sources provides a potential way since it is cheap, clean and environmentally friendly [11].

Besides H<sub>2</sub> production, photocatalytic N<sub>2</sub> reduction to ammonia is another promising application. Being a fertiliser or precursors to other nitrogen fertilisers, ammonia has been considered as a potential carbon-free energy storage chemical since it is eco-friendly, safe and, most importantly, non-CO<sub>2</sub> emissions [12]. It can also be regarded as a hydrogen carrier due to its high gravimetric hydrogen density (17.6 wt. %) and can be readily transformed into a liquid for easy transportation [13]. As one of the most widely used industrial feedstocks, the market price of ammonia is highly competitive and at least an order of magnitude less than other hydrogen storage materials [14]. Over the past century, industrially the reaction of N<sub>2</sub> with H<sub>2</sub> to produce ammonia has been accomplished by the Haber-Bosch process that uses iron-based catalysts and requires high temperature and pressure in its operation [15]. Such a process is energy demanding and not environmentally friendly as it consumes more than 1-2 % of the annual energy supply around the world and accounts for 1 % of the global greenhouse-gas emissions [16]. Alternatively, employing solar energy to activate inert N<sub>2</sub> by artificial photosynthesis is of considerable interest since it takes place under sunlight irradiation and under ambient conditions without extra energy input [17].

Nowadays, numerous semiconductors have been designed and prepared at the micro or nanometer scale. Nevertheless, most of the photocatalysts are metal oxide semiconductors and with a wide bandgap, thereby leading to weak light harvesting in visible and near-infrared (NIR) light region that accounts for ~96 % of the solar energy [18, 19]. Graphitic carbon nitride (g-C<sub>3</sub>N<sub>4</sub>) in the form of 2-dimensional (2D) sheets, consists of interconnected tri-s-triazines repeating units. It has elicited ripples of excitement as the next generation photocatalyst because of its facile synthesis from earth-abundant nitrogen-rich precursors, visible-light response, well-suited band positions, appealing electronic structure and high physicochemical

stability [20-22]. These advantages facilitate its wide application in carbon dioxide ( $\text{CO}_2$ ) reduction, ammonia synthesis, and organics degradation, as well as water splitting into  $\text{H}_2$  and oxygen [23, 24]. However, utilisation of g- $\text{C}_3\text{N}_4$  in the field of heterogeneous catalysis started in 2006 [25]. Visible-light-induced photocatalytic water splitting over g- $\text{C}_3\text{N}_4$  was firstly reported by Wang et al [26]. Since then, the photocatalytic exploration has been shifted potentially from inorganic semiconductors to polymer conjugated photocatalysts [27].

At present, a large number of approaches have been developed to improve the photocatalytic activity of bulk g- $\text{C}_3\text{N}_4$  [23]. Morphology control and surface modification of the g- $\text{C}_3\text{N}_4$  nanostructure are effective strategies to promote g- $\text{C}_3\text{N}_4$  photocatalysis, with larger specific surface areas and efficient mass diffusion during the photocatalytic process [28]. Thus, besides ordered mesoporous g- $\text{C}_3\text{N}_4$ , intensive efforts have been devoted to endow g- $\text{C}_3\text{N}_4$  with specific nanoarchitectures, such as nanospheres, nanorods, nanotubes, nanosheets, etc. Recent studies have shown the superior activities of g- $\text{C}_3\text{N}_4$  nanotubes ( $\text{C}_3\text{N}_4$  NTs) under visible light irradiation [29]. However, the high recombination rate of the photogenerated electron-hole pairs and the low light absorbance still hinder their widespread applications. Therefore, it is highly desirable to construct  $\text{C}_3\text{N}_4$  NT-based heterojunction nanohybrids in order to accelerate the charge separation rate and maximise the light harvesting [18].

Decoration of metal nanoparticles (NPs) on the surface of  $\text{C}_3\text{N}_4$  NTs is an appealing way to create metal/ $\text{C}_3\text{N}_4$  NT heterojunction in which metal NPs work as cocatalysts [29]. Bimetallic NPs have been studied in heterogeneous photocatalysis, which can result in improved properties and activities compared to the monometallic ones, attributed to the synergistic effects within the bimetallic NPs [30]. Incorporating another semiconductor with appropriate band potentials with  $\text{C}_3\text{N}_4$  NTs is regarded as an effective approach to form semiconductor/ $\text{C}_3\text{N}_4$  NT heterojunctions because of the synergistic effects. To further extend the absorption of visible-light response toward near-infrared (NIR) light, sensitisation is

another typical strategy to efficiently harvest solar energy. Typically, a NIR-triggered  $C_3N_4$  NT-based heterojunction can be designed by incorporating upconversion nanoparticles (UCNPs). Besides the optimisation of  $C_3N_4$  NT-based photocatalysts, understanding the photocatalytic mechanism is of great significance as well for developing more effective systems in the future. Therefore, the aim of this thesis is to fabricate highly active  $C_3N_4$  NT-based nanocatalysts for  $H_2$  production and ammonia synthesis and understand the photocatalytic process with different techniques including liquid chromatography-mass spectrometry, Kelvin probe force microscopy and time-resolved photoluminescence.

## 1.2 Scope and objectives

This thesis presents the fabrication of active  $C_3N_4$  NT-based photocatalysts for the applications in  $H_2$  production and ammonia synthesis and the mechanistic studies on the photocatalytic processes as well as the dynamics of the photogenerated charge carriers. The specific objectives of this thesis are:

- 1) To fabricate and understand the physicochemical characteristics of bare  $C_3N_4$  NTs and its photocatalytic behaviour; also study the role of sacrificial reagents in the photocatalytic  $H_2$  generation process
- 2) To modify  $C_3N_4$  NT photocatalysts by Ag-Cu bimetallic NPs and evaluate the photocatalytic performance in  $H_2$  production in comparison with the monometallic catalysts
- 3) To fabricate tunable heterojunction architectures of  $CoO_x$  on  $C_3N_4$  NTs and define the charge transfer pathways in the two types of heterojunctions
- 4) To prepare and characterise the NYFG NPs anchored  $C_3N_4$  NTs and study the photocatalytic activities in  $H_2$  generation under NIR light irradiation
- 5) To fabricate NYF NPs decorated  $C_3N_4$  NTs with abundant NVs and analyse the effect of NVs and NYF NPs on the energy transfer mechanism

The background and the scope of this thesis are described in **Chapter 1**. In **Chapter 2** the photocatalytic process of H<sub>2</sub> generation and N<sub>2</sub> reduction over C<sub>3</sub>N<sub>4</sub>-based nanostructures, and heterojunction systems of metal/C<sub>3</sub>N<sub>4</sub> NTs, semiconductor/C<sub>3</sub>N<sub>4</sub> NTs and sensitiser/C<sub>3</sub>N<sub>4</sub> NTs are reviewed. **Chapter 3** presents a modified method to fabricate C<sub>3</sub>N<sub>4</sub> NTs and a facile way to decorate bimetallic Ag-Cu NPs along the nanotubes as well as the mechanistic studies on the role of sacrificial reagents in photocatalytic H<sub>2</sub> evolution. **Chapter 4** presents tunable heterojunction architectures of CoO<sub>x</sub> nanoparticles confined on well-arrayed C<sub>3</sub>N<sub>4</sub> NTs by using the same one-pot method after annealing under vacuum or static air atmosphere. Besides, the charge transfer pathways and reaction mechanisms in the visible-light-induced photocatalytic H<sub>2</sub> production are established. **Chapter 5** introduces C<sub>3</sub>N<sub>4</sub> NTs attached with Gd-ion-doped NYF NPs in order to effectively use NIR light. The role of Gd ions in the energy transfer process between UCNPs and C<sub>3</sub>N<sub>4</sub> NTs for efficient H<sub>2</sub> production is investigated. **Chapter 6** extends light absorption to NIR by anchoring NaYF<sub>4</sub>:Yb,Tm (NYF) NPs along nitrogen-deficient C<sub>3</sub>N<sub>4</sub> NTs; this nanostructure achieves high ammonia quantum efficiency under NIR light irradiation. The energy transfer process is investigated by the time-resolved photoluminescence. Finally, **Chapter 7** summarises the main findings of this work and suggests the prospects for the future work on C<sub>3</sub>N<sub>4</sub> NT-based photocatalysis.

## References

- [1] H. Tong, S. Ouyang, Y. Bi, N. Umezawa, M. Oshikiri, J. Ye, *Advanced Materials*, 24 (2012) 229-251.
- [2] A. Kudo, Y. Miseki, *Chemical Society Reviews*, 38 (2009) 253-278.
- [3] C. Chen, W. Ma, J. Zhao, *Chemical Society Reviews*, 39 (2010) 4206.
- [4] A. Fujishima, K. Honda, *Nature*, 238 (1972) 37.
- [5] X. Li, J. Yu, M. Jaroniec, *Chemical Society Reviews*, 45 (2016) 2603-2636.

- [6] F. Fresno, R. Portela, S. Suárez, J.M. Coronado, *Journal of Materials Chemistry A*, 2 (2014) 2863-2884.
- [7] W. Lubitz, W. Tumas, *Chemical Reviews*, 107 (2007) 3900-3903.
- [8] P.L. Spath, M.K. Mann, National Renewable Energy Laboratory, Golden, CO (US), 2000.
- [9] R. Abe, *Journal of Photochemistry and Photobiology C: Photochemistry Reviews*, 11 (2010) 179-209.
- [10] C. Grimes, O. Varghese, S. Ranjan, Springer Science & Business Media, 2007.
- [11] A. Kudo, H. Kato, I. Tsuji, *Chemistry Letters*, 33 (2004) 1534-1539.
- [12] X. Chen, N. Li, Z. Kong, W.-J. Ong, X. Zhao, *Materials Horizons*, 5 (2018) 9-27.
- [13] M. Ali, F. Zhou, K. Chen, C. Kotzur, C. Xiao, L. Bourgeois, X. Zhang, D.R. MacFarlane, *Nature Communications*, 7 (2016) 11335.
- [14] L. Li, Y. Wang, S. Vanka, X. Mu, Z. Mi, C.J. Li, *Angewandte Chemie*, 56 (2017) 8701-8705.
- [15] M. Kitano, S. Kanbara, Y. Inoue, N. Kuganathan, P.V. Sushko, T. Yokoyama, M. Hara, H. Hosono, *Nature Communications*, 6 (2015) 6731.
- [16] G. Dong, W. Ho, C. Wang, *Journal of Materials Chemistry A*, 3 (2015) 23435-23441.
- [17] A.J. Medford, M.C. Hatzell, *ACS Catalysis*, 7 (2017) 2624-2643.
- [18] W.J. Ong, L.L. Tan, Y.H. Ng, S.T. Yong, S.P. Chai, *Chemical Reviews*, 116 (2016) 7159-7329.
- [19] S. Ye, R. Wang, M.-Z. Wu, Y.-P. Yuan, *Applied Surface Science*, 358 (2015) 15-27.
- [20] Y. Gong, M. Li, Y. Wang, *ChemSusChem*, 8 (2015) 931-946.
- [21] G. Liu, T. Wang, H. Zhang, X. Meng, D. Hao, K. Chang, P. Li, T. Kako, J. Ye, *Angewandte Chemie*, 54 (2015) 13561-13565.
- [22] S. Cao, J. Low, J. Yu, M. Jaroniec, *Advanced Materials*, 27 (2015) 2150-2176.
- [23] S. Cao, J. Yu, *The Journal of Physical Chemistry Letters*, 5 (2014) 2101-2107.

- [24] Y. Zheng, J. Liu, J. Liang, M. Jaroniec, S.Z. Qiao, *Energy & Environmental Science*, 5 (2012) 6717.
- [25] F. Goettmann, A. Fischer, M. Antonietti, A. Thomas, *Chemical Communication*, (2006) 4530-4532.
- [26] X. Wang, K. Maeda, A. Thomas, K. Takanabe, G. Xin, J.M. Carlsson, K. Domen, M. Antonietti, *Nature Materials*, 8 (2009) 76-80.
- [27] Y. Wang, X. Wang, M. Antonietti, *Angewandte Chemie*, 51 (2012) 68-89.
- [28] Y. Wang, X. Liu, J. Liu, B. Han, X. Hu, F. Yang, Z. Xu, Y. Li, S. Jia, Z. Li, Y. Zhao, *Angewandte Chemie*, 57 (2018) 5765-5771.
- [29] K. Li, Z. Zeng, L. Yan, S. Luo, X. Luo, M. Huo, Y. Guo, *Applied Catalysis B: Environmental*, 165 (2015) 428-437.
- [30] O. Rosseler, C. Ulhaq-Bouillet, A. Bonnefont, S. Pronkin, E. Savinova, A. Louvet, V. Keller, N. Keller, *Applied Catalysis B: Environmental*, 166-167 (2015) 381-392.

## **Chapter 2 Literature review**

### **2.1 Photocatalysis**

#### **2.1.1 The mechanism of the photocatalytic process**

Semiconductor photocatalysis is based on the energy band theory in solids. For a semiconductor photocatalyst, which has a conductivity between that of an insulator and that of a conductor, the difference is that a semiconductor contains a discontinuous band structure consisting of an empty conduction band (CB) with high energy and a low-energy valence band (VB) full of electrons. This feature determines their electrical and optical properties. The energy gap between the top of the VB and the bottom of the CB is defined as the band gap ( $E_g$ ).

As shown in Figure 2.1, when a semiconductor absorbs photons whose energy matches or exceeds its band gap, the electrons in the VB will be excited and transfer to the CB [1]. Within a very short time (normally 100 ps - 10 ns), photoelectrons and holes will recombine in the bulk or on the surface of the semiconductor, releasing energy in the form of heat or photons. Any electrons and holes not recombined will migrate to the surface and have reduction and oxidation reactions with the reactants adsorbed on the semiconductor, respectively (Potential should be matched; 100 ns - ms) [2]. Thus, the above three consecutive tandem steps will govern the photocatalytic performance. The structure and crystallinity of the semiconductors have a great influence on the charge separation and migration. The surface photocatalytic process can be improved by controlling the nano-sized semiconductors and achieving more active surface sites [3, 4].

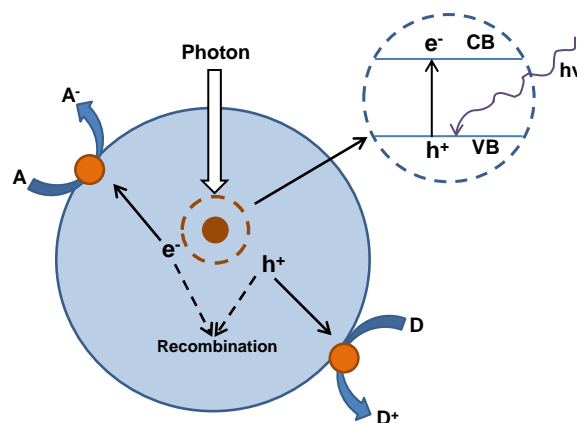


Figure 2.1 Illustration of main processes in photocatalytic reactions on semiconductors

Unlike the conventional thermal catalysis, not only uphill reactions ( $\Delta G < 0$ ), but also downhill reactions ( $\Delta G > 0$ ) can be promoted by photocatalysis as shown in Figure 2.2 [5, 6]. In the former case, the input energy is used to overcome the activation barrier so as to facilitate or accelerate photocatalysis under mild conditions. In this reaction, the photon energy is converted into chemical energy, as seen in the photosynthesis over green plants. Thus, this reaction is defined as artificial photosynthesis such as water splitting into  $O_2$  and  $H_2$ ,  $CO_2$  reduction and ammonia synthesis. However, the surface multi-electron reaction kinetics lead to an inevitable accumulation of charges, causing unexpected electron-hole recombination, which is a serious problem for the uphill reactions [7]. In the latter case, part of the input energy is converted into chemical energy which will be accumulated in the reaction products. This reaction proceeds irreversibly like photodegradation of organic compounds [8].

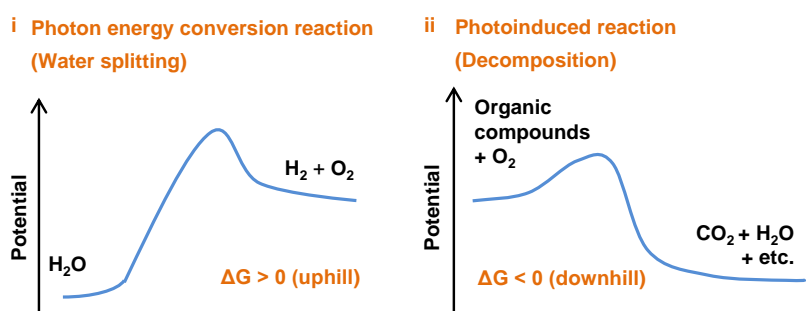
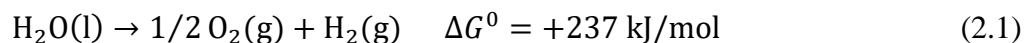


Figure 2.2 Classification of photocatalytic reactions according to Gibbs free energy



### 2.1.2 Photocatalytic hydrogen generation

As described above, producing  $H_2$  from water is an uphill reaction ( $\Delta G^0$  of 237 kJ/mol, Eq. 2.1) [9]. At present, there are two ways for artificial photocatalytic  $H_2$  production: the photo-electrochemical water splitting and the suspension system.



But the latter system is much simpler and more suitable for industrial production as presented in Figure 2.3a. In a suspension system, photocatalyst powders are dispersed in a reactor with water under sunlight, then  $H_2$  is readily generated upon light irradiation. The photocatalytic reactions proceed on semiconductor catalyst as schematically shown in Figure 2.3b. The positions of the CB and VB of the semiconductor materials are the key points. The bottom level of the CB has to be more negative than the redox potential of  $H^+/H_2$  (0 eV vs NHE), whereas the upper level of the VB is more positive than the redox potential of  $O_2/H_2O$  (1.23 eV vs NHE) [10, 11]. Therefore, the theoretical minimum band gap for water splitting is 1.23 eV, corresponding to the light of around 1100 nm (from Eq. 2.2). However, a larger band gap ( $> 2.0$  eV) is usually needed for appreciable water splitting because of the additional overpotential related to the steps of each electron transfer and gas generation [6].

$$\text{Band gap (eV)} = 1240/\lambda \text{ (nm)} \quad (2.2)$$

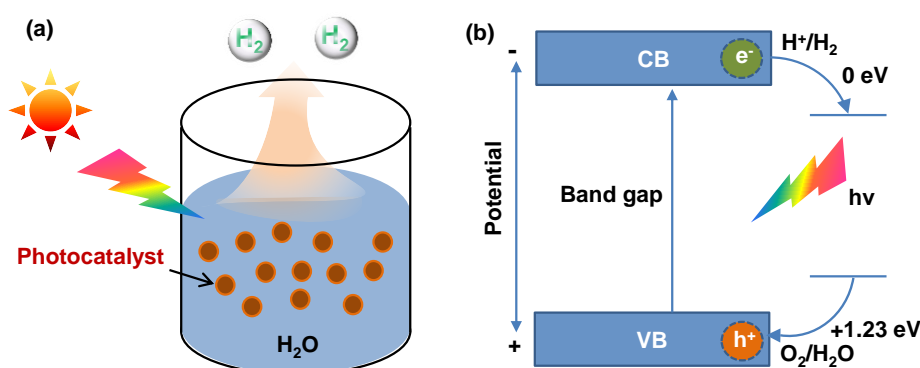


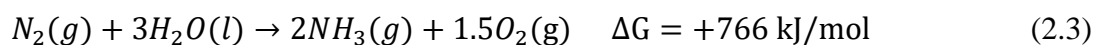
Figure 2.3 Solar  $H_2$  production from water splitting over powdered photocatalysts (a) and the principle of water splitting on semiconductors (b).

The necessity to separate  $H_2$  from the mixed gases is disadvantageous toward the efficient photocatalytic  $H_2$  production. Thus, sacrificial reagents are normally employed to promote the photocatalytic  $H_2$  generation [2]. When a reducing reagent (electron donor or hole scavenger) is utilised in an aqueous solution during the photocatalytic process, the photoinduced holes will irreversibly oxidise the reducing reagent instead of water, thus enriching electrons in the semiconductor. Therefore, the  $H_2$  generation rate is remarkably enhanced. As  $O_2$  is not generated, the back reaction to produce water is hindered, it does not require an auxiliary gas-separation process [12]. Furthermore, the half reaction becomes attractive for practical  $H_2$  production when biomass and compounds abundant in industries and nature are used as the reducing reagents. These sacrificial reagents can be classified as organic and inorganic hole scavengers [13]. Various organic compounds such as organic acids, alcohols, and hydrocarbons have been employed as hole acceptors [14, 15], and sulphide ( $S^{2-}$ ) and sulphite ( $SO_3^{2-}$ ) reagents are mostly utilised as inorganic sacrificial electron donors for the photocatalytic  $H_2$  generation [16-19].

### **2.1.3 Photocatalytic ammonia synthesis**

As shown in Eq 2.3, reducing  $N_2$  for ammonia synthesis is an uphill reaction as well with a  $\Delta G^0$  of 766 kJ/mol. The first study on  $TiO_2$ -based photocatalysts for  $N_2$  reduction under UV light irradiation was in 1977 [20]. The earlier studies on the photocatalytic ammonia synthesis mainly focused on sand and soil minerals in nature [21, 22]. Because traces of  $TiO_2$  are found in the mineral surface it was suggested that  $N_2$  photoreduction may occur in arid or semiarid regions, which can also be part of the nitrogen cycle [23]. To date, numerous semiconductors have been studied for photocatalytic ammonia synthesis. Nowadays, in industry ammonia has mostly been prepared by the Haber-Bosch process, which is regarded as the most important discovery of the 20th century. However, this process consumes a large amount of energy because of the harsh reaction conditions ( $\sim 250$  atm and  $300-500$  °C) [24]. Alternatively,

photocatalytic ammonia synthesis from  $N_2$  reduction under mild conditions is attracting increased attention.



The photocatalytic ammonia synthesis proceeds on a semiconductor as illustrated in Figure 2.4. It is important that the CB position of the semiconductor should be more negative than the reduction potential of  $N_2$ , whereas the VB position should be more positive than the oxidation potential of water (1.23 eV vs NHE). In particular, the reduction of  $N_2$  to  $NH_3$  in nature involves a multi-step process of the photoinduced electrons and protons transfer. The maximum reduction potential lies in the first step of  $N_2$  reduction (-4.16 eV vs NHE) and the process of the proton-coupled electron transfer (-3.2 eV vs NHE), which hinders the overall kinetic reactions [25, 26]. Thus, there are two main bottlenecks that need to be overcome in order to activate  $N_2$  for ammonia synthesis. To satisfy the thermodynamic reduction potential, a semiconductor with a narrow bandgap is required. It is also critical to inhibit the recombination of the photogenerated electron-holes and thus improve the solar energy conversion efficiency.

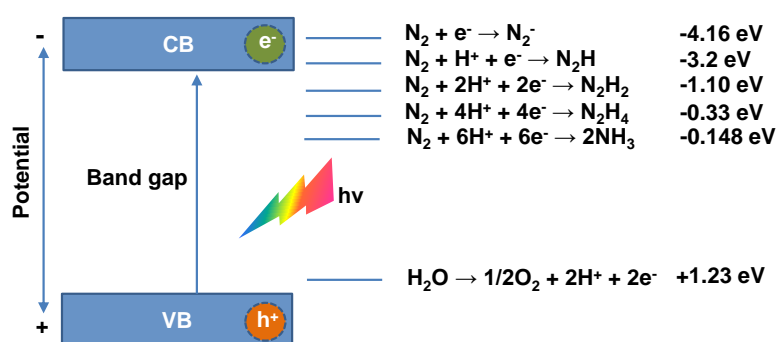


Figure 2.4 Principle of photocatalytic ammonia synthesis on a semiconductor.

It is well-accepted that photocatalytic  $NH_3$  synthesis mainly involves two mechanisms, namely associative and dissociative mechanisms (Figure 2.5) [27]. In the associative mechanism, each  $N_2$  molecule adsorbs onto the surface of a catalyst undergoes hydrogenation with its N atoms bound to each other. The  $NH_3$  is released only after the final N-N bond is broken. In this case,

the hydrogenation process can take two pathways, alternating and distal pathways. In the alternating pathway, the two N atoms undergo single hydrogenation steps in turn until one of them is converted to  $\text{NH}_3$ . In the distal pathway, the N atoms furthest from the surface undergoes hydrogenation preferentially until the release of one  $\text{NH}_3$  and then the continuing hydrogenation process occurs on the other one. On the other hand, in the dissociative mechanism, before the hydrogenation occurs the triple bond of  $\text{N}_2$  molecule is broken, leaving two adsorbed N-atoms on the catalyst surface which are independently converted to  $\text{NH}_3$  [28, 29]. Both the associative and dissociative mechanisms presented above are still under debate, and different photocatalysts may undergo distinct reaction mechanisms for  $\text{N}_2$  reduction.

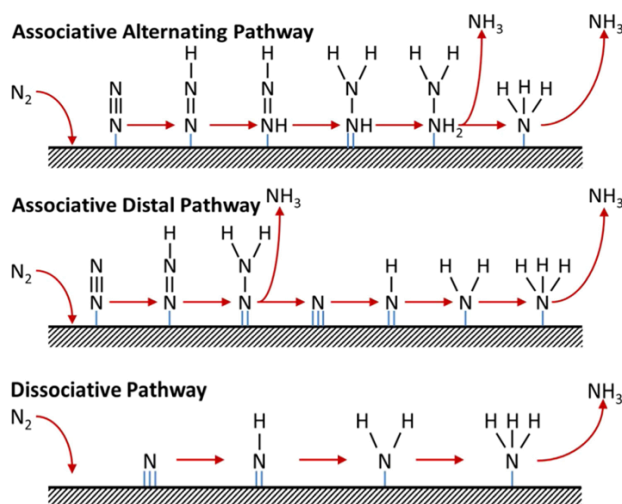


Figure 2.5 Possible photocatalytic reaction mechanisms for  $\text{N}_2$  reduction to  $\text{NH}_3$  [27].

## 2.2 $\text{C}_3\text{N}_4$ -based semiconductors

### 2.2.1 Introduction of $\text{C}_3\text{N}_4$

Carbonic nitride ( $\text{C}_3\text{N}_4$ ) polymers were first developed by Berzelius and Liebig in 1834 [30]. Melem, melam, melamine, and melon were considered as heptazine- and triazine-based compounds. A yellow, insoluble and amorphous material, i.e. melon was discovered, but not all of the compounds were well defined. The potassium hydromelonate derived via annealing the sulphur and potassium ferricyanide precursors was discovered by Gmelin one year later

[31]. In 1922  $C_3N_4$  was firstly introduced by Franklin, who identified  $C_3N_4$  as the final product upon calcination of melon and proposed its structure. Besides, he also found that the composition of melon derivatives changed with the fabrication methods when mercuric thiocyanate was used as a precursor [32]. From X-ray crystallography analysis, Pauling and Sturdivant first proposed a coplanar tri-s-triazine unit as the structural motif of the derivatives in 1937 [33]. Three years later, Redemann and Lucas found that the molecules were relatively large and that a single crystal structure was not indexed to melon because the graphite structure was composed of various sizes and architectures [34]. In 1982, the first crystal structure of the cyameluric derivative with a coplanar arrangement was observed, which confirmed Pauling's structure [35].

However, none has paid attention to the above melon-based  $C_3N_4$  as unconfirmed species for a long time due to its insolubility in many solvents and chemical inertness [36]. Surprisingly, more than 150 years later, interest in  $C_3N_4$  was re-inspired by the theoretical calculation. In 1985, Liu and Cohen proposed the  $\beta$ - $C_3N_4$  structure and suggested that the compressibility of  $\beta$ - $C_3N_4$  was comparable to or greater than diamond. However, it was challenging to fabricate  $\beta$ - $C_3N_4$  due to its very low thermodynamic stability [37]. After that, many researchers have devoted strenuous efforts to the theoretical calculation and experimental synthesis. Kroke and Schwarz have reviewed the  $C_3N_4$  structures [38]. Among all the allotropes of  $C_3N_4$ , g- $C_3N_4$  is considered to be the most stable one. To date, studies on its fabrication and characterisation are still underway. It is difficult to develop a crystalline and perfect g- $C_3N_4$  nanostructure. It is evident that the defect-containing g- $C_3N_4$  including terminations and surface defects is more reactive in various heterogeneous catalysis. In 2006 Goettmann et al. started using g- $C_3N_4$  in catalytic activation of benzene [39]. In 2009 Wang and co-workers discovered that g- $C_3N_4$  is able to split water for  $H_2$  and  $O_2$  production [40]. Dong et al. reported for the first time that nitrogen deficient g- $C_3N_4$  had the ability of photocatalytic  $N_2$  reduction [41].

### 2.2.2 Properties of $C_3N_4$ NTs

Generally, there are seven phases of  $C_3N_4$ , namely,  $\alpha$ - $C_3N_4$ ,  $\beta$ - $C_3N_4$ , pseudocubic  $C_3N_4$ , g-h-triazine, cubic  $C_3N_4$ , g-o-triazine and g-h-heptazine [42]. Among them, tri-s-triazine-based g- $C_3N_4$  is the most stable and energetically favourable allotrope in the ambient environment as evidenced by density functional theory (DFT) calculations as shown in Figure 2.6 [43]. Thus, tri-s-triazine is widely identified as the basic unit to form g- $C_3N_4$ . Polymeric g- $C_3N_4$  is a metal-free p-type semiconductor [44]. Unlike  $TiO_2$ , which is only active in the UV region, bare g- $C_3N_4$  possesses a bandgap of ca. 2.7 eV, with the CB formed by C 2p orbitals at ca. -1.3 eV (vs NHE) and the VB constituted by N 2p orbitals at ca. +1.4 eV (vs NHE) respectively, resulting in an onset of visible light absorbance at approximately 450 nm.

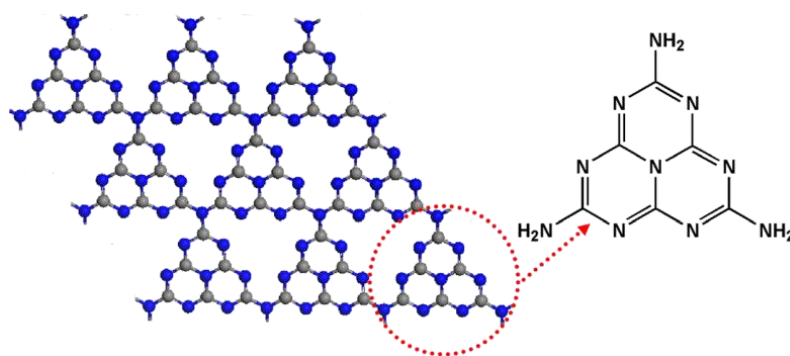


Figure 2.6 Tri-s-triazine-based structure of g- $C_3N_4$ . The C and N atoms are indicated by gray and blue balls.

Thermogravimetric analysis (TGA) analyses demonstrated that g- $C_3N_4$  is thermally stable up to ca. 600 °C in air, which can be attributed to the aromatic C-N heterocycles [45]. Because of the strong van der Waals interactions, g- $C_3N_4$  is of high chemical stability in most solvents such as N,N-dimethylformamide (DMF), alcohols, water, and tetrahydrofuran (THF) [46]. Importantly, g- $C_3N_4$  consists of only two earth-abundant elements: carbon and nitrogen, which implies that this semiconductor can be fabricated at low cost and its properties can be tuned simply and without any significant modification. In addition, its polymeric nature makes the

surface chemistry controllable via surface modification [47]. Also, its polymeric nature ensures the flexibility of the nanostructure, which can serve as a host matrix to some inorganic NPs. Therefore, these unique aforementioned features endow its wide applications including photocatalytic  $H_2$  generation and  $N_2$  reduction.

Bulk  $g\text{-}C_3N_4$  materials prepared by self-condensation of nitrogen-rich precursors have a small surface area, normally below  $10\text{ m}^2\text{ g}^{-1}$  and limited active sites, which are unfavourable for photocatalysis [48]. This problem can be solved by introducing different morphologies and ordered porosity in bulk  $g\text{-}C_3N_4$  based on the nanocasting and nanotemplating approach, thus leading to their enhanced structural properties and photocatalytic activity. Controllable nanoarchitecture design of  $g\text{-}C_3N_4$ , such as  $C_3N_4$  nanosheets, porous  $g\text{-}C_3N_4$ , nanoribbons,  $C_3N_4$  NTs, hollow  $g\text{-}C_3N_4$  nanospheres, and so forth, have been extensively reported [49].

Considerable efforts have been devoted to studying  $C_3N_4$  NTs due to the high surface-to-volume ratio, extraordinary electronic, optical properties, as well as abundant chemically active sites. As presented in Figure 2.7a-c, given that  $C_3N_4$  NTs are formed by rolling up the monolayer along one direction, the theoretical total energy of optimised  $C_3N_4$  NTs decreases with the increasing diameter, indicating  $C_3N_4$  NTs is more stable than the monolayer and  $g\text{-}C_3N_4$ . Besides, the calculated bands of  $C_3N_4$  NTs with an increase of layer sizes (Figure 2.7d) exhibit distinct properties. As seen, the bandgap of the nanotubes becomes wider with the increased layer due to structure distortion in the nanotubes, which is in line with that of  $BC_2N$  nanotubes. Also, unlike the monolayer the charge mobility of  $C_3N_4$  NTs was enhanced attributed to the reduced effective mass, resulting in an improved activity of  $C_3N_4$  NTs [50]. On the other hand, the theoretical results revealed that the acceptor-nanotubedonor paradigm exhibits the largest static value for  $C_3N_4$  NT systems, which is different from carbon NTs [51]. More importantly, this 1D structure facilitates easy access of reactants to more active sites and product diffusion in the channel [52].

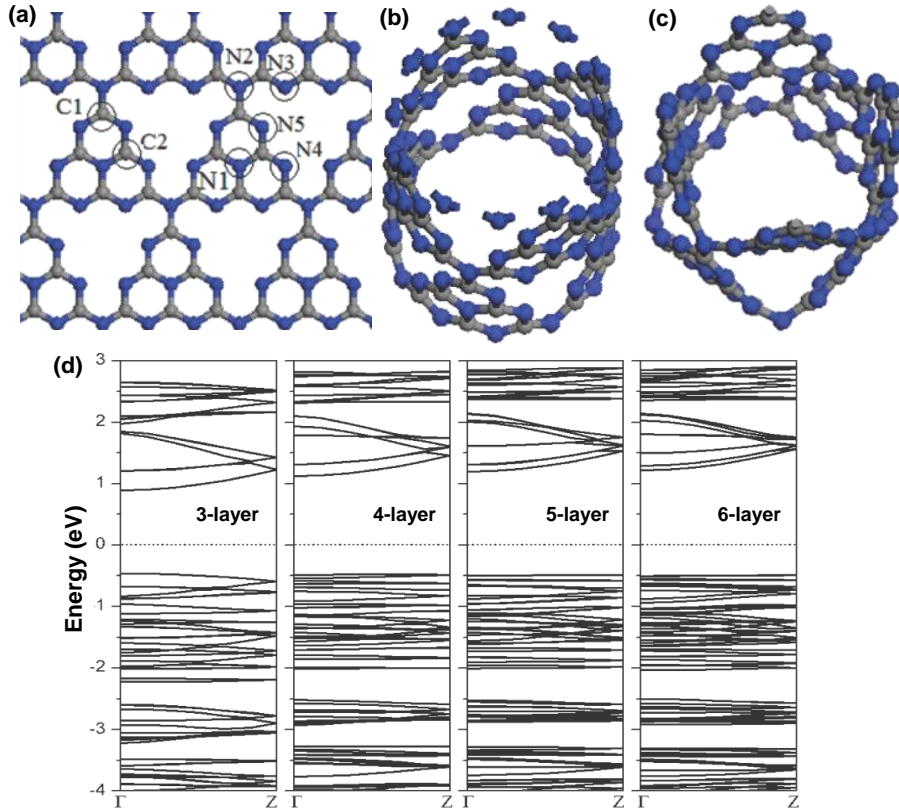


Figure 2.7 Atomic configurations of g- $\text{C}_3\text{N}_4$  with monolayer (a), and nanotube before (b) and after (c) geometry optimisation (The gray and blue balls denote C and N atoms), and the calculated band structures of  $\text{C}_3\text{N}_4$  NTs with an increase in the number of layers (d) [50].

### 2.2.3 Synthesis of $\text{C}_3\text{N}_4$ NTs

As shown in Figure 2.8 g- $\text{C}_3\text{N}_4$  can be facily fabricated via the thermal treatment of low-cost nitrogen-rich precursors such as urea, melamine, dicyandiamide, cyanamide, thiourea, and so forth [46]. Selection of precursors and synthesis conditions affects the properties of g- $\text{C}_3\text{N}_4$ . Melamine is commonly used as the precursors to prepare  $\text{C}_3\text{N}_4$  NTs [53-58]. Other precursors such as urea, ethylenediamine, dicyandiamide and cyanuric chloride have also been reported [59-64].



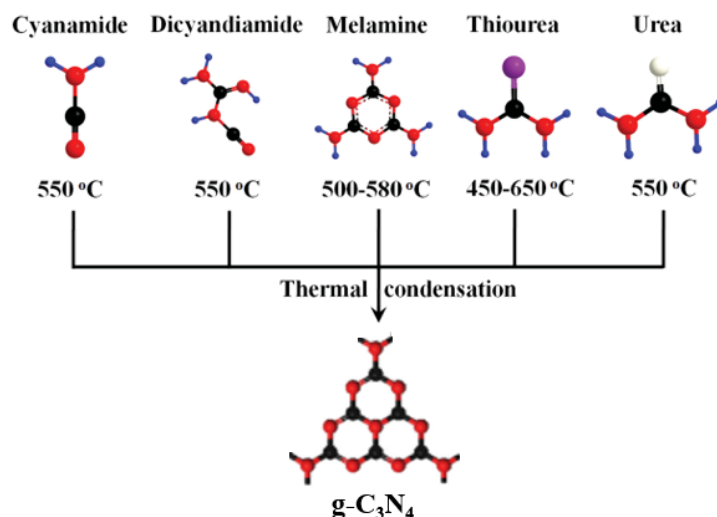


Figure 2.8 Schematic illustration of g-C<sub>3</sub>N<sub>4</sub> synthesis by thermal condensation of the corresponding precursors. The black, red, blue, purple and white balls denote C, N, H, S and O atoms.

Mo et al. reported a two-step process from melamine precursor for preparing C<sub>3</sub>N<sub>4</sub> NTs with high yield and controllable sizes as shown in Figure 2.9a [53]. The possible formation of the nanotubes was based on the NH<sub>3</sub> assisted rolling-up mechanism. During the thermal condensation process, NH<sub>3</sub> gas is released and goes through the supramolecules to form tube-like structures due to pyrolysis of the intermediate. Upon an increase of the annealing temperature, the intermediates become interact and roll up into tubes. Following the same mechanism, controllable fabrication of C<sub>3</sub>N<sub>4</sub> NTs was developed by Gong group. As shown in Figure 2.9b the diameter of about 30 nm with a length over one micron was achieved [54]. A water-induced morphological transformation method was developed based on the nanosheets roll-up mechanism, but the length and the diameter are not controllable (Figure 2.9c) [55]. Li and co-workers fabricated C<sub>3</sub>N<sub>4</sub> NTs by a one-step hydrothermal treatment of melamine. As shown in Figure 2.9d, the prepared nanotubes are uncontrollable due to the distinct sizes of the C<sub>3</sub>N<sub>4</sub> nanosheets [56].

Li et al. reported a one-step solvothermal method to prepare  $C_3N_4$  NTs. It was proposed that the tubular nanostructure was formed via the condensation of -OH groups on the surface of  $C_3N_4$  nanosheets. However, the size of the nanotubes was out of control (Figure 2.9e) [65]. Jin and co-workers synthesised  $C_3N_4$  NTs with a large surface area of  $71.7 \text{ m}^2 \text{ g}^{-1}$  by a two-step condensation of melamine. Firstly, melamine was hydrothermally treated in water for a certain time. Secondly, the samples were treated by condensation. Thus, the diameter of the nanotubes can be controlled by varying the time of thermal treatment as shown in Figure 2.9f [58].

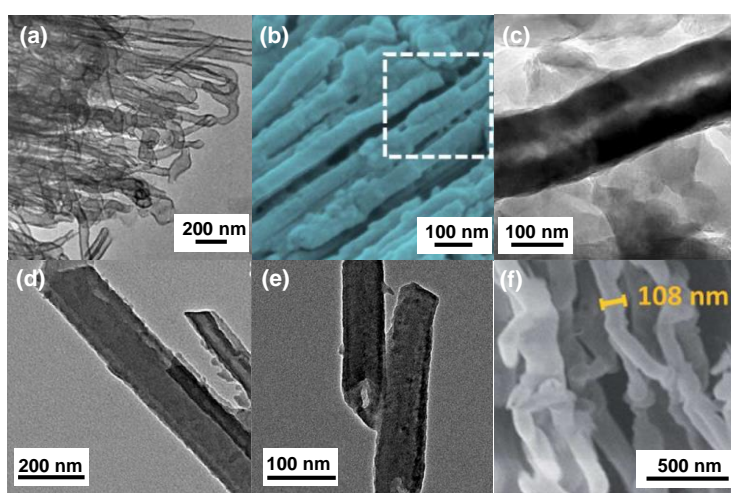


Figure 2.9 TEM images of  $C_3N_4$  NTs made from melamine reported by several groups (a [53], b [54], c [55], d [56], e [65], f [58]).

Wang et al. reported tubular  $C_3N_4$  with different sizes via thermal polymerisation of freeze-dried urea precursor and the morphology is shown in Figure 2.10a [59].  $C_3N_4$  NTs were fabricated with template method by the thermal polymerisation of ethylenediamine and carbon tetrachloride precursors. All the nanotubes were hollow with uniform diameters of approximately 100 nm, which can be seen in Figure 2.10b [60]. The same template strategy was applied by Bian et al. but they used a treated with different heating atmosphere and etching process, resulting in ordered nanotubes with an inner diameter of about 250 nm (Figure 2.10c) [61]. Lee et al. reported a special microwave plasma-enhanced chemical vapour-deposition

process using  $\text{CH}_4$  and  $\text{N}_2$  gases as precursors. In Figure 2.10d the resulting nanotubes were vertically aligned on the silicon substrate and are about  $40\ \mu\text{m}$  in length [62]. Dicyandiamide was used as a precursor along with melamine after their polycondensation at high pressure. The prepared  $\text{C}_3\text{N}_4$  NTs had a diameter of 70-200 nm and a length of about several micrometers (Figure 2.10e) [63]. Huang and co-workers utilised anhydrous  $\text{C}_3\text{N}_3\text{Cl}_3$ , sodium, and  $\text{NiCl}_2$  as precursors to fabricate  $\text{C}_3\text{N}_4$  NTs at 1.8 MPa. As seen in Figure 2.10f the outer diameter of an ordered array is about 50-60 nm array [64].

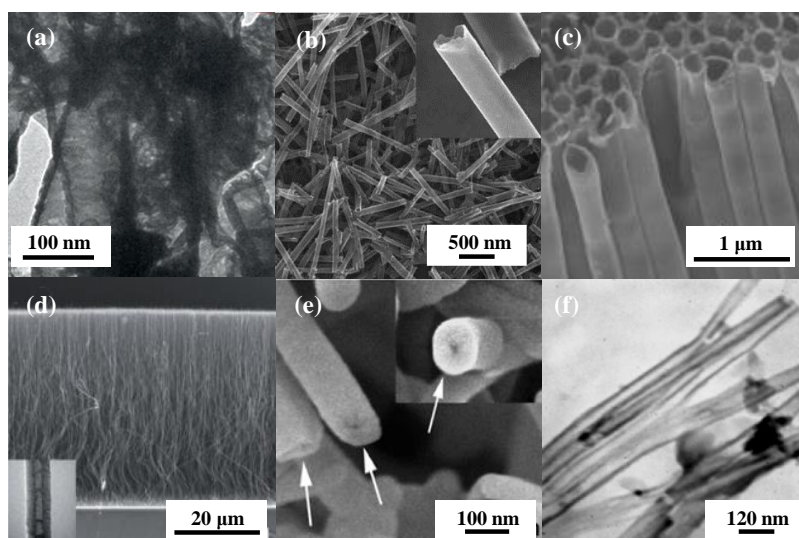


Figure 2.10 The reported TEM images of  $\text{C}_3\text{N}_4$  NTs made from other precursors (a [59], b [60], c [61], d [62], e [63], f [64]).

#### 2.2.4 Modification of $\text{C}_3\text{N}_4$ NTs

$\text{C}_3\text{N}_4$  NTs suffer several intrinsic shortcomings such as low electrical conductivity, low visible light response, and rapid photoinduced charge recombination. To prepare highly efficient  $\text{C}_3\text{N}_4$  NT-based nanostructures, three important criteria must be fulfilled: (i) accelerated charge migration and separation, (ii) improved harvesting of solar light, and (iii) high photochemical stability for prolonged reactions. Design of heterojunction composites has become a feasible and appealing strategy to overcome the above issues, thus improving the photocatalytic activity. Herein, three main strategies, namely metal/ $\text{C}_3\text{N}_4$  NT heterojunctions,

semiconductor/ $\text{C}_3\text{N}_4$  NT heterojunctions and sensitiser/ $\text{C}_3\text{N}_4$  NT heterojunctions will be discussed.

### 2.2.4.1 Metal/ $\text{C}_3\text{N}_4$ NT heterojunctions

Modification of  $\text{C}_3\text{N}_4$  NTs with metal NPs is a fascinating approach to construct metal/ $\text{C}_3\text{N}_4$  NT heterojunctions through the coherent interface. Typical metal NPs employed in  $\text{C}_3\text{N}_4$ -based nanocomposites are noble metals such as Pt, Ag, Pd, and Au [66-70]. By and large, they play three roles: (i) lower the overpotential or the activation energy of  $\text{H}_2$ - or  $\text{NH}_3$ -evolution reactions on the surface of the nanocomposites. (ii) hinder the electron-hole recombination at the interface. (iii) prevent the photo-corrosion and enhance their photochemical stability [4]. As shown in Figure 2.11, when the metal and  $\text{C}_3\text{N}_4$  come into close interaction, their different Fermi levels and work functions act to generate a Schottky barrier and also a depletion layer between the metal and  $\text{C}_3\text{N}_4$ . This induces a built-in electric field as a result of the redistribution of charges at the interface of the metal- $\text{C}_3\text{N}_4$  heterojunction. The resulting band bending accelerates the capture and storage of the excited electrons from  $\text{C}_3\text{N}_4$  to inhibit the recombination of charge carriers. Apart from the typical noble metals, some effective and low-cost transitional metals, such as Cu, Co, and Fe, are also utilised to drive the electron transfer from  $\text{C}_3\text{N}_4$  [71-73].

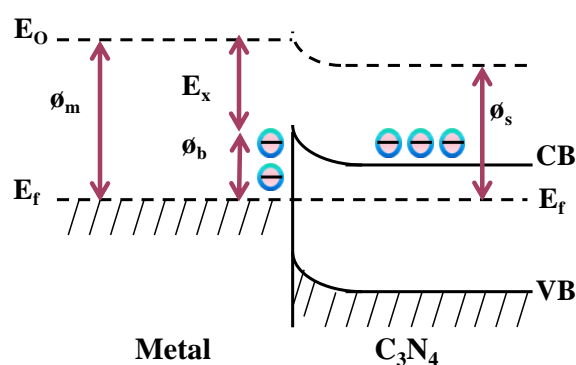


Figure 2.11 Illustrative diagram of the Schottky barrier.

Shiraishi and co-workers loaded Pt NPs less than 4 nm in diameter on  $C_3N_4$  nanosheets for photocatalytic  $H_2$  generation under visible light irradiation. Two different methods, i.e.  $H_2$  reduction under elevated temperatures and photoreduction of Pt precursors, were used to anchor Pt NPs. It is found that the resulting nanocatalysts upon  $H_2$  reduction exhibited 10 times higher activities than those by photoreduction method [74]. Di et al. deposited Au NPs on bulk  $C_3N_4$  by photodeposition, impregnation, and deposition-precipitation approach. The results showed that the nanocomposites fabricated by the deposition-precipitation method revealed the highest  $H_2$  generation rate. Also, alloying with a second metal such as Pt, Pd, Ru, Ag, and Ni, respectively, was explored to enhance the activities [75].

At present, only Pt NPs have been used as cocatalysts on  $C_3N_4$  NTs for simultaneous photocatalytic  $H_2$  generation and organic pollutant degradation by a one-step solvothermal approach. In the presence of ethanol,  $Pt^{4+}$  ions were reduced to metallic Pt NPs under the solvothermal treatment. As shown in Figure 2.12, the sphere-like Pt NPs with an average diameter of about 5 nm were homogeneously dispersed on the internal and external surfaces of  $C_3N_4$  NTs. With an optimal loading content of 2 wt. %, the nanocomposites exhibited the best activity [57].

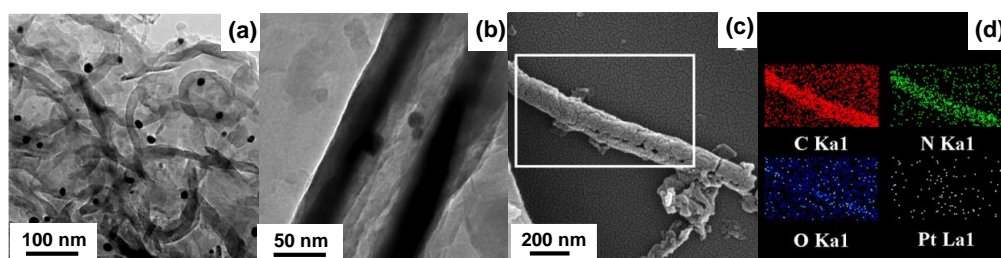


Figure 2.12 TEM images of Pt/ $C_3N_4$  NTs and corresponding EDX mappings [57].

Bimetallic NPs have extensive catalytic applications attributed to their extraordinary physiochemical properties driven from the synergistic effects between the two metals [76]. It is worth noting that the bimetallic systems can achieve chemical transformations, which can

barely be accomplished by the monometallic metals because of the fact that the different metals exhibit a designated role in the catalytic activity, stability, and selectivity. The distribution of the metal atoms can significantly affect the final architectures [77]. Thus far, bimetallic NPs with various architectures including crown-jewel structure, heterostructure, hollow structure, alloyed structure, core-shell structure, and porous structure have emerged. Generally, three different methods consisting of chemical reduction, in situ photoreduction and impregnation-calcination have been explored to load these metals on semiconductor supports.

There are only two bimetallic NPs loaded on bulk  $C_3N_4$  or  $C_3N_4$  nanosheets reported so far. Han et al. developed the AuPd/ $C_3N_4$  nanostructure showing enhancement of visible light absorbance and much higher activities in photocatalytic  $H_2$  generation than the monometallic counterpart and bare bulk  $C_3N_4$  [78]. Furthermore, this group presented an in situ chemical deposition strategy to anchor the PtCo bimetallic NPs on porous  $C_3N_4$  nanosheets. For the PtCo NPs, the surface defects were substantially increased and the Fermi level became lower attributed to the synergistic effect induced by Pt and Co NPs. As a result, they exhibited higher electron capturing capability to decrease the recombination rate of photoinduced electron-holes [79]. Nevertheless, bimetallic nanoparticle-supported  $C_3N_4$  NTs have yet to be studied except for our reported work [80].

#### **2.2.4.2 Semiconductor/ $C_3N_4$ NT heterojunctions**

Upon hybridisation of  $C_3N_4$  with another semiconductor, the band bending is created at the interface of the heterojunction due to the potential difference between the two components. In turn, an internal electric field is formed within a space charge region to spatially separate the photoexcited charges. Figure 2.13 summarises the band potentials of some selected semiconductors in contrast to  $C_3N_4$ . Based on the band positions of the semiconductors, the electronic structures of the formed heterojunction are categorised into three different types as depicted in Figure 2.14 [81, 82].

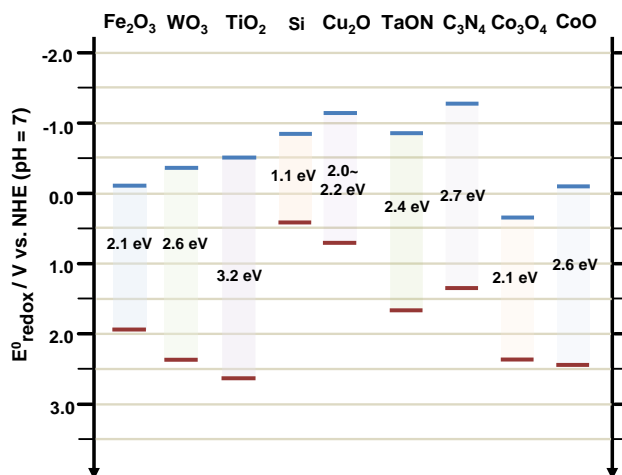


Figure 2.13 Band gap energies of various semiconductor photocatalysts.

As illustrated in Figure 2.14, in a Type I heterojunction, the VB position of semiconductor B is lower than that of semiconductor A, while the CB is higher. Since the electrons will move up and down to get energy balance, they will transfer and accumulate on semiconductor A. Such arrangements are also called straddling gap. In a Type II alignment, both the CB and VB positions of semiconductor B lie higher than those of semiconductor A. The photogenerated electrons will transfer from the CB of semiconductor B to the CB of semiconductor A, and holes transfer from VB(A) to VB(B) simultaneously. The overpotentials between the two components induce upward or downward band bending, resulting in charge migration in the opposite direction. Therefore, Type II (staggered gap) provides the optimum band positions for efficient electron-hole pair separation resulting in enhanced electron lifetimes, thus improved photocatalytic activity. Type III heterojunction shows the same charge carrier transfer as in Type II, only that the band edge potentials are even further set off. This alignment of band gap and potentials is defined as a broken gap [81]. In this context, C<sub>3</sub>N<sub>4</sub> NTs can be recognised as either semiconductor A or semiconductor B depending on the band potentials of the other semiconductor. Coupling C<sub>3</sub>N<sub>4</sub> NTs with an appropriate semiconductor in the heterostructure is of utmost importance, not only to extend the light absorbance but also to ameliorate the charge separation and migration.

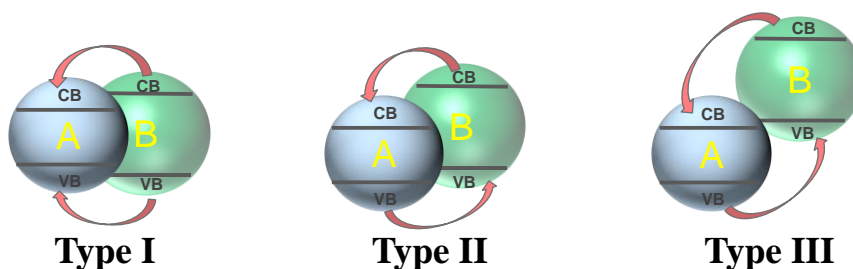


Figure 2.14 Schematic illustration of the charge transfer for the three types of heterojunctions.

Until now, a large number of semiconductors have been constructed with  $C_3N_4$  to form heterojunctions for applications in solar energy conversion, including metal oxides (e.g.  $TiO_2$  [83],  $NiO$  [84],  $WO_3$  [85-87],  $ZnO$  [88],  $Al_2O_3$  [89],  $Ag_2O$  [90],  $V_2O_5$  [91],  $CeO_2$  [92],  $Co_3O_4$  [93],  $CoO$  [94],  $Cu_2O$  [95],  $MoO_3$  [96],  $SnO_2$  [97],  $In_2O_3$  [98] and  $Nb_2O_5$  [99]), multi-component oxides (e.g.  $ZnWO_4$  [100],  $Zn_2GeO_4$  [101],  $ZnFe_2O_4$  [102],  $NaNbO_3$  [103],  $SrTiO_3$  [104],  $DyVO_4$  [105],  $SmVO_4$  [106],  $In_2TiO_5$  [107],  $YVO_4$  [108],  $NaTaO_3$  [109],  $LaVO_4$  [110],  $HNb_3O_8$  [111],  $Zn_2GeO_4$  [101],  $SnNb_2O_6$  [112],  $Bi_2WO_6$  [113],  $BiVO_4$  [114] and 12-tungstophosphoric acid ( $H_3PW_{12}O_{40}$ ) [115]), transition metal hydroxides such as  $Ni(OH)_2$  [116],  $Co(OH)_2$  [117] and  $Cu(OH)_2$  [118], metal sulphides ( $CdS$  [119],  $NiS$  [120],  $MoS_2$  [121],  $WS_2$  [122],  $SnS_2$  [123],  $NiS_2$  [124],  $ZnS$  [125],  $Ag_2S$  [126]), metal organic framework such as Ti-benzenedicarboxylate [127] and UiO-66 [128], organic semiconductors (such as polypyrrole [129], poly(3-hexylthiophene) [130], and graphitised polyacrylonitrile [131]) and other systems like  $AgX$  ( $X = Cl, Br$  and  $I$ ) [132]. Among them, engineering of metal oxides, which are earth-abundant, chemically stable, non-toxic and with easy preparation, will be discussed in detail.

Several studies on the  $TiO_2/C_3N_4$  hybrid nanocomposites have been reported to improve the activities by different methods. Zhou et al. presented the synthesis of  $TiO_2/C_3N_4$  nanocomposites by a simple ball milling strategy [133]. In the work of Muñoz-Batista et al. a simple impregnation process was applied to load  $TiO_2$  on the  $C_3N_4$  surface [83]. In another



work, Shen et al. developed the protonation and in situ deposition for  $\text{TiO}_2/\text{C}_3\text{N}_4$  nanohybrids [134]. A seed-induced solvothermal method was explored to deposit various  $\text{TiO}_2$  nanostructures, such as NPs, 1D nanowires, 2D nanosheets, and 3D nanocrystals, on the surface of  $\text{C}_3\text{N}_4$  as anchoring sites [135]. Additionally, Gu et al. demonstrated a solvent evaporation process to decorate  $\text{TiO}_2$  with exposed (001) facets on  $\text{C}_3\text{N}_4$  nanosheets [136].

Apart from the most intensively studied  $\text{TiO}_2/\text{C}_3\text{N}_4$  nanocomposites,  $\text{ZnO}$ , another type of metal oxide with a wide band gap of about 3.2 eV has been engineered with  $\text{C}_3\text{N}_4$  as well. For example, Wang et al. documented an enhanced photocatalytic performance of  $\text{ZnO}/\text{C}_3\text{N}_4$  prepared by a facile impregnation method. A strong interaction between the two components was evidenced by XPS analyses as shown in Figure 2.15, which accelerated the charge transfer rate. The resulting  $\text{ZnO}/\text{C}_3\text{N}_4$  nanohybrids exhibited the Type II heterojunction charge transfer process [88]. Similarly, binary  $\text{ZnO}/\text{C}_3\text{N}_4$  nanocomposites were fabricated by a one-step facile calcination process by Yu and co-workers. In Figure 2.16 a direct Z-scheme mechanism rather than the conventional heterojunction-type photocatalytic mechanism was proposed on the basis of the photoluminescence analyses of hydroxyl radicals [137]. Kumar and co-workers prepared N-doped  $\text{ZnO}/\text{C}_3\text{N}_4$  core-shell nanoplates, generating a reduced band gap in the nanocomposites, thereby extending the visible light absorbance [138]. A C-doped  $\text{ZnO}/\text{C}_3\text{N}_4$  hybrid nanostructure was synthesised to enhance the visible light response and to separate the photogenerated charge carriers [139].

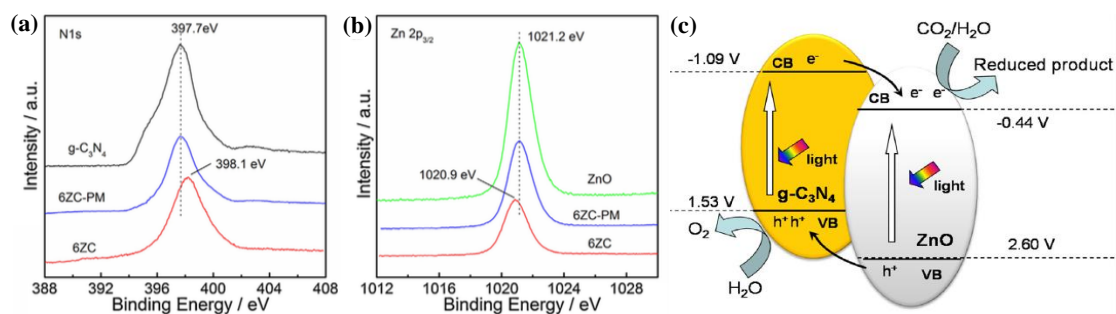


Figure 2.15 XPS analysis (a, b) and charge transfer mechanism across the ZnO/C<sub>3</sub>N<sub>4</sub> heterojunction (c) (6ZC stands for 6 wt. % ZnO to g-C<sub>3</sub>N<sub>4</sub> by an impregnation method and 6ZC-PM represents a physical mixture of 6 wt. % ZnO and C<sub>3</sub>N<sub>4</sub>) [88].

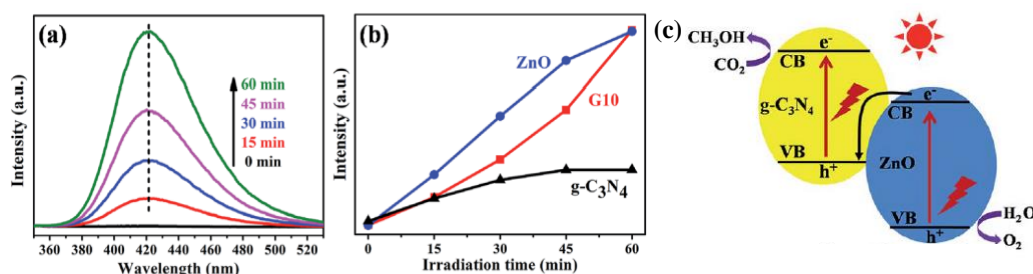


Figure 2.16 Photoluminescence spectral changes (a, b) and schematic illustration of the proposed photocatalytic process on the ZnO/C<sub>3</sub>N<sub>4</sub> heterojunction (c) [137].

Other than decoration with UV-responsive TiO<sub>2</sub> and ZnO semiconductors, Co<sub>3</sub>O<sub>4</sub> has a relatively low band gap of around 2.1 eV, which corresponds to visible light response, thus increasing the potential applications. Visible-light-driven Co<sub>3</sub>O<sub>4</sub>/C<sub>3</sub>N<sub>4</sub> heterostructures were constructed for degrading methyl orange (MO) [140]. The intercalation of Co<sub>3</sub>O<sub>4</sub> NPs into the C<sub>3</sub>N<sub>4</sub> interlayers was beneficial for the detection of environmental phenolic hormones [141]. Similarly, nanostructured Co<sub>3</sub>O<sub>4</sub> NPs with 10-15 nm in size on the C<sub>3</sub>N<sub>4</sub> nanosheets were prepared by one-pot synthetic technique [142]. The same loading method was used to load Co<sub>3</sub>O<sub>4</sub> on the C<sub>3</sub>N<sub>4</sub> surface for H<sub>2</sub> production [143].

Recently, CoO NPs decorated with C<sub>3</sub>N<sub>4</sub> photocatalysts were prepared by a facile one-pot process. The CoO NP sizes are in the range of 30-50 nm. The composites exhibited remarkably

increased photocatalytic  $\text{H}_2$  generation, which was mainly attributed to the synergistic effect of CoO and  $\text{C}_3\text{N}_4$  [144]. A series of CoO/ $\text{C}_3\text{N}_4$  composites were constructed by Han and co-workers for overall water splitting without any sacrificial reagent. It is found that during the oxidation process of water, CoO accelerated the decomposition of  $\text{H}_2\text{O}_2$  [145]. The Type II CoO/ $\text{C}_3\text{N}_4$  heterojunction was fabricated by another solvothermal technique for overall water splitting under visible light irradiation [94].

Until now,  $\text{TiO}_2$  and  $\text{H}_3\text{PW}_{12}\text{O}_{40}$  have been reported to decorate with  $\text{C}_3\text{N}_4$  NTs to form heterojunctions [56, 115]. A series of non-metallic elements co-doped  $\text{TiO}_2$  were deposited on  $\text{C}_3\text{N}_4$  NTs for organic photodegradation and  $\text{H}_2$  production under visible light irradiation. An appropriate bandgap structure of  $\text{TiO}_2$  component is beneficial for the separation and transport of the photoexcited charges between  $\text{TiO}_2$  and  $\text{C}_3\text{N}_4$  [56].  $\text{H}_3\text{PW}_{12}\text{O}_{40}$ , a polyoxometalate, is widely used in homogeneous photocatalytic reactions attributed to its low cost, low toxicity, efficient electron trapping property and well-defined Keggin structure.  $\text{H}_3\text{PW}_{12}\text{O}_{40}$ -decorated  $\text{C}_3\text{N}_4$  NT nanostructure as shown in Figure 2.17, exhibited significantly high visible-light activity and stability in degrading MO. The good performance was attributed to the unique tubular nanostructure, strong light absorption, as well as high stability because of the strong chemical bonding between the Keggin unit and  $\text{C}_3\text{N}_4$  NTs [115].

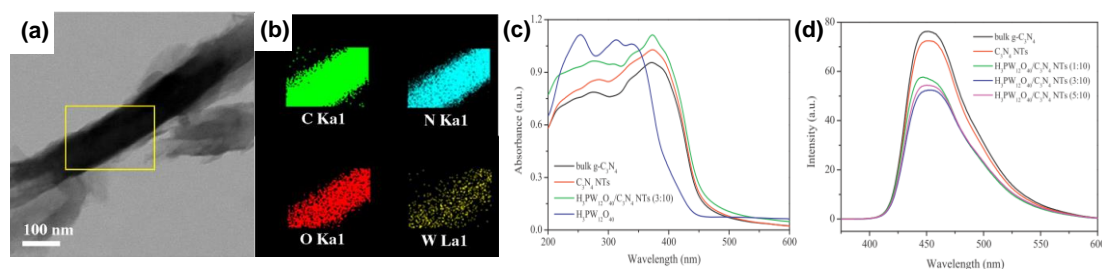


Figure 2.17 TEM images of  $\text{H}_3\text{PW}_{12}\text{O}_{40}/\text{C}_3\text{N}_4$  NTs (a) and corresponding EDX mappings (b); UV-vis/DRS (c) and PL (d) spectra of bulk  $\text{C}_3\text{N}_4$ ,  $\text{C}_3\text{N}_4$  NTs,  $\text{H}_3\text{PW}_{12}\text{O}_{40}$  and  $\text{H}_3\text{PW}_{12}\text{O}_{40}/\text{C}_3\text{N}_4$  NTs [115].

### 2.2.4.3 Sensitiser/C<sub>3</sub>N<sub>4</sub> NT heterojunctions

Despite the above endeavours, the absorption of C<sub>3</sub>N<sub>4</sub> NT-based catalysts with a longer wavelength absorption of sunlight is still a challenge. Sensitisation is one of the attractive techniques to extend the light absorption toward a higher wavelength range. As a case in point, dye organic molecules such as Rose Bengal [146], Eosin Y [147, 148], fluorescein [69], dibromofluorescein [149], indole-based D- $\pi$ -A [150], Erythrosin B [151] and so forth have been applied as a sensitiser to efficiently harvest solar energy by absorbing light with wavelengths longer than 600 nm during the photocatalytic process.

Lanthanide upconversion nanoparticles (UCNPs), a kind of fluorescein, which are generally comprised of an inorganic host and lanthanide dopant ions acting as sensitisers and activators as shown in Figure 2.18. The UCNPs convert NIR light with two or more low-energy excitation photons into shorter wavelength emissions like visible and UV light. There are five basic mechanisms of lanthanide upconversion processes: excited-state absorption, energy-transfer upconversion, cross relaxation, cooperative sensitisation upconversion, and photon avalanche. Comparatively, cooperative sensitisation upconversion is an inefficient process and photon avalanche is rarely found in lanthanide nanomaterials [152, 153]. Basically, ideal host materials should be transparent and have low lattice phonon energies in order to maximise the radiative emission and minimise the nonradiative loss. Generally, fluorides exhibit high chemical stability and low phonon energies and thus are usually used as the host materials. By far, NaYF<sub>4</sub> has been recognised as the most popular host for lanthanide dopant ions for upconversion processes.

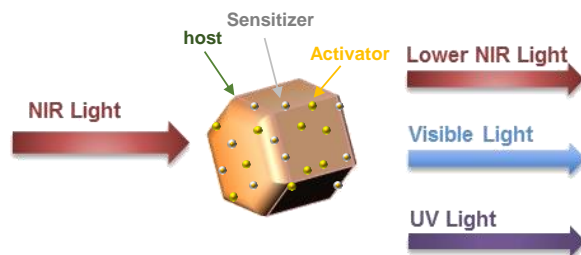


Figure 2.18 Illustration of lanthanide UCNPs.

In a work by Li et al. they designed NIR-triggered NaYF<sub>4</sub>:Yb,Tm/ hybrid nanocomposites, as shown in Figure 2.19 via the energy gap engineering [154]. The C<sub>3</sub>N<sub>4</sub> nanosheets were formed by a copolymerisation technique using dicyandiamide and an organic monomer 2-aminobenzonitrile followed by an exfoliation process. After that, C<sub>3</sub>N<sub>4</sub> nanosheets were coated on NaYF<sub>4</sub>:Yb,Tm microrods. The molecularly grafted C<sub>3</sub>N<sub>4</sub> endowed various intriguing properties such as extended  $\pi$ -conjugated electronic structures, increased surface area, decreased band gap, enhanced light absorption, and ameliorated charge separation. As a result of the ingenious energy gap match of molecularly grafted C<sub>3</sub>N<sub>4</sub> nanosheets and upconversion phosphors, the assembled composites can convert NIR to visible light and afford high activity in photocatalytic RhB degradation.

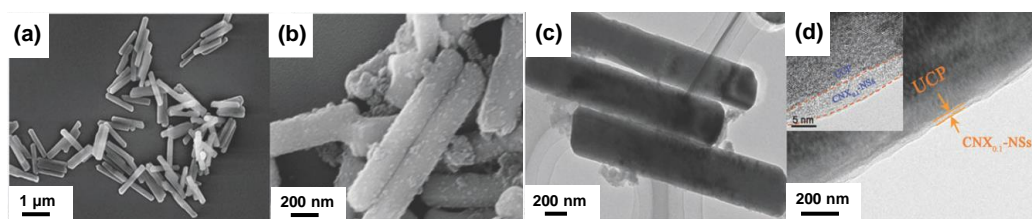


Figure 2.19 SEM images of NaYF<sub>4</sub>:Yb,Tm (a) and UCNPs/CNX 0.1-NSs (b); (c) TEM and (d) HRTEM images of UCNPs/CNX 0.1-NSs (The inset in d is a further magnified image) [154].

Besides that, NaYF<sub>4</sub>:Yb,Tm NPs were facilely integrated on C<sub>3</sub>N<sub>4</sub> nanosheets by a stepwise method [155]. In the heterojunction NaYF<sub>4</sub>:Yb,Tm NPs function as a light converter to provide UV and visible light by absorbing NIR light for the photoexcitation in C<sub>3</sub>N<sub>4</sub> to create more

electron-hole pairs. As such, this broadens the whole solar spectrum to effectively utilise sunlight for photocatalytic decoloration of methylene blue and phenol. Similar material construction and photocatalytic application were also found by Li's group [156, 157]. Nevertheless, the detailed mechanism in the energy transfer within the  $C_3N_4$ -based heterojunctions has yet to be investigated, not to mention the support as  $C_3N_4$  NTs, although there have been studies of the energy transfer mechanisms in heterojunctions of  $NaYF_4:Yb,Tm/TiO_2$  [158-160] and  $NaYF_4:Yb,Tm/ZnO$  [161].

## 2.3 Summary

This chapter begins with the general introduction of photocatalysis, followed by the fundamentals of photocatalytic  $H_2$  generation and  $N_2$  fixation. After that, the basic characteristics of  $C_3N_4$  NTs, including the crystal structure, electronic and optical properties are presented. In order to overcome the shortcomings of low visible light response and fast electron-hole recombination, constructing heterojunction architectures of metal/ $C_3N_4$  NTs, semiconductor/ $C_3N_4$  NTs and sensitiser/ $C_3N_4$  NTs has been put forward and discussed in-depth. Although numerous efforts have been put into the research, more efficient catalysts to meet commercially acceptable quantum efficiency are still required. In addition, a better understanding including the charge carrier dynamics and the reaction mechanisms is of great importance for photocatalytic  $H_2$  generation and  $N_2$  fixation. The next few chapters will demonstrate the efforts undertaken on the synthesis of efficient  $C_3N_4$  NT-based catalysts for photocatalytic  $H_2$  generation and  $N_2$  fixation.

## References

- [1] M.R. Hoffmann, S.T. Martin, W. Choi, D.W. Chemical Reviews, 95 (1995) 69-96.
- [2] A. Kudo, Y. Miseki, Chemical Society Reviews, 38 (2009) 253-278.

- [3] H. Tong, S. Ouyang, Y. Bi, N. Umezawa, M. Oshikiri, J. Ye, *Advanced Materials*, 24 (2012) 229-251.
- [4] J. Ran, J. Zhang, J. Yu, M. Jaroniec, S.Z. Qiao, *Chemical Society Reviews*, 43 (2014) 7787-7812.
- [5] A. Kudo, H. Kato, I. Tsuji, *Chemistry Letters*, 33 (2004) 1534-1539.
- [6] Y. Qu, X. Duan, *Chemical Society Reviews*, 42 (2013) 2568-2580.
- [7] X. Li, J. Yu, M. Jaroniec, *Chemical Society Reviews*, 45 (2016) 2603-2636.
- [8] C. Chen, W. Ma, J. Zhao, *Chemical Society Reviews*, 39 (2010) 4206.
- [9] Z. Han, R. Eisenberg, *Accounts of Chemical Research*, 47 (2014) 2537-2544.
- [10] C.-H. Liao, C.-W. Huang, J.C.S. Wu, *Catalysts*, 2 (2012) 490-516.
- [11] S.Y. Tee, K.Y. Win, W.S. Teo, L.D. Koh, S. Liu, C.P. Teng, M.Y. Han, *Advanced Science*, 4 (2017) 1600337.
- [12] C. Grimes, O. Varghese, S. Ranjan, Springer Science & Business Media, 2007.
- [13] J. Schneider, D.W. Bahnemann, *The Journal of Physical Chemistry Letters*, 4 (2013) 3479-3483.
- [14] X. Chen, S. Shen, L. Guo, S.S. Mao, *Chemical Reviews*, 110 (2010) 6503-6570.
- [15] Y. Pellegrin, F. Odobel, *Comptes Rendus Chimie*, (2016).
- [16] T. Peng, K. Li, P. Zeng, Q. Zhang, X. Zhang, *The Journal of Physical Chemistry C*, 116 (2012) 22720-22726.
- [17] Y. Zhu, Y. Wang, Z. Chen, L. Qin, L. Yang, L. Zhu, P. Tang, T. Gao, Y. Huang, Z. Sha, G. Tang, *Applied Catalysis A: General*, 498 (2015) 159-166.
- [18] I. Tsuji, H. Kato, H. Kobayashi, A. Kudo, *Journal of the American Chemical Society*, 126 (2004) 13406-13413.
- [19] F. Fresno, R. Portela, S. Suárez, J.M. Coronado, *Journal of Materials Chemistry A*, 2 (2014) 2863-2884.

- [20] G. Schrauzer, T. Guth, *Journal of the American Chemical Society*, 99 (1977) 7189-7193.
- [21] A.J. Medford, M.C. Hatzell, *ACS Catalysis*, 7 (2017) 2624-2643.
- [22] L. Zang, Springer, 2011.
- [23] G.N. Schrauzer, N. Strampach, L.N. Hui, M.R. Palmer, J. Salehi, *Proceedings of the National Academy of Sciences*, 80 (1983) 3873-3876.
- [24] A. Banerjee, B.D. Yuhas, E.A. Margulies, Y. Zhang, Y. Shim, M.R. Wasielewski, M.G. Kanatzidis, *Journal of the American Chemical Society*, 137 (2015) 2030-2034.
- [25] C.J. van der Ham, M.T. Koper, D.G. Hetterscheid, *Chemical Society Reviews*, 43 (2014) 5183-5191.
- [26] S. Sun, X. Li, W. Wang, L. Zhang, X. Sun, *Applied Catalysis B: Environmental*, 200 (2017) 323-329.
- [27] M.A. Shipman, M.D. Symes, *Catalysis Today*, 286 (2017) 57-68.
- [28] C. Guo, J. Ran, A. Vasileff, S.-Z. Qiao, *Energy & Environmental Science*, 11 (2018) 45-56.
- [29] X. Chen, N. Li, Z. Kong, W.-J. Ong, X. Zhao, *Materials Horizons*, 5 (2018) 9-27.
- [30] W.J. Ong, L.L. Tan, Y.H. Ng, S.T. Yong, S.P. Chai, *Chemical Reviews*, 116 (2016) 7159-7329.
- [31] L. Gmelin, *Annalen der Pharmacie*, 15 (1835) 252-258.
- [32] E.C. Franklin, *Journal of the American Chemical Society*, 44 (1922) 486-509.
- [33] L. Pauling, J. Sturdivant, *Proceedings of the National Academy of Sciences*, 23 (1937) 615-620.
- [34] C. Redemann, H. Lucas, *Journal of the American Chemical Society*, 62 (1940) 842-846.
- [35] R.S. Hosmane, M.A. Rossman, N.J. Leonard, *Journal of the American Chemical Society*, 104 (1982) 5497-5499.
- [36] X. Wang, S. Blechert, M. Antonietti, *ACS Catalysis*, 2 (2012) 1596-1606.



- [37] A.Y. Liu, M.L. Cohen, *Science*, 245 (1989) 841-842.
- [38] E. Kroke, Novel group 14 nitrides, *Coordination Chemistry Reviews*, 248 (2004) 493-532.
- [39] F. Goettmann, A. Fischer, M. Antonietti, A. Thomas, *Chemical Communications*, (2006) 4530-4532.
- [40] X. Wang, K. Maeda, A. Thomas, K. Takanabe, G. Xin, J.M. Carlsson, K. Domen, M. Antonietti, *Nature Materials*, 8 (2009) 76-80.
- [41] G. Dong, W. Ho, C. Wang, *Journal of Materials Chemistry A*, 3 (2015) 23435-23441.
- [42] D.M. Teter, R.J. Hemley, *Science*, 271 (1996) 53-55.
- [43] Q. Han, N. Chen, J. Zhang, L. Qu, *Materials Horizons*, 4 (2017) 832-850.
- [44] D. Masih, Y. Ma, S. Rohani, *Applied Catalysis B: Environmental*, 206 (2017) 556-588.
- [45] S.C. Yan, Z.S. Li, Z.G. Zou, *Langmuir: the ACS journal of surfaces and colloids*, 25 (2009) 10397-10401.
- [46] S. Cao, J. Low, J. Yu, M. Jaroniec, *Advanced Materials*, 27 (2015) 2150-2176.
- [47] G. Dong, Y. Zhang, Q. Pan, J. Qiu, *Journal of Photochemistry and Photobiology C: Photochemistry Reviews*, 20 (2014) 33-50.
- [48] Y. Gong, M. Li, Y. Wang, *ChemSusChem*, 8 (2015) 931-946.
- [49] S. Cao, J. Yu, *The journal of physical chemistry letters*, 5 (2014) 2101-2107.
- [50] H. Pan, Y.-W. Zhang, V.B. Shenoy, H. Gao, *ACS Catalysis*, 1 (2011) 99-104.
- [51] G.L. Chai, C.S. Lin, J. Wei, M.Y. Zhang, W.D. Cheng, *Physical chemistry chemical physics: PCCP*, 14 (2012) 835-839.
- [52] H. Pan, Y.P. Feng, J. Lin, *Physical Review B*, 74 (2006) 045409.
- [53] Z. Mo, H. Xu, Z. Chen, X. She, Y. Song, J. Wu, P. Yan, L. Xu, Y. Lei, S. Yuan, H. Li, *Applied Catalysis B: Environmental*, 225 (2018) 154-161.
- [54] S. Wang, C. Li, T. Wang, P. Zhang, A. Li, J. Gong, *Journal of Materials Chemistry A*, 2 (2014) 2885.

- [55] Z. Zeng, K. Li, L. Yan, Y. Dai, H. Guo, M. Huo, Y. Guo, *RSC Advances*, 4 (2014) 59513-59518.
- [56] K. Li, Z. Zeng, L. Yan, M. Huo, Y. Guo, S. Luo, X. Luo, *Applied Catalysis B: Environmental*, 187 (2016) 269-280.
- [57] K. Li, Z. Zeng, L. Yan, S. Luo, X. Luo, M. Huo, Y. Guo, *Applied Catalysis B: Environmental*, 165 (2015) 428-437.
- [58] Z. Jin, Q. Zhang, S. Yuan, T. Ohno, *RSC Advances*, 5 (2015) 4026-4029.
- [59] Y. Wang, X. Liu, J. Liu, B. Han, X. Hu, F. Yang, Z. Xu, Y. Li, S. Jia, Z. Li, Y. Zhao, *Angewandte Chemie*, 57 (2018) 5765-5771.
- [60] X. Lu, H. Wang, S. Zhang, D. Cui, Q. Wang, *Solid State Sciences*, 11 (2009) 428-432.
- [61] S. Bian, Z. Ma, W. Song, *The Journal of Physical Chemistry C*, 113 (2009) 8668-8672.
- [62] J.W. Lee, R. Viswan, Y.J. Choi, Y. Lee, S.Y. Kim, J. Cho, Y. Jo, J.K. Kang, *Advanced Functional Materials*, 19 (2009) 2213-2218.
- [63] J. Li, C. Cao, H. Zhu, *Nanotechnology*, 18 (2007) 115605.
- [64] F. Huang, *Chinese Science Bulletin*, 50 (2005) 626.
- [65] K. Li, Z. Zeng, L. Yan, S. Luo, X. Luo, M. Huo, Y. Guo, *Applied Catalysis B: Environmental*, 165 (2015) 428-437.
- [66] J. Xue, S. Ma, Y. Zhou, Z. Zhang, M. He, *ACS Applied Materials & Interfaces*, 7 (2015) 9630-9637.
- [67] S. Liang, Y. Xia, S. Zhu, S. Zheng, Y. He, J. Bi, M. Liu, L. Wu, *Applied Surface Science*, 358 (2015) 304-312.
- [68] S.P. Adhikari, H.R. Pant, J.H. Kim, H.J. Kim, C.H. Park, C.S. Kim, *Colloids and Surfaces A: Physicochemical and Engineering Aspects*, 482 (2015) 477-484.
- [69] J. Qin, J. Huo, P. Zhang, J. Zeng, T. Wang, H. Zeng, *Nanoscale*, 8 (2016) 2249-2259.
- [70] Y. Li, X. Xu, P. Zhang, Y. Gong, H. Li, Y. Wang, *RSC Advances*, 3 (2013) 10973.

- [71] W. Zhang, J. Albero, L. Xi, K.M. Lange, H. Garcia, X. Wang, M. Shalom, *ACS Applied Materials & Interfaces*, 9 (2017) 32667-32677.
- [72] V. Di Noto, E. Negro, *Fuel Cells*, 10 (2010) 234-244.
- [73] P. Zhang, T. Wang, H. Zeng, *Applied Surface Science*, 391 (2017) 404-414.
- [74] Y. Shiraishi, Y. Kofuji, S. Kanazawa, H. Sakamoto, S. Ichikawa, S. Tanaka, T. Hirai, *Chemical Communications*, 50 (2014) 15255-15258.
- [75] Y. Di, X. Wang, A. Thomas, M. Antonietti, *ChemCatChem*, 2 (2010) 834-838.
- [76] X. Liu, D. Wang, Y. Li, *Nano Today*, 7 (2012) 448-466.
- [77] J.W. Hong, D. Kim, Y.W. Lee, M. Kim, S.W. Kang, S.W. Han, *Angewandte Chemie*, 50 (2011) 8876-8880.
- [78] C. Han, L. Wu, L. Ge, Y. Li, Z. Zhao, *Carbon*, 92 (2015) 31-40.
- [79] C. Han, Y. Lu, J. Zhang, L. Ge, Y. Li, C. Chen, Y. Xin, L. Wu, S. Fang, *Journal of Materials Chemistry A*, 3 (2015) 23274-23282.
- [80] Y. Zhu, A. Marianov, H. Xu, C. Lang, Y. Jiang, *ACS Applied Materials & Interfaces*, 10 (2018) 9468-9477.
- [81] S.J.A. Moniz, S.A. Shevlin, D.J. Martin, Z.-X. Guo, J. Tang, *Energy & Environmental Science*, 8 (2015) 731-759.
- [82] R. Marschall, *Advanced Functional Materials*, 24 (2014) 2421-2440.
- [83] M.J. Muñoz-Batista, A. Kubacka, M. Fernández-García, *Catalysis Science & Technology*, 4 (2014) 2006.
- [84] H. Chen, L. Qiu, J. Xiao, S. Ye, X. Jiang, Y. Yuan, *RSC Advances*, 4 (2014) 22491.
- [85] W. Zhu, F. Sun, R. Goei, Y. Zhou, *Catalysis Science & Technology*, 7 (2017) 2591-2600.
- [86] T. Xiao, Z. Tang, Y. Yang, L. Tang, Y. Zhou, Z. Zou, *Applied Catalysis B: Environmental*, 220 (2018) 417-428.

- [87] W. Yu, J. Chen, T. Shang, L. Chen, L. Gu, T. Peng, *Applied Catalysis B: Environmental*, 219 (2017) 693-704.
- [88] Y. He, Y. Wang, L. Zhang, B. Teng, M. Fan, *Applied Catalysis B: Environmental*, 168-169 (2015) 1-8.
- [89] F.T. Li, Y. Zhao, Q. Wang, X.J. Wang, Y.J. Hao, R.H. Liu, D. Zhao, *Journal of hazardous materials*, 283 (2015) 371-381.
- [90] M. Xu, L. Han, S. Dong, *ACS Applied Materials & Interfaces*, 5 (2013) 12533-12540.
- [91] Y. Hong, Y. Jiang, C. Li, W. Fan, X. Yan, M. Yan, W. Shi, *Applied Catalysis B: Environmental*, 180 (2016) 663-673.
- [92] M. Li, L. Zhang, M. Wu, Y. Du, X. Fan, M. Wang, L. Zhang, Q. Kong, J. Shi, *Nano Energy*, 19 (2016) 145-155.
- [93] X. Hao, Z. Jin, G. Lu, *Chemistry Letters*, 45 (2016) 116-118.
- [94] F. Guo, W. Shi, C. Zhu, H. Li, Z. Kang, *Applied Catalysis B: Environmental*, 226 (2018) 412-420.
- [95] J. Chen, S. Shen, P. Guo, M. Wang, P. Wu, X. Wang, L. Guo, *Applied Catalysis B: Environmental*, 152-153 (2014) 335-341.
- [96] L. Huang, H. Xu, R. Zhang, X. Cheng, J. Xia, Y. Xu, H. Li, *Applied Surface Science*, 283 (2013) 25-32.
- [97] Y. He, L. Zhang, M. Fan, X. Wang, M.L. Walbridge, Q. Nong, Y. Wu, L. Zhao, *Solar Energy Materials and Solar Cells*, 137 (2015) 175-184.
- [98] S. Cao, X. Liu, Y. Yuan, Z. Zhang, Y. Liao, J. Fang, S.C.J. Loo, T. Sum, C. Xue, *Applied Catalysis B: Environmental*, 147 (2014) 940-946.
- [99] X. Wang, G. Chen, C. Zhou, Y. Yu, G. Wang, *European Journal of Inorganic Chemistry*, 2012 (2012) 1742-1749.

- [100] L. Sun, X. Zhao, C.-J. Jia, Y. Zhou, X. Cheng, P. Li, L. Liu, W. Fan, *Journal of Materials Chemistry*, 22 (2012) 23428.
- [101] L. Sun, Y. Qi, C.J. Jia, Z. Jin, W. Fan, *Nanoscale*, 6 (2014) 2649-2659.
- [102] J. Chen, S. Shen, P. Guo, P. Wu, L. Guo, *Journal of Materials Chemistry A*, 2 (2014) 4605-4612.
- [103] H. Shi, G. Chen, C. Zhang, Z. Zou, *ACS Catalysis*, 4 (2014) 3637-3643.
- [104] S. Kumar, S. Tonda, A. Baruah, B. Kumar, V. Shanker, *Dalton Transactions*, 43 (2014) 16105-16114.
- [105] H. Li, Y. Liu, Y. Cui, W. Zhang, C. Fu, X. Wang, *Applied Catalysis B: Environmental*, 183 (2016) 426-432.
- [106] T. Li, L. Zhao, Y. He, J. Cai, M. Luo, J. Lin, *Applied Catalysis B: Environmental*, 129 (2013) 255-263.
- [107] Y. Liu, G. Chen, C. Zhou, Y. Hu, D. Fu, J. Liu, Q. Wang, *Journal of Hazardous Materials*, 190 (2011) 75-80.
- [108] J. Cai, Y. He, X. Wang, L. Zhang, L. Dong, H. Lin, L. Zhao, X. Yi, W. Weng, H. Wan, *RSC Advances*, 3 (2013) 20862.
- [109] S. Kumar, B. Kumar, T. Surendar, V. Shanker, *Materials Research Bulletin*, 49 (2014) 310-318.
- [110] Y. He, J. Cai, L. Zhang, X. Wang, H. Lin, B. Teng, L. Zhao, W. Weng, H. Wan, M. Fan, *Industrial & Engineering Chemistry Research*, 53 (2014) 5905-5915.
- [111] H. Pan, X. Li, Z. Zhuang, C. Zhang, *Journal of Molecular Catalysis A: Chemical*, 345 (2011) 90-95.
- [112] Z. Zhang, D. Jiang, D. Li, M. He, M. Chen, *Applied Catalysis B: Environmental*, 183 (2016) 113-123.

- [113] Y. Tian, B. Chang, J. Lu, J. Fu, F. Xi, X. Dong, *ACS Applied Materials & Interfaces*, 5 (2013) 7079-7085.
- [114] C. Li, S. Wang, T. Wang, Y. Wei, P. Zhang, J. Gong, *Small*, 10 (2014) 2783-2790.
- [115] K. Li, L. Yan, Z. Zeng, S. Luo, X. Luo, X. Liu, H. Guo, Y. Guo, *Applied Catalysis B: Environmental*, 156-157 (2014) 141-152.
- [116] J. Yu, S. Wang, B. Cheng, Z. Lin, F. Huang, *Catalysis Science & Technology*, 3 (2013) 1782.
- [117] G. Zhang, S. Zang, X. Wang, *ACS Catalysis*, 5 (2015) 941-947.
- [118] X. Zhou, Z. Luo, P. Tao, B. Jin, Z. Wu, Y. Huang, *Materials Chemistry and Physics*, 143 (2014) 1462-1468.
- [119] X. Yang, W. Xin, X. Yin, X. Shao, *Chemical Physics Letters*, 651 (2016) 127-132.
- [120] Y. Lu, D. Chu, M. Zhu, Y. Du, P. Yang, *Physical Chemistry Chemical Physics: PCCP*, 17 (2015) 17355-17361.
- [121] J. Wang, Z. Guan, J. Huang, Q. Li, J. Yang, *Journal of Materials Chemistry A*, 2 (2014) 7960.
- [122] Y. Hou, Y. Zhu, Y. Xu, X. Wang, *Applied Catalysis B: Environmental*, 156-157 (2014) 122-127.
- [123] Z. Zhang, J. Huang, M. Zhang, Q. Yuan, B. Dong, *Applied Catalysis B: Environmental*, 163 (2015) 298-305.
- [124] L. Yin, Y.-P. Yuan, S.-W. Cao, Z. Zhang, C. Xue, *RSC Advances*, 4 (2014) 6127.
- [125] J. Wang, P. Guo, Q. Guo, P.G. Jönsson, Z. Zhao, *CrystEngComm*, 16 (2014) 4485-4492.
- [126] D. Jiang, L. Chen, J. Xie, M. Chen, *Dalton Transactions*, 43 (2014) 4878-4885.
- [127] H. Wang, X. Yuan, Y. Wu, G. Zeng, X. Chen, L. Leng, H. Li, *Applied Catalysis B: Environmental*, 174-175 (2015) 445-454.

- [128] R. Wang, L. Gu, J. Zhou, X. Liu, F. Teng, C. Li, Y. Shen, Y. Yuan, *Advanced Materials Interfaces*, 2 (2015) 1500037.
- [129] S. Hu, L. Ma, H. Wang, L. Zhang, Y. Zhao, G. Wu, *RSC Advances*, 5 (2015) 31947-31953.
- [130] H. Yan, Y. Huang, *Chemical Communications*, 47 (2011) 4168-4170.
- [131] F. He, G. Chen, Y. Yu, S. Hao, Y. Zhou, Y. Zheng, *ACS Applied Materials & Interfaces*, 6 (2014) 7171-7179.
- [132] W.-J. Ong, L.K. Putri, L.-L. Tan, S.-P. Chai, S.-T. Yong, *Applied Catalysis B: Environmental*, 180 (2016) 530-543.
- [133] J. Zhou, M. Zhang, Y. Zhu, *Physical chemistry chemical physics : PCCP*, 17 (2015) 3647-3652.
- [134] J. Shen, H. Yang, Q. Shen, Y. Feng, Q. Cai, *CrystEngComm*, 16 (2014) 1868-1872.
- [135] Y. Li, J. Wang, Y. Yang, Y. Zhang, D. He, Q. An, G. Cao, *Journal of Hazardous Materials*, 292 (2015) 79-89.
- [136] L. Gu, J. Wang, Z. Zou, X. Han, *Journal of Hazardous Materials*, 268 (2014) 216-223.
- [137] W. Yu, D. Xu, T. Peng, *Journal of Materials Chemistry A*, 3 (2015) 19936-19947.
- [138] S. Kumar, A. Baruah, S. Tonda, B. Kumar, V. Shanker, B. Sreedhar, *Nanoscale*, 6 (2014) 4830-4842.
- [139] Y. Zhu, M. Li, Y. Liu, T. Ren, Z. Yuan, *The Journal of Physical Chemistry C*, 118 (2014) 10963-10971.
- [140] C. Han, L. Ge, C. Chen, Y. Li, X. Xiao, Y. Zhang, L. Guo, *Applied Catalysis B: Environmental*, 147 (2014) 546-553.
- [141] Y. Sun, J. Jiang, Y. Liu, S. Wu, J. Zou, *Applied Surface Science*, 430 (2018) 362-370.
- [142] P. Suyana, P. Ganguly, B.N. Nair, A.P. Mohamed, K.G.K. Warriar, U.S. Hareesh, *Environmental Science: Nano*, 4 (2017) 212-221.

- [143] S. Guo, S. Zhao, X. Wu, H. Li, Y. Zhou, C. Zhu, N. Yang, X. Jiang, J. Gao, L. Bai, Y. Liu, Y. Lifshitz, S.T. Lee, Z. Kang, *Nature Communications*, 8 (2017) 1828.
- [144] Z. Mao, J. Chen, Y. Yang, D. Wang, L. Bie, B.D. Fahlman, *ACS Applied Materials & Interfaces*, 9 (2017) 12427-12435.
- [145] M. Han, H. Wang, S. Zhao, L. Hu, H. Huang, Y. Liu, *Inorganic Chemistry Frontiers*, 4 (2017) 1691-1696.
- [146] Z. Li, Y. Wu, G. Lu, *Applied Catalysis B: Environmental*, 188 (2016) 56-64.
- [147] J. Xu, Y. Li, S. Peng, G. Lu, S. Li, *Physical Chemistry Chemical Physics: PCCP*, 15 (2013) 7657-7665.
- [148] S. Min, G. Lu, *The Journal of Physical Chemistry C*, 116 (2012) 19644-19652.
- [149] H. Zhang, S. Li, R. Lu, A. Yu, *ACS Applied Materials & Interfaces*, 7 (2015) 21868-21874.
- [150] X. Zhang, T. Peng, L. Yu, R. Li, Q. Li, Z. Li, *ACS Catalysis*, 5 (2015) 504-510.
- [151] Y. Wang, J. Hong, W. Zhang, R. Xu, *Catalysis Science & Technology*, 3 (2013) 1703.
- [152] G. Chen, H. Qiu, P.N. Prasad, X. Chen, *Chemical Reviews*, 114 (2014) 5161-5214.
- [153] J. Zhou, Q. Liu, W. Feng, Y. Sun, F. Li, *Chemical Reviews*, 115 (2015) 395-465.
- [154] X. Li, H. Ren, Z. Zou, J. Sun, J. Wang, Z. Liu, *Chemical Communications*, 52 (2016) 453-456.
- [155] M.Z. Huang, B. Yuan, L. Dai, M.L. Fu, *Journal of Colloid and Interface Science*, 460 (2015) 264-272.
- [156] E. Cheng, S. Zhou, M. Li, Z. Li, *Applied Surface Science*, 410 (2017) 383-392.
- [157] E. Cheng, W. Yin, S. Bai, R. Qiao, Y. Zhong, Z. Li, *Materials Letters*, 146 (2015) 87-90.
- [158] Y. Tang, W. Di, X. Zhai, R. Yang, W. Qin, *ACS Catalysis*, 3 (2013) 405-412.
- [159] D.-X. Xu, Z.-W. Lian, M.-L. Fu, B. Yuan, J.-W. Shi, H.-J. Cui, *Applied Catalysis B: Environmental*, 142-143 (2013) 377-386.



[160] W. Wang, Y. Li, Z. Kang, F. Wang, J.C. Yu, *Applied Catalysis B: Environmental*, 182 (2016) 184-192.

[161] X. Guo, W. Song, C. Chen, W. Di, W. Qin, *Physical Chemistry Chemical Physics: PCCP*, 15 (2013) 14681-14688.

## **Chapter 3 Bimetallic Ag-Cu supported on C<sub>3</sub>N<sub>4</sub> NTs for improved visible-light photocatalytic hydrogen production**

### **3.1 Introduction**

As a clean energy carrier, hydrogen (H<sub>2</sub>) has been considered as one of the most promising alternatives to fossil fuels. Semiconductor-based photocatalysis offers a possible avenue to produce H<sub>2</sub> by photocatalytic water splitting. This process requires cost-effective semiconductor photocatalysts that maximise the use of solar energy [1, 2]. Most of these semiconductors are wide-bandgap metal oxides that require ultraviolet illumination for bandgap excitations and/or demand high costs for practical applications [3]. This requires the development of cost-effective narrow-bandgap photocatalysts that can utilise the visible portion of the solar spectrum. Graphitic carbon nitride (g-C<sub>3</sub>N<sub>4</sub>), consisting of tri-s-triazine units, is the most stable allotrope of carbon nitride and has attracted great interest as a visible-light photocatalyst due to its earth-abundant nature, excellent controllability, and nitrogen richness [4-6]. However, the photocatalytic performance of bare g-C<sub>3</sub>N<sub>4</sub> is hindered by its bulk layered structure and low electron transfer efficiency.

Design of efficient nanostructured g-C<sub>3</sub>N<sub>4</sub> to enhance its photocatalytic performance is a promising approach. Notably, g-C<sub>3</sub>N<sub>4</sub> has a flexible structure and various architectures of g-C<sub>3</sub>N<sub>4</sub> can be fabricated [7]. Ordered g-C<sub>3</sub>N<sub>4</sub> nanotubes (C<sub>3</sub>N<sub>4</sub> NTs) offer various advantages over nanoparticulate assemblies because of their defined one-dimensional geometry, which allows fast carrier transport and thus lower undesirable recombination losses [8, 9]. Due to the sophisticated control of C<sub>3</sub>N<sub>4</sub> NTs synthesis, their application on photocatalysis has been rarely reported. Bian et al. attempted to use a template-assisted process to synthesise C<sub>3</sub>N<sub>4</sub> NTs. The material obtained was in fact a nitrogen-doped carbon material rather than C<sub>3</sub>N<sub>4</sub> NTs due to the partial oxidation [10]. Kang's group employed a

N<sub>2</sub>-plasma enhanced chemical vapour deposition method using Fe growth catalysts to synthesise C<sub>3</sub>N<sub>4</sub> NTs [11]. Jin et al. reported a two-step condensation treatment of melamine to fabricate disordered nanotube-like g-C<sub>3</sub>N<sub>4</sub> materials [12]. Zeng et al. developed a simple water-induced morphological transformation process to prepare C<sub>3</sub>N<sub>4</sub> NTs from the nanosheet structure. The prepared C<sub>3</sub>N<sub>4</sub> NTs loaded with 3 wt. % platinum (Pt) displayed enhanced H<sub>2</sub> generation and degradation rate of Rhodamine B compared to those of their bulk and nanosheet counterparts [13].

Sacrificial reagents such as triethylamine (TEA), triethanolamine (TEOA), and methanol (MeOH) are often required to capture holes and inject electrons in a photocatalyst and thus drive photoinduced H<sub>2</sub> evolution. In Wang et al.'s work using Pt-loaded bulk g-C<sub>3</sub>N<sub>4</sub>, the highest H<sub>2</sub> yield was achieved when TEOA was used compared to using other sacrificial reagents including ethylenediaminetetraacetic acid, MeOH, and ethanol [14]; similar results were also reported by Lau et al [15]. Li et al. revealed that H<sub>2</sub> was released from visible-light photocatalysis of TEA on Pt-deposited C<sub>3</sub>N<sub>4</sub> NTs [16]. In the presence of TEA, however, Co<sub>3</sub>O<sub>4</sub>/TiO<sub>2</sub> composites were almost inactive in photocatalytic H<sub>2</sub> generation, as studied by Bala et al [17]. The recent *in situ* liquid NMR results found that MeOH, acting as a sacrificial reagent, underwent a two-electron oxidation reaction during the photocatalytic hydrogen production process on metal-supported TiO<sub>2</sub> catalysts [18].

It has been reported that no H<sub>2</sub> was produced over the bare C<sub>3</sub>N<sub>4</sub> NTs in the absence of a co-catalyst [16]. A co-catalyst is thus highly desirable to capture electrons preventing their recombination and enhancing charge separation [18]. Because the g-C<sub>3</sub>N<sub>4</sub> semiconductor contains many sp<sup>2</sup>-hybridized nitrogen atoms, it can be used as a scaffold on which metal nanoparticle cocatalysts could be effectively dispersed. To date, Pt nanoparticles have been used as cocatalysts deposited on C<sub>3</sub>N<sub>4</sub> NTs for photocatalytic H<sub>2</sub> generation [16]. Bimetallic nanoparticles supported C<sub>3</sub>N<sub>4</sub> NTs have yet to be explored. It is found that bimetallic

nanoparticles deposited on TiO<sub>2</sub> showed higher photocatalytic performance [19, 20]. Only Au-Pd and Pt-Co bimetallic nanoparticles deposited on bulk and g-C<sub>3</sub>N<sub>4</sub> nanosheets have been reported for photocatalytic hydrogen evolution [21, 22]. Owing to the high cost and low reserves of noble metals, their practical application has been impeded. Inexpensive metals including Ag and Cu as cocatalysts have many advantages due to their low cost and good stability [23-25]. Nevertheless, the H<sub>2</sub> yield over inexpensive metal-based composites still remains a serious challenge.

In the present work, we report for the first time that the bare C<sub>3</sub>N<sub>4</sub> NTs, synthesised using a modified water-induced morphological transformation process, exhibit visible-light photocatalytic H<sub>2</sub> generation without any cocatalyst. We show that instead of using water, ethanol facilitates better dispersion of the as-prepared C<sub>3</sub>N<sub>4</sub> nanosheets and prevents them from aggregating, which in turn improves the morphology of nanotubes significantly based on the roll-up mechanism of the nanosheets [26]. The bimetallic Ag-Cu/C<sub>3</sub>N<sub>4</sub> NT catalysts exhibit considerably higher activity than the bare, monometallic C<sub>3</sub>N<sub>4</sub> NTs including Pt/C<sub>3</sub>N<sub>4</sub> NTs. Acting as a sacrificial reagent, TEA outperforms TEOA, whereas no H<sub>2</sub> was produced when MeOH was employed. Mechanistic studies on the role of sacrificial reagents were performed.

## **3.2 Experimental section**

### **3.2.1 Catalyst fabrication**

C<sub>3</sub>N<sub>4</sub> NTs were synthesised by a modified water-induced morphological transformation process [13]. 5 g of melamine powder was calcined at 550 °C for 2 h in static air. Then, the bulk g-C<sub>3</sub>N<sub>4</sub> was exfoliated by sonication for 1 h in ethanol rather than water. The as-synthesised g-C<sub>3</sub>N<sub>4</sub> nanosheet solid materials were then heated up to 350 °C with a heating rate of 10 °C/min and kept at this temperature for 10 min. Subsequently, the hot powder of

g-C<sub>3</sub>N<sub>4</sub> nanosheets was rapidly transferred into an ice-water bath. The C<sub>3</sub>N<sub>4</sub> NTs samples were finally obtained by filtration and drying at 120 °C for 12 h under vacuum conditions.

Ag-Cu bimetallic NPs were deposited on C<sub>3</sub>N<sub>4</sub> NTs with a nominal mass ratio of bimetallic NPs to C<sub>3</sub>N<sub>4</sub> NTs through a chemical reduction method [18]. Typically, the as-prepared C<sub>3</sub>N<sub>4</sub> NTs were suspended in 200 mL of deionized water under magnetic stirring. A nominal amount of silver nitrate and copper nitrate was then added. The suspension was further stirred for 1 h in an ice bath. Then an excess of ice-cold NaBH<sub>4</sub> aqueous solution (0.1 M) was quickly injected into the suspension and further stirred for 1 h. The mixture was aged for 1.5 h. After filtration and washing with ethanol and water, the samples were dried at 80 °C under vacuum for 12 h. Ag(1)/C<sub>3</sub>N<sub>4</sub> NTs, Ag(3)/C<sub>3</sub>N<sub>4</sub> NTs, Ag(5)/C<sub>3</sub>N<sub>4</sub> NTs with Ag/C<sub>3</sub>N<sub>4</sub> mass ratios of 1 %, 3 %, 5 %, and Cu(3)/C<sub>3</sub>N<sub>4</sub> NT, Cu(5)/C<sub>3</sub>N<sub>4</sub> NT, Cu(7)/C<sub>3</sub>N<sub>4</sub> NT samples with Cu/C<sub>3</sub>N<sub>4</sub> mass ratios of 3 %, 5 %, 7 % were synthesised. The bimetallic catalysts were denoted Ag-Cu/C<sub>3</sub>N<sub>4</sub> NTs (*x* : *y*), where *x*: *y* represents the molar ratio of Ag to Cu. For comparison, Pt/C<sub>3</sub>N<sub>4</sub> NTs with mass ratios of 1-3 wt. % were prepared using the same procedure.

### 3.2.2 Structural characterisation

X-ray diffraction (XRD) patterns were obtained using a Panalytical X'Pert PRO diffractometer via Cu K<sub>α1</sub> radiation. Scanning electron microscopy (SEM) with energy dispersive X-ray spectroscopy (EDX) was performed on a JCM-6000PLUS at a voltage of 15 kV. Transmission electron microscopy (TEM) images were obtained using a JEOL-2100F microscope operating at 200 kV, by depositing a drop of sample suspension onto 200 mesh Ni grids. X-ray photoelectron spectroscopy (XPS) was carried out on an ESCALAB250Xi spectrometer (Thermo Scientific, U.K.) with a monochromated Al K<sub>α</sub> X-ray radiation source (*E* = 1486.68 eV).

The ultraviolet-visible (UV-Vis) diffuse reflectance spectra (DRS) were recorded on a Varian Cary 500 Scan UV-Vis spectrophotometer. Photoluminescence (PL) measurements were carried out on a Fluorolog-Tau3 fluorescence spectrophotometer with an excitation wavelength of 330 nm at room temperature. Photocurrent measurements were carried out using a three-electrode setup connected to a potentiostat (SP-300, BioLogic Science Instruments). In this electrochemical system, the prepared catalyst/Ti sheet was used as a working electrode; The Ag/AgCl electrode (saturated KCl) was used as a reference electrode and the Pt wire as a counter electrode. The electrolyte was 0.01 M Na<sub>2</sub>SO<sub>4</sub> aqueous solution (100 mL). The measurements were carried out at a constant potential of +1.0 V and a 300 W Xenon arc lamp (Y1089, Hidesada Toriyama, Inc.) served as a light source.

### **3.2.3 Photocatalytic performance**

The visible-light illumination was obtained by removing the UV part of the spectrum from a 300 W Xenon arc lamp using a 420 nm cut-off filter. In a typical procedure, 40 mg of the prepared catalysts and 40 mL of deionized water containing 10 vol. % of a sacrificial reagent were mixed in a 100 mL reactor. Subsequently, argon was purged through the system for at least 30 min in order to completely vent out the air. Then the solution was irradiated from the top through a quartz window under stirring, and an external cooling jacket was employed to absorb the heat. The resulting gas was analyzed every 30 min using a gas chromatograph (GC 2014; Shimadzu Corporation) equipped with a thermal conductivity detector (TCD) and a 5Å molecular sieve column.

### **3.2.4 Mechanistic studies on the role of sacrificial reagents**

An Agilent 1260 high-performance liquid chromatograph (HPLC) equipped with a Phenomenex C18, 4-µm particle size analytical column coupled with a diode array detector was used at ambient temperature. The mobile phase for TEA and TEOA solutions were

prepared by mixing water and MeOH in a volume ratio of 75/25, while in the study of MeOH the mobile phase was water/acetonitrile (75/25, v/v). In addition, an Agilent 6130 series quadrupole liquid chromatography mass spectrometry (LC/MS) system equipped with an electrospray ionization source and an atmospheric pressure chemical ionization source in the positive ion mode was used. Detection using Phenomenex C18, 3- $\mu$ m particle size column (40°C) and water/acetonitrile (95/5, v/v) as the mobile phase were carried out.

### **3.3 Results and discussion**

#### **3.3.1 Photocatalytic hydrogen production**

##### **3.3.1.1 Without any co-catalyst**

Figure 3.1a shows H<sub>2</sub> production over the bare g-C<sub>3</sub>N<sub>4</sub> bulk, nanosheets and C<sub>3</sub>N<sub>4</sub> NTs in the absence of any co-catalyst in 10 vol% TEA aqueous solution irradiated by visible-light ( $\lambda > 420$  nm). It is clear that the C<sub>3</sub>N<sub>4</sub> NTs catalyst is more active in H<sub>2</sub> production than the bulk and nanosheet structures are. A similar trend was also observed by Zeng et al. [13] using 3 wt. % of Pt co-catalyst. It is worth pointing out that in their work no hydrogen can be produced over the bare C<sub>3</sub>N<sub>4</sub> NTs in the absence of any co-catalyst. This shows that the bare C<sub>3</sub>N<sub>4</sub> NTs synthesised in the present study exhibit unexpected visible-light activity in H<sub>2</sub> production, suggesting that the unique tubular nanostructure is favourable for proton reduction and mass transfer. The effect of the co-catalysts on bulk C<sub>3</sub>N<sub>4</sub> and nanosheets has been studied in PtCo/C<sub>3</sub>N<sub>4</sub> nanomaterial [27]. In the following section, only C<sub>3</sub>N<sub>4</sub> NT materials were selected for further studies.

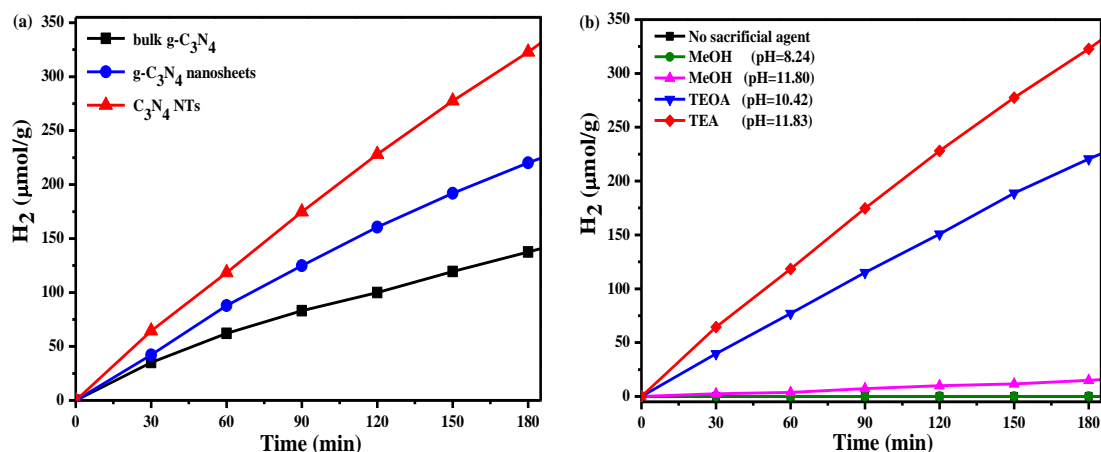


Figure 3.1 H<sub>2</sub> production over the bare C<sub>3</sub>N<sub>4</sub> bulk, nanosheets and nanotubes using TEA as sacrificial reagent but without any co-catalyst (a); H<sub>2</sub> generation over the bare C<sub>3</sub>N<sub>4</sub> NTs using different sacrificial reagents including TEA, TEOA, and MeOH under various pH values (b).

### 3.3.1.2 Effect of sacrificial reagents

The effect of sacrificial reagents including TEA, TEOA, and MeOH on the H<sub>2</sub> production from water over the bare C<sub>3</sub>N<sub>4</sub> NTs were studied under visible-light irradiation ( $\lambda > 420$  nm). Figure 3.1b depicts the photocatalytic H<sub>2</sub> production over the bare C<sub>3</sub>N<sub>4</sub> NTs with and without sacrificial reagents. It is apparent that the bare C<sub>3</sub>N<sub>4</sub> NTs are inactive for photocatalytic H<sub>2</sub> production when no sacrificial reagent was employed or when MeOH was used as a sacrificial reagent. TEA shows the best H<sub>2</sub> evolution rate, while TEOA affords moderate H<sub>2</sub> generation.

It has been reported that the H<sub>2</sub> evolution may depend on the pH values of the reaction suspension containing photocatalyst, water, and sacrificial reagents [28]. The higher the pH value, the faster the hydrogen abstraction and the greater the hydrogen production. In the present study, the pH value of the suspension containing MeOH is 8.24, whereas it is 10.42 and 11.83 when TEOA or TEA, respectively was used as the sacrificial reagent. However, adding NaOH to increase the pH value of the suspension did not result in an improved



hydrogen production rate when MeOH was used as a sacrificial reagent, as shown in Figure 3.1b. It is probably because the high oxidation potentials of the sacrificial reagents led to improved hydrogen production.

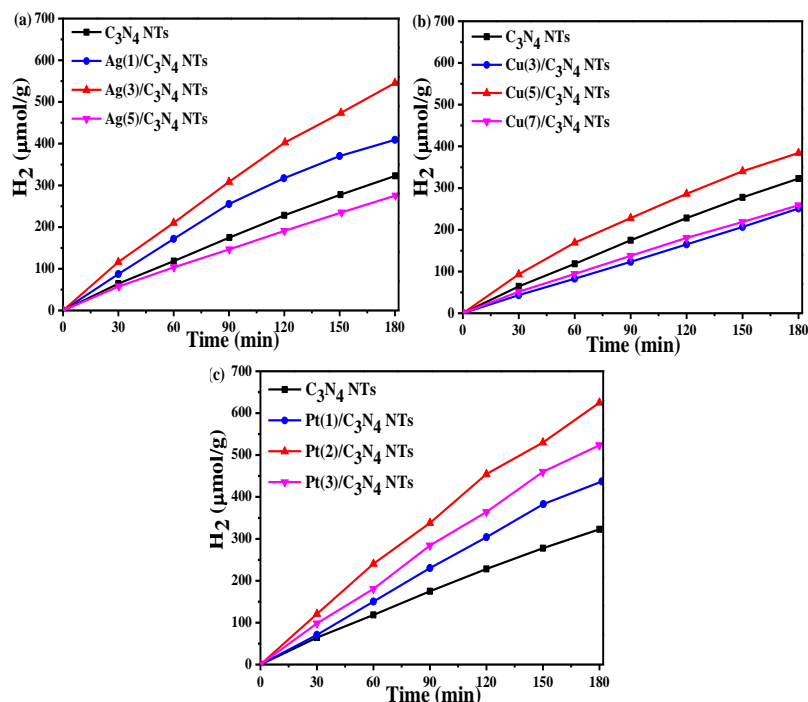


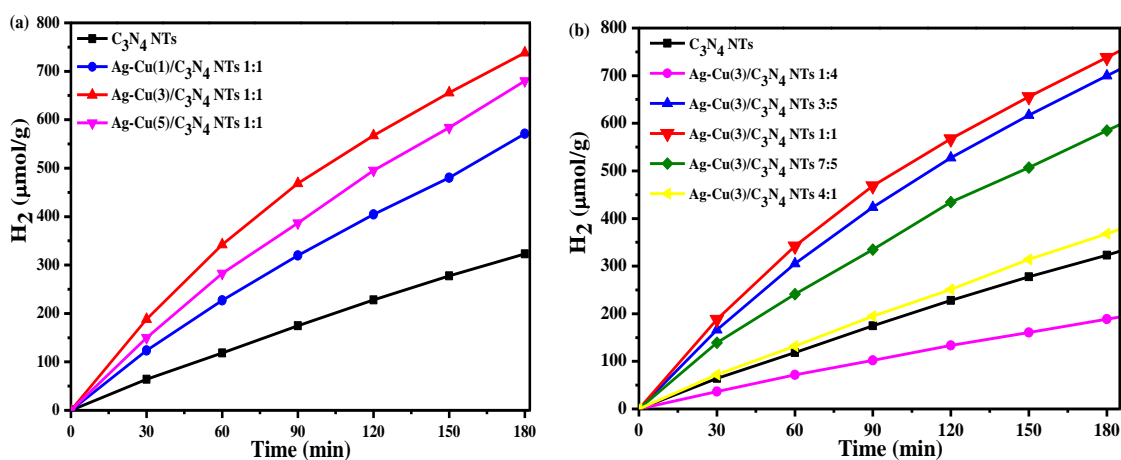
Figure 3.2 H<sub>2</sub> production on the Ag/C<sub>3</sub>N<sub>4</sub> NTs (b), Cu/C<sub>3</sub>N<sub>4</sub> NTs (b) and Pt/C<sub>3</sub>N<sub>4</sub> NTs (c) with different metal loading amounts.

### 3.3.1.3 With metal nanoparticles as co-catalysts

To study the beneficial effect of Ag-Cu bimetallic NPs in the photocatalytic process, the H<sub>2</sub> production rates over Ag/C<sub>3</sub>N<sub>4</sub> NT and Cu/C<sub>3</sub>N<sub>4</sub> NT samples were evaluated. H<sub>2</sub> production on the bare C<sub>3</sub>N<sub>4</sub> NTs is compared to the monometallic Ag/C<sub>3</sub>N<sub>4</sub> NTs, Cu/C<sub>3</sub>N<sub>4</sub> NTs, and Pt/C<sub>3</sub>N<sub>4</sub> NTs with different metal loadings as shown in Figure 3.2. The highest H<sub>2</sub> production rate was observed when the metal loading of Ag and Cu was 3 wt. % and 5 wt. %, respectively. However, further increase of the Ag and Cu loading up to 5 and 7 wt. %, respectively, led to a decrease in H<sub>2</sub> evolution efficiency. This could be attributed to growth and aggregation of metal nanoparticles at higher loading amounts, resulting in partial blockage of the pores of C<sub>3</sub>N<sub>4</sub> NTs. It can reduce the accessibility of light and

reagents to the surface active sites in the nanochannels, thus suppressing the charge separation and resulting in decreased activity [29]. It is noted that Ag(5)/C<sub>3</sub>N<sub>4</sub> NTs, Cu(3)/C<sub>3</sub>N<sub>4</sub> NTs, and Cu(7)/C<sub>3</sub>N<sub>4</sub> NTs present lower activity than the bare C<sub>3</sub>N<sub>4</sub> NTs. The same phenomenon appeared in the Pt/C<sub>3</sub>N<sub>4</sub> NT sample reported by Li et al [16]. For comparison, the noble metal Pt nanoparticles were decorated on the bare C<sub>3</sub>N<sub>4</sub> NTs via the same chemical reduction method. As shown in Figure 3.2c, the H<sub>2</sub> yield evolved from the best Pt(2)/C<sub>3</sub>N<sub>4</sub> NTs is lower than the Ag-Cu(3)/C<sub>3</sub>N<sub>4</sub> NTs (1:1) sample.

Figure 3.3a presents the H<sub>2</sub> evolution over Ag-Cu/C<sub>3</sub>N<sub>4</sub> NTs (1:1) with different bimetallic loadings (1 wt. %, 3 wt. % and 5 wt. %). The Ag-Cu(3)/C<sub>3</sub>N<sub>4</sub> NT (1:1) sample with 3 wt. % of the total bimetallic loading achieves the highest H<sub>2</sub> yield. Moreover, Figure 3.3b demonstrates that the molar composition of the Ag-Cu particles had a strong influence on the efficiency of the nanomaterial in H<sub>2</sub> production. Increasing the Ag content from 20 to 50 at% relative to the Cu led to 3-4 times higher H<sub>2</sub> production. The maximum yield of H<sub>2</sub> production was achieved at the optimal Ag/Cu molar ratio of 1:1, where homogeneous intermixing of Ag and Cu may occur [30]. Any further increase of the molar ratio results in a decrease of H<sub>2</sub> generation.



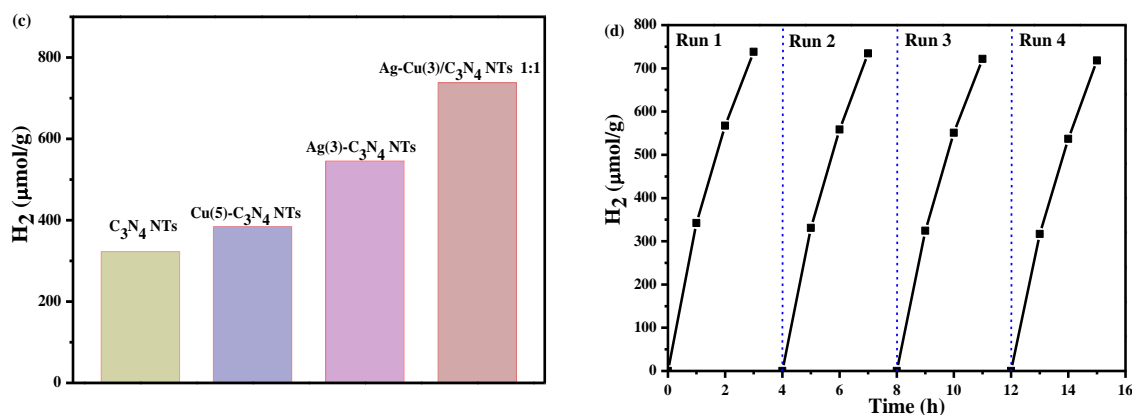


Figure 3.3 H<sub>2</sub> generation over Ag-Cu/C<sub>3</sub>N<sub>4</sub> NTs (1:1) with different mass ratios (1 wt. %, 3 wt. % and 5 wt. %) (a) and over Ag-Cu(3)/C<sub>3</sub>N<sub>4</sub> NTs under various atomic ratios of Ag to Cu (b) as a function of reaction time; the comparison of H<sub>2</sub> evolution on the bare and metallic C<sub>3</sub>N<sub>4</sub> NTs photocatalysts (c) and reusability test on Ag-Cu(3)/C<sub>3</sub>N<sub>4</sub> NTs (1:1) (d). Reaction condition: 40 mg catalyst in 40 mL water/TEA solution (volume ratio of 9/1) and visible light irradiation (> 420 nm) for 3 h.

Figure 3.3c compares the H<sub>2</sub> production on the bare C<sub>3</sub>N<sub>4</sub> NTs, Ag(3)/C<sub>3</sub>N<sub>4</sub> NTs, Cu(5)/C<sub>3</sub>N<sub>4</sub> NTs, and Ag-Cu(3)/C<sub>3</sub>N<sub>4</sub> NTs (1:1) after 3 h illumination. It clearly shows that the H<sub>2</sub> evolution of 738 μmol/g from the bimetallic catalyst is about 1.4, 1.9 and 2.3 times higher than that of the Ag(3)/C<sub>3</sub>N<sub>4</sub> NTs, Cu(5)/C<sub>3</sub>N<sub>4</sub> NTs and the bare C<sub>3</sub>N<sub>4</sub> NTs, respectively. This clearly shows that the Ag-Cu bimetallic NPs boosted H<sub>2</sub> evolution.

The reusability of Ag-Cu(3)/C<sub>3</sub>N<sub>4</sub> NTs (1:1) for visible-light hydrogen generation was investigated. As shown in Figure 3.3d, the good performance of this material was maintained for at least up to four recycles. These results show that there was no significant decrease in H<sub>2</sub> production, illustrating that bimetallic nanoparticles supported C<sub>3</sub>N<sub>4</sub> NTs have satisfactory reusability. In the next sections, the bare C<sub>3</sub>N<sub>4</sub> NTs, Ag(3)/C<sub>3</sub>N<sub>4</sub> NTs, Cu(5)/C<sub>3</sub>N<sub>4</sub> NTs, and Ag-Cu(3)/C<sub>3</sub>N<sub>4</sub> NTs (1:1) were selected for the following characterisations.

### 3.3.2 Textural and structural properties

As shown in Figure 3.4, the XRD pattern of  $C_3N_4$  NTs shows a dominant peak at  $27.5^\circ$  indexed to the (002) plane, which is attributed to the periodic graphitic stacking of conjugated aromatic systems. The (100) peak at  $12.6^\circ$  is derived from the in-plane structural units of tri-s-triazine [31]. For the Ag(3)/ $C_3N_4$  NTs sample, the three diffraction peaks of (111) at  $38.2^\circ$ , (200) at  $44.6^\circ$  and (220) at  $64.8^\circ$  match well with the face-centered-cubic phases of metallic silver (JCPDS 87-1526), indicating that metallic silver was deposited on the  $C_3N_4$  NTs. For the Cu(5)/ $C_3N_4$  NTs sample, the peaks at  $36.7^\circ$  and  $43.4^\circ$  are assigned to the (111) crystal face of oxidised and metallic Cu (JCPDS 04-0836) [32]. The enlarged XRD pattern view of Ag-Cu(3)/ $C_3N_4$  NTs (1:1) (from  $35^\circ$  to  $48^\circ$ ) reveals that the peak intensities from the metal nanoparticles decreased due to the smaller crystal sizes compared to the monometallic materials, implying that the formation of bimetallic nanoparticles suppressed further aggregation of the silver nanoparticles [22, 33]. Besides, the size of the nanocrystals was calculated to be around 3 nm from the Debye-Scherrer equation.

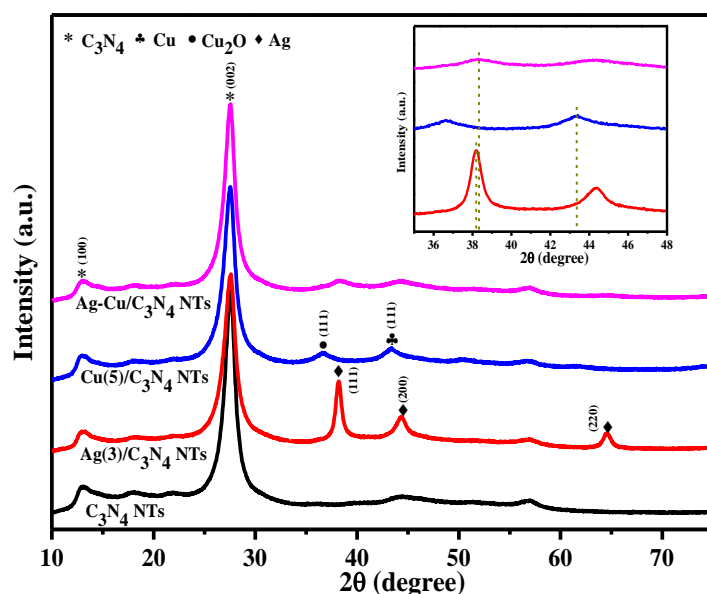


Figure 3.4 XRD patterns of the bare  $C_3N_4$  NTs, Ag(3)/ $C_3N_4$  NTs, Cu(5)/ $C_3N_4$  NTs, and Ag-Cu(3)/ $C_3N_4$  NTs (1:1).

The morphology and microstructure of the as-prepared samples were analyzed by TEM. Figures 3.5a-c show that the bare  $C_3N_4$  NTs have a hollow tubular nanostructure with open ends, demonstrating that  $C_3N_4$  NTs were successfully prepared through the modified water-induced morphological transformation method. The outer diameters of the two individual  $C_3N_4$  NTs in Figures 3.5b-c are approximately 200 and 400 nm, respectively. It seems that the sizes of individual  $C_3N_4$  NTs were not well controlled because of the nanosheets roll-up mechanism that depends on the size and thickness of bent g- $C_3N_4$  nanosheet units. In Figure 3.4d and the inset, high magnification images illustrate that Ag-Cu bimetallic NPs with a particle size of around 10 nm were well dispersed on the surface of  $C_3N_4$  NTs. A high resolution TEM image in Figure 3.5e gives a lattice spacing of 0.229 nm, which is assigned to the (111) plane of Ag-Cu bimetallic nanoparticles [34], confirming the presence of Ag-Cu bimetallic nanoparticles. Figure 3.5f shows C, N, Ag and Cu element distribution maps of the region in Figure 3.5d, illustrating the uniform dispersion of the bimetallic nanoparticles on  $C_3N_4$  NTs. The composition of Ag and Cu in the bimetallic catalysts was also analyzed by SEM-EDX, and the Ag/Cu molar ratio of *ca.* 1 is confirmed in Figure A1 (Appendix). This matches well with the nominal amount during sample preparation.

XPS was used to identify the chemical state of the metal nanoparticles deposited on  $C_3N_4$  NTs. In Figure 3.6a the XPS survey spectrum confirms the existence of the C, N, Ag and Cu elements. The content of Ag and Cu detected is 1.3 at% and 1.4 at%, respectively, which aligns well with the above SEM-EDX results. Figures 3.6b-c show the C 1s and N 1s XPS spectra of the Ag-Cu(3)/ $C_3N_4$  NT (1:1) sample, confirming the presence of a well-ordered g- $C_3N_4$  structure. The peak of Ag-Cu(3)/ $C_3N_4$  NTs (1:1) in C 1s binding energy regions centred at 284.7 eV and 288.2 eV can be assigned to C-C and/or C=C and N=C-N<sub>2</sub> coordination, while the N 1s peak can be de-convoluted into three peaks at 398.8, 399.8 and 401.1 eV, which are ascribed to N atoms in C=N-C groups, N-(C)<sub>3</sub> groups or amino

groups carrying hydrogen and three carbon atoms in the aromatic cycles, respectively [35]. As shown in Figure 3.7a, the silver species in the Ag(3)/C<sub>3</sub>N<sub>4</sub> NT and Ag-Cu(3)/C<sub>3</sub>N<sub>4</sub> NT (1:1) catalysts exist in the metallic Ag<sup>0</sup> states, as indicated by the Ag 3d XPS spectra, which are composed of Ag 3d<sub>5/2</sub> and Ag 3d<sub>3/2</sub> peaks. In the bimetallic sample, the two peaks located at 368.4 eV and 374.4 eV exhibit positive upshifts, indicating a stronger metal-support interaction compared to the monometallic counterpart [27, 33].

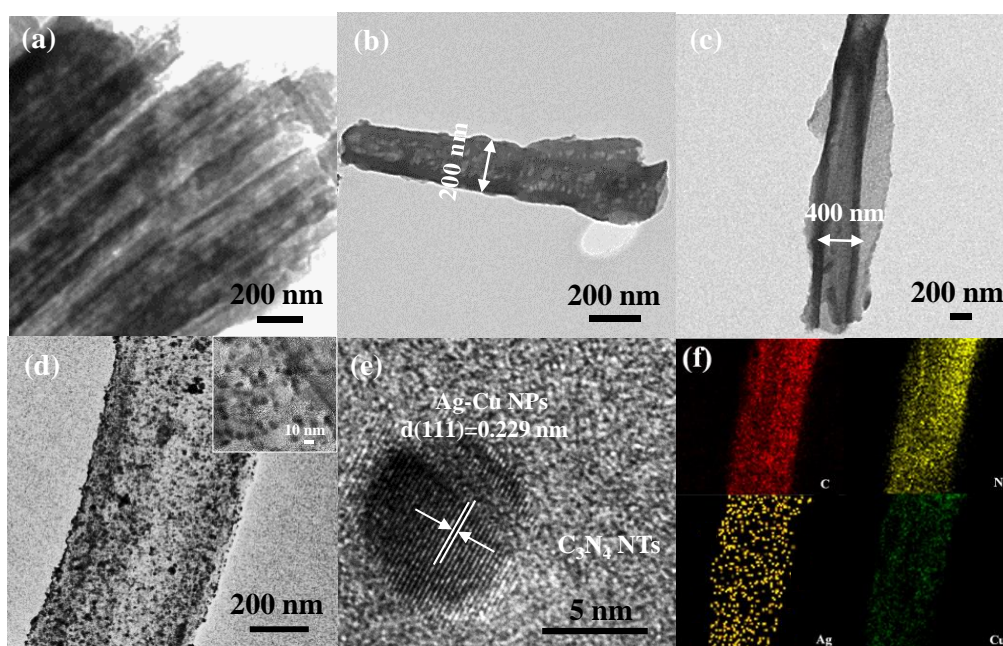
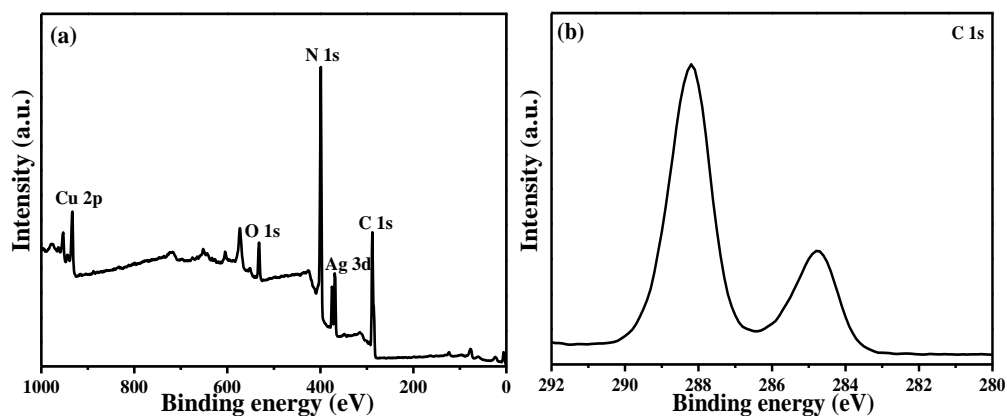


Figure 3.5 TEM images of the bare C<sub>3</sub>N<sub>4</sub> NTs (a, b, c) and Ag-Cu(3)/C<sub>3</sub>N<sub>4</sub> NTs (1:1) (d, e) and EDX mapping (f) of Ag-Cu(3)/C<sub>3</sub>N<sub>4</sub> NTs (1:1) from the area in Figure 3.5d.



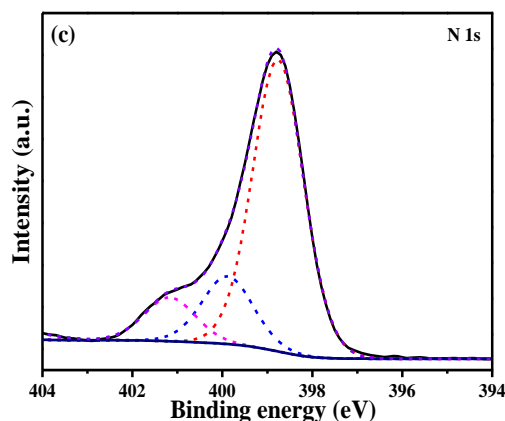


Figure 3.6 XPS survey (wide-scan) spectrum (a), C 1s XPS spectrum (b), and N 1s XPS spectrum (c) of the Ag-Cu(3)/C<sub>3</sub>N<sub>4</sub> NT (1:1) sample.

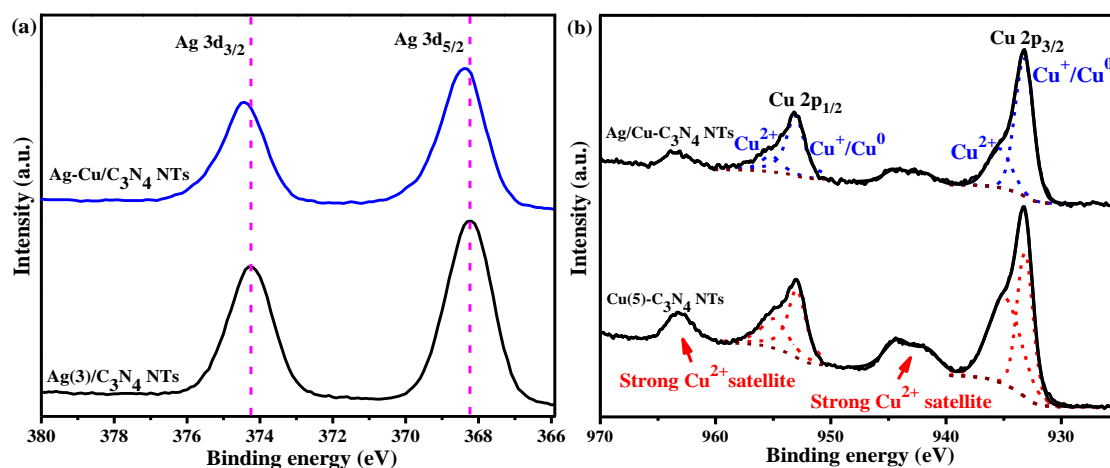


Figure 3.7 Ag 3d XPS spectra of Ag-Cu(3)/C<sub>3</sub>N<sub>4</sub> NTs (1:1) and Ag(3)/C<sub>3</sub>N<sub>4</sub> NTs (a), and Cu 2p XPS spectra of the Ag-Cu(3)/C<sub>3</sub>N<sub>4</sub> NT (1:1) and Cu(5)/C<sub>3</sub>N<sub>4</sub> NT samples (b).

Figure 3.7b shows the XPS core level spectra of Cu 2p orbitals for the bimetallic nanomaterial and Cu(5)/C<sub>3</sub>N<sub>4</sub> NTs samples. Two characteristic bands between 939.6-947.1 eV and 959.7-965.8 eV are referred to Cu<sup>2+</sup> satellite signals. The peaks at approximately 932.9 eV and 952.8 eV correspond to Cu 2p<sub>3/2</sub> and Cu 2p<sub>1/2</sub> of Cu<sup>+</sup> or metallic Cu. Differentiation of Cu<sup>+</sup> and Cu<sup>0</sup> signals is ambiguous due to peak overlap [36]. The copper species make up of a large proportion of oxidised Cu<sup>2+</sup> in the monometallic Cu(5)/C<sub>3</sub>N<sub>4</sub> NT sample, while the bimetallic Ag-Cu(3)/C<sub>3</sub>N<sub>4</sub> NT (1:1) sample possesses more reduced or

metallic state metal species, favouring the reduction of protons. The same phenomenon was observed in the Ag-Cu/ZrO<sub>2</sub> sample as well [37].

Figure 3.8a depicts the UV-Vis spectra of the bare and metallic C<sub>3</sub>N<sub>4</sub> NT catalysts. The bare C<sub>3</sub>N<sub>4</sub> NTs display a characteristic absorption edge at around 450 nm with a band gap of  $\sim 2.77$  eV determined by the Tauc plot [38], which has a blue shift compared to the bulk *g*-C<sub>3</sub>N<sub>4</sub> ( $\sim 2.70$  eV). It probably originates from the well-known quantum size effect induced by a decrease of particle size [12, 39]. Compared with the bare C<sub>3</sub>N<sub>4</sub> NTs, Ag/C<sub>3</sub>N<sub>4</sub> NTs show enhanced absorption over a broad range of wavelengths in the visible-light region, but no obvious surface plasmonic resonance effect was observed probably due to the low content of Ag nanoparticles [24].

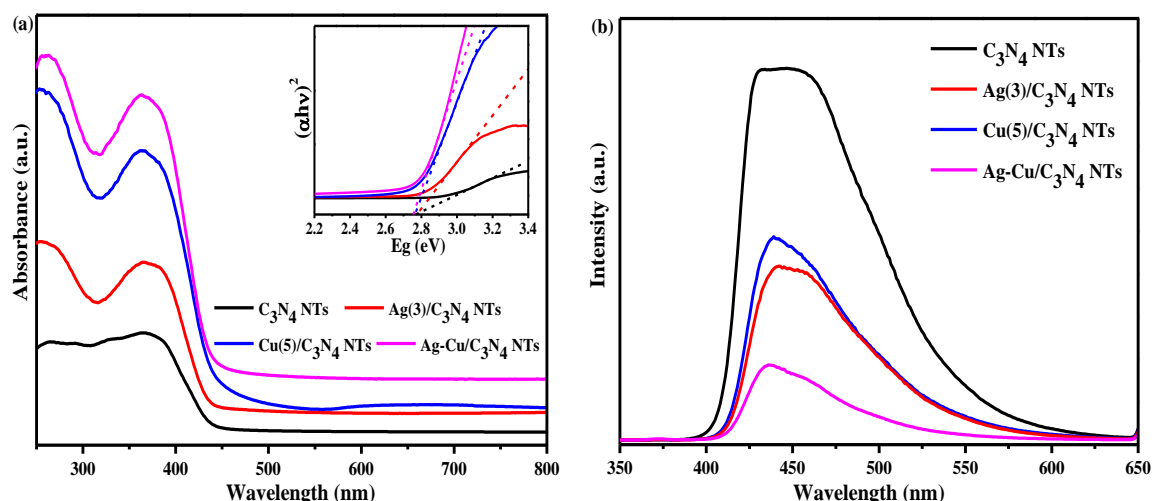


Figure 3.8 UV-Vis diffuse reflectance spectra (a) and PL spectra (b) of the bare C<sub>3</sub>N<sub>4</sub> NTs, Ag(3)/C<sub>3</sub>N<sub>4</sub> NTs, Cu(5)/C<sub>3</sub>N<sub>4</sub> NTs, and Ag-Cu(3)/C<sub>3</sub>N<sub>4</sub> NTs (1:1).

For the Cu(5)/C<sub>3</sub>N<sub>4</sub> NT sample, the weak absorbance band approximately centered at 650 nm is attributed to a very small amount of *d-d* transition in Cu(II) d-orbital, confirming the existence of Cu<sup>2+</sup> species [40, 41]. It is worth noting that the *d-d* transition was not observed in the Ag-Cu(3)/C<sub>3</sub>N<sub>4</sub> NTs (1:1), corroborating the XPS results that reduced and/or metallic Cu species predominantly present in the bimetallic sample. The bimetallic Ag-Cu(3)/C<sub>3</sub>N<sub>4</sub>



NT (1:1) sample has the strongest light absorbance among all the samples in this study. From the results presented above the conclusion could be drawn that the bimetallic system provides more charge carriers upon illumination and, therefore, may contribute to the enhanced photocatalytic activity in H<sub>2</sub> generation.

### **3.3.3 Charge separation studies**

PL spectroscopy was used to investigate the effect of metal nanoparticles on the separation of photo-generated electrons and holes in the nanocomposites. It is generally accepted that a lower PL emission intensity corresponds to a lower carrier recombination rate, i.e. a longer lifetime of the electron-hole pairs [42, 43]. In Figure 3.8b, the bare C<sub>3</sub>N<sub>4</sub> NTs present a strong fluorescence band at 450 nm. It becomes lower upon incorporation with Cu nanoparticles, whereas the Ag(3)/C<sub>3</sub>N<sub>4</sub> NTs displays a slightly lower fluorescence intensity compared to the Cu(5)/C<sub>3</sub>N<sub>4</sub> NT sample. It is apparent that the Ag-Cu(3)/C<sub>3</sub>N<sub>4</sub> NTs (1:1) sample exhibits the lowest intensity of the PL signal with a blue shift, suggesting the highest separation efficiency of photo-induced electron-hole pairs, among the materials studied. This may be ascribed to the fact that the photo-induced electrons in the conduction band of C<sub>3</sub>N<sub>4</sub> NTs can be more efficiently transferred to the bimetallic nanoparticles as a result of the formation of a Schottky barrier, thus prolonging the lifetime of the electron-hole pairs and improving the photocatalytic activity of the bimetallic system. To further confirm the enhanced charge separation on the metal/C<sub>3</sub>N<sub>4</sub> NT materials, their transient photocurrent responses were investigated by three on-off cycles of intermittent light irradiation. As shown in Figure 3.9, the electrodes bearing catalysts on the surface were prompt in generating photocurrent with a good reproducibility in the on-off cycles. When the light was switched on, the instantaneous over-high current was due to the flux of holes into the surface. When the light was turned off, the current overshoot was due to the continuing flux of electrons into the surface [44]. The prompt increase in the photocurrent response may be

ascribed to the promotion of exciton splitting and the quick separation and transportation of photo-induced electrons on the surfaces of the working electrodes [45, 46]. Apparently, the photocurrents generated on both the Cu/C<sub>3</sub>N<sub>4</sub> NTs and Ag/C<sub>3</sub>N<sub>4</sub> NTs electrodes are higher compared to the bare C<sub>3</sub>N<sub>4</sub> NTs. It should be noted that an enhanced photocurrent was generated on the Ag-Cu(3)/C<sub>3</sub>N<sub>4</sub> NT (1:1) sample, which is about 2.4 times as high as that of the bare C<sub>3</sub>N<sub>4</sub> NTs. This indicates that the bimetallic catalyst exhibits better separation of photo-induced charge carriers, confirming the PL results already presented.

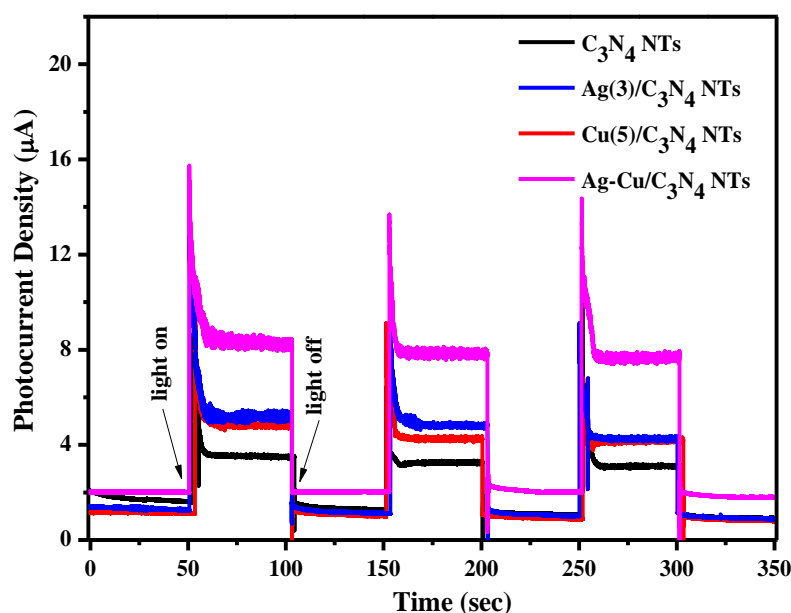


Figure 3.9 Photocurrent responses under irradiation with 50 s light on/off cycles of the bare C<sub>3</sub>N<sub>4</sub> NTs, Ag(3)/C<sub>3</sub>N<sub>4</sub> NTs, Cu(5)/C<sub>3</sub>N<sub>4</sub> NTs, and Ag-Cu(3)/C<sub>3</sub>N<sub>4</sub> NTs (1:1).

### 3.3.4 Degradation mechanism of sacrificial reagents

The role of three different sacrificial reagents was investigated to understand the mechanism of visible-light photocatalytic H<sub>2</sub> production over the Ag-Cu(3)/C<sub>3</sub>N<sub>4</sub> NTs (1:1). As shown in Figure 3.10a, prior to visible-light irradiation only TEA was detected in the aqueous suspension by HPLC. After 60 min of illumination, a peak assigned to acetaldehyde appeared and its intensity grew with increased irradiation time, indicating the

formation of acetaldehyde derived from TEA photodegradation. LC-MS was used to identify the components of the peak fraction from 3.0 - 3.8 min after irradiation for 180 min (Figure A2, Appendix). A small amount of diethylamine (DEA) was identified by LC-MS, suggesting that DEA was generated after visible-light irradiation of TEA in addition to acetaldehyde. It can be inferred that when TEA was used as the sacrificial reagent during the photocatalytic process, it captured holes forming positively charged  $\text{TEA}^+$ , with the following [1,2]-radical carbon and loss of proton. The neutral radical thus formed went through a second one-electron oxidation forming an imine-like cationic intermediate. Finally, the cation reacted with water and released DEA and acetaldehyde. The proposed mechanism of irreversible oxidation of TEA is described in Figure 3.10b.

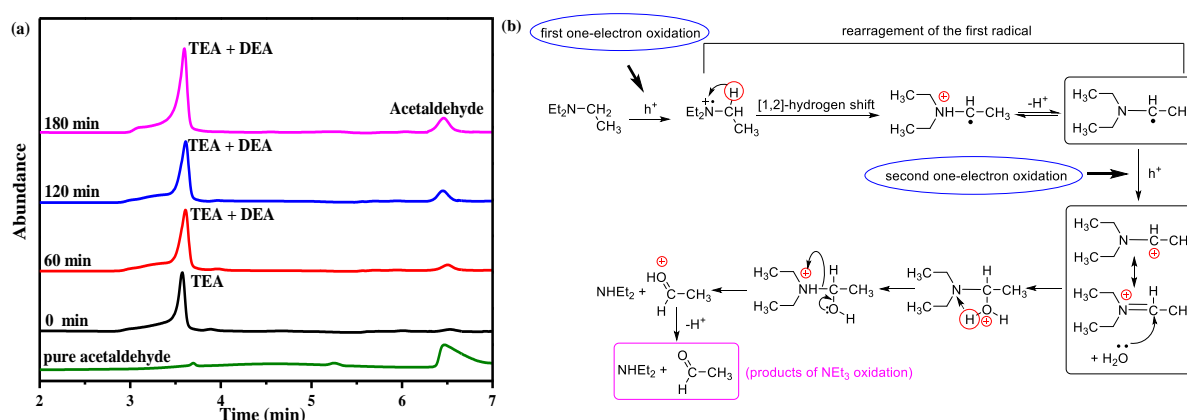


Figure 3.10 (a) HPLC results of the intermediates and products at intervals from the sacrificial reagent, TEA 10 vol.% in the suspension containing the Ag-Cu(3)/C<sub>3</sub>N<sub>4</sub> NTs (1:1) under visible light irradiation; (b) degradation pathway of TEA upon monoelectronic oxidation.

Early studies by DeLaive and co-workers detected the formation of acetaldehyde upon the photolysis of TEA on a metal complex in a 10 % oxygen-free solution of water in acetonitrile. They proposed that TEA degrades to diethylamine (DEA) in the presence of water while in anhydrous condition it could participate in a back electron transfer process

[47]. In the research conducted by Cline et al. for iridium and rhodium complexes the aliphatic amine TEA could give a dramatic increase in the catalytic rate for  $\text{H}_2$  production compared to TEOA. According to the oxidation potential ( $E_{\text{OX}} = 0.69 \text{ V}_{\text{vs. SCE}}$ ) for TEA in water [48], it has been speculated that TEA could be oxidised to diethylamine (DEA) and acetaldehyde in a two-electron pathway.

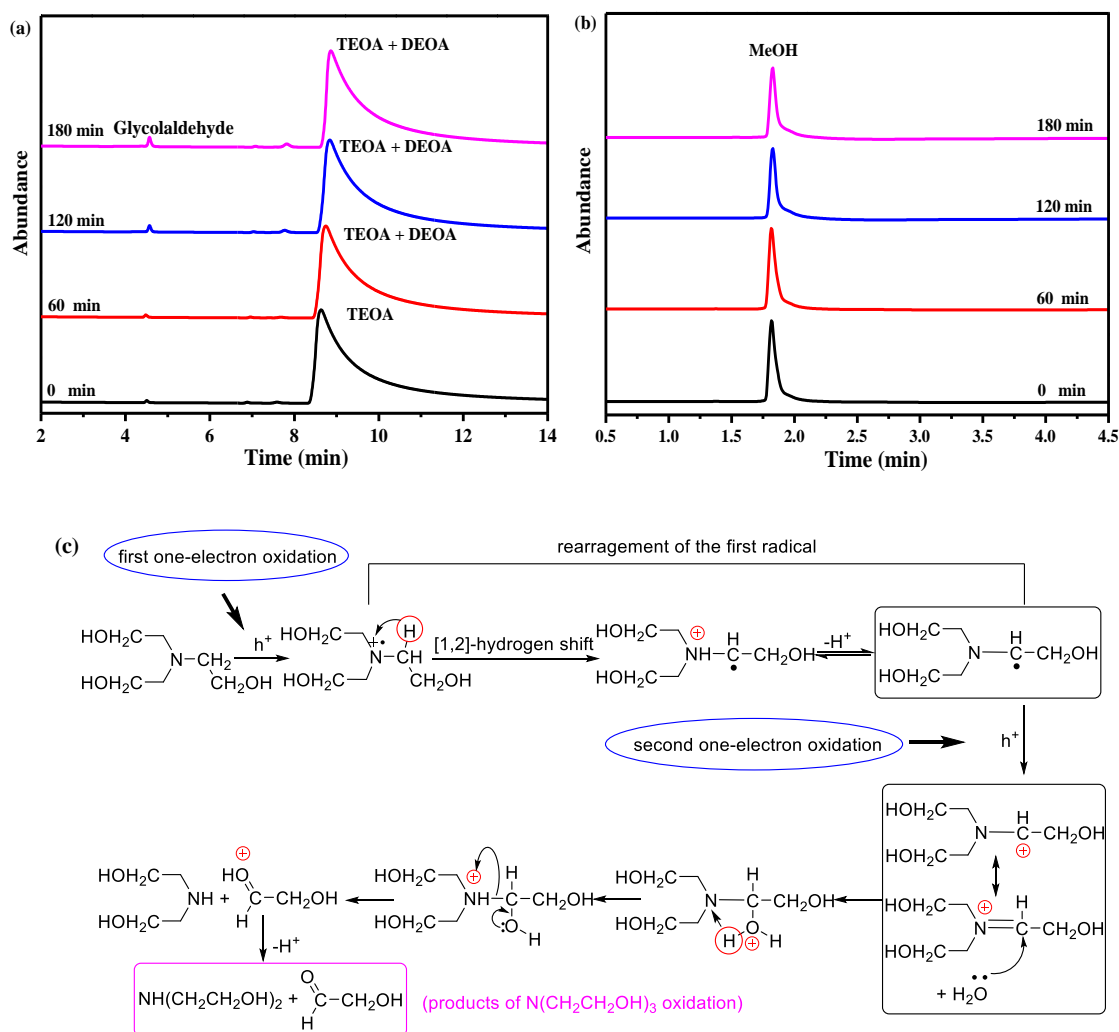


Figure 3.11 HPLC results of the intermediates and products at intervals from the sacrificial reagents, TEOA 10 vol.% (a) or MeOH 10 vol.% (b) in the suspension containing the Ag-Cu(3)/C<sub>3</sub>N<sub>4</sub> NTs (1:1) under visible light irradiation; (c) degradation pathway of TEOA upon monoelectronic oxidation.

When TEOA was used as the sacrificial reagent, the HPLC profile (Figure 3.11a) shows that one dominant peak corresponding to TEOA and a minor peak due to glycolaldehyde were observed prior to visible-light irradiation, confirmed by LC-MS results (Figure A3, Appendix). Prolonging the irradiation time up to 60 min, a small amount of diethanolamine (DEOA) was detected by LC-MC (Figure A4, Appendix). The degradation pathway of TEOA during the photocatalytic hydrogen generation presents in Figure 3.11c. Analogous to the TEA photodegradation, TEOA ( $E_{\text{ox}} = 0.57 \text{ V}_{\text{vs. SCE}}$ ) was oxidised to DEOA and glycolaldehyde upon mono-electronic oxidation [28, 47, 49, 50].

From the reaction mechanisms of TEA and TEOA in Figures 3.10b and 3.11c, the loss of an electron from the lone pair on nitrogen is a crucial step to form the highly reductive carbon radical and prevent charge recombination, leading to an improved hydrogen yield. However, no hydrogen was produced when MeOH was used as the sacrificial reagent. From Figure 3.8b, MeOH was not oxidised by the photo-induced holes. Compared to TEA and TEOA, the oxidation potential of MeOH ( $E_{\text{ox}} = 0.36 \text{ V}_{\text{vs. SCE}}$ ) may be too low and thus not be oxidised in the valence band of the bimetallic catalyst [51].

Based on the above HPLC and LC-MS results, a possible mechanistic explanation of the improved photocatalytic  $\text{H}_2$  generation on the Ag-Cu(3)/ $\text{C}_3\text{N}_4$  NT (1:1) system with TEA as a sacrificial reagent is proposed in Figure 3.12. The bimetallic Ag-Cu NPs are loaded along the channels of  $\text{C}_3\text{N}_4$  NTs and the outside surface as well. When the nanocomposites are illuminated and excited by the photons with energy higher than the bandgap of  $\text{C}_3\text{N}_4$  NTs, the electrons ( $\text{e}^-$ ) of the valence band are excited into the conduction band of  $\text{C}_3\text{N}_4$  NTs and then quickly injected into bimetallic Ag-Cu NPs sites to form new traps. This injection could result in the formation of a Schottky barrier, which can effectively capture photo-induced electrons and facilitate the separation rate of electron-hole pairs, thus enhancing the photocatalytic activity. Electrons arriving at Ag-Cu NPs could efficiently

react with  $\text{H}_2\text{O}$  to generate  $\text{H}_2$  molecules. In the meanwhile, the positively charged holes ( $\text{h}^+$ ) could accumulate in the valence band of  $\text{C}_3\text{N}_4$  NTs and escape onto the surface, subsequently oxidising TEA into  $\text{TEA}^+$ , and further to DEA and acetaldehyde.

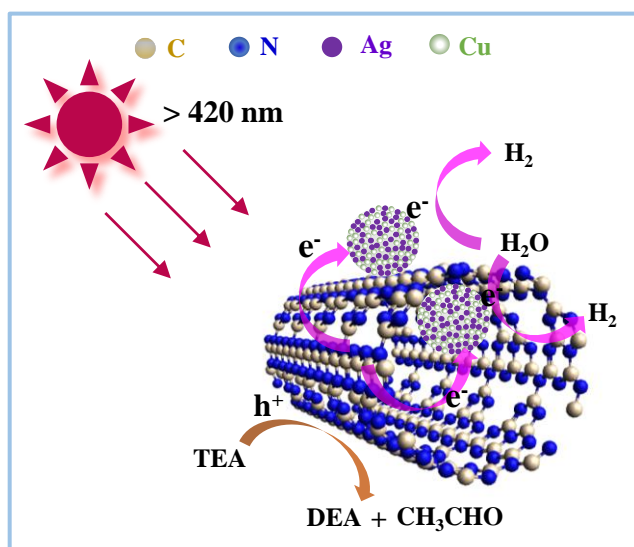


Figure 3.12 Schematic diagram of the Ag-Cu(3)/ $\text{C}_3\text{N}_4$  NT (1:1) nanostructure and its reaction pathway.

### 3.4 Conclusion

Visible-light active bare  $\text{C}_3\text{N}_4$  nanotubes were successfully fabricated by a modified water-induced morphological transformation process. The Ag-Cu bimetallic nanoparticles were homogeneously deposited on the well-ordered  $\text{C}_3\text{N}_4$  NTs. The effects of the Ag/Cu composition in the bimetallic nanoparticles and their loading amounts on the photocatalytic  $\text{H}_2$  production were studied under visible-light irradiation. The highest  $\text{H}_2$  yield ( $738 \mu\text{mol/g}$ ) achieved on the Ag-Cu(3)/ $\text{C}_3\text{N}_4$  NTs (1:1) and it is higher than that of the Pt/ $\text{C}_3\text{N}_4$  NTs and is more than twice of the bare  $\text{C}_3\text{N}_4$  NTs after 3 h visible-light irradiation. The composites are recyclable with no significant loss of hydrogen evolution. The improved activity may be explained by the tubular nanostructure, strong metal-support interaction, high light absorption intensity and efficient separation of photo-generated electron-hole pairs. Mechanistic investigations of various sacrificial reagents suggest that the

photocatalytic H<sub>2</sub> production may more depend on the oxidation potential rather than the pH values of the suspension. It is found that TEA underwent monoelectronic oxidation. This produced DEA and acetaldehyde in water under the oxygen-free conditions, owing to its relatively high oxidation potential, whereas MeOH cannot be easily oxidised by the photo-induced holes. This work presents a green and facile synthetic method for visible-light active photocatalysts; it further advances knowledge of how sacrificial reagents work in the process of photocatalytic H<sub>2</sub> production.

## References

- [1] Z. Han, R. Eisenberg, *Accounts of Chemical Research*, 47 (2014) 2537-2544.
- [2] X. Li, J. Yu, M. Jaroniec, *Chemical Society reviews*, 45 (2016) 2603-2636.
- [3] S. Ye, R. Wang, M.-Z. Wu, Y.-P. Yuan, *Applied Surface Science*, 358 (2015) 15-27.
- [4] W. Ong, L. Tan, Y.H. Ng, S. Yong, S. Chai, *Chemical Reviews*, 116 (2016) 7159-7329.
- [5] D. Deng, K.S. Novoselov, Q. Fu, N. Zheng, Z. Tian, X. Bao, *Nature Nanotechnology*, 11 (2016) 218-230.
- [6] J. Xu, T.J. Brenner, Z. Chen, D. Neher, M. Antonietti, M. Shalom, *ACS Applied Materials & Interfaces*, 6 (2014) 16481-16486.
- [7] F. Fresno, R. Portela, S. Suárez, J.M. Coronado, *Journal of Materials Chemistry A*, 2 (2014) 2863-2884.
- [8] S. Cao, J. Low, J. Yu, M. Jaroniec, *Advanced Materials*, 27 (2015) 2150-2176.
- [9] J. Gracia, P. Kroll, *Journal of Materials Chemistry*, 19 (2009) 3020.
- [10] S. Bian, Z. Ma, W. Song, *The Journal of Physical Chemistry C*, 113 (2009) 8668-8672.
- [11] J.W. Lee, R. Viswan, Y.J. Choi, Y. Lee, S.Y. Kim, J. Cho, Y. Jo, J.K. Kang, *Advanced Functional Materials*, 19 (2009) 2213-2218.
- [12] Z. Jin, Q. Zhang, S. Yuan, T. Ohno, *RSC Advances*, 5 (2015) 4026-4029.

- [13] Z. Zeng, K. Li, L. Yan, Y. Dai, H. Guo, M. Huo, Y. Guo, *RSC Advances*, 4 (2014) 59513-59518.
- [14] X. Wang, K. Maeda, A. Thomas, K. Takanabe, G. Xin, J.M. Carlsson, K. Domen, M. Antonietti, *Nature Materials*, 8 (2009) 76-80.
- [15] V.W. Lau, I. Moudrakovski, T. Botari, S. Weinberger, M.B. Mesch, V. Duppel, J. Senker, V. Blum, B.V. Lotsch, *Nature Communications*, 7 (2016) 12165.
- [16] K. Li, Z. Zeng, L. Yan, S. Luo, X. Luo, M. Huo, Y. Guo, *Applied Catalysis B: Environmental*, 165 (2015) 428-437.
- [17] S. Bala, I. Mondal, A. Goswami, U. Pal, R. Mondal, *Journal of Materials Chemistry A*, 3 (2015) 20288-20296.
- [18] F. Wang, Y. Jiang, D.J. Lawes, G.E. Ball, C. Zhou, Z. Liu, R. Amal, *ACS Catalysis*, 5 (2015) 3924-3931.
- [19] K. Czelej, K. Cwieka, J.C. Colmenares, K.J. Kurzydowski, Y.J. Xu, *ACS Applied Materials & Interfaces*, 9 (2017) 31825-31833.
- [20] K. Czelej, K. Cwieka, J.C. Colmenares, K.J. Kurzydowski, *Langmuir: the ACS journal of surfaces and colloids*, 32 (2016) 7493-7502.
- [21] C. Han, Y. Lu, J. Zhang, L. Ge, Y. Li, C. Chen, Y. Xin, L. Wu, S. Fang, *Journal of Materials Chemistry A*, 3 (2015) 23274-23282.
- [22] C. Han, L. Wu, L. Ge, Y. Li, Z. Zhao, *Carbon*, 92 (2015) 31-40.
- [23] L. Delannoy, G. Thrimurthulu, P.S. Reddy, C. Methivier, J. Nelayah, B.M. Reddy, C. Ricolleau, C. Louis, *Physical Chemistry Chemical Physics: PCCP*, 16 (2014) 26514-26527.
- [24] J. Qin, J. Huo, P. Zhang, J. Zeng, T. Wang, H. Zeng, *Nanoscale*, 8 (2016) 2249-2259.
- [25] H. Tian, X.L. Zhang, J. Scott, C. Ng, R. Amal, *Journal of Materials Chemistry A*, 2 (2014) 6432-6438.



- [26] P. Liu, H. Zhang, H. Liu, Y. Wang, X. Yao, G. Zhu, S. Zhang, H. Zhao, *Journal of the American Chemical Society*, 133 (2011) 19032-19035.
- [27] C. Han, Y. Lu, J. Zhang, L. Ge, Y. Li, C. Chen, Y. Xin, L. Wu, S. Fang, *Journal of Materials Chemistry A*, 3 (2015) 23274-23282.
- [28] Y. Pellegrin, F. Odobel, *Comptes Rendus Chimie*, 20 (2017) 283-295.
- [29] Y. Zhu, Y. Wang, Z. Chen, L. Qin, L. Yang, L. Zhu, P. Tang, T. Gao, Y. Huang, Z. Sha, G. Tang, *Applied Catalysis A: General*, 498 (2015) 159-166.
- [30] O. Rosseler, C. Ulhaq-Bouillet, A. Bonnefont, S. Pronkin, E. Savinova, A. Louvet, V. Keller, N. Keller, *Applied Catalysis B: Environmental*, 166-167 (2015) 381-392.
- [31] Y. Sun, T. Xiong, Z. Ni, J. Liu, F. Dong, W. Zhang, W.-K. Ho, *Applied Surface Science*, 358 (2015) 356-362.
- [32] J. Yang, H. Zhang, B. Chen, H. Tang, C. Li, Z. Zhang, *RSC Advances*, 5 (2015) 64254-64260.
- [33] H. Qian, S. Chen, Y. Fu, X. Wang, *Journal of Power Sources*, 300 (2015) 41-48.
- [34] Z. Liu, Y. Huang, Q. Xiao, H. Zhu, *Green Chemistry*, 18 (2016) 817-825.
- [35] K. Li, L. Yan, Z. Zeng, S. Luo, X. Luo, X. Liu, H. Guo, Y. Guo, *Applied Catalysis B: Environmental*, 156-157 (2014) 141-152.
- [36] M. Jung, J.N. Hart, J. Scott, Y.H. Ng, Y. Jiang, R. Amal, *Applied Catalysis A: General*, 521 (2015) 190-201.
- [37] Z. Liu, Y. Huang, Q. Xiao, H. Zhu, *Green Chemistry*, 18 (2016) 817-825.
- [38] J. Liu, Y. Liu, N. Liu, Y. Han, X. Zhang, H. Huang, Y. Lifshitz, S.-T. Lee, J. Zhong, Z. Kang, *Science*, 347 (2015) 970-974.
- [39] Y. Zhu, Z. Chen, T. Gao, Q. Huang, F. Niu, L. Qin, P. Tang, Y. Huang, Z. Sha, Y. Wang, *Applied Catalysis B: Environmental*, 163 (2015) 16-22.

- [40] I. Pastoriza-Santos, A. Sanchez-Iglesias, B. Rodriguez-Gonzalez, L.M. Liz-Marzan, *Small*, 5 (2009) 440-443.
- [41] D. Chen, K. Wang, W. Hong, R. Zong, W. Yao, Y. Zhu, *Applied Catalysis B: Environmental*, 166-167 (2015) 366-373.
- [42] H. Shi, G. Chen, C. Zhang, Z. Zou, *ACS Catalysis*, 4 (2014) 3637-3643.
- [43] Z. Xiong, Z. Lei, C.-C. Kuang, X. Chen, B. Gong, Y. Zhao, J. Zhang, C. Zheng, J.C.S. Wu, *Applied Catalysis B: Environmental*, 202 (2017) 695-703.
- [44] C.Y. Cummings, F. Marken, L.M. Peter, A.A. Tahir, K.G. Wijayantha, *Chemical Communications*, 48 (2012) 2027-2029.
- [45] M. Zhang, X. Wang, *Energy & Environmental Science*, 7 (2014) 1902.
- [46] X. Bai, L. Wang, Y. Wang, W. Yao, Y. Zhu, 152-153 (2014) 262-270.
- [47] P.J. DeLaive, T.K. Foreman, C. Giannotti, D.G. Whitten, *Journal of the American Chemical Society*, 102 (1980) 5627-5631.
- [48] Y.L. Chow, W.C. Danen, S.F. Nelsen, D.H. Rosenblatt, *Chemical Reviews*, 78 (1978) 243-274.
- [49] E.D. Cline, S.E. Adamson, S. Bernhard, *Inorganic Chemistry*, 47 (2008) 10378-10388.
- [50] D.G. Whitten, *Accounts of Chemical Research*, 13 (1980) 83-90.
- [51] P. Ferrin, A.U. Nilekar, J. Greeley, M. Mavrikakis, J. Rossmeisl, *Surface Science*, 602 (2008) 3424-3431.

## Chapter 4 Tunable Type I and II heterojunction of $\text{CoO}_x$ nanoparticles confined in $\text{C}_3\text{N}_4$ NTs for photocatalytic $\text{H}_2$ production

### 4.1 Introduction

$\text{H}_2$  is potentially an ideal energy carrier, since it is environmentally benign and has the highest specific enthalpy of combustion of any chemical fuel [1]. Producing  $\text{H}_2$  from water splitting is the most extensively studied process for storing solar energy in chemical bonds. This artificial photosynthesis requires efficient photocatalysts with proper band edge, maximum light harvesting and high stability [2]. Recently a metal-free *n*-type semiconductor, graphitic carbon nitride (*g*- $\text{C}_3\text{N}_4$ ), has been intensively studied and applied as visible-light active photocatalyst because of its intriguing 2D layered molecular structure and tunable band gap [3, 4]. We recently reported visible-light active graphitic carbon nitride nanotubes ( $\text{C}_3\text{N}_4$  NTs) for photocatalytic hydrogen generation even in the absence of any co-catalyst [5]. The  $\text{C}_3\text{N}_4$  NTs show better performance than the bulk and nanosheet (NS) counterparts. Attempts are therefore being made to develop cost-effective  $\text{C}_3\text{N}_4$  NT-based composites with improved photocatalytic activity.

Cobalt oxides ( $\text{CoO}_x$ ) including cobalt monoxide ( $\text{CoO}$ ) and tricobalt tetraoxide ( $\text{Co}_3\text{O}_4$ ), the earth-abundant transition metal oxides, as alternatives to precious metals, have received tremendous attention owing to their fascinating electronic and optical properties [6]. Both  $\text{CoO}$  and  $\text{Co}_3\text{O}_4$  are nontoxic and low-cost *p*-type semiconductors.  $\text{CoO}$  has a relatively narrow band gap of around 2.6 eV which allows visible-light absorption. Nevertheless, bulk  $\text{CoO}$  was inactive in photocatalytic hydrogen production since the band positions were not suitable for water splitting. On account of quantum confinement, the edge positions of the conduction band (CB) for nanoscale  $\text{CoO}$  could be altered and become more negative than the reduction potential of  $\text{H}^+/\text{H}_2$ . Liao et al revealed that the CB edge potential of nanostructured  $\text{CoO}$  with

an average particle size of less than 10 nm rose well above the hydrogen-evolution potential compared to its micropowder counterpart. The samples exhibited a solar-to-hydrogen efficiency of 5 % but became deactivated after one hour of reaction [7]. Zhan and his co-workers reported that CoO nanowires composed of assembled nanoparticles (NPs) with two different sizes ( $\sim 34$  nm and  $\sim 65$  nm), exhibited different positions of the band edges and distinctive photocatalytic performance in  $H_2$  generation [8].

Nanostructured  $Co_3O_4$ , with a direct bandgap of about 2.1 eV and comprising both Co(II) and Co(III), is thermodynamically stable under a wide range of temperatures [9].  $Co_3O_4$  nanomaterial is mostly used in photocatalytic oxidation owing to its excellent oxidation capacity [10].  $Co_3O_4$  has a larger visible-light absorption range than that of CoO owing to its narrower band gap. It was demonstrated that  $Co_3O_4$  quantum dots were able to reduce water for  $H_2$  production [11]. On the other hand, the CB edges for bulk CoO and  $Co_3O_4$  are -0.11 eV and 0.37 eV; it is easier for CoO to elevate the CB minimum of the  $H^+$  reduction potential (-0.42 eV vs NHE) [3]. Nevertheless, little work on CoO has been reported owing to its hard synthesis, which requires a special approach to force cobalt into the low valence state. Besides, CoO NPs suffer from a short lifetime, that is, after a certain irradiation they become deactivated due to corroded or oxidised surfaces. Integrating CoO NPs with other nanostructures is a promising way to overcome this shortcoming.

Strategic design of heterojunction architectures with the *n*-type and *p*-type semiconductors possessing suitable band structures, could accelerate water splitting reaction, taking into account the enhanced visible-light absorption and efficient charge separation between two semiconductors [8]. Basically, the band alignments commonly found in junction composites can be categorised into three different types (namely Type I, Type II, and Type III) [12]. Coupling of  $CoO_x$  with  $C_3N_4$  NTs to construct heterojunction structures is a promising route to improve their photocatalytic performance. To date, *n*-type  $C_3N_4$  has been coupled with

different *p*-type semiconductors such as Cu<sub>2</sub>O, TiO<sub>2</sub>, ZnO, Fe<sub>2</sub>O<sub>3</sub>, Fe<sub>3</sub>O<sub>4</sub>, WO<sub>3</sub>, CeO<sub>2</sub>, CoO, and Co<sub>3</sub>O<sub>4</sub> to design heterojunctions for photocatalysis research [3]. Mao *et al.* fabricated C<sub>3</sub>N<sub>4</sub> NS/CoO nanocomposites through a one-pot method applied in photocatalytic H<sub>2</sub> generation, nevertheless, the encased CoO NPs with large a particle size of 30-50 nm were aggregated, resulting in a loss of 17 % activity up to 3 recyclings [13]. Guo *et al.* synthesised CoO/C<sub>3</sub>N<sub>4</sub> NSs through a solvothermal method for overall water splitting under visible light irradiation (> 400 nm), showing high stability of the sample containing 30 wt. % of CoO in the range of 10-20 nm [14]. On the other hand, Co<sub>3</sub>O<sub>4</sub>/C<sub>3</sub>N<sub>4</sub> heterojunctions were reported for photocatalytic water oxidation [15] and methyl orange degradation [16].

The structural property and energy band profile of semiconductor heterojunctions depend largely on their synthesis procedures. This work presents tunable heterojunction architectures of CoO<sub>x</sub> nanoparticles confined on well-arrayed C<sub>3</sub>N<sub>4</sub> NTs by using the same one-pot method after annealing under vacuum or static air atmosphere. The resulting CoO/C<sub>3</sub>N<sub>4</sub> NT (Type II) and Co<sub>3</sub>O<sub>4</sub>/C<sub>3</sub>N<sub>4</sub> NT (Type I) heterojunctions exhibited distinct photocatalytic activity and stability in hydrogen production under visible-light irradiation. Comparative studies on the morphological and structural properties, band positions, electron lifetimes, and charge transfer pathways were undertaken by various characterisation techniques. Finally, the charge transfer pathways and reaction mechanisms are established and evidenced by Kelvin probe force microscopy. This research presents a new strategy to tune Type I and Type II heterojunction architectures of two semiconductors. The results demonstrate the potential widespread utility of this method for developing cost-effective photocatalysts using metal oxides that are abundant in nature.

## 4.2 Experimental section

### 4.2.1 Catalyst fabrication

C<sub>3</sub>N<sub>4</sub> NTs were prepared by a modified process according to the literature [11]. Firstly, 5 g melamine and 30 mL water were placed into a crucible under ultrasonication for 15 min. It was heated at 80 °C to achieve a moderately compact packing degree and then the floating part was removed. Secondly, the crucible was heated up to 500 °C for 2 h with a heating rate of 10 °C min<sup>-1</sup>, then the temperature was increased to 550 °C at a heating rate of 2 °C min<sup>-1</sup>, and kept for another 2 h. Finally, the obtained products were ground into fine powders for future use.

CoO<sub>x</sub> were decorated on C<sub>3</sub>N<sub>4</sub> NTs via a one-pot method that is a single binder-free, low-cost process [13]. 0.5 g of C<sub>3</sub>N<sub>4</sub> NT powder was dispersed in 50 mL of ethanol and stirred for 1 h, followed by adding a nominal amount of cobalt acetate. Then the solution was stirred overnight and dried at 80 °C for 1 h. Finally, the dried powder was annealed at 400 °C for 4 h with a heating rate of 10 °C min<sup>-1</sup> under vacuum, leading to CoO/C<sub>3</sub>N<sub>4</sub> NT composites, or in a static air atmosphere to form Co<sub>3</sub>O<sub>4</sub>/C<sub>3</sub>N<sub>4</sub> NTs, and then naturally cooled to room temperature. Samples are designed as CoO(x)/C<sub>3</sub>N<sub>4</sub> NTs or Co<sub>3</sub>O<sub>4</sub>(y)/C<sub>3</sub>N<sub>4</sub> NTs, where x and y denote the CoO or Co<sub>3</sub>O<sub>4</sub> content in wt. %, respectively. For comparison, CoO and Co<sub>3</sub>O<sub>4</sub> NPs were fabricated through the same procedure but without adding C<sub>3</sub>N<sub>4</sub> NTs.

### 4.2.2 Characterisation

X-ray diffraction (XRD) analysis was performed using a PANalytical X'Pert PRO diffractometer via Cu K<sub>α1</sub> radiation. Field emission scanning electron microscopy (FE-SEM) images were obtained by a JEOL-7100F microscope operating at a voltage of 5 kV. Elemental analysis was conducted on a Phenom XL scanning electron microscope with an energy dispersive X-ray spectrometer (EDS). High-resolution transmission electron microscopy (HRTEM) images and selected area electron diffraction (SAED) were recorded using a JEOL-

2100F microscope operating at 200 kV. X-ray photoelectron spectroscopy (XPS) was recorded on an ESCALAB 250Xi spectrometer (Thermo Scientific, U.K.).

Ultraviolet-visible (UV-vis) diffuse reflectance spectra were obtained on a Cary 5000 spectrophotometer using BaSO<sub>4</sub> as the reference. The steady-state photoluminescence (PL) spectra were recorded on a Fluorolog-Tau3 fluorescence spectrophotometer with an excitation wavelength of 330 nm. Time-resolved PL was measured using the time correlated single photon counting (TCSPC) technique on an MT200 microscope (Picoquant). A 405 nm laser with a pulse repetition rate of 10 MHz was applied as excitation and the signal was detected by a single photon avalanche photodiode (APD) through a 460/40 nm band-pass filter. The decay curves were fitted by the double-exponential decay function  $y = A_1 \exp(-t/\tau_1) + A_2 \exp(-t/\tau_2)$  and the average lifetime was obtained by  $\tau_{AV} = (A_1 \tau_1^2 + A_2 \tau_2^2) / (A_1 \tau_1 + A_2 \tau_2)$ . The photocurrent measurements were performed on a potentiostat (SP-300, BioLogic Science Instruments) using a three-electrode setup with a Pt wire as the counter electrode, the Ag/AgCl electrode (saturated KCl) as the reference electrode and the prepared catalyst/Ti sheet as the working electrode. The electrolyte was a 0.1 M Na<sub>2</sub>SO<sub>4</sub> aqueous solution. Transient photocurrent responses were carried out as light on and off at a constant potential of + 0.1 V, and a 300 W Xenon arc lamp (LX300, Peccell Technologies, Inc.) was employed as the light source.

Kelvin probe force microscopy (KPFM) was performed at ambient conditions using a Bruker Dimension ICON SPM with a Pt-coated probe. The surface potential difference between the sample and the probe was measured with a tip lift height of 30 nm. The probe-sample distance was precisely controlled by the software of Kelvin probe system. The powder sample dispersed in Milli-Q water was spin-coated on a silicon wafer that was previously cleaned with ethanol

and dried by N<sub>2</sub> gas. The obtained sample was dried for 24 h prior to the KPFM measurements. The potential results were analyzed by the software NanoScope Analysis.

### 4.2.3 Photocatalytic hydrogen production

The detailed procedure of photocatalytic H<sub>2</sub> production over the nanocomposites synthesised in the study is referred to Section 3.2.3 in Chapter 3. TEA was used as the sacrificial reagent.

## 4.3 Results and discussion

### 4.3.1 Photocatalytic performance

As shown in Figure 4.1a the photocatalytic performance of bare CoO and C<sub>3</sub>N<sub>4</sub> NTs decorated with different CoO content from 3 to 10 wt. % were investigated for photocatalytic H<sub>2</sub> generation from water splitting under visible-light irradiation. CoO NPs yielded 209.6  $\mu\text{mol/g}$  of H<sub>2</sub> within 3 h, lower than the bare C<sub>3</sub>N<sub>4</sub> NTs (360.0  $\mu\text{mol/g}$ ). The activities of all CoO/C<sub>3</sub>N<sub>4</sub> NT heterojunctions are higher than that of the bare C<sub>3</sub>N<sub>4</sub> NTs. In detail, after 3 h illumination H<sub>2</sub> yields over the CoO/C<sub>3</sub>N<sub>4</sub> NTs composites with 3, 5, 7 and 10 wt. % of CoO content correspond to be 484.9, 587.1, 788.6 and 533.5  $\mu\text{mol/g}$ , respectively. It is noted that the rate of H<sub>2</sub> evolution over the CoO(7)/C<sub>3</sub>N<sub>4</sub> NT sample is almost 2.2 times as high as that of the bare C<sub>3</sub>N<sub>4</sub> NTs. A lower H<sub>2</sub> evolution was observed when the CoO loading was increased further (CoO(10)/C<sub>3</sub>N<sub>4</sub> NTs), which may be attributed to the decoration of excessive CoO leading to larger CoO particles and a considerable amount of C<sub>3</sub>N<sub>4</sub> NT surface active sites inaccessible to the light and the reactants. Figure 4.1b shows the H<sub>2</sub> evolution profile of the Co<sub>3</sub>O<sub>4</sub>/C<sub>3</sub>N<sub>4</sub> NT composites with different Co<sub>3</sub>O<sub>4</sub> content (3, 5, 7 and 10 wt. %). Among them, the Co<sub>3</sub>O<sub>4</sub>(7)/C<sub>3</sub>N<sub>4</sub> NT catalyst exhibits the highest amount of H<sub>2</sub> generation (725.7  $\mu\text{mol/g}$ ) which is about twice that of C<sub>3</sub>N<sub>4</sub> NTs. Notably, the activity is lower than that of CoO(7)/C<sub>3</sub>N<sub>4</sub> NTs. The AQE of CoO(7)/C<sub>3</sub>N<sub>4</sub> NTs, Co<sub>3</sub>O<sub>4</sub>(7)/C<sub>3</sub>N<sub>4</sub> NTs, and C<sub>3</sub>N<sub>4</sub> NTs is determined to be 4.928, 4.077, 2.209 %, respectively. The AQE of 1.9 % for the CoO/C<sub>3</sub>N<sub>4</sub> was reported at the 420 nm



wavelength. However, the transmittance was not provided for comparison [14]. In contrast, the photocatalytic performance of CoO and Co<sub>3</sub>O<sub>4</sub> NPs were also evaluated. It can be seen that Co<sub>3</sub>O<sub>4</sub> NPs resulted in a lower H<sub>2</sub> evolution rate than CoO NPs.

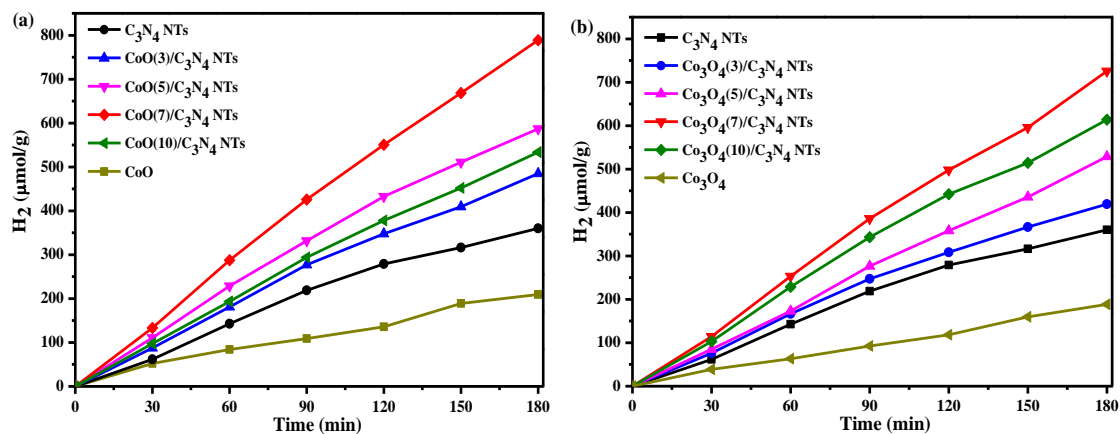


Figure 4.1 H<sub>2</sub> generation over C<sub>3</sub>N<sub>4</sub> NTs loaded with different content of CoO (a) and Co<sub>3</sub>O<sub>4</sub> NPs (b) under visible light irradiation. Reaction condition: 40 mg catalyst in 40 mL water/TEA solution (volume ratio of 9/1) and visible light irradiation (> 420 nm) for 3 h.

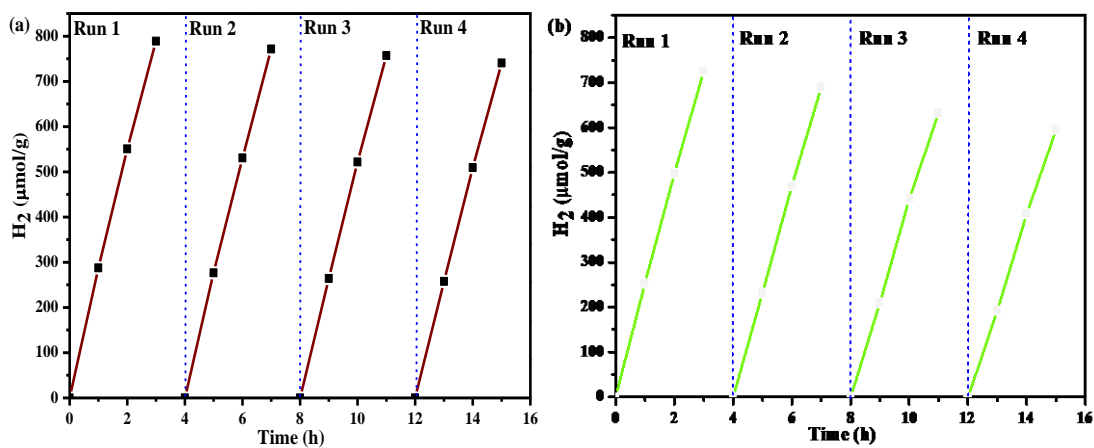


Figure 4.2 Cycling runs for H<sub>2</sub> evolution over CoO(7)/C<sub>3</sub>N<sub>4</sub> NTs (a) and Co<sub>3</sub>O<sub>4</sub>(7)/C<sub>3</sub>N<sub>4</sub> NTs (b). Reaction condition: 40 mg catalyst in 40 mL water/TEA solution (volume ratio of 9/1) and visible light irradiation (> 420 nm) for 3 h.

The stability of the CoO(7)/C<sub>3</sub>N<sub>4</sub> NT and Co<sub>3</sub>O<sub>4</sub>(7)/C<sub>3</sub>N<sub>4</sub> NT photocatalysts was investigated after they were recovered from the reaction mixture and reused for another fresh solution. As

shown in Figure 4.2, good photocatalytic performance of CoO(7)/C<sub>3</sub>N<sub>4</sub> NTs was maintained for at least four cycling runs, only losing 6.0 %. However, the Co<sub>3</sub>O<sub>4</sub>(7)/C<sub>3</sub>N<sub>4</sub> NT nanostructure lost almost 18.0 % of the H<sub>2</sub> yield. It is apparent that CoO(7)/C<sub>3</sub>N<sub>4</sub> NTs exhibit much better stability than that of Co<sub>3</sub>O<sub>4</sub>(7)/C<sub>3</sub>N<sub>4</sub> NTs. In the next sections, CoO(7)/C<sub>3</sub>N<sub>4</sub> NTs, Co<sub>3</sub>O<sub>4</sub>(7)/C<sub>3</sub>N<sub>4</sub> NTs, bare C<sub>3</sub>N<sub>4</sub> NTs, CoO and Co<sub>3</sub>O<sub>4</sub> NPs were selected for further investigations.

### 4.3.2 Structure characterisation

Figure 4.3 shows the XRD patterns for CoO(7)/C<sub>3</sub>N<sub>4</sub> NTs, Co<sub>3</sub>O<sub>4</sub>(7)/C<sub>3</sub>N<sub>4</sub> NTs, bare C<sub>3</sub>N<sub>4</sub> NTs, CoO and Co<sub>3</sub>O<sub>4</sub> NPs. The bare C<sub>3</sub>N<sub>4</sub> NTs reveal two XRD peaks at  $2\theta = 13.0^\circ$  and  $27.4^\circ$ . The former is indexed as the (100) diffraction of graphitic C<sub>3</sub>N<sub>4</sub> and can be related to an in-plane structural packing motif, whereas the latter is due to the (002) plane with characteristic interlayer stacking of conjugated aromatic systems [17, 18]. These two diffraction peaks are also observed for both CoO(7)/C<sub>3</sub>N<sub>4</sub> NT and Co<sub>3</sub>O<sub>4</sub>(7)/C<sub>3</sub>N<sub>4</sub> NT samples indicating that the typical structure of graphitic C<sub>3</sub>N<sub>4</sub> did not alter upon surface modification with cobalt oxides. For CoO NPs, the peaks at  $36.5^\circ$ ,  $42.4^\circ$ ,  $61.5^\circ$ ,  $73.7^\circ$  and  $77.5^\circ$  can be assigned to the (111), (200), (220), (311) and (222) facets of cubic CoO, respectively (JCPDS no. 48-1719) [19, 20]. The XRD profile of CoO(7)/C<sub>3</sub>N<sub>4</sub> NTs shows the same characteristic humps of CoO NPs, which verifies the presence of CoO NPs on the C<sub>3</sub>N<sub>4</sub> NTs.

The XRD patterns of Co<sub>3</sub>O<sub>4</sub> NPs demonstrate that they are face-centered cubic phase (JCPDS no. 42-1467) [21]. Except for the typical peaks of graphitic C<sub>3</sub>N<sub>4</sub> in the XRD profile of Co<sub>3</sub>O<sub>4</sub>/C<sub>3</sub>N<sub>4</sub> NT nanocomposites, the Co<sub>3</sub>O<sub>4</sub> NP crystal planes were clearly observed, indicating the success of Co<sub>3</sub>O<sub>4</sub> deposition on the C<sub>3</sub>N<sub>4</sub> NTs. Furthermore, we examined the crystal structures of CoO(7)/C<sub>3</sub>N<sub>4</sub> NTs and Co<sub>3</sub>O<sub>4</sub>(7)/C<sub>3</sub>N<sub>4</sub> NTs before and after recycling experiments by XRD analysis (Figure 4.4). No significant change in their patterns was observed, which confirms that CoO/C<sub>3</sub>N<sub>4</sub> NTs and Co<sub>3</sub>O<sub>4</sub>/C<sub>3</sub>N<sub>4</sub> NTs are stable and reusable photocatalysts.

Furthermore, from the enlarged patterns in the inset, the slightly decreased intensity of the main peaks indexed to  $\text{Co}_3\text{O}_4$  NPs was detected, implying a tiny portion of  $\text{Co}_3\text{O}_4$  NPs deposited on the surface of  $\text{C}_3\text{N}_4$  NTs may be lost during the recycling process due to the relatively larger  $\text{Co}_3\text{O}_4$  particle size and lower binding force between  $\text{Co}_3\text{O}_4$  and  $\text{C}_3\text{N}_4$  support. This explains the relatively lower stability of  $\text{Co}_3\text{O}_4/\text{C}_3\text{N}_4$  NT catalyst.

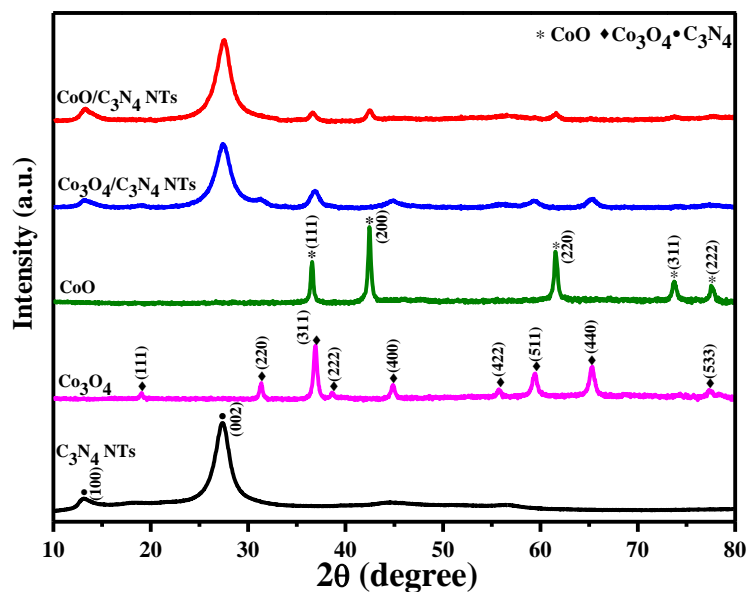


Figure 4.3 XRD patterns of  $\text{C}_3\text{N}_4$  NTs,  $\text{Co}_3\text{O}_4$ ,  $\text{CoO}$ ,  $\text{CoO}(7)/\text{C}_3\text{N}_4$  NTs and  $\text{Co}_3\text{O}_4(7)/\text{C}_3\text{N}_4$  NTs.

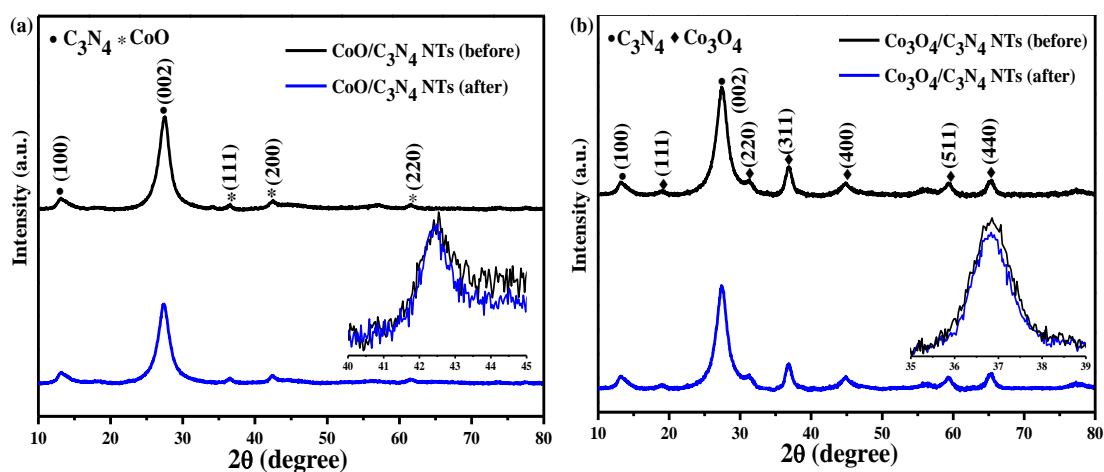


Figure 4.4 XRD patterns of  $\text{CoO}(7)/\text{C}_3\text{N}_4$  NTs (a) and  $\text{Co}_3\text{O}_4(7)/\text{C}_3\text{N}_4$  NTs (b) before and after reaction.

The as-synthesised bare  $C_3N_4$  NT materials exhibit tube-like morphology with an average diameter of about 80 nm as seen in the FE-SEM and TEM images (Figure 4.5). The nanotubes are well arranged in a compact ordered array and some are even longer than 10  $\mu m$ . The elemental mapping of  $CoO(7)/C_3N_4$  NTs and  $Co_3O_4(7)/C_3N_4$  NTs determined by SEM-EDS in Figure 4.6 reveals the homogenous distribution of cobalt, oxygen, and nitrogen elements in the nanostructures. The atomic and weight ratios of Co, O, C and N are summarised in the inset tables. The atomic ratios of Co/N determined from SEM-EDS resembles the nominal content of CoO and  $Co_3O_4$ , which further confirms that CoO and  $Co_3O_4$  NPs were successfully deposited on the surface of  $C_3N_4$  NTs.

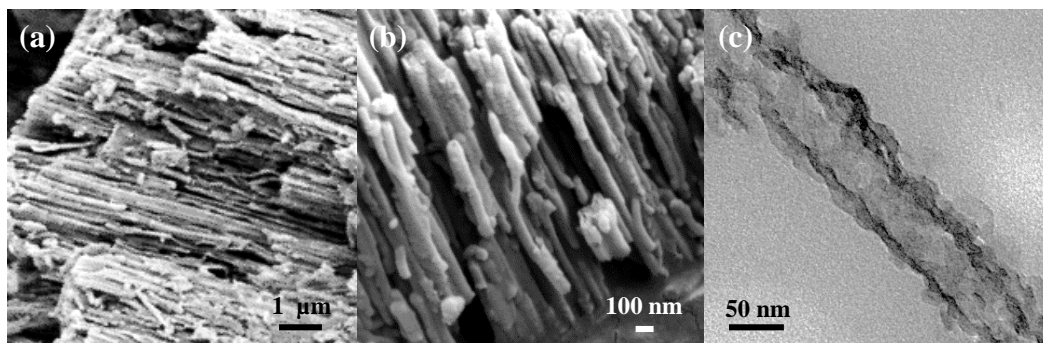


Figure 4.5 SEM (a, b) and TEM (c) images of the bare  $C_3N_4$  NTs.

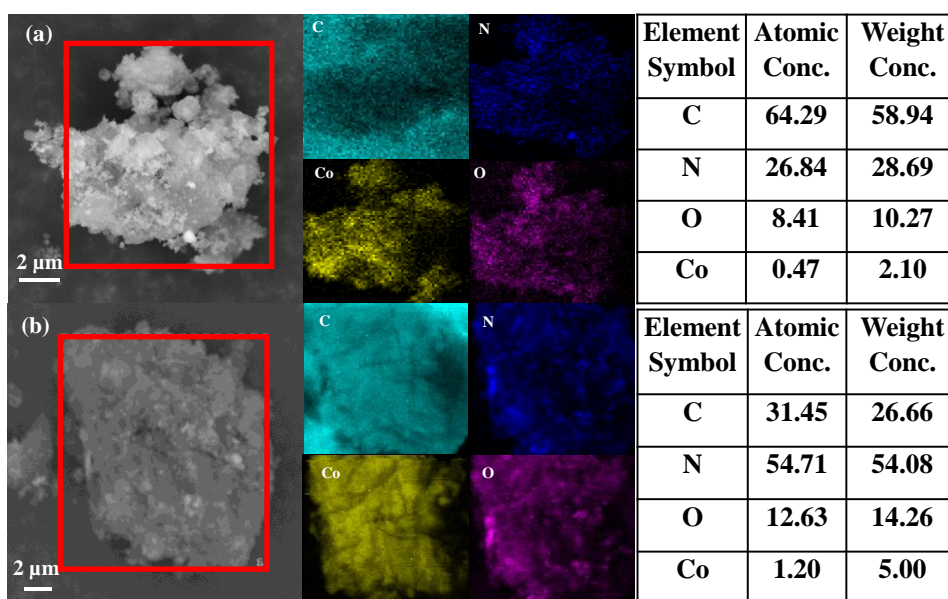


Figure 4.6 SEM-EDS of  $CoO(7)/C_3N_4$  NTs (a) and  $Co_3O_4(7)/C_3N_4$  NTs (b).

High-resolution TEM and SAED were employed to investigate the microstructure of CoO and Co<sub>3</sub>O<sub>4</sub> NP deposited samples. Figures 4.7a-c show the TEM images of CoO(7)/C<sub>3</sub>N<sub>4</sub> NTs. From the low-magnification image (Figure 4.7a), well-distributed CoO NPs are observed on the surface of the C<sub>3</sub>N<sub>4</sub> NTs. The high-resolution TEM images in Figure 4.7b demonstrate that the CoO NPs, with a uniform particle size of around 8 nm, are tightly anchored on the well-defined C<sub>3</sub>N<sub>4</sub> framework, illustrating the existence of an interface between CoO and C<sub>3</sub>N<sub>4</sub> NTs. Lattice spacings of 0.213, 0.246 and 0.151 nm were determined and assigned to the (200), (111) and (220) planes of CoO crystals, respectively. The diffraction rings of the SAED pattern in Figure 4.7c reveal the cubic lattice structure of CoO NPs [7], corroborating well with the previous XRD results.

Figures 4.7d-f show the TEM images of Co<sub>3</sub>O<sub>4</sub>(7)/C<sub>3</sub>N<sub>4</sub> NT nanocomposites. In Figure 4.7d it is found that Co<sub>3</sub>O<sub>4</sub> NPs with the particle size from 10 to 50 nm, were deposited with a certain aggregation on the surface of the nanotubes. This can explain the poor activity and stability of Co<sub>3</sub>O<sub>4</sub>(7)/C<sub>3</sub>N<sub>4</sub> NTs in H<sub>2</sub> generation compared with the CoO(7)/C<sub>3</sub>N<sub>4</sub> NT sample. The lattice fringe (Figure 4.7e), allows the identification of crystallographic spacings of  $d = 0.202$ ,  $0.244$  and  $0.142$  nm matching well with the (400), (311) and (440) planes of Co<sub>3</sub>O<sub>4</sub> NPs. In the SAED patterns (Figure 4.7f) the three planes are observed, further demonstrating the cubic structure of Co<sub>3</sub>O<sub>4</sub> [21]. In Figures 4.8a-b, TEM images of CoO(10)/C<sub>3</sub>N<sub>4</sub> NTs and Co<sub>3</sub>O<sub>4</sub>(10)/C<sub>3</sub>N<sub>4</sub> NTs show that most CoO NPs were deposited on the surface of C<sub>3</sub>N<sub>4</sub> NTs, whereas a single C<sub>3</sub>N<sub>4</sub> nanotube is fully encased with larger Co<sub>3</sub>O<sub>4</sub> NPs. It is interesting to note that a great number of Co<sub>3</sub>O<sub>4</sub> NPs aggregated in the vicinity of C<sub>3</sub>N<sub>4</sub> NTs. The low actual content of Co<sub>3</sub>O<sub>4</sub> NPs on the nanotube may explain the higher activity of Co<sub>3</sub>O<sub>4</sub>(10)/C<sub>3</sub>N<sub>4</sub> NTs than CoO(10)/C<sub>3</sub>N<sub>4</sub> NTs. For comparison, the particle sizes of the bare CoO and Co<sub>3</sub>O<sub>4</sub> NPs were determined to be approximately 10 nm and 20-80 nm, respectively (Figures 4.8c-d).

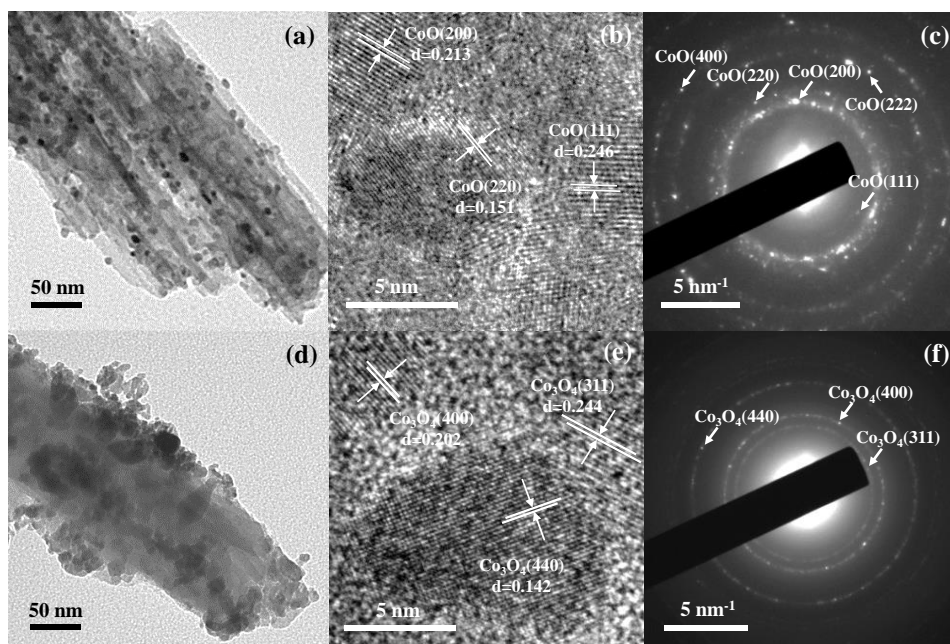


Figure 4.7 TEM images of CoO(7)/C<sub>3</sub>N<sub>4</sub> NT (a-c) and Co<sub>3</sub>O<sub>4</sub>(7)/C<sub>3</sub>N<sub>4</sub> NT (d-f).

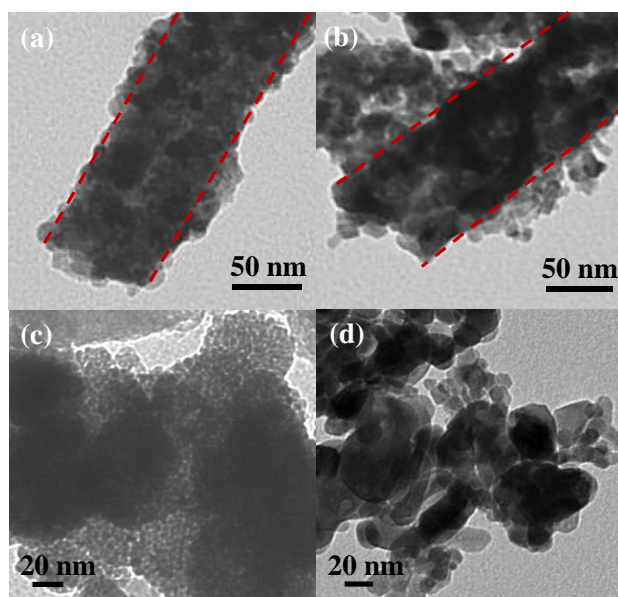


Figure 4.8 TEM images of CoO(10)/C<sub>3</sub>N<sub>4</sub> NTs (a), Co<sub>3</sub>O<sub>4</sub>(10)/C<sub>3</sub>N<sub>4</sub> NTs (b), CoO (c) and Co<sub>3</sub>O<sub>4</sub> NPs (d).

Figure 4.9 shows the UV-vis diffuse reflectance spectra (DRS) of the bare C<sub>3</sub>N<sub>4</sub> NTs, CoO(7)/C<sub>3</sub>N<sub>4</sub> NTs, Co<sub>3</sub>O<sub>4</sub>(7)/C<sub>3</sub>N<sub>4</sub> NTs, CoO and Co<sub>3</sub>O<sub>4</sub> NPs. The spectrum of the bare C<sub>3</sub>N<sub>4</sub> NTs presents a steep absorption edge at near 460 nm. The band gap of C<sub>3</sub>N<sub>4</sub> NTs (Figure 4.9b) was determined to be around 2.74 eV by applying the Kubelka-Munk transformation, which



gives a slight blue shift relative to that of bulk  $C_3N_4$  ( $\sim 2.70$  eV) because of the quantum confinement [22, 23]. The UV-vis spectrum of CoO NP catalysts presents an absorption band edge at around 500 nm ascribed to ligand-metal charge transfer events  $O^{II} \rightarrow Co^{II}$ . The other broad band edge at approximately 760 nm arises from Co(II)  $d-d$  transitions, implying that the  $Co^{2+}$  ions are tetrahedrally coordinated [24]. The spectrum of the CoO(7)/ $C_3N_4$  NTs exhibits a new absorption broad edge at about 670 nm (enlarged in the inset part), compared with the bare  $C_3N_4$  NTs, which can be attributed to the CoO component. This indicates that the loading of CoO NPs resulted in more visible-light response on the  $C_3N_4$  NT-based material due to the synergetic effect between two semiconductors. The spectrum of the bare  $Co_3O_4$  NPs shows two absorptions centered at around 330 and 650 nm, which are attributed to ligand-metal charge transfer between  $O^{II} \rightarrow Co^{II}$  and  $O^{II} \rightarrow Co^{III}$ , respectively [11, 25]. As shown in Figure 4.9b, the  $Co_3O_4/C_3N_4$  NTs display very similar properties with two light absorptions at *ca.* 2.12 eV and *ca.* 2.46 eV, which presents combined behaviours from the  $Co_3O_4$  and  $C_3N_4$  NT materials.

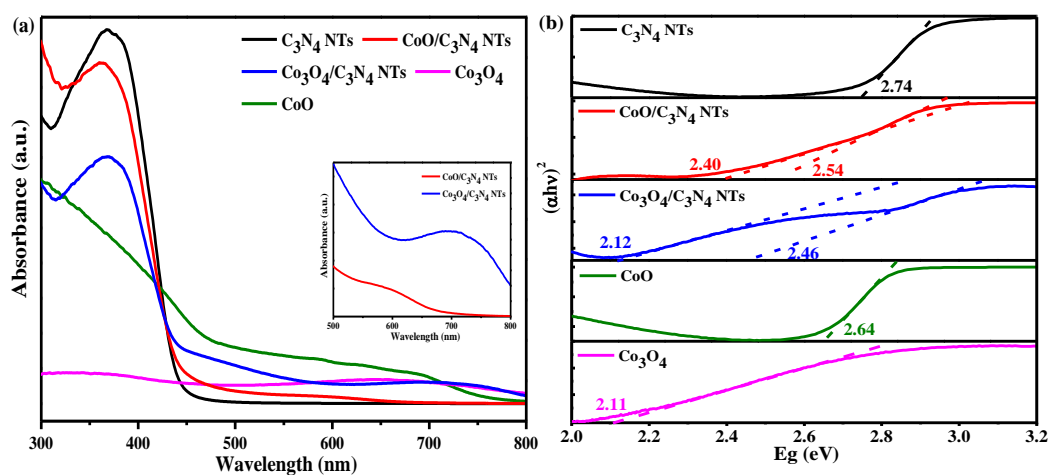


Figure 4.9 UV-vis diffuse reflectance spectra of the photocatalysts studied in this work.

To further explore the origin of the improved photocatalytic performance, the steady-state photoluminescence spectra of the nanocomposites are shown in Figure 4.10a. The bare  $C_3N_4$  NTs exhibit a broad PL emission band with a peak centred at approximately 460 nm, which matches well with our UV-Vis DRS results, demonstrating that the  $C_3N_4$  NT material can act

as a blue light-emitting material [11, 26]. Integrating  $C_3N_4$  NTs with CoO NPs led to a decreased intensity compared to that with  $Co_3O_4$  NPs. This indicates that the deposition of CoO on  $C_3N_4$  NTs could greatly inhibit the recombination of photo-generated carriers. The PL spectra of CoO and  $Co_3O_4$  NPs were much weaker than those of the two nanocomposites and  $C_3N_4$  NTs. They exhibit negligible PL intensity. As shown in the inset of Figure 4.10a, it can be seen that the PL intensity of CoO is slightly lower than that of  $Co_3O_4$ . This can be one of the reasons that CoO NPs exhibit better photocatalytic performance than  $Co_3O_4$  as depicted in Figure 4.1.

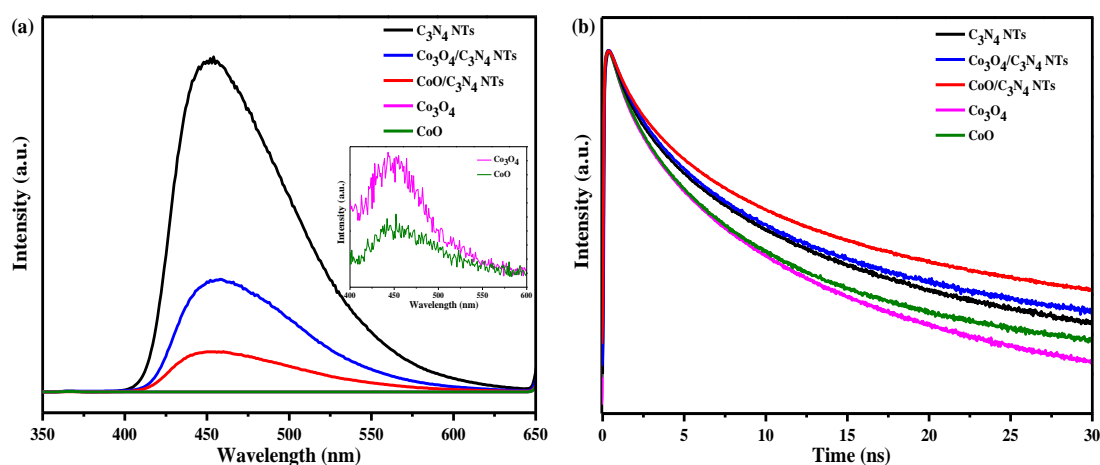


Figure 4.10 Photoluminescence spectra (a) and transient decay curves (b) of the photocatalysts studied in this work.

The lifetimes of the excited electrons on the nanocomposites were measured by the TCSPC technique. The average lifetimes of  $(9.47 \pm 0.03)$ ,  $(8.02 \pm 0.04)$ ,  $(7.60 \pm 0.03)$ ,  $(5.80 \pm 0.03)$  and  $(5.63 \pm 0.02)$  ns were obtained on CoO(7)/ $C_3N_4$  NTs,  $Co_3O_4$ (7)/ $C_3N_4$  NTs,  $C_3N_4$  NTs, CoO and  $Co_3O_4$ , respectively in Figure 4.10b. A longer lifetime of the material generally means a greater opportunity of contributing more excited electrons to the semiconductor [27]. This finding also explains why CoO(7)/ $C_3N_4$  NTs exhibit the best photocatalytic performance in hydrogen generation among all the materials studied in this work.



As shown in Figure 4.11, the transient photocurrent responses of the samples were investigated by three on-off cycles of intermittent visible-light irradiation with good reproducibility. A considerably enhanced photocurrent was generated on CoO(7)/C<sub>3</sub>N<sub>4</sub> NTs, about 1.6 times as high as that of Co<sub>3</sub>O<sub>4</sub>(7)/C<sub>3</sub>N<sub>4</sub> NTs and higher than all the other nanomaterials present in this work. The sequence of photocurrent densities in order is CoO(7)/C<sub>3</sub>N<sub>4</sub> NTs > Co<sub>3</sub>O<sub>4</sub>(7)/C<sub>3</sub>N<sub>4</sub> NTs > C<sub>3</sub>N<sub>4</sub> NTs > CoO > Co<sub>3</sub>O<sub>4</sub>. This result reveals that recombination of electron-hole pairs was greatly retarded and the separation of charge carriers at the interface between CoO and C<sub>3</sub>N<sub>4</sub> NTs was improved. It further confirms the above PL results. It is worth noting that the CoO(7)/C<sub>3</sub>N<sub>4</sub> NTs performs higher stability than the Co<sub>3</sub>O<sub>4</sub>(7)/C<sub>3</sub>N<sub>4</sub> NTs, agreeing with the stability test results depicted in Figure 4.2. In comparison with Co<sub>3</sub>O<sub>4</sub>(7)/C<sub>3</sub>N<sub>4</sub> NT nanocomposites, the higher stability of CoO(7)/C<sub>3</sub>N<sub>4</sub> NTs may be attributed to the smaller CoO particle size and good dispersion along the channel of the tubes as confirmed in the TEM images.

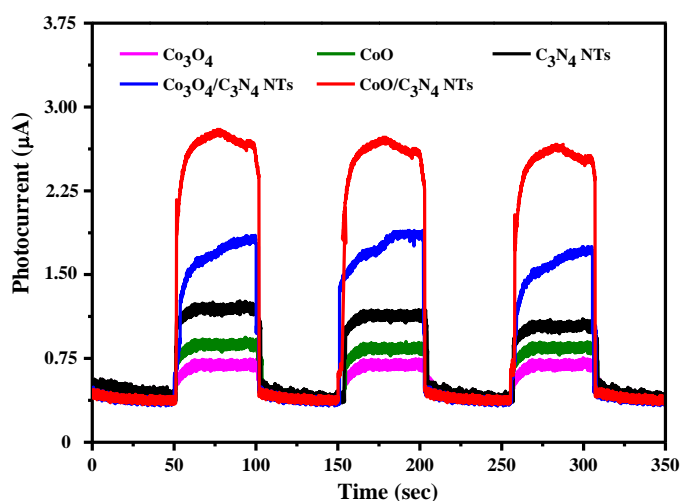


Figure 4.11 The periodic on/off photocurrent response of the photocatalysts studied in this work.

The surface chemical compositions and oxidation states of the nanocomposites studied in this work were analyzed by XPS. The wide-scan XPS spectra implied that CoO/C<sub>3</sub>N<sub>4</sub> NTs and

Co<sub>3</sub>O<sub>4</sub>/C<sub>3</sub>N<sub>4</sub> NTs consisted of C, N, Co and O elements (Figure 4.12 and Table 4.1). Based on the Co/N atom ratios determined by XPS, the CoO and Co<sub>3</sub>O<sub>4</sub> content on the C<sub>3</sub>N<sub>4</sub> NT surface were obtained, respectively, agreeing very well with the above SEM-EDS results. In Figure 4.13a, the binding energy at 780.8 and 796.4 eV is assigned to Co 2p<sub>3/2</sub> and 2p<sub>1/2</sub> species on the surface of CoO/C<sub>3</sub>N<sub>4</sub> NTs, respectively. Moreover, the shake-up satellite structures apart from the main peaks verify the existence of Co(II) species [19, 28], confirming the successful deposition of pure CoO. This is in line with the XRD and TEM results. Compared to the XPS spectrum of the bare CoO NPs, the Co 2p<sub>3/2</sub> and 2p<sub>1/2</sub> peaks were slightly shifted toward a lower binding energy region at 780.5 eV and 796.0 eV, indicating a strong interaction between CoO and the underlying C<sub>3</sub>N<sub>4</sub> NT support.

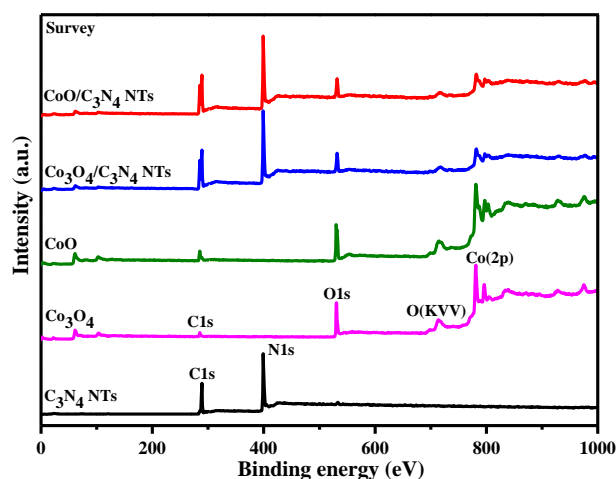


Figure 4.12 XPS wide-scan spectra of CoO(7)/C<sub>3</sub>N<sub>4</sub> NTs, Co<sub>3</sub>O<sub>4</sub>(7)/C<sub>3</sub>N<sub>4</sub> NTs, the bare C<sub>3</sub>N<sub>4</sub> NTs, CoO and Co<sub>3</sub>O<sub>4</sub> NPs.

Table 4.1 Atomic ratios of various elements in XPS analysis.

Name	Co <sub>3</sub> O <sub>4</sub> (7)/C <sub>3</sub> N <sub>4</sub> NTs Atomic %	CoO(7)/C <sub>3</sub> N <sub>4</sub> NTs Atomic %
C1s	30.49	52.84
O1s	13.89	17.41
N1s	54.41	29.13
Co2p	1.21	0.62

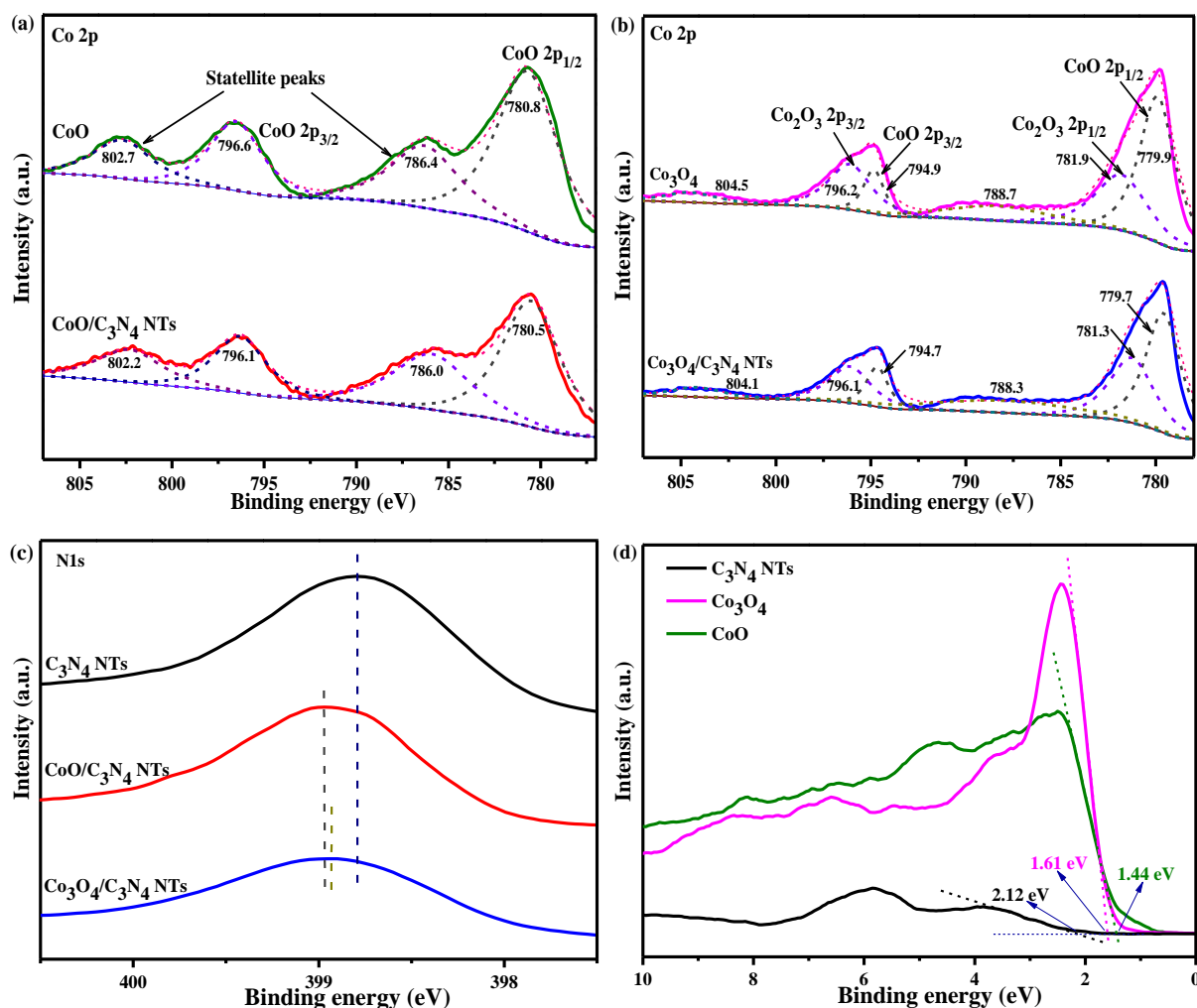


Figure 4.13 Co 2p XPS spectra of CoO NPs and CoO(7)/C<sub>3</sub>N<sub>4</sub> NTs (a), and Co<sub>3</sub>O<sub>4</sub> NPs and Co<sub>3</sub>O<sub>4</sub>(7)/C<sub>3</sub>N<sub>4</sub> NTs (b); N 1s XPS spectra of the bare C<sub>3</sub>N<sub>4</sub> NTs and cobalt oxide modified samples (c); VB XPS of C<sub>3</sub>N<sub>4</sub> NTs, CoO and Co<sub>3</sub>O<sub>4</sub> NPs (d).

A similar phenomenon was also observed in the Co 2p XPS spectra of Co<sub>3</sub>O<sub>4</sub>(7)/C<sub>3</sub>N<sub>4</sub> NT and Co<sub>3</sub>O<sub>4</sub> samples as depicted in Figure 4.13b. Two peaks at 779.8 eV and 794.8 eV of Co<sub>3</sub>O<sub>4</sub>(7)/C<sub>3</sub>N<sub>4</sub> NTs are about 0.1 eV lower than those of Co<sub>3</sub>O<sub>4</sub> samples. On the other hand, as shown in Figure 4.13c, the N 1s XPS spectra of both CoO(7)/C<sub>3</sub>N<sub>4</sub> NTs and Co<sub>3</sub>O<sub>4</sub>(7)/C<sub>3</sub>N<sub>4</sub> NTs exhibit a positive shift as compared to the bare C<sub>3</sub>N<sub>4</sub> NTs, indicating a strong interaction between Co and N atoms. He *et al.* reported that chemical bonds between ZnO and C<sub>3</sub>N<sub>4</sub> were formed [29]. The larger shifts in Co 2p and N 1s XPS spectra were observed for CoO(7)/C<sub>3</sub>N<sub>4</sub> NTs compared with that for Co<sub>3</sub>O<sub>4</sub>(7)/C<sub>3</sub>N<sub>4</sub> NTs, implying stronger interaction between CoO

and C<sub>3</sub>N<sub>4</sub> NTs. The strong interaction between cobalt oxides and C<sub>3</sub>N<sub>4</sub> NT support is beneficial for the formation of heterojunctions, thus promoting a smooth charge transfer between the two semiconductors.

The VB XPS spectra as shown in Figure 4.13d reveal that the VB potentials ( $E_{VB}$ ) of CoO, Co<sub>3</sub>O<sub>4</sub>, and C<sub>3</sub>N<sub>4</sub> NTs are 1.44, 1.61 and 2.12 eV relative to the normal hydrogen electrode (NHE), respectively. These values are all more positive than the redox potential of O<sub>2</sub>/H<sub>2</sub>O (1.23 eV *vs* NHE). Considering the band gap determined by the UV-Vis DRS, the CB potentials ( $E_{CB}$ ) of CoO, Co<sub>3</sub>O<sub>4</sub>, and C<sub>3</sub>N<sub>4</sub> NTs are located at -1.20, -0.50 and -0.62 eV *vs* NHE, respectively, which are much more negative than the reduction potential of H<sup>+</sup>/H<sub>2</sub> (-0.42 eV *vs* NHE). Therefore, the band structures of CoO, Co<sub>3</sub>O<sub>4</sub>, and C<sub>3</sub>N<sub>4</sub> NTs studied in this work are suitable for hydrogen production from water splitting. It is also noted that the CB and VB positions of CoO NPs, Co<sub>3</sub>O<sub>4</sub> NPs and C<sub>3</sub>N<sub>4</sub> NTs were upshifted in comparison with the bulk CoO [7], Co<sub>3</sub>O<sub>4</sub> [30] and C<sub>3</sub>N<sub>4</sub> [31]. Both of the CB band edges of CoO NPs and Co<sub>3</sub>O<sub>4</sub> NPs are higher than the level of H<sup>+</sup>/H<sub>2</sub> at -0.42 eV, which confirms the feasibility for H<sub>2</sub> generation.

To further verify the band edge potentials, the flat band potentials of C<sub>3</sub>N<sub>4</sub> NTs, CoO NPs and Co<sub>3</sub>O<sub>4</sub> NPs were recorded by the Mott-Schottky plots from electrochemical impedance spectroscopy. As shown in Figure 4.14a, the positive slope of the Mott-Schottky plot indicates that the C<sub>3</sub>N<sub>4</sub> NT is an *n*-type semiconductor. The  $E_{CB}$  for *n*-type semiconductors is very close to the flat-band potential value, i.e.,  $E_{CB}$  of C<sub>3</sub>N<sub>4</sub> NTs at *ca.* -0.83 eV *versus* Ag/AgCl (equivalent to -0.63 eV *vs* NHE). In the case of *p*-type semiconductors,  $E_{VB}$  is generally located near the flat-band potential [32]. Both CoO NPs and Co<sub>3</sub>O<sub>4</sub> NPs exhibit a Mott-Schottky plot with negative slopes, suggesting that these cobalt oxides act as *p*-type semiconductors. Figure 4.14b-c gives the  $E_{VB}$  of CoO and Co<sub>3</sub>O<sub>4</sub> at *ca.* 1.24 eV and 1.41 eV, respectively (corresponding to 1.44 eV and 1.61 eV *vs* NHE). The results agree well with the above VB XPS and UV-Vis DRS analysis.

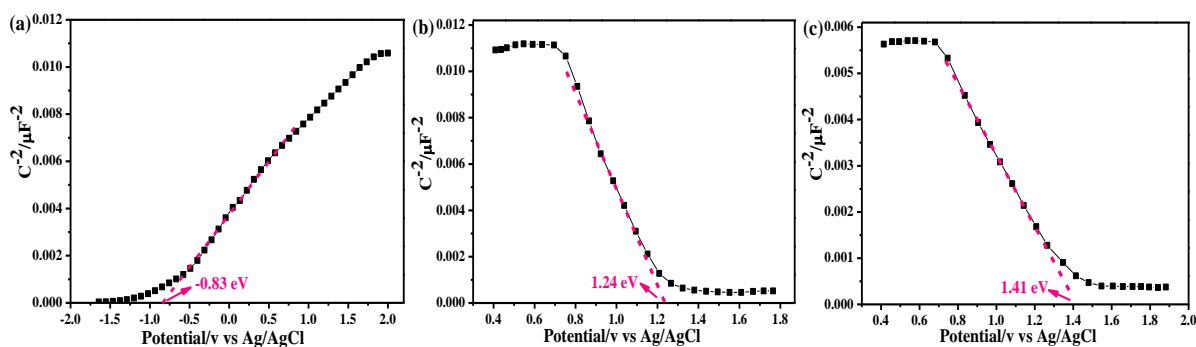


Figure 4.14 The Mott-Schottky plots of  $C_3N_4$  NTs (a), CoO NPs (b) and  $Co_3O_4$  NPs (c) with a frequency of 1.6 kHz in the dark

### 4.3.3 Interpretation of charge transfer and reaction pathways

A schematic diagram proposing the photocatalytic hydrogen production process occurring on  $CoO(7)/C_3N_4$  NT and  $Co_3O_4(7)/C_3N_4$  NT heterojunctions is depicted in Figure 4.15. Finer CoO NPs were more evenly distributed on the surface of  $C_3N_4$  NTs, whereas  $Co_3O_4$  in larger particle sizes were aggregated to some extent. On the basis of the above results, the CB edge of CoO is more negative than that of  $C_3N_4$  NTs, while the VB level of  $C_3N_4$  NTs is more positive than that of CoO. Upon visible-light irradiation ( $> 420$  nm) CoO and  $C_3N_4$  NTs can be activated simultaneously, and the excited electrons will immediately transfer from the VB to CB within the semiconductors. The electrons on the CB of the *p*-type CoO semiconductor will directly transfer to that of *n*-type  $C_3N_4$  NTs, and the holes on the VB of  $C_3N_4$  NTs can be spontaneously injected to that of CoO under the potential of the band energy difference. The migration of these photo-generated carriers can be promoted by the strongly interacting interface. As a result, the synergistic effect between  $C_3N_4$  NTs and CoO formed a staggered gap of Type II alignment [33]. The electrons at the CB of the semiconductors are able to reduce  $H_2O$  to  $H_2$ , whereas holes in the VB can be consumed through the oxidation of TEA to diethylamine (DEA) and acetaldehyde spontaneously as we reported previously [5]. Compared to the recently reported  $CoO/C_3N_4$  NS photocatalyst synthesised by solvothermal method, the photo-excited

electrons transfer from  $C_3N_4$  NSs to CoO, while the holes in the VB of CoO migrate to that of  $C_3N_4$  NSs, which is due to the large particle size of anchored CoO NPs (10-20 nm) [14].

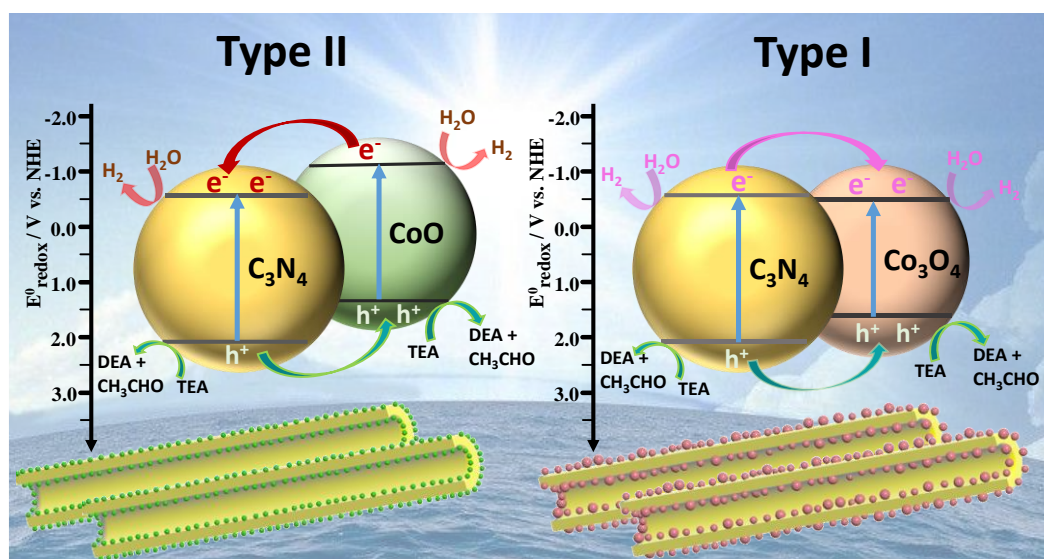


Figure 4.15 Schematic illustration of the proposed mechanism in the tunable cobalt oxide/ $C_3N_4$  NT heterojunction architectures.

On the other hand, the CB edge of  $Co_3O_4$  is lower than that of  $C_3N_4$  NTs, and its VB position is above that of  $C_3N_4$  NTs. When  $Co_3O_4(7)/C_3N_4$  NTs are exposed to visible light, both  $Co_3O_4$  and  $C_3N_4$  NTs will be excited. The electrons on the CB of  $C_3N_4$  NTs will quickly transfer to that of  $Co_3O_4$ , and the holes on the VB of the  $C_3N_4$  NTs will simultaneously hop into that of  $Co_3O_4$  as well. Therefore, the electrons and holes will accumulate in the  $Co_3O_4$  semiconductor and recombine rapidly. Hence,  $Co_3O_4(7)/C_3N_4$  NTs exhibit the Type I straddled band alignment [33]. Unlike the Type I, the Type II heterojunction provides the optimum band positions for separating charge carriers efficiently, hindering charge recombination significantly, and prolonging electron lifetimes, thus leading to enhanced photocatalytic activity.

To further verify the charge transfer pathways firstly proposed in this work, KPFM was conducted to obtain topography images and electrostatic potentials above the sample surface simultaneously. Figure 4.16 shows the topography images, surface potentials, line-scanning

profile through one cobalt oxide particle, and the corresponding Kelvin probe signals of CoO(7)/C<sub>3</sub>N<sub>4</sub> NTs (a-d) and Co<sub>3</sub>O<sub>4</sub>(7)/C<sub>3</sub>N<sub>4</sub> NTs (e-h), respectively. From Figure 4.16a, small CoO NPs were observed on the surface of C<sub>3</sub>N<sub>4</sub> NTs. The particle size of CoO is about 8 nm as depicted in the line-scanning profile through one CoO particle in Figure 4.16c. Similar in the TEM images, the line scanning profile through one Co<sub>3</sub>O<sub>4</sub> particle gives a particle size of around 50-80 nm as shown in Figure 4.16g, confirming that CoO(7)/C<sub>3</sub>N<sub>4</sub> NT sample exhibits finer CoO particle than Co<sub>3</sub>O<sub>4</sub>(7)/C<sub>3</sub>N<sub>4</sub> NT. Moreover, it is observed that the surface electrical potential gradient of CoO(7)/C<sub>3</sub>N<sub>4</sub> NTs (90 mV) is higher than that of Co<sub>3</sub>O<sub>4</sub>(7)/C<sub>3</sub>N<sub>4</sub> NTs (76 mV), indicating stronger electronic interaction between CoO and C<sub>3</sub>N<sub>4</sub> NTs. Hence, it is understandable that CoO(7)/C<sub>3</sub>N<sub>4</sub> NTs exhibited an enhanced visible-light photocatalytic activity compared to Co<sub>3</sub>O<sub>4</sub>(7)/C<sub>3</sub>N<sub>4</sub> NTs.

The Kelvin probe signal is defined as the electrostatic potential offset between a probe tip and the surface [34]. As shown in Figure 4.16d, a negative Kelvin probe signal of around 14 mV corresponding to a positive electrostatic potential at the position of tip was observed on the surface of CoO(7)/C<sub>3</sub>N<sub>4</sub> NT sample, implying a transfer of negative charges, i.e. electrons, from the CoO particle to the underlying C<sub>3</sub>N<sub>4</sub> NT surface. On the other hand, a positive Kelvin probe signal of about 6 mV was recorded on the surface of Co<sub>3</sub>O<sub>4</sub>(7)/C<sub>3</sub>N<sub>4</sub> NT nanomaterials (Figure 4.16h), which reflects a negative electrostatic potential at the position of tip and therefore indicates a transfer of electrons from the C<sub>3</sub>N<sub>4</sub> NT support to the Co<sub>3</sub>O<sub>4</sub> particle. These experimental evidences firmly verify the direction of charge transfer pathways as proposed in Figure 4.15. It is worth mentioning that the electrostatic potential offset of CoO(7)/C<sub>3</sub>N<sub>4</sub> NT (14 mV) is larger than that of Co<sub>3</sub>O<sub>4</sub>(7)/C<sub>3</sub>N<sub>4</sub> NT sample (6 mV), further proving a higher driving force for electron transfer from CoO to C<sub>3</sub>N<sub>4</sub> NTs than that from C<sub>3</sub>N<sub>4</sub> NTs to Co<sub>3</sub>O<sub>4</sub>. Therefore, the Type II heterojunction coupling of CoO NPs with C<sub>3</sub>N<sub>4</sub> NTs led to the improved hydrogen production performance.

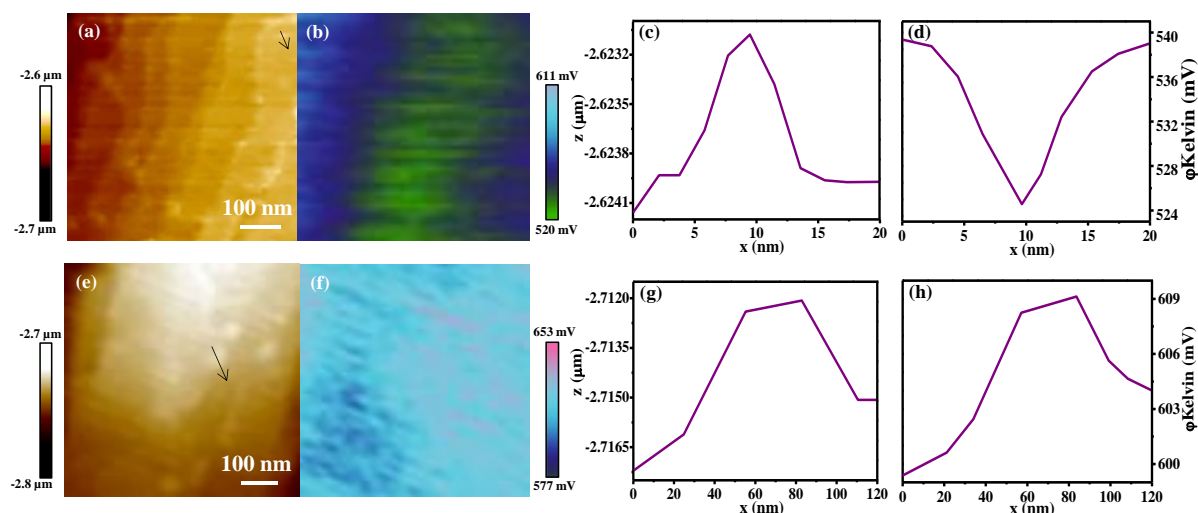


Figure 4.16 Topography images, surface potentials, line-scanning profile through one cobalt oxide particle, and the corresponding Kelvin probe signals of CoO(7)/C<sub>3</sub>N<sub>4</sub> NT (a-d) and Co<sub>3</sub>O<sub>4</sub>(7)/C<sub>3</sub>N<sub>4</sub> NT (e-h).

#### 4.4 Conclusion

The present work successfully designed tunable heterojunction architectures of CoO<sub>x</sub> NPs confined on well-arrayed C<sub>3</sub>N<sub>4</sub> NTs by using the same one-pot method under different annealing atmospheres. Annealing under vacuum condition ensured a Type II heterojunction with a good dispersion of CoO NPs with a particle size of less than 8 nm along the C<sub>3</sub>N<sub>4</sub> NTs surface. Annealing under static air led to a Type I heterojunction of Co<sub>3</sub>O<sub>4</sub>/C<sub>3</sub>N<sub>4</sub> NT with an enlarged particle size of Co<sub>3</sub>O<sub>4</sub> NPs up to a wide range of 10-80 nm and certain aggregation. These two heterojunctions present a distinct activity and stability in photocatalytic hydrogen production process. More specifically, CoO/C<sub>3</sub>N<sub>4</sub> NTs with a CoO content of 7 wt. % exhibit the highest H<sub>2</sub> generation rate and the best stability compared with Co<sub>3</sub>O<sub>4</sub>/C<sub>3</sub>N<sub>4</sub> NTs. The steady-state fluorescence and TCSPC technique confirm the fastest electron transfer between the conduction band of CoO and C<sub>3</sub>N<sub>4</sub>. According to the band edge potentials of the semiconductors determined in this work, CoO/C<sub>3</sub>N<sub>4</sub> NT and Co<sub>3</sub>O<sub>4</sub>/C<sub>3</sub>N<sub>4</sub> NT nanostructures are identified as Type II and Type I heterojunctions, respectively. Experimental evidences



obtained from KPFM firmly verify the charge transfer pathways established in this work. This research provided a greater understanding of charge transfer pathways in different heterojunction architectures and identified the beneficial attributes to the efficient visible-light photocatalytic hydrogen production process.

## References

- [1] W. Lubitz, W. Tumas, ACS Publications, 2007.
- [2] A. Kudo, Y. Miseki, Chemical Society Reviews, 38 (2009) 253-278.
- [3] W.J. Ong, L.L. Tan, Y.H. Ng, S.T. Yong, S.P. Chai, Chemical Reviews, 116 (2016) 7159-7329.
- [4] Y. Li, P. Li, J. Wang, Y. Yang, W. Yao, Z. Wei, J. Wu, X. Yan, X. Xu, Y. Liu, Y. Zhu, Applied Catalysis B: Environmental, 225 (2018) 519-529.
- [5] Y. Zhu, A. Marianov, H. Xu, C. Lang, Y. Jiang, ACS Applied Materials & Interfaces, 10 (2018) 9468-9477.
- [6] F. Jiao, H. Frei, Energy & Environmental Science, 3 (2010) 1018-1027.
- [7] L. Liao, Q. Zhang, Z. Su, Z. Zhao, Y. Wang, Y. Li, X. Lu, D. Wei, G. Feng, Q. Yu, X. Cai, J. Zhao, Z. Ren, H. Fang, F. Robles-Hernandez, S. Baldelli, J. Bao, Nature Nanotechnology, 9 (2014) 69-73.
- [8] X. Zhan, Z. Wang, F. Wang, Z. Cheng, K. Xu, Q. Wang, M. Safdar, J. He, Applied Physics Letters, 105 (2014) 153903.
- [9] H.Q. Sun, H.M. Ang, M.O. Tade, S.B. Wang, Journal of Materials Chemistry A, 1 (2013) 14427-14442.
- [10] A. Agiral, H.S. Soo, H. Frei, Chemistry of Materials, 25 (2013) 2264-2273.
- [11] S. Wang, C. Li, T. Wang, P. Zhang, A. Li, J. Gong, Journal of Materials Chemistry A, 2 (2014) 2885.

- [12] S.J.A. Moniz, S.A. Shevlin, D.J. Martin, Z.-X. Guo, J. Tang, *Energy & Environmental Science*, 8 (2015) 731-759.
- [13] Z. Mao, J. Chen, Y. Yang, D. Wang, L. Bie, B.D. Fahlman, *ACS Applied Materials & Interfaces*, 9 (2017) 12427-12435.
- [14] F. Guo, W. Shi, C. Zhu, H. Li, Z. Kang, *Applied Catalysis B: Environmental*, 226 (2018) 412-420.
- [15] J. Zhang, M. Grzelczak, Y. Hou, K. Maeda, K. Domen, X. Fu, M. Antonietti, X. Wang, *Chemical Science*, 3 (2012) 443-446.
- [16] C. Han, L. Ge, C. Chen, Y. Li, X. Xiao, Y. Zhang, L. Guo, *Applied Catalysis B: Environmental*, 147 (2014) 546-553.
- [17] G. Zhang, S. Zang, X. Wang, *ACS Catalysis*, 5 (2015) 941-947.
- [18] J. Yu, S. Wang, B. Cheng, Z. Lin, F. Huang, *Catalysis Science & Technology*, 3 (2013) 1782.
- [19] B. Liu, L. Ma, L.C. Ning, C.J. Zhang, G.P. Han, C.J. Pei, H. Zhao, S.Z. Liu, H.Q. Yang, *ACS Appl Mater Interfaces*, 7 (2015) 6109-6117.
- [20] C. Peng, B. Chen, Y. Qin, S. Yang, C. Li, Y. Zuo, S. Liu, J. Yang, *ACS nano*, 6 (2012) 1074-1081.
- [21] Y. Mao, W. Li, P. Liu, J. Chen, E. Liang, *Materials Letters*, 134 (2014) 276-280.
- [22] Z. Khan, M. Khannam, N. Vinothkumar, M. De, M. Qureshi, *Journal of Materials Chemistry*, 22 (2012) 12090-12095.
- [23] Z. Jin, Q. Zhang, S. Yuan, T. Ohno, *RSC Advances*, 5 (2015) 4026-4029.
- [24] D.S. Negi, B. Loukya, K. Dileep, R. Sahu, K.K. Nagaraja, N. Kumar, R. Datta, *Applied Physics Letters*, 103 (2013) 242407.
- [25] C. Tang, E. Liu, J. Wan, X. Hu, J. Fan, *Applied Catalysis B: Environmental*, 181 (2016) 707-715.

- [26] A. Gasparotto, D. Barreca, D. Bekermann, A. Devi, R.A. Fischer, P. Fornasiero, V. Gombac, O.I. Lebedev, C. Maccato, T. Montini, G. Van Tendeloo, E. Tondello, *Journal of the American Chemical Society*, 133 (2011) 19362-19365.
- [27] N.M. Tzollas, G.A. Zachariadis, A.N. Anthemidis, J.A. Stratis, *International Journal of Environmental Analytical Chemistry*, 90 (2010) 115-126.
- [28] D. Gallant, M. Pezolet, S. Simard, *The Journal of Physical Chemistry B*, 110 (2006) 6871-6880.
- [29] Y. He, Y. Wang, L. Zhang, B. Teng, M. Fan, *Applied Catalysis B: Environmental*, 168-169 (2015) 1-8.
- [30] M. Long, W. Cai, J. Cai, B. Zhou, X. Chai, Y. Wu, *The Journal of Physical Chemistry B*, 110 (2006) 20211-20216.
- [31] H. Huang, K. Xiao, N. Tian, F. Dong, T. Zhang, X. Du, Y. Zhang, *J. Mater. Chem. A*, 5 (2017) 17452-17463.
- [32] L. Zhang, Y. Hu, J. Zheng, *Journal of Materials Chemistry A*, 5 (2017) 18664-18673.
- [33] R. Marschall, *Advanced Functional Materials*, 24 (2014) 2421-2440.
- [34] T. Kittel, E. Roduner, *Journal of Physical Chemistry C*, 120 (2016) 8907-8916.

## **Chapter 5 NIR-driven photocatalytic H<sub>2</sub> production over upconversion nanoparticle engineered C<sub>3</sub>N<sub>4</sub> NTs**

### **5.1 Introduction**

Photocatalytic water splitting has been a focus of great attention as a possible means for converting solar energy to chemical energy in the form of clean and renewable hydrogen fuel since the Fujishima-Honda effect of TiO<sub>2</sub> photoelectrode was first reported in 1972 [1]. Though many semiconductors have been demonstrated as potential photocatalysts for H<sub>2</sub> evolution, the overall energy-conversion efficiency is still low, which is mainly because the three crucial steps during the water-splitting process: solar-light harvesting, charge separation and catalytic reduction reactions, are not efficient enough [2, 3]. Recently, polymeric graphitic carbon nitride nanotubes (C<sub>3</sub>N<sub>4</sub> NTs) has attracted tremendous attention because this metal-free and low-cost catalyst has unique one-dimensional geometry, visible-light response, suitable energy position and nitrogen richness beneficial for anchoring other nanoparticles (NPs) [4, 5]. As is well-known, the percentage of UV light in the solar spectrum is only ca. 5 %, whereas visible and near-infrared light (NIR), occupy ca. 49 % and ca. 46 %, respectively [6-8]. C<sub>3</sub>N<sub>4</sub> NTs still has the obstacles of the low utilisation of the solar light spectrum. Lanthanide-doped upconversion nanoparticles (UCNPs) are capable of converting NIR excitation to visible and even UV emissions [9]. Thus, it is highly desirable to couple C<sub>3</sub>N<sub>4</sub> NTs with UCNPs for constructing sensitiser/C<sub>3</sub>N<sub>4</sub> NT heterojunctions in order to extend the absorption into the NIR region, thus maximising sunlight harvesting.

UCNPs hold great promise owing to their unique optical features, including narrow emission bands, high efficiency and long luminescence lifetimes. Also, UCNPs are less light scattering, nonblinking and allow for deep penetration [10]. These attributes make them well-suited for use in biolabelling, biosensing, therapeutics, as well as in photocatalysis and photovoltaics [11, 12]. To date, NaYF<sub>4</sub> crystals have been regarded as the most efficient host material for UC

matrixes, and higher UC efficiency can be expected in rare-earth ions ( $\text{RE}^{3+}$ ) doped  $\text{NaYF}_4$  crystals because of their high chemical stability and unique optical properties arising from the intra-4f transitions [13].

Many semiconductors like  $\text{TiO}_2$ ,  $\text{MoS}_2$ ,  $\text{ZnO}$  and graphene have been used as supports for  $\text{NaYF}_4\text{:Yb,Tm}$  (NYF) NPs in the application of NIR-driven pollutant degradation [14-17]. In particular, Chen et al. decorated NYF NPs as a NIR-to-UV converter on the  $\text{MoS}_2\text{-NaTaO}_3$  nanocomposite to extend light absorbance toward the NIR region for  $\text{H}_2$  generation from water splitting. As such,  $\text{H}_2$  production was improved by about  $54 \mu\text{mol/g/h}$  in comparison with the catalyst in the absence of NYF NPs under visible-infrared light illumination [18]. In photoelectrochemical water splitting,  $\text{NaYF}_4\text{:Yb,Er}$  contained Au-CdTe-ZnO heterojunction achieved a high overall conversion efficiency to be around 0.06% from the NIR to  $\text{H}_2$  and  $\text{O}_2$  [19]. Bulk  $\text{C}_3\text{N}_4$  doped with erbium ions ( $\text{Er}^{3+}$ ) as upconversion agents were explored to achieve  $\text{H}_2$  generation under red-light irradiation [20]. Notably,  $\text{C}_3\text{N}_4$  nanosheets have been successfully assembled on the surface of NYF microrods for enhanced photocatalytic rhodamine B (RhB) degradation under 980 nm and UV-filtered irradiation [21]. In contrast, NYF NPs with a diameter of 50 nm were integrated on  $\text{C}_3\text{N}_4$  nanosheets showing improved degradation of RhB under visible and NIR light [22]. The same material construction was reported in methyl blue and phenol degradation under 980 nm illumination [23]. The application of UCNP supported  $\text{C}_3\text{N}_4$  nanocomposites in  $\text{H}_2$  production has yet to be reported.

On the other hand, the efficiency of harvesting NIR light is still poor for NYF NPs because of the low light-emission intensity in UV and the visible light range. Trivalent gadolinium ions ( $\text{Gd}^{3+}$ ) have spectral characteristics with a  $4f^7$  electronic configuration and a large energy gap between the first excited state  $^6P_{7/2}$  and the ground state  $^8S_{7/2}$ . An observation of NIR-to-UV UC emissions from  $\text{Gd}^{3+}$  ions was presented by Cao et al. in  $\text{Gd}^{3+}\text{-Yb}^{3+}\text{-Tm}^{3+}$  coexisting nanocrystals [24]. Lately, it has been demonstrated that in  $\text{NaYF}_4\text{:Yb/Er}$  nanocrystals doped

with  $\text{Gd}^{3+}$ , the lowest excited level ( ${}^6\text{P}_{7/2}$ ) of  $\text{Gd}^{3+}$  is situated in the UV region, which is far higher than most excited levels of  $\text{Yb}^{3+}$  and  $\text{Tm}^{3+}$  involved in the upconversion processes [25]. Also,  $\text{Gd}^{3+}$  can be used as an efficient mediate for tuning upconversion emission colours in the UCNPs [26]. Thus, it is much feasible to dope  $\text{Gd}^{3+}$  ions in NYF NPs for efficient light converting, with great significance by improving the photocatalytic activities. Unfortunately, few related works have been reported to date.

Herein, 2.5 %  $\text{Gd}^{3+}$  ions doped NYF NPs (named NYFG) was attached along  $\text{C}_3\text{N}_4$  NT channels in order to effectively harvest NIR light. The activities of NYFG/ $\text{C}_3\text{N}_4$  NT heterojunctions in photocatalytic  $\text{H}_2$  production were studied and compared with that of an NYF/ $\text{C}_3\text{N}_4$  NT nanostructure. In contrast to NYF NPs, NYFG NPs can offer higher UV and visible-light emission, and it is reasonable that the emitted bright fluorescence can be absorbed by  $\text{C}_3\text{N}_4$  NTs. The energy transfer process between UCNPs and  $\text{C}_3\text{N}_4$  for an efficient  $\text{H}_2$  generation was investigated. This initial work shows the feasibility of using UCNPs to absorb NIR light, thus improving the efficiency of existing solar materials for  $\text{H}_2$  production.

## 5.2 Experimental section

### 5.2.1 Catalyst synthesis

$\text{C}_3\text{N}_4$  NTs were synthesised by our reported water-induced morphological transformation method [5]. The detailed synthesised procedure of  $\text{C}_3\text{N}_4$  NTs is referred to Section 3.2.1, Chapter 3.  $\text{NaYF}_4\text{:}20\%\text{Yb},0.5\%\text{Tm},2.5\%\text{Gd}$  nanoparticles were prepared by a solvothermal method [27]. Firstly, 6 mL of a MeOH solution of  $\text{LnCl}_3$  (Ln includes Y, Yb, Tm and Gd) was stirred with 12 mL oleic acid (OA) and 30 mL 1-octadecene in a three-neck round-bottom flask. The mixture was then heated to form a transparent solution before being degassed under Ar. Secondly, a MeOH solution containing  $\text{NH}_4\text{F}$  and NaOH was added to the solution and stirred for 30 min. Then, the solution was quickly heated to 302 °C and maintained for 95 min under

Ar, before being slowly heated to completely remove MeOH and water. Finally, the product was isolated and washed, the nanocrystals were re-dispersed in ethanol for their further use.

The as-synthesised NYFG NPs with nominal amounts were dissolved into 1 mL polyvinylpyrrolidone (PVP)/ethanol solution (0.2 g/mL), and then sonicated at room temperature for 15 min. Then  $C_3N_4$  NT powders and 50 mL ethanol was added and stirred for another 12 h. After that, the solution was aged for 10 h. Finally, they were dried at 80 °C in static air for 2 h to remove ethanol [14]. NYFG(5)/ $C_3N_4$  NTs, NYFG(15)/ $C_3N_4$  NTs and NYFG(25)/ $C_3N_4$  NTs have nominal mass ratios of NYFG NPs and  $C_3N_4$  NTs at 5 %, 15 %, and 25 % respectively. NYF/ $C_3N_4$  NTs nanomaterials were fabricated by the same procedure.

### **5.2.2 Characterisation**

X-ray diffraction (XRD) patterns were collected by a Panalytical X'Pert PRO diffractometer via Cu  $K\alpha_1$  radiation. The morphologies were measured on a high-resolution transmission electron microscope (HRTEM) JEOL-2100F with an accelerating voltage at 200 kV. Scanning electron microscopy (SEM) images and elemental analyses were conducted on a Phenom XL scanning electron microscope with an energy dispersive X-ray spectrometer (EDX). Ultraviolet-visible (UV-vis) diffuse reflectance spectra were recorded on a Cary 5000 spectrophotometer.  $BaSO_4$  was used as the reference sample. Photoluminescence (PL) spectra were recorded at room temperature with a fiber-coupled spectrometer (Ocean Optics 2000) with excitation from a 980 nm diode laser (Lumics, LU0975M400). Confocal images were obtained by a confocal laser-scanning microscope Olympus FV1200 equipped with a 980 nm NIR laser.

### **5.2.3 Photocatalytic $H_2$ generation**

The monochromatic light irradiation (455 nm, 550 nm, and 600 nm) was obtained from a 300 W Xenon arc lamp with a monochromator (OPS-A500, NewSpec Pty Ltd). LED light

(M940L3-C5, M365LP1-C1, and M405LP1-C1, Thorlabs, Inc.) was used as 340 nm, 365 nm, and 405 nm light source. The procedure was referred to Section 3.2.3, Chapter 3.

The apparent quantum efficiency (AQE) was calculated as the following equations:

$$AQE(\%) = \frac{\text{no. of reacted electrons}}{\text{no. of incident photons}} \times 100\% = \frac{N_{H_2}}{N_p} = \frac{2 \times \text{no. of evolved } H_2 \text{ molecules}}{\text{no. of incident photons}} \times 100\%$$

## 5.3 Results and discussion

### 5.3.1 Photocatalytic performance

The AQE of water splitting over  $C_3N_4$  NTs was measured at different monochromatic wavelengths (Figure 5.1a). The trend in AQE closely followed that of the absorbance measured by the UV-vis diffuse reflectance spectrum, revealing that the  $H_2$  generation strongly depends on the bandgap transition. Also, it indicates that  $H_2$  evolution mainly comes from a range of 300-500 nm. Thus, the correlation of the catalytic activity on the irradiation intensity of the three different monochromatic light sources (340 nm, 365 nm, and 405 nm) was investigated. The transmittance of the three monochromatic lights are presented in Figure A5 in Appendix. From Figure 5.1b, we can observe that, after 3 h light irradiation, the  $H_2$  generation rate increased with increasing light irradiance because a higher light intensity can excite a larger amount of light energetic electrons. The highest population of energetic electrons can be generated when the light intensity increases to 24.5 mW/cm<sup>2</sup> for 340 nm, 19.8 mW/cm<sup>2</sup> for 365 nm and 21.7 mW/cm<sup>2</sup> for 405 nm respectively.

To study the influence of UCNPs on the photocatalytic  $H_2$  generation, the  $H_2$  evolution rates of all the nanomaterials studied in this work were measured under the 980 nm laser. As shown in Figure 5.2a, the control experiment shows that, during 3 h of illumination, no  $H_2$  was released in the absence of any nanomaterials and in the presence of NYFG NPs, NYF NPs or  $C_3N_4$  NTs. Clearly, upon modifying the  $C_3N_4$  NTs by UCNPs,  $H_2$  was produced under 980 nm NIR light irradiation. The  $H_2$  generation rate was improved by increasing the NYFG NP loading content,



and the highest H<sub>2</sub> yield was achieved at a NYFG content of 15 wt. %. Noteworthy, a further increase to 25 wt. % of content leads to a decrease of the performance. It can be explained that a larger amount of NYFG NPs on the surface might block the active sites on the C<sub>3</sub>N<sub>4</sub> NTs responsible for H<sub>2</sub> evolution. Keeping the same loading amount, NYFG(15)/C<sub>3</sub>N<sub>4</sub> NTs exhibit H<sub>2</sub> production of 311.6  $\mu\text{mol/g}$ , which is 1.4 times as high as that of NYF(15)/C<sub>3</sub>N<sub>4</sub> NTs (221.1  $\mu\text{mol/g}$ ) after 3 h irradiation, implying higher energy transfer efficiency between NYFG NPs and C<sub>3</sub>N<sub>4</sub> NTs in comparison with NYF(15)/C<sub>3</sub>N<sub>4</sub> NT nanostructure. The AQE of NYFG(15)/C<sub>3</sub>N<sub>4</sub> NTs and NYF(15)/C<sub>3</sub>N<sub>4</sub> NTs under 980 nm illumination were 0.80 % and 0.56 %, respectively.

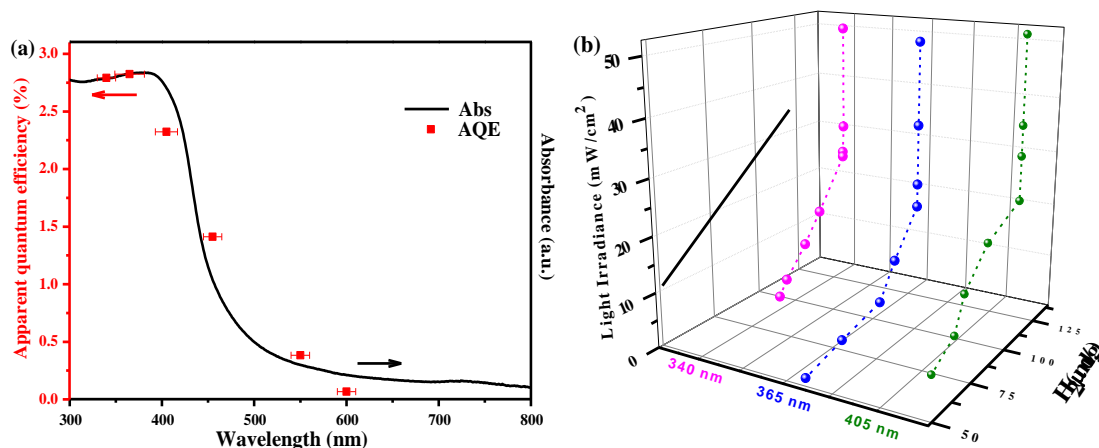
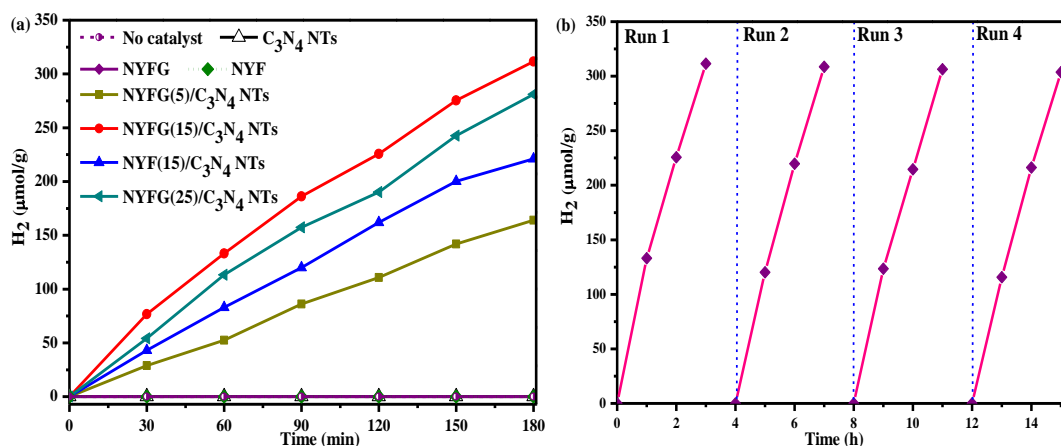


Figure 5.1 Ultraviolet-visible DRS spectrum and apparent quantum efficiency for C<sub>3</sub>N<sub>4</sub> NTs (a) and dependence of H<sub>2</sub> generation over bare C<sub>3</sub>N<sub>4</sub> NTs on different intensities of 340 nm, 365 nm and 405 nm monochromatic light irradiation (b).

The photocatalytic stability of NYFG(15)/C<sub>3</sub>N<sub>4</sub> NTs was investigated by running the reaction for 12 h under NIR light irradiation, and the system was intermittently evacuated every 3 h with substitution of fresh sacrificial reagent, TEA. As shown in Figure 5.2b, after 12 h the nanocomposite can generate H<sub>2</sub> with a total amount of 303.7  $\mu\text{mol/g}$  with no significant deactivation occurred, indicating that this nanocatalyst is highly stable during the whole photocatalytic processes.

To identify the effective contribution of NIR-photocatalysis in overall natural light-driven photocatalytic H<sub>2</sub> production, the activity evaluation of these materials were conducted under simulated sunlight irradiation by using a 300 W xenon lamp. As shown in Figure 5.2c, after 3h of irradiation no H<sub>2</sub> production was observed over NYFG and NYF NPs. Generally, the bare C<sub>3</sub>N<sub>4</sub> NTs exhibits H<sub>2</sub> generation of 618.3  $\mu\text{mol/g}$ , but the yield is higher on NYF(15)/C<sub>3</sub>N<sub>4</sub> NTs (768.1  $\mu\text{mol/g}$ ). A further boost of H<sub>2</sub> evolution was achieved on NYFG(15)/C<sub>3</sub>N<sub>4</sub> NTs (844.4  $\mu\text{mol/g}$ ), which is about 1.4 times as high as that of the bare C<sub>3</sub>N<sub>4</sub> NTs. According to the Xenon-light emission bands, it is confirmed that NIR light could excite UCNPs available for energy transfer to C<sub>3</sub>N<sub>4</sub> NTs. Approximately 226.1  $\mu\text{mol/g}$  is ascribed to NIR-photocatalysis across an NYFG(15)/C<sub>3</sub>N<sub>4</sub> NT catalyst, but it is less than 311.6  $\mu\text{mol/g}$  under 980 nm-induced catalysis. This can be attributed to the lower intensity in the NIR region of Xenon light than from a 980 nm laser, although there is a wider range of NIR light from the Xenon light (Figure A6, Appendix). Figure 5.2d compares the H<sub>2</sub> production rates under natural-light illumination over the different catalysts. It clearly shows that the highest H<sub>2</sub> evolution rate of 281.5  $\mu\text{mol/g/h}$  is achieved on NYFG(15)/C<sub>3</sub>N<sub>4</sub> NT catalyst.



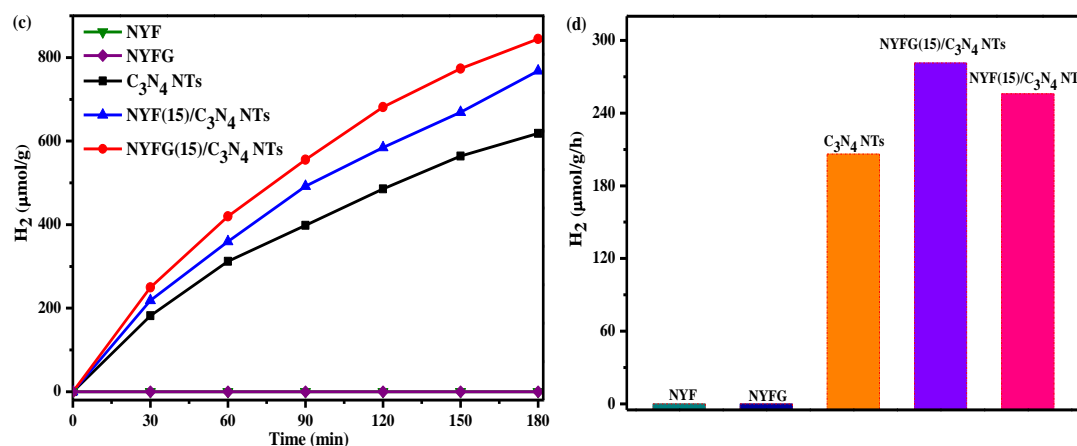


Figure 5.2 H<sub>2</sub> production over different photocatalysts (a) and the stability test of NYFG(15)/C<sub>3</sub>N<sub>4</sub> NTs under the 980 nm laser irradiation (b); Simulated sunlight-induced H<sub>2</sub> generation over the catalysts (c-d)

### 5.3.2 Characterisation of the photocatalysts

The crystal structures of the photocatalysts studied in this work were investigated by XRD analysis. As shown in Figure 5.3, without Gd<sup>3+</sup> ions, the XRD pattern of NYF NPs can be indexed to the bare hexagonal NaYF<sub>4</sub> phase (JCPDS card 28-1192) [28], and no diffraction peaks corresponding to impurities were observed. Hexagonal NaFY<sub>4</sub> (β-phase) is a more efficient host for higher UC luminescence efficiency than cubic NaFY<sub>4</sub> (α-phase) [29]. The diffractions in NYFG NPs exhibit no extra peaks after doping with Gd<sup>3+</sup> ions, suggesting that the presence of Gd<sup>3+</sup> ions did not induce any phase transformation in NPs. But the intensities of two diffraction peaks at 29.9° and 30.8° were changed, indicating that Gd<sup>3+</sup> ions may increase the electron charge density of the crystal surface [30]. Two characteristic peaks of bare C<sub>3</sub>N<sub>4</sub> NTs were observed at 27.6° and 13.3°, which can be indexed to the (002) and the (100) planes, respectively. The former is the characteristic peak for interlayer stacking aromatic systems, while the latter is attributed to in-plane repeating units. After decorating UCNP NPs along C<sub>3</sub>N<sub>4</sub> NTs, the XRD pattern exhibits the mixed phase of hexagonal NaFY<sub>4</sub> and graphitic C<sub>3</sub>N<sub>4</sub>, confirming that UCNP NPs were successfully loaded on the C<sub>3</sub>N<sub>4</sub> NTs. Additionally, the

intensities of the diffraction peaks of  $C_3N_4$  NTs become weaker, which may illustrate that the nanotubes are surrounded by the UCNPs. This structure could be beneficial for absorbing the converted light [31]. Moreover, the crystal structures of NYFG(15)/ $C_3N_4$  NTs before and after recycling experiments were examined by XRD analysis (Figure A7, Appendix). No significant change in their patterns was observed, which confirms that NYFG(15)/ $C_3N_4$  NTs is a stable and reusable photocatalyst.

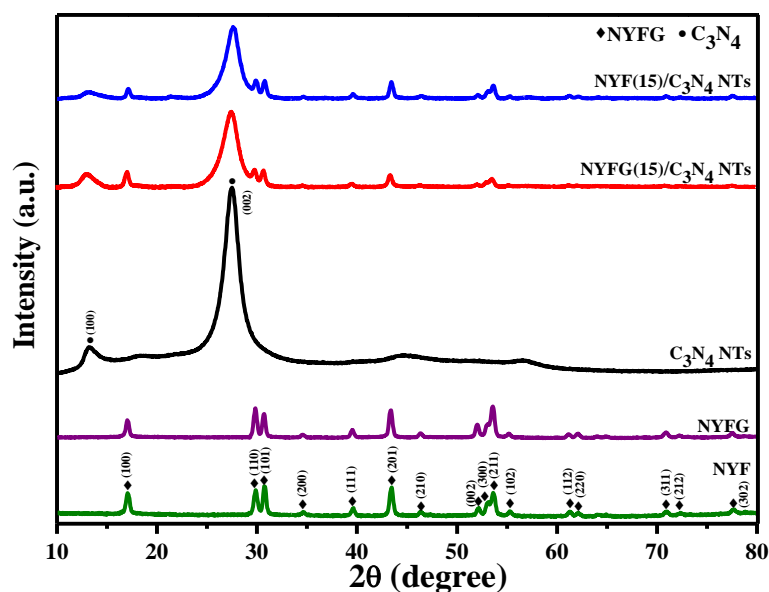


Figure 5.3 X-ray diffraction (XRD) patterns of the catalysts studied in this work.

The UV-Vis-NIR optical absorption spectra of the five samples are shown in Figure 5.4. The bare  $C_3N_4$  NTs exhibits a strong absorption band at about 460 nm with a band gap of  $\sim 2.77$  eV, which shows a slight blue shift compared to that of the bulk ( $\sim 2.70$  eV) due to the quantum size effect [5]. No absorbance in the range of 300-900 nm and semiconductor characteristics are found in the patterns of NYF and NYFG NPs, but a relatively wide absorption range in the NIR region arising from the  $Yb^{3+}$  ions between 900 nm and 1100 nm was detected [32, 33]. Moreover, the absorption intensity of NYFG NPs is higher than that of NYF NPs. In the spectrum of  $C_3N_4$  NTs with a loading of UCNP NPs, the characteristic from the bare  $C_3N_4$  NTs

is observed. However, no peaks indexed to NIR absorption can be seen, suggesting that the loading amount may be too low to be detected.

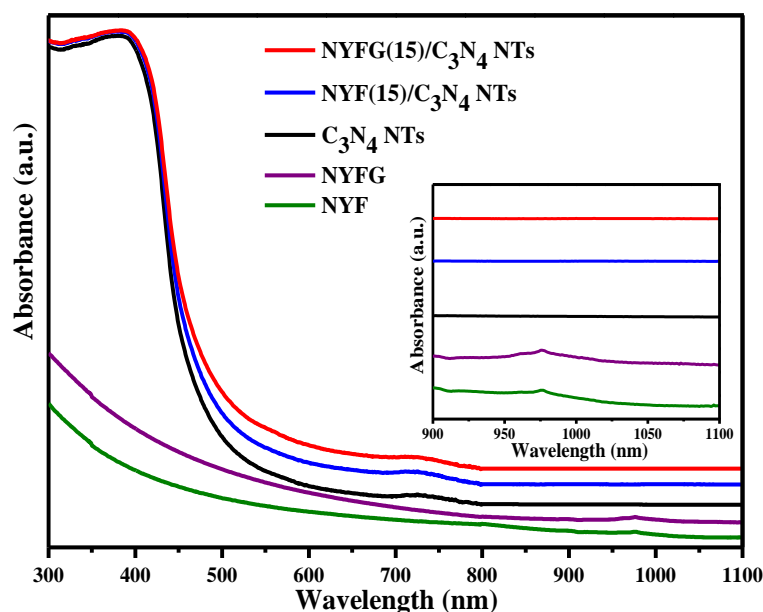


Figure 5.4 The UV-Vis-NIR absorption spectrum of the samples (inset: the magnified spectra ranging from 800 nm to 1100 nm).

The morphologies of the as-synthesised nanomaterials are analyzed by TEM. In Figure 5.5a the bare  $C_3N_4$  NTs exhibit a tube-like nanostructure with a diameter of about 250 nm. The sizes of the nanotubes prepared by a water-induced morphological transformation method are in a range of 200-400 nm, not well controlled due to the nanosheet roll-up mechanism in our recent report. TEM images of NYFG and NYF NPs are shown in Figure A8 in Appendix. All the NYF NPs display single crystalline spheres with a size of about 20 nm. After doping with  $Gd^{3+}$  ions, the nanocrystals mostly remain spherical-like morphology with the same size, whereas some of them present a hexagonal shape. The shape variation induced by doping  $Gd^{3+}$  ions may be due to substituting  $Y^{3+}$  ions by  $Gd^{3+}$  ions, which results in increased electron charge densities of the upconversion crystal surface. Figure 5.5b reveals that NYFG NPs are uniformly dispersed on the surfaces of  $C_3N_4$  NTs. No obvious change is observed in the morphologies of NYFG NPs and  $C_3N_4$  NTs, confirming the successful preparation. From the high-resolution

TEM image (Figure 5.5c), the lattice fringes of the (100) plane with an interplanar distance of 0.52 nm is identified corresponding to the hexagonal  $\text{NaYF}_4$ . In Figure 5.5d, the line-scan analysis indicates that the UCNPs and  $\text{C}_3\text{N}_4$  are interacted with each other, promoting the energy transfer between the two components. Furthermore, SEM-EDX analyses show that these nanocomposites are mainly composed of C, N, Na, Y, F, Yb and Gd, and these elements are homogeneously distributed (Figure 5.6).

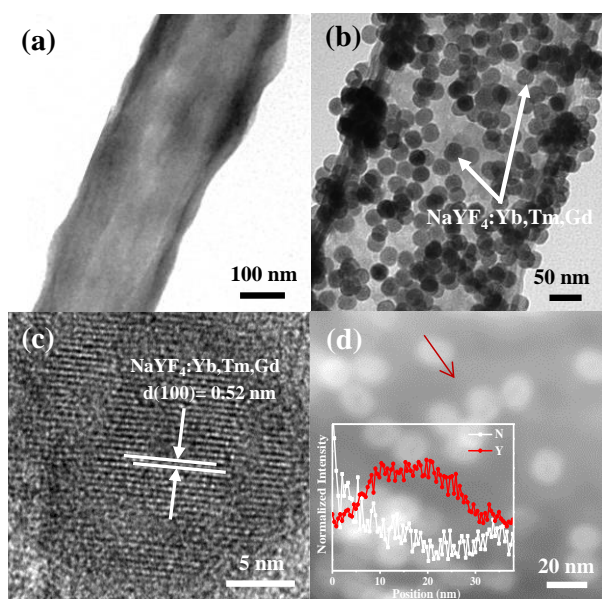


Figure 5.5 TEM images of bare  $\text{C}_3\text{N}_4$  NTs (a), NYFG(15)/ $\text{C}_3\text{N}_4$  NTs (b), and high-resolution TEM images of NYFG(15)/ $\text{C}_3\text{N}_4$  NTs (c-d).

In order to reveal the NIR-driven photogenerated charge separation and transfer process, the photocurrent responses of the catalysts were measured as a function of radiation time and potential, respectively, by turning the 980 nm laser on and off. Figure 5.7 shows that the current responses for NYFG(15)/ $\text{C}_3\text{N}_4$  NTs and NYF(15)/ $\text{C}_3\text{N}_4$  NTs were prompt, reproducible and steady during the three on-off cycles. In contrast, no photocurrent responses were found for NYFG NPs, NYF NPs, and  $\text{C}_3\text{N}_4$  NTs, which agrees with their activities in  $\text{H}_2$  generation under NIR illumination. The steady photocurrent for NYFG(15)/ $\text{C}_3\text{N}_4$  NTs is about 1.5 times as high as that of NYF(15)/ $\text{C}_3\text{N}_4$  NTs, indicating a higher charge transfer rate in the nanocomposite.

The NYFG(15)/C<sub>3</sub>N<sub>4</sub> NTs sample exhibits both strong UV and visible light emission and low electron-hole recombination, leading to the highest photocurrent response and thus the highest activity in H<sub>2</sub> generation among the photocatalysts studied in this work.

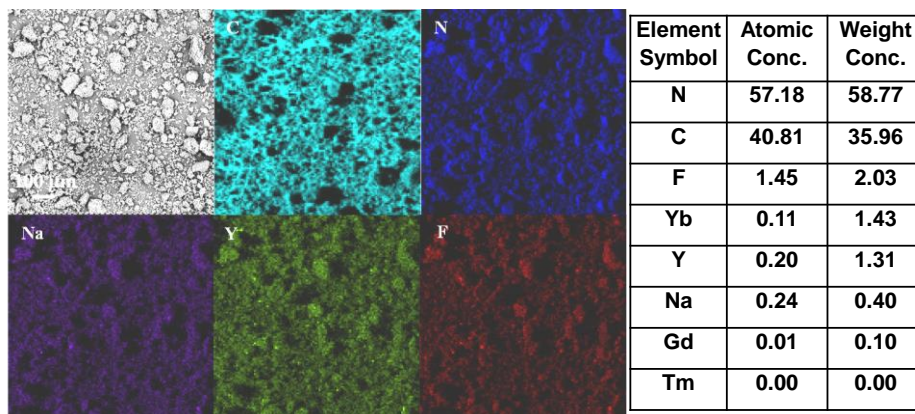


Figure 5.6 SEM-EDX of NYFG(15)/C<sub>3</sub>N<sub>4</sub> NTs.

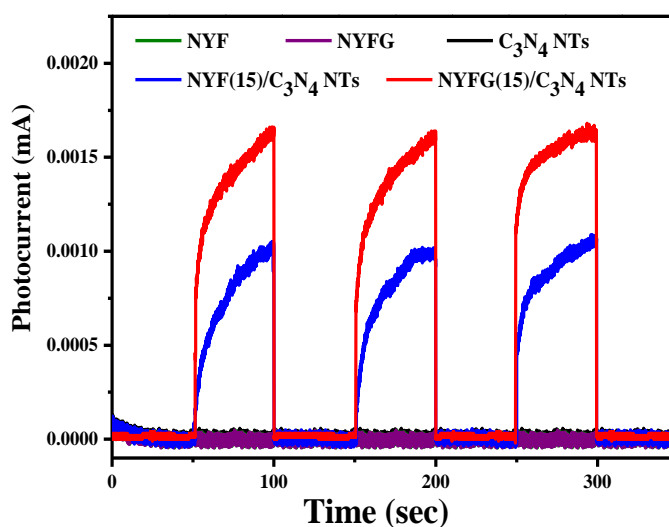


Figure 5.7 Transient photocurrent of the catalysts studied in this work.

XPS analysis was applied to verify the chemical compositions of the prepared composite. The XPS survey spectrum of NYFG(15)/C<sub>3</sub>N<sub>4</sub> NTs reveals the presence of Na, F, O, N, C, Y (Figure 5.8a). The peaks at 186.3 and 174.2 eV are attributed to Yb 4d and Tm 4d, respectively (Figure 5.8b). Figures 5.8c-d illustrates a comparison of the high-resolution XPS analysis of N 1s and F 1s for NYFG(15)/C<sub>3</sub>N<sub>4</sub> NTs and NYF(15)/C<sub>3</sub>N<sub>4</sub> NTs catalysts. The XPS spectrum of N1s

(Figure 5.8c) in NYFG(15)/C<sub>3</sub>N<sub>4</sub> NTs can be fitted by three peaks at 398.1, 399.1 and 399.9 eV, corresponding to C-N=C, N-(C)<sub>3</sub> and C-N-H, respectively [34]. In contrast with NYF(15)/C<sub>3</sub>N<sub>4</sub> NTs, the three peaks shifted to a lower bonding energy. In the high-resolution of F 1s XPS spectra from Figure 5.8d, two doublets fit the raw peaks very well. As to NYFG(15)/C<sub>3</sub>N<sub>4</sub> NTs, 686.1 and 684.9 eV can be associated with the F atoms in the NYFG NPs and F-C [33, 35]. Compared to the XPS data taken from NYF(15)/C<sub>3</sub>N<sub>4</sub> NTs, the F 1s peaks were shifted toward the higher binding energy region. This phenomenon showed that the Gd<sup>3+</sup> ions may bring strong interaction, thus attributing the efficient energy transfer in the NYFG(15)/C<sub>3</sub>N<sub>4</sub> NT nanocomposites.

Figure 5.9a shows the PL spectra of the materials employing the 980 nm laser as the excitation light source. In the pattern of NYFG and NYF NPs emission peaks at 343 nm (3.62 eV), 360 nm (3.44 eV), 450 nm (2.73 eV), 475 nm (2.61 eV) and 644 nm (1.93 eV) are observed, corresponding to the <sup>1</sup>I<sub>6</sub> → <sup>3</sup>F<sub>4</sub>, <sup>1</sup>D<sub>2</sub> → <sup>3</sup>H<sub>6</sub>, <sup>1</sup>D<sub>2</sub> → <sup>3</sup>F<sub>4</sub>, <sup>1</sup>G<sub>4</sub> → <sup>3</sup>H<sub>6</sub>, <sup>1</sup>G<sub>4</sub> → <sup>3</sup>F<sub>4</sub> transitions of Tm<sup>3+</sup> ions doped in the UPCNs, respectively [36-38]. The light-emission intensity increased after incorporating Gd<sup>3+</sup> ions, and the highest intensity at 475 nm is about doubled. Since the particle size of NYFG and NYF NPs are quite similar, we will more focus on the luminescence intensity and photon energy effects on the photocatalytic activity. According to the light absorbance of C<sub>3</sub>N<sub>4</sub> NTs in Figure 5.4, the converted emission lights are in the absorption range of C<sub>3</sub>N<sub>4</sub> NTs. When NYFG NPs were introduced on the C<sub>3</sub>N<sub>4</sub> NTs, apparently, weaker emission intensity was detected compared to the bare NYFG NPs, suggesting an energy transfer from NYFG NPs to C<sub>3</sub>N<sub>4</sub> NTs within the nanostructure. Similar properties are observed in the NYF(15)/C<sub>3</sub>N<sub>4</sub> NT nanocomposite as well. Notably, the intense upconverted red-light and blue-light emissions from the NYFG(15)/C<sub>3</sub>N<sub>4</sub> NT catalyst were readily observed by laser scanning confocal microscopy images (Figure 5.10). This not only clearly confirmed



evenly distributed NYFG NPs on  $C_3N_4$  NTs, corroborating the above SEM-EDX results, but also further evidenced strong fluorescence signals from the heterojunction.

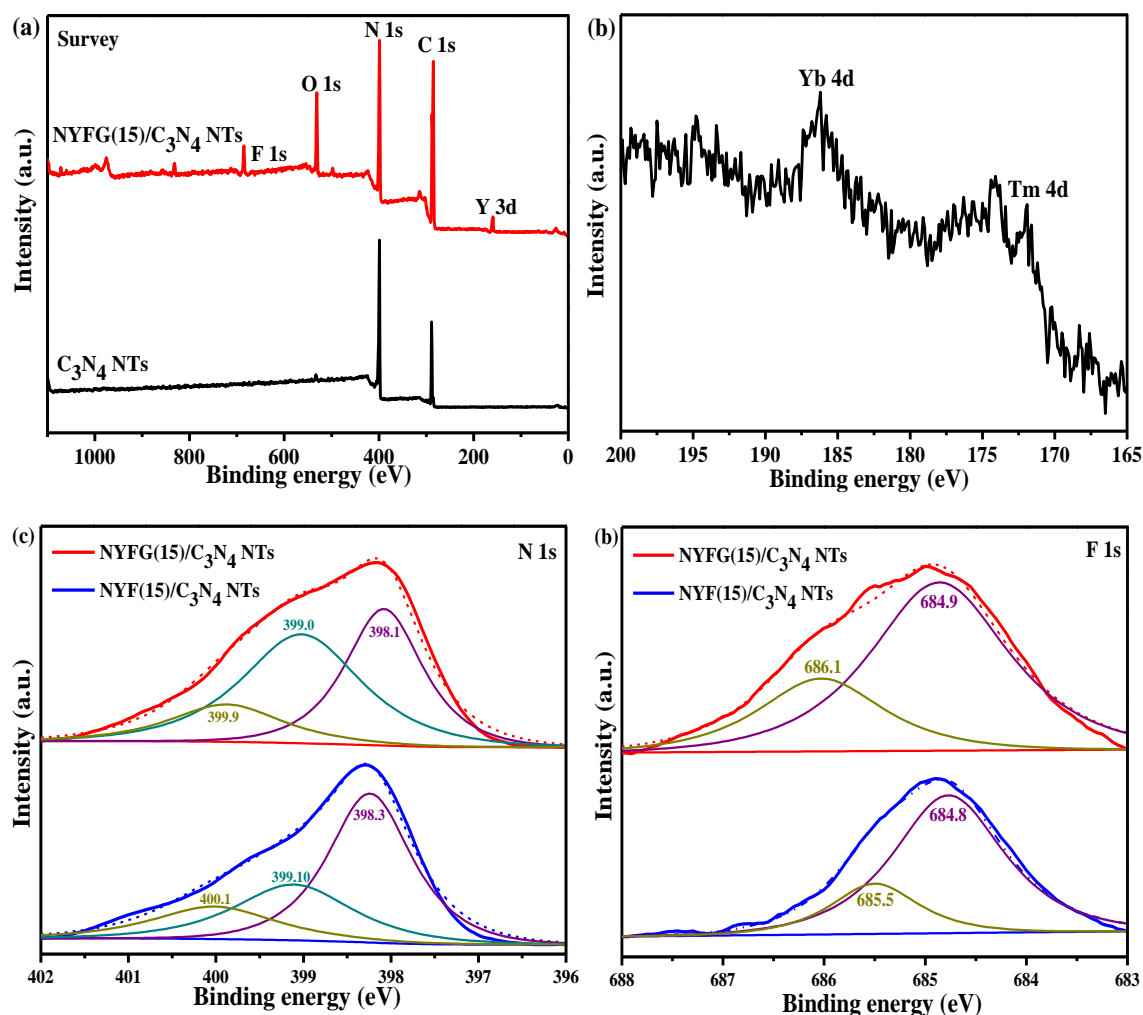


Figure 5.8 XPS wide-scan spectra of  $C_3N_4$  NTs and NYFG(15)/ $C_3N_4$  NTs (a); high-resolution XPS spectra of Yb 4d and Tm 4d, (b) N 1s (c) and F 1s (d).

Figure 5.9b presents the PL spectra of the catalysts under an excitation of 360 nm. The bare  $C_3N_4$  NTs have a strong PL emission peak at about 460 nm, which is ascribed to the fast radiative recombination of electron-hole pairs from the planar structure of graphitic  $C_3N_4$  [39]. When NYF NPs were attached on the surface of  $C_3N_4$  NTs, the PL intensity is lower than that of bare  $C_3N_4$  NTs. Obviously, NYFG/ $C_3N_4$  NTs exhibits the greatest quenched fluorescence. The drop of PL intensity suggests that more photoexcited charges relax via a nonradiative

pathway, probably by the transfer of electron-hole pairs within the rare-earth metal and  $C_3N_4$  as such. Similar results were observed on NYF/ $TiO_2$  and  $Er^{3+}$  doped  $C_3N_4$  catalysts by other groups [20, 40]. In the inset of the enlarged spectra, the peak at around 430 nm is observed for NYFG and NYF NPs, which is attributed to the down-shift emission of  $Tm^{3+}$  ions [41, 42]. Also, NYFG NPs shows a lower intensity than NYF NPs, which may be due to the doping of  $Gd^{3+}$  ions.

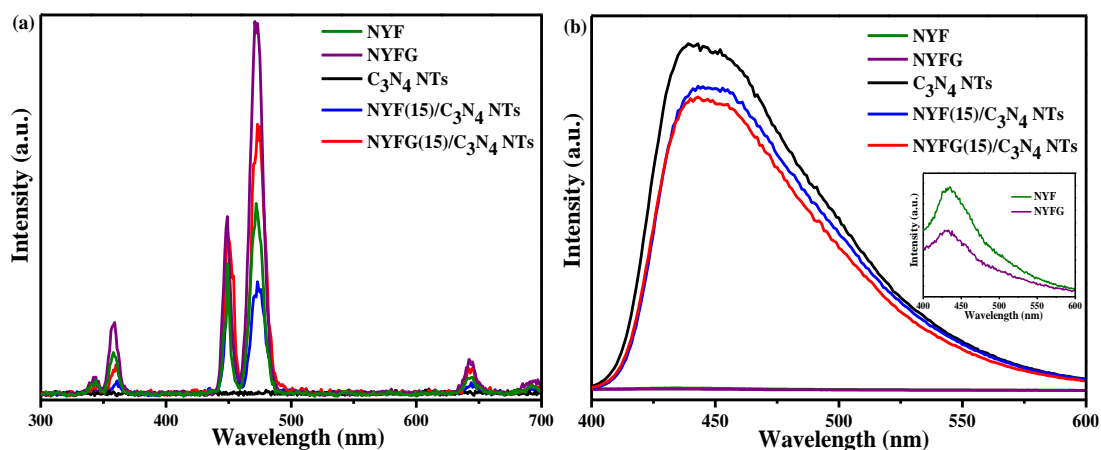


Figure 5.9 PL spectra of the nanocomposites excited by the 980 nm laser (a) and 360 nm from the Xenon lamp (b).

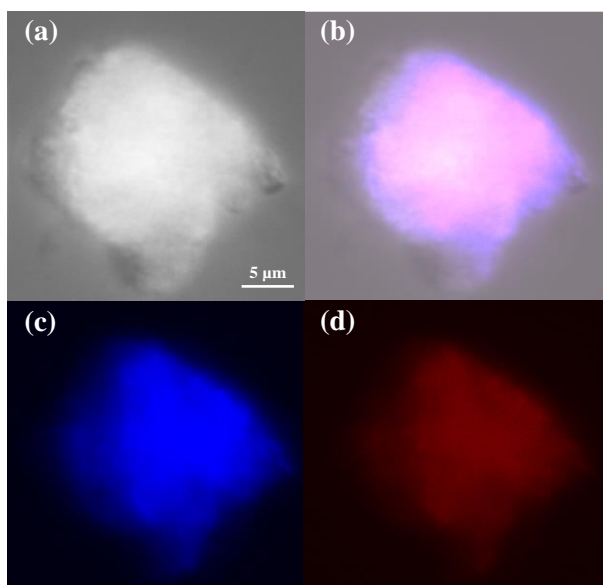


Figure 5.10 Confocal microscopy studies of NYFG(15)/ $C_3N_4$  NTs ( $\lambda_{ex} = 980$  nm).

In order to study the energy transfer process between UCNPs and  $C_3N_4$ , the lifetimes of the catalysts were investigated under a 980 nm pulsed laser. Figure 5.11a records the lifetime of the emission at 475 nm for the five samples, and average lifetimes of 532, 485, 417, 430 and 0  $\mu s$  were obtained for NYFG NPs, NYF NPs, NYFG(15)/ $C_3N_4$  NTs, NYF(15)/ $C_3N_4$  NTs and  $C_3N_4$  NTs, respectively. The shortening of the fluorescence lifetime of the nanocomposites indicates that the energy migration between UCNPs and  $C_3N_4$  NTs is a fluorescence resonance energy transfer (FRET) process, rather than a radiation-reabsorption process, since in the latter process the fluorescence lifetime does not change [15, 17, 43].

In Figure 5.11b, for the emitted 455 nm light, the lifetimes of NYFG(15)/ $C_3N_4$  NTs and NYF(15)/ $C_3N_4$  NTs are 182 and 140  $\mu s$ , which are greater than those of the bare NYFG NPs (147  $\mu s$ ) and NYF NPs (115  $\mu s$ ), respectively. One possible explanation is that many UCNPs were inside the nanotubes due to the unique tubular structure of  $C_3N_4$ , bringing a significantly decreased surface quenching effect of UCNPs. In this way, the energy transfer between  $^1D_2$  and  $C_3N_4$  is dominated by the surface quenching effect, rather than the FRET process, resulting in longer lifetimes [44]. However, the less the surface quenching centres affecting all the emission of  $Tm^{3+}$ , the longer the lifetime that should be detected in 455 nm emission. As depicted in Figure 5.9b,  $C_3N_4$  NT materials can act as a blue light-emitting material under an excitation of UV light. After  $C_3N_4$  NTs absorb the energy at 343 nm and 360 nm light emitted by UCNPs, a high emission at 455 nm can be generated, thus a longer lifetime at 455 nm emission is detected. However, the FRET process from  $C_3N_4$  NTs to NYFG NPs can also occur on account of the larger energy gap (2.77 eV) of  $C_3N_4$  NTs than of  $^1D_2 \rightarrow ^3F_4$  (2.73 eV). Since NYFG NPs exhibits higher emission in the UV region than NYF NPs, NYFG(15)/ $C_3N_4$  NTs have a longer lifetime than NYF(15)/ $C_3N_4$  NTs. A long lifetime usually means highly efficient upconversion luminescence, therefore, this kind of energy transfer indirectly contributes to the highly enhanced AQE of NYF(15)/ $C_3N_4$  NTs. Herein, the PL intensities and the lifetimes

demonstrate a clear trend and the energy migration to  $C_3N_4$  NTs. The energy transfer is a prerequisite to realising NIR-responsive photocatalysis of  $C_3N_4$  NT based catalysts.

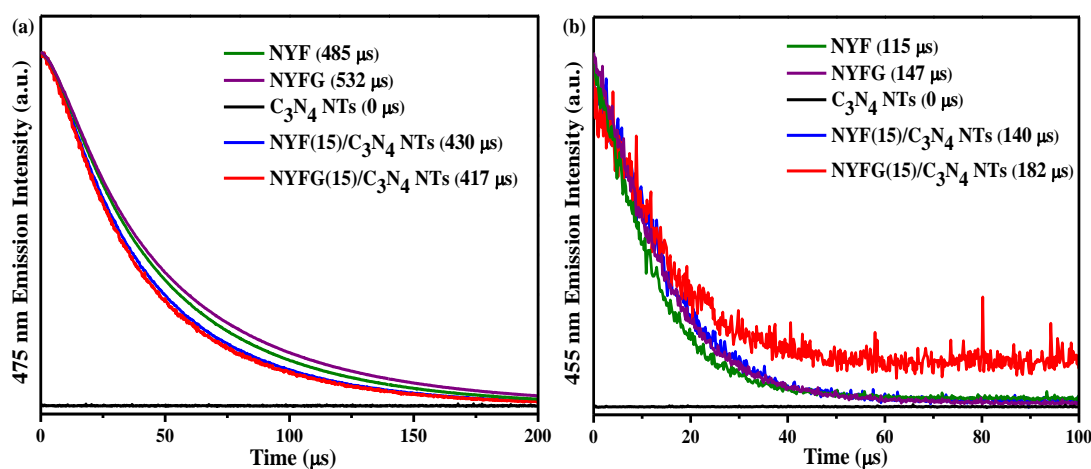


Figure 5.11 The time-resolved fluorescence decay curves at 475 nm (a) and 455 nm (b) emission of the studied catalysts.

### 5.3.3 Photocatalytic mechanism

To gain more insight into the NIR-driven photocatalytic mechanism of the fabricated NYFG/ $C_3N_4$  NT heterojunction for  $H_2$  generation, a schematic of the charge transfer processes is proposed, as shown in Figure 5.12. NYFG NPs of about 20 nm in size are uniformly distributed along the  $C_3N_4$  NTs. Under NIR irradiation, the pumping of 980 nm light only excites the  $Yb^{3+}$  ions.  $Yb^{3+}$  ions act as the sensitizer, and three successive energy transfers from  $Yb^{3+}$  to  $Tm^{3+}$  ions populate its  $^3H_5$ ,  $^3F_{2,3}$  and  $^1G_4$  levels. The cross-relaxation process between  $Tm^{3+}$  is responsible for populating the  $^1D_2$  level.  $Gd^{3+}$  ions cannot absorb 980 nm photons directly. In the  $Yb^{3+}$ - $Tm^{3+}$ - $Gd^{3+}$  tridoped system, the excited  $Tm^{3+}$  ions in the high level can transfer energy to  $Gd^{3+}$  to promote its excitation. After the excitation of NYFG NPs, the  $C_3N_4$  NTs is directly excited by the energy transfer from the high levels of  $Tm^{3+}$  and  $Yb^{3+}$  ions by the FRET process. Consequently, the photo-generated electrons are excited from the valence band to the conduction band of  $C_3N_4$  NTs, leaving holes in the valence band (VB). The separated electrons are trapped by  $H_2O$  to produce  $H_2$ , whereas the holes accumulated on VB

will react with TEA to form diethylamine (DEA) and acetaldehyde. By all these steps, the as-prepared upconversion photocatalysts can absorb the NIR efficiently for photocatalysis.

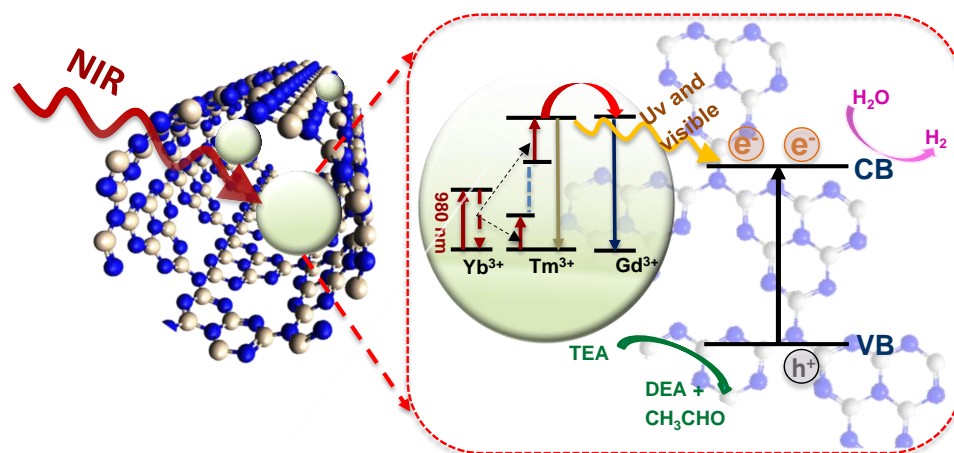


Figure 5.12 Illustrative diagrams of energy transfer among NYFG(15)/C<sub>3</sub>N<sub>4</sub> NTs.

## 5.4 Conclusions

In summary, for the first time we have fabricated novel NYFG/C<sub>3</sub>N<sub>4</sub> NTs and NYF/C<sub>3</sub>N<sub>4</sub> NTs heterojunctions in which UCNPs were uniformly decorated on the surface of C<sub>3</sub>N<sub>4</sub> NTs for NIR-responsive photocatalysis. The resultant NYFG/C<sub>3</sub>N<sub>4</sub> NT nanostructure showed intimate interfacial contact, which thus facilitates energy transfer from NYFG NPs to C<sub>3</sub>N<sub>4</sub> NTs and a good NIR response of the nanocomposites. With a UCNP loading content of 15 wt. %, NYFG/C<sub>3</sub>N<sub>4</sub> NTs presented about 1.4 times the H<sub>2</sub> production than NYF/C<sub>3</sub>N<sub>4</sub> NTs did under NIR light illumination, and the multiple was 1.1 with natural-light irradiation. Moreover, the NIR-driven photocatalytic activity is highly stable after four cycles. The steady state and fluorescence spectra indicated that the energy migration between NYFG NPs and C<sub>3</sub>N<sub>4</sub> NTs was a fluorescence resonance energy transfer (FRET) process, which was also dominated by the surface quenching effect. This study provides an effective strategy to design NIR-responsive photocatalysts based on sensitizer/semiconductor heterojunctions for solar to chemical energy conversion.

## References

- [1] X. Li, J. Yu, M. Jaroniec, *Chemical Society Reviews*, 45 (2016) 2603-2636.
- [2] J. Ran, J. Zhang, J. Yu, M. Jaroniec, S.Z. Qiao, *Chemical Society Reviews*, 43 (2014) 7787-7812.
- [3] J. Yang, D. Wang, H. Han, C. Li, *Accounts of Chemical Research*, 46 (2013) 1900-1909.
- [4] S. Cao, J. Low, J. Yu, M. Jaroniec, *Advanced Materials*, 27 (2015) 2150-2176.
- [5] Y. Zhu, A. Marianov, H. Xu, C. Lang, Y. Jiang, *ACS Applied Materials & Interfaces*, 10 (2018) 9468-9477.
- [6] W. Qin, D. Zhang, D. Zhao, L. Wang, K. Zheng, *Chemical Communications*, 46 (2010) 2304-2306.
- [7] T. Oshikiri, K. Ueno, H. Misawa, *Angewandte Chemie*, 53 (2014) 9802-9805.
- [8] S.Y. Tee, K.Y. Win, W.S. Teo, L.D. Koh, S. Liu, C.P. Teng, M.Y. Han, *Advanced Science*, 4 (2017) 1600337.
- [9] W.J. Ong, L.L. Tan, Y.H. Ng, S.T. Yong, S.P. Chai, *Chemical Reviews*, 116 (2016) 7159-7329.
- [10] G. Chen, H. Qiu, P.N. Prasad, X. Chen, *Chemical Reviews*, 114 (2014) 5161-5214.
- [11] L. Wang, X. Li, Z. Li, W. Chu, R. Li, K. Lin, H. Qian, Y. Wang, C. Wu, J. Li, D. Tu, Q. Zhang, L. Song, J. Jiang, X. Chen, Y. Luo, Y. Xie, Y. Xiong, *Advanced Materials*, 27 (2015) 5528-5533.
- [12] H. Dong, L.D. Sun, C.H. Yan, *Nanoscale*, 5 (2013) 5703-5714.
- [13] G. Chen, T.Y. Ohulchanskyy, R. Kumar, H. Ågren, P.N. Prasad, *ACS nano*, 4 (2010) 3163-3168.
- [14] W. Wang, Y. Li, Z. Kang, F. Wang, J.C. Yu, *Applied Catalysis B: Environmental*, 182 (2016) 184-192.
- [15] Y. Tang, W. Di, X. Zhai, R. Yang, W. Qin, *ACS Catalysis*, 3 (2013) 405-412.

- [16] M. Chatti, V.N. Adusumalli, S. Ganguli, V. Mahalingam, *Dalton Transactions*, 45 (2016) 12384-12392.
- [17] X. Guo, W. Song, C. Chen, W. Di, W. Qin, *Physical Chemistry Chemical Physics: PCCP*, 15 (2013) 14681-14688.
- [18] Y. Chen, C. Lu, L. Tang, S. Wei, Y. Song, J. Wang, *Solar Energy Materials and Solar Cells*, 149 (2016) 128-136.
- [19] C.K. Chen, H.M. Chen, C.J. Chen, R.S. Liu, *Chemical Communications*, 49 (2013) 7917-7919.
- [20] J. Xu, T.J. Brenner, Z. Chen, D. Neher, M. Antonietti, M. Shalom, *ACS Applied Materials & Interfaces*, 6 (2014) 16481-16486.
- [21] X. Li, H. Ren, Z. Zou, J. Sun, J. Wang, Z. Liu, *Chemical Communications*, 52 (2016) 453-456.
- [22] E. Cheng, W. Yin, S. Bai, R. Qiao, Y. Zhong, Z. Li, *Materials Letters*, 146 (2015) 87-90.
- [23] M.Z. Huang, B. Yuan, L. Dai, M.L. Fu, *Journal of Colloid and Interface Science*, 460 (2015) 264-272.
- [24] C. Cao, W. Qin, J. Zhang, Y. Wang, P. Zhu, G. Wei, G. Wang, R. Kim, L. Wang, *Optics Letters*, 33 (2008) 857-859.
- [25] F. Wang, Y. Han, C.S. Lim, Y. Lu, J. Wang, J. Xu, H. Chen, C. Zhang, M. Hong, X. Liu, *Nature*, 463 (2010) 1061-1065.
- [26] S. Wen, J. Zhou, K. Zheng, A. Bednarkiewicz, X. Liu, D. Jin, *Nature Communications*, 9 (2018) 2415.
- [27] J. Zhao, D. Jin, E.P. Schartner, Y. Lu, Y. Liu, A.V. Zvyagin, L. Zhang, J.M. Dawes, P. Xi, J.A. Piper, E.M. Goldys, T.M. Monro, *Nature Nanotechnology*, 8 (2013) 729-734.
- [28] S. Xu, W. Xu, Y. Wang, S. Zhang, Y. Zhu, L. Tao, L. Xia, P. Zhou, H. Song, *Nanoscale*, 6 (2014) 5859-5870.

- [29] Y. Ma, H. Liu, Z. Han, L. Yang, J. Liu, *Journal of Materials Chemistry A*, 3 (2015) 14642-14650.
- [30] F. Shi, Y. Zhao, *Journal of Materials Chemistry C*, 2 (2014) 2198-2203.
- [31] W. Wang, W. Huang, Y. Ni, C. Lu, L. Tan, Z. Xu, *Applied Surface Science*, 282 (2013) 832-837.
- [32] G. Boulon, A. Collombet, A. Brenier, M.T. Cohen-Adad, A. Yoshikawa, K. Lebbou, *Advanced Functional Materials*, 11 (2001) 263-270.
- [33] W. Wang, W. Huang, Y. Ni, C. Lu, Z. Xu, *ACS Applied Materials & Interfaces*, 6 (2014) 340-348.
- [34] S. Thaweesak, M. Lyu, P. Peerakiatkhajohn, T. Butburee, B. Luo, H. Chen, L. Wang, *Applied Catalysis B: Environmental*, 202 (2017) 184-190.
- [35] H.L. Hsu, K.R. Leong, I.J. Teng, M. Halamicsek, J.Y. Juang, S.R. Jian, L. Qian, N.P. Kherani, *Materials*, 7 (2014) 5643-5663.
- [36] N. Liu, W. Qin, G. Qin, T. Jiang, D. Zhao, *Chemical Communications*, 47 (2011) 7671-7673.
- [37] F. Shi, J. Wang, D. Zhang, G. Qin, W. Qin, *Journal of Materials Chemistry*, 21 (2011) 13413.
- [38] X. Guo, W. Di, C. Chen, C. Liu, X. Wang, W. Qin, *Dalton Transactions*, 43 (2014) 1048-1054.
- [39] M. Reli, P. Huo, M. Sihor, N. Ambrozova, I. Troppova, L. Matejova, J. Lang, L. Svoboda, P. Kustrowski, M. Ritz, P. Praus, K. Koci, *The Journal of Physical Chemistry A*, 120 (2016) 8564-8573.
- [40] E. Cheng, S. Zhou, M. Li, Z. Li, *Applied Surface Science*, 410 (2017) 383-392.
- [41] X. Huang, S. Han, W. Huang, X. Liu, *Chemical Society Reviews*, 42 (2013) 173-201.
- [42] G. Wang, Q. Peng, Y. Li, *Accounts of Chemical Research*, 44 (2011) 322-332.



[43] A. Bednarkiewicz, M. Nyk, M. Samoc, W. Strek, *The Journal of Physical Chemistry C*, 114 (2010) 17535-17541.

[44] D.-X. Xu, Z.-W. Lian, M.-L. Fu, B. Yuan, J.-W. Shi, H.-J. Cui, *Applied Catalysis B: Environmental*, 142-143 (2013) 377-386.

## **Chapter 6 NIR-responsive ammonia synthesis over NaYF<sub>4</sub>:Yb,Tm nanoparticle assembled C<sub>3</sub>N<sub>4</sub> NTs with nitrogen vacancies**

### **6.1 Introduction**

Nitrogen element is essential to living organisms in building proteins, nucleic acids and many other biomolecules [1]. However, nitrogen molecule (N<sub>2</sub>), making up 78 vol. % of the earth's atmosphere, is thermodynamically stable due to the N≡N triple-bond energy. Ammonia (NH<sub>3</sub>), easily condensed to a liquid, has garnered attention as a fuel for vehicles and a potential hydrogen carrier. Nowadays, industrial NH<sub>3</sub> production is still dominated by the conventional Haber-Bosch process with iron or ruthenium-based catalysts at high temperatures (400-600 °C) and pressures (20-40 MPa) [2]. Therefore, developing sustainable nitrogen fixation under milder conditions is one of the most crucial subjects facing us today.

Recently, photocatalytic nitrogen-fixation technology appears to be an ideal approach, attributing to its advantages of mild conditions, green, low cost and low power consumption [3, 4]. The pioneering work can be traced back to 1977 when Schrauzer *et al.* reported that Fe-doped TiO<sub>2</sub> could reduce N<sub>2</sub> to NH<sub>3</sub> under UV light illumination [5]. To date, a variety of photocatalysts such as metal oxides, metal sulphide-based materials, bismuth oxyhalides and etc., have been explored to realize photocatalytic ammonia synthesis [6]. Unfortunately, further commercial development of this technology as well as large-scale manufacture of the catalysts have met obstacles. One of the main limitations of its application is well known that most catalysts are only active under UV light (< 400 nm), which covers only about 5 % of the solar spectrum, whereas visible light (400-800 nm) occupies 49 % and near-infrared (NIR) light (> 800 nm) comprises the remaining 46 % [7, 8]. Therefore, extending solar-energy conversion to a broader spectral range, especially in the visible and NIR regions, is an important objective.

Upconversion nanoparticles (UCNPs) doped with trivalent rare-earth ions (nanophosphors) have shown great potential in solar cells and photocatalysis owing to their unique merits, such as tunable emissions, photostability, long luminescence lifetime and, most importantly, the ability to display UC emission [9]. UC emission is a nonlinear multiphoton transition process, in which the UC material can convert low-intensity NIR light to shorter-wavelength NIR, visible or UV light (higher-energy photons) [10, 11]. Among them, a sodium yttrium fluoride (NaYF<sub>4</sub>) lattice co-doped with lanthanide ions, including ytterbium (Yb<sup>3+</sup>) sensitizer ions and activator ions (Tm<sup>3+</sup>) usually exhibit high chemical stability and a low phonon energy, and fascinating optical properties [12]. On the other hand, crucial progress in artificial photosynthesis has been made using graphitic carbon nitride (g-C<sub>3</sub>N<sub>4</sub>), an effective metal-free polymer as a semiconductor, attributed to the low cost, suitable band structure and visible-light response. In particular, carbon nitride nanotubes (C<sub>3</sub>N<sub>4</sub> NTs) exhibit a high surface-to-volume ratio, fascinating electronic properties and many chemically active sites [13-15].

Hence, there is considerable interest to apply NaYF<sub>4</sub>:Yb,Tm (NYF) NPs serving as a medium that can transfer energy to C<sub>3</sub>N<sub>4</sub> NTs after absorbing NIR light, to generate oxidative holes and reductive electrons. To the best of our knowledge, photocatalytic ammonia synthesis over UCNPs decorated catalysts has yet to be explored. A ternary nanocomposite, consisting of NYF NPs, TiO<sub>2</sub> and reduced graphene oxide, exhibits about 1.7 times the phenol degradation rate of bare TiO<sub>2</sub> under simulated sunlight irradiation [16]. Very recently, the UCNPs (NaYF<sub>4</sub>:Yb/Tm@NaYF<sub>4</sub>:Yb/Er) and Zn<sub>x</sub>Cd<sub>1-x</sub>S yolk-shell nanoparticles with high UC efficiency were able to decompose 65 % of RhB dyes in 30 min under NIR light irradiation [17]. Huang *et al.* applied a stepwise method to deposit NYF NPs on C<sub>3</sub>N<sub>4</sub> nanosheets, which presented a 22 % activity loss in Rhodamine B (RhB) degradation after a four-cycle test [18]. Meanwhile, Cheng *et al.* used an ionic surfactant, cetyltrimethyl ammonium bromide, to load NYF NPs on the surface of C<sub>3</sub>N<sub>4</sub> nanosheets, showing unfavourable performance, only about

20 % of RhB was degraded after NIR irradiation for 7 h [19]. UCNPs have also been successfully applied to other substrates like MoS<sub>2</sub>, TiO<sub>2</sub>, CdS and Graphene in order to effectively utilize the deeply penetrating NIR light for photocatalytic hydrogen generation or organics degradation [20-23].

However, these studies focused on material coating strategies to improve the energy transfer from UCNPs to the semiconductors. Alternatively, element vacancies like sulfur, oxygen and nitrogen, are capable to activate inert molecules and increase of optical absorption and surface area [24-26]. Among them, nitrogen vacancies (NVs) with their typical defect states are favoured for nitrogen atom occupation, and dynamically trapping the excited electrons [27, 28]. In this case, NVs incorporation may promote the energy transfer of the multiple photons emitted by UCNPs, which further leads to efficient ammonia generation under NIR light irradiation. In this work, we present a binary photocatalyst, NYF/NV-C<sub>3</sub>N<sub>4</sub> NTs, in which NVs play a great role in the energy transfer process between NYF NPs, NIR absorbers and C<sub>3</sub>N<sub>4</sub> NTs. This is the first time to apply such a synergy giving rise to high ammonia quantum efficiency illuminated with NIR light. Detailed investigations were conducted to study the chemical and structural properties of the nanocomposite, and the functions of NYF NPs and NVs in the system. This work opens a versatile approach to refine photocatalysts, in efforts to develop green chemical manufacturing by NIR-responsive photocatalysis.

## **6.2 Experimental section**

### **6.2.1 Catalyst synthesis**

C<sub>3</sub>N<sub>4</sub> NTs were synthesised by our reported water-induced morphological transformation process [29]. The detailed synthesised procedure of C<sub>3</sub>N<sub>4</sub> NTs is referred to Section 3.2.1, Chapter 3. The nitrogen vacancies-incorporated C<sub>3</sub>N<sub>4</sub> NTs (NV-C<sub>3</sub>N<sub>4</sub> NTs) were realised by calcining the as-prepared C<sub>3</sub>N<sub>4</sub> NTs at 550 °C under a N<sub>2</sub> flow for 2 h [27].

NaYF<sub>4</sub>:20%Yb,0.5%Tm nanoparticles were prepared by a solvothermal process [30]. The detailed preparation process of NYF NPs is referred to Section 5.2.1, Chapter 5.

Nominal amounts of the as-obtained NaYF<sub>4</sub>:Yb,Tm (NYF) were dissolved into 1 mL of polyvinylpyrrolidone (PVP)/Ethanol solution (0.2 g/mL), and then sonicated at room temperature for 15 min. Then NV-C<sub>3</sub>N<sub>4</sub> NT powder and 50 mL of Ethanol were added and stirred for another 12 h. After that, the solution was aged for 10 h. Finally, they were dried at 80 °C in static air for 2 h to remove Ethanol [16]. NYF(5)/NV-C<sub>3</sub>N<sub>4</sub> NTs, NYF(15)/NV-C<sub>3</sub>N<sub>4</sub> NTs and NYF(25)/NV-C<sub>3</sub>N<sub>4</sub> NTs represent that the nominal mass ratios of NYF NPs and C<sub>3</sub>N<sub>4</sub> NTs were at 5 %, 15 %, and 25 % respectively.

### **6.2.2 Characterisation**

Powder X-ray diffraction (XRD) patterns were accomplished on a Panalytical X'Pert PRO diffractometer via Cu K $\alpha$ 1 radiation. High-resolution transmission electron microscope (HRTEM) JEOL-2100F working with the accelerating voltage at 200 kV was used for morphology measurements. Scanning electron microscopy (SEM) images and elemental analysis were performed on a Phenom XL scanning electron microscope with an energy-dispersive X-ray spectrometer (EDX). The nitrogen adsorption and desorption isotherms were recorded on an Autosorb-iQ analyzer (TriStar II 3020) after the samples were vacuum-dried at 120 °C overnight. Ultraviolet-visible (UV-vis) diffuse reflectance spectra (DRS) were obtained on a Cary 5000 spectrophotometer using BaSO<sub>4</sub> as the reference sample. The nitrogen adsorption and desorption isotherms were conducted on an Autosorb-iQ analyser (TriStar II 3020). The specific surface area was calculated with the Brunauer-Emmett-Teller (BET) method. Photoluminescence (PL) spectra were recorded at room temperature with a fiber-coupled spectrometer (Ocean Optics 2000) with excitation of a 980 nm diode laser (Lumics, LU0975M400). Confocal images were investigated by a confocal laser scanning microscope Olympus FV1200 equipped with a 980 nm NIR laser.

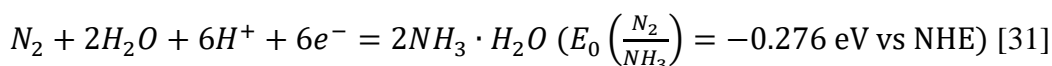
### 6.2.3 Photocatalytic ammonia synthesis

The photoreduction of  $N_2$  was conducted in a reactor at atmospheric pressure and room temperature. In a typical experiment, 40 mg of photocatalyst powder was suspended in 40 mL of a 10 vol. % sacrificial reagent contained aqueous solution.  $N_2$  was continually bubbled through this solution, which was irradiated with a 980 nm NIR laser at 2 W. After that, approximately 1.5 mL of the suspension was obtained from the reactor at given intervals for subsequent  $NH_4^+$  concentration analysis, which was conducted by the indophenol-blue method [5], and the concentration of  $NH_4^+$  was tested using an UV-vis spectrophotometer (DR/4000, Hach Inc.). In order to investigate the photocatalytic activity under solar-light irradiation, a 300 W Xe lamp through a UV cut-off filter ( $> 420$  nm) was used as the light source. The power density of 980 nm light was measured with a photometer (LPM 100/A, Coherent Inc.).

The apparent quantum efficiency (AQE) was calculated as follows:

$$AQE(\%) = \frac{\text{no. of reacted electrons}}{\text{no. of incident photons}} \times 100\% = \frac{N_{NH_3}}{N_p} = \frac{6 \times \text{no. of evolved } NH_3 \text{ molecules}}{\text{no. of incident photons}} \times 100\%$$

Based on the following main reaction:



## 6.3 Results and discussion

### 6.3.1 Photocatalytic performance

Control experiments of photocatalytic nitrogen fixation at different reaction conditions were measured under the UV-filtered light irradiation. The transmittance properties of the reactor and the filter ( $> 420$  nm) and the calibration curves for the indophenol method are shown in Figure A9 (Appendix). The ammonia generation rate is negligible in the absence of  $N_2$ , or sacrificial reagents, or UV-filtered light, confirming the ammonia produced is originated from  $N_2$  reduction rather than from  $C_3N_4$  NT decomposition (Figure 6.1). The effect of sacrificial reagents, including ethanol, MeOH and  $Na_2SO_3$  on the ammonia production rate was studied.

The best ammonia yield was achieved with the addition of ethanol, thus in the following experiment ethanol was selected to the sacrificial electron donor of photogenerated holes.

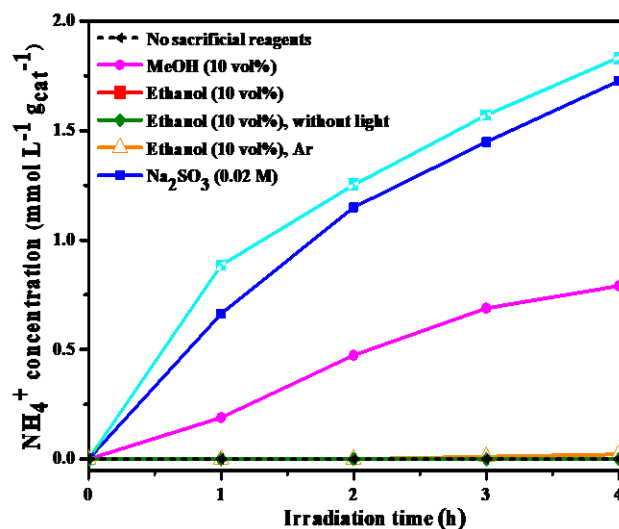
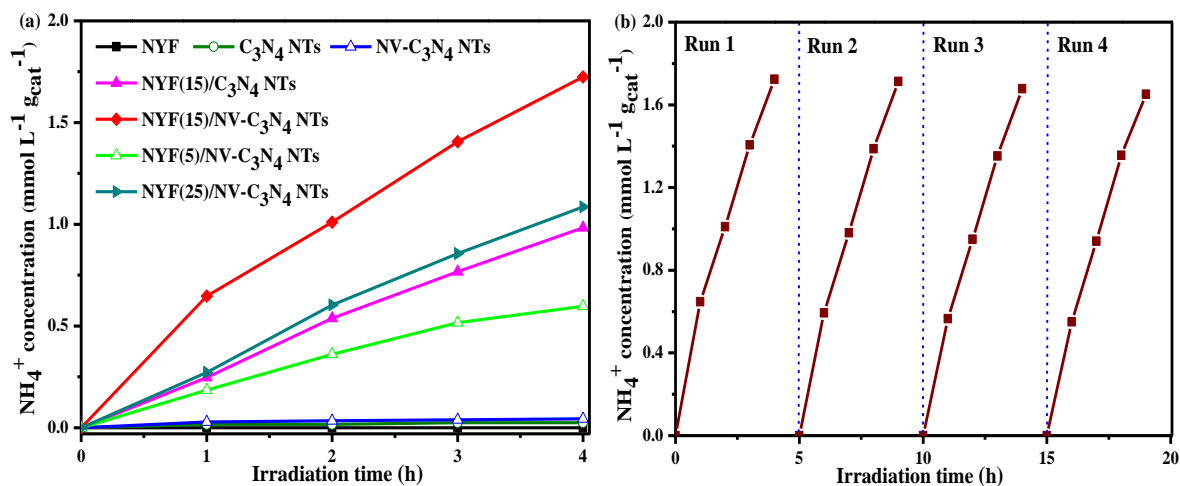


Figure 6.1 UV-filtered ( $\lambda > 420$  nm) light photocatalytic nitrogen fixation over bare C<sub>3</sub>N<sub>4</sub> NTs in different systems.



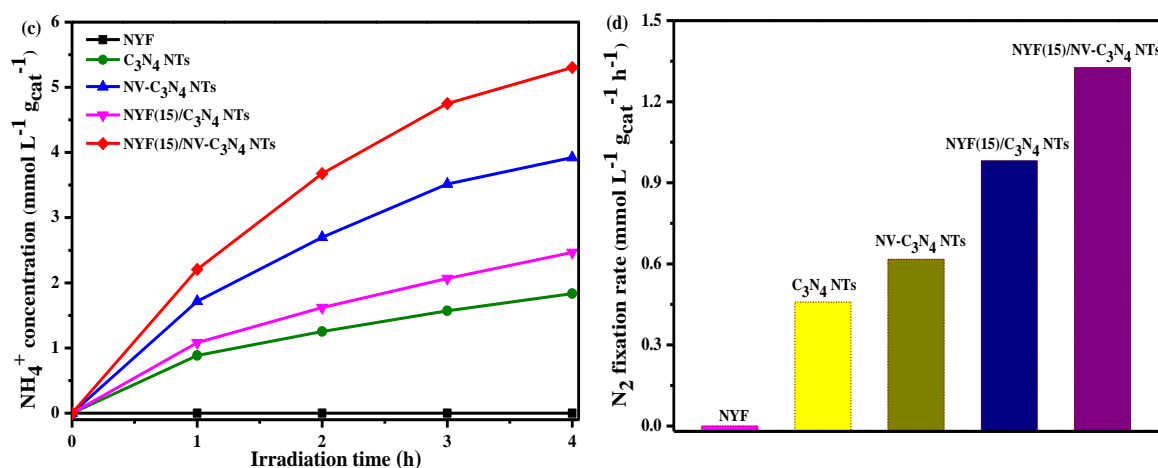


Figure 6.2 Ammonia production over various photocatalysts (a) and the cyclic experiment over NYF(15)/NV-C<sub>3</sub>N<sub>4</sub> NTs (b) under 980 nm laser illumination; concentration of generated  $\text{NH}_4^+$  (c) and the photocatalytic N<sub>2</sub> fixation rate (d) of the samples under simulated UV-filtered solar light.

The photocatalytic activities in nitrogen fixation of the materials under 980 nm laser irradiation are shown in Figure 6.2a. Apparently negligible ammonia was detected over bare C<sub>3</sub>N<sub>4</sub> NTs, NYF NPs and NV-C<sub>3</sub>N<sub>4</sub> NTs. Upon decorating NYF NPs on NV-C<sub>3</sub>N<sub>4</sub> NTs, ammonia was produced attributed to the absorbance of 980 nm NIR light. NV-C<sub>3</sub>N<sub>4</sub> NTs decorated with various NYF NP loading amounts were investigated. The activities were improved with an increase of the NYF NP content. The best performance was reached at a NYF NP content of 15 wt. %, with a nitrogen fixation rate of 1.72 mmol L<sup>-1</sup> g<sub>cat</sub><sup>-1</sup>, corresponding to a AQE of 0.99 %, which is 2.2 times as high as that of NYF(15)/C<sub>3</sub>N<sub>4</sub> NTs (0.80 mmol L<sup>-1</sup> g<sub>cat</sub><sup>-1</sup>; 0.46 %). However, the ammonia generation rate of NYF(25)/NV-C<sub>3</sub>N<sub>4</sub> NTs was declined, which may be due to the decrease in surface-active sites owing to the excessive loading amount. The stability test of NYF(15)/NV-C<sub>3</sub>N<sub>4</sub> NTs was performed as shown in Figure 6.2b. After 16 h illumination under a 980 nm laser, no obvious decrease in the ammonia generation was observed, suggesting excellent photochemical stability of the nanocomposite.

On the other hand, as depicted in Figure 6.2c, under UV-filtered solar light illumination the



dependence of ammonia formation on the irradiation time was conducted over these materials. Noteworthy, bare  $C_3N_4$  NTs and NV- $C_3N_4$  NTs are able to reduce  $N_2$ , whereas no ammonia was generated over NYF NPs. After 4 h, the concentrations of generated  $NH_4^+$  were 5.30, 3.92, 2.47 and 1.83  $mmol\ L^{-1}\ g_{cat}^{-1}$  for NYF(15)/NV- $C_3N_4$  NTs, NV- $C_3N_4$  NTs, NYF(15)/ $C_3N_4$  NTs and  $C_3N_4$  NTs, respectively. In comparison with the bare NV- $C_3N_4$  NTs and  $C_3N_4$  NTs, the improvement for NYF(15)/NV- $C_3N_4$  NTs and NYF(15)/ $C_3N_4$  NTs contributed to NYF NPs in NIR absorption are 1.38 and 0.64  $mmol\ L^{-1}\ g_{cat}^{-1}$ , respectively. Nevertheless, they are lower than the activities under 980 nm laser illumination, which may be caused by the lower Xenon-light irradiance. From Figure 6.2d, it can be seen that the photocatalytic  $N_2$  fixation rate of NYF(15)/NV- $C_3N_4$  NTs is 1.33  $mmol\ L^{-1}\ g_{cat}^{-1}\ h^{-1}$ , which is approximately 3 times as high as that of the bare  $C_3N_4$  NTs (0.46  $mmol\ L^{-1}\ g_{cat}^{-1}\ h^{-1}$ ).

### 6.3.2 Structure characterisation

The structures of the prepared catalysts were characterised by XRD analysis, shown in Figure 6.3a. For the NYF NP sample, all the diffraction peaks are indexed to bare hexagonal  $NaYF_4$  phase (JCPDS card 28-1192) [32].  $C_3N_4$  NTs shows two typical diffraction peaks at  $27.5^\circ$  and  $13.0^\circ$ , indexed as the (002) plane of the interlayer stacking of aromatic systems and the (100) plane of the in-plane structural packing motif, respectively [29]. After incorporated with NVs, the peak at  $13.0^\circ$  became weaker than that of  $C_3N_4$  NT samples, which is attributed to the lowered long-range order of in-plane structural packing, suggesting that defects may exist in the NV- $C_3N_4$  NT framework [33]. In addition, close inspection of Figure 6.3b shows that the (002) peak shifts from  $27.5^\circ$  to  $27.7^\circ$ , corresponding to a decrease in the interlayer stacking distance from 0.324 nm to 0.322 nm, which might be due to an improved interlayer stacking intensity caused by the removal of nitrogen-containing species [34]. Both the hexagonal  $NaYF_4$  phase and the graphitic  $C_3N_4$  phase are observed in NYF/ $C_3N_4$  NT and NYF/NV- $C_3N_4$  NT nanocomposites, confirming the successful decoration of NYF NPs. Notably, compared with

the XRD patterns of  $C_3N_4$  NTs and NV- $C_3N_4$  NTs, the overall diffraction intensities of the nanocomposites are weaker, indicating that grafting NYF NPs could decrease the planar size of the  $C_3N_4$  layers. Moreover, the crystal structures of NYF(15)/NV- $C_3N_4$  NTs before and after recycling experiments were analysed by XRD (Figure 6.3c). No significant change in the patterns was observed, confirming that this photocatalyst is stable and reusable.

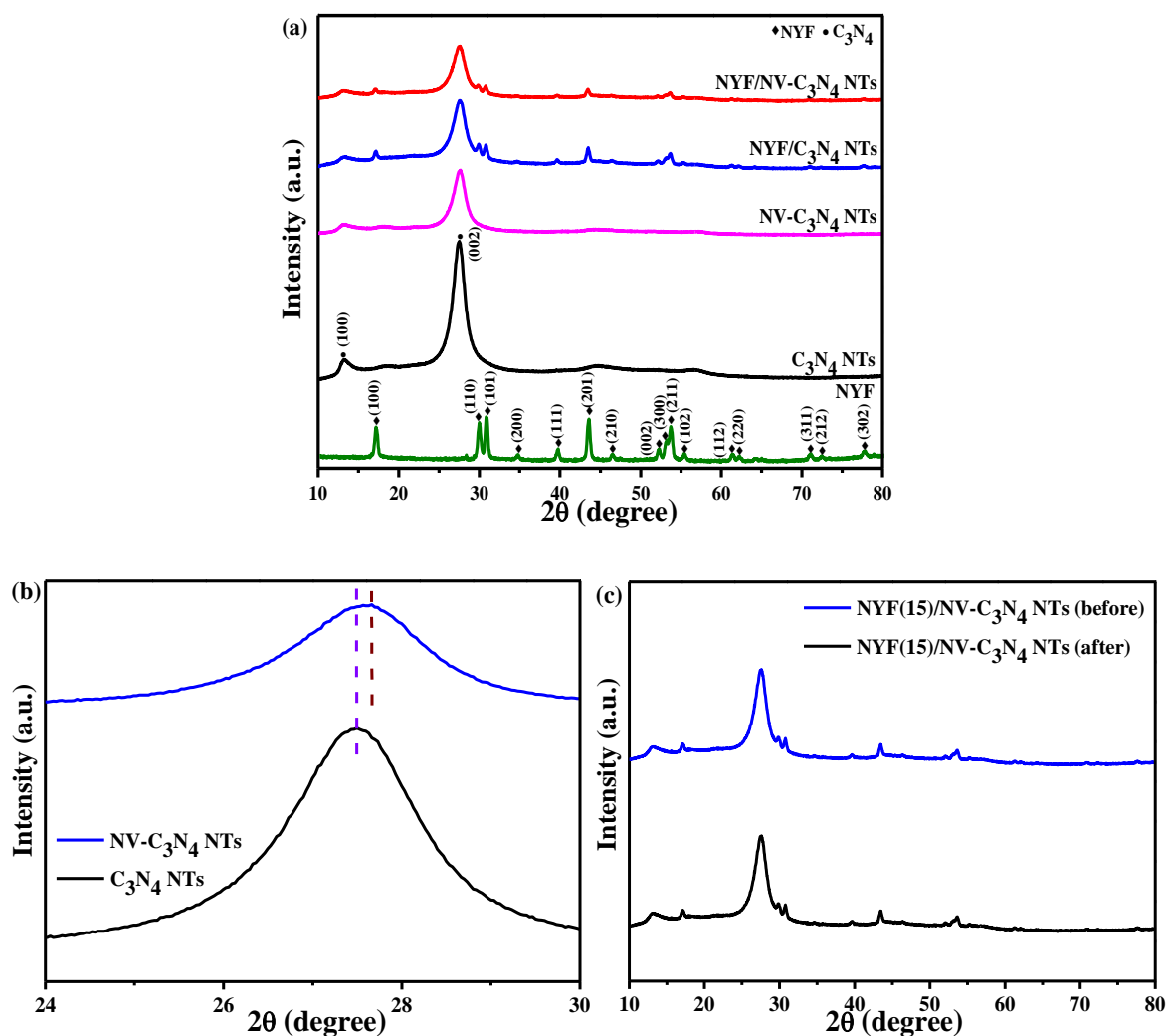


Figure 6.3 XRD patterns of the various samples (a); XRD patterns of  $C_3N_4$  NTs and NV- $C_3N_4$  NTs from 12° to 34° (b); and the patterns of NYF(15)/NV- $C_3N_4$  NTs before and after reaction (c).

The morphologies of the prepared samples were characterised by TEM observations. As shown in Figure 3.5a-c, Chapter 3, bare  $C_3N_4$  NTs exhibit hollowed tubular structures with diameters

in the range of 200-400 nm, confirming that the nanotubes were constructed by the nanosheet roll-up mechanism. In Figure 6.4, NYF NPs show single crystalline spheres approximately 20 nm in diameter. There is no difference in the morphology of NV-C<sub>3</sub>N<sub>4</sub> NTs (Figure 6.5a) and C<sub>3</sub>N<sub>4</sub> NTs, indicating a stable tubular characteristic upon N<sub>2</sub> treatment. Figures 6.5b-d present TEM images of NYF(15)/NV-C<sub>3</sub>N<sub>4</sub> NTs. From the low-magnification image (Figure 6.5b), it is found that NYF NPs are uniformly anchored on the internal and external surfaces of the nanotubes. The high-resolution TEM image in Figure 6.5c illustrates the existence of an interface between NYF NPs and C<sub>3</sub>N<sub>4</sub> NTs, and the lattice spacing of 0.52 nm is defined assigning to the (100) plane of the hexagonal NaYF<sub>4</sub> [35], agreeing well with the previous XRD results. The line-scan profiles in Figure 6.5d record the signals of N and Y elements along the red line. It is clearly seen that with scanning through the particle, the intensity of N drops, whereas Y increases, providing additional evidence for the strong coupling of NYF NPs on the nanotubes. TEM images of NYF(5)/NV-C<sub>3</sub>N<sub>4</sub> NTs and NYF(25)/NV-C<sub>3</sub>N<sub>4</sub> NTs are shown in Figures 6.4b-c. It is worth noting that large quantities of particles almost block up the tube entrance with 25 wt. % of NYF NP deposition, which verifies the explanation of the decrease in ammonia generation because of overloading. In addition, the SEM-EDX spectrum shown in Figure 6.6 further confirms that the NYF(15)/NV-C<sub>3</sub>N<sub>4</sub> NT nanocomposite consists of C, N, Na, Y, F, and Yb elements without any other impurities, and they are well distributed. Element Tm was not detected due to its low content.

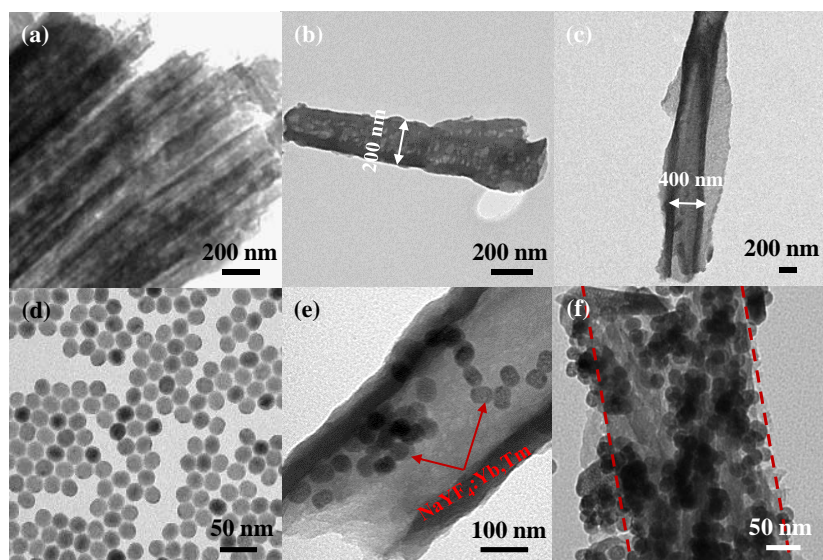


Figure 6.4 TEM images of bare  $C_3N_4$  NTs (a-c), NYF NPs (d), NYF(5)/NV- $C_3N_4$  NTs (e) and NYF(25)/NV- $C_3N_4$  NTs (f).

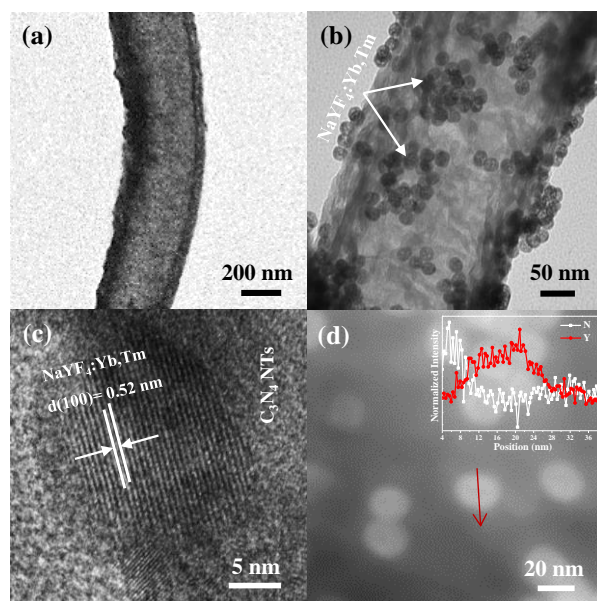
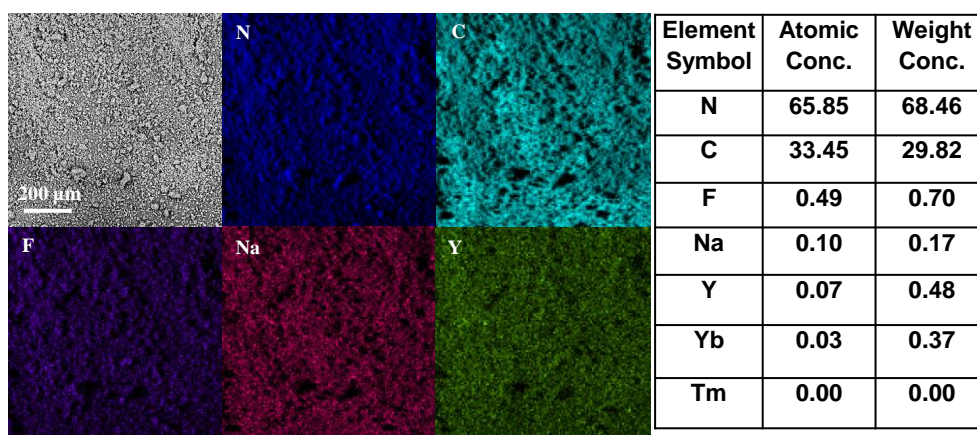


Figure 6.5 TEM images of NV- $C_3N_4$  NTs (a) and NYF(15)/NV- $C_3N_4$  NTs (b-d).

Figure 6.6 SEM-EDS of NYF(15)/NV-C<sub>3</sub>N<sub>4</sub> NTs.

UV-vis diffuse reflectance spectra of these materials are shown in Figure 6.7. For the pure NYF NPs, no absorption in the range from 300 to 900 nm were observed, but a relatively wide absorption range from 900 nm to 1050 nm was detected, which is a typical band of Yb<sup>3+</sup> ions [36]. It can be seen that the bare C<sub>3</sub>N<sub>4</sub> NTs presents a strong absorption edge at around 460 nm. In contrast to C<sub>3</sub>N<sub>4</sub> NTs, a significant shift in the long-wavelength range to the infrared region was observed for NV-C<sub>3</sub>N<sub>4</sub> NTs, and the Tauc plots show a bandgap narrowing from 2.76 eV to 2.73 eV (Figure S7, SI). This indicates that the incorporation of NVs results in better light response on the C<sub>3</sub>N<sub>4</sub> NTs [26]. The NYF(15)/NV-C<sub>3</sub>N<sub>4</sub> NTs show a light-absorption edge before 460 nm, which overlaps that of NV-C<sub>3</sub>N<sub>4</sub> NTs. No obvious absorbance attributed to Yb<sup>3+</sup> ions, suggesting that the loaded content may be too low to be detected. Similar phenomenon can be seen in the report from Huang and his co-workers [18]. Moreover, the absorption intensity of the nanocomposite is enhanced compared to that of bare C<sub>3</sub>N<sub>4</sub> NTs, indicating an extension of the light-responsive range.

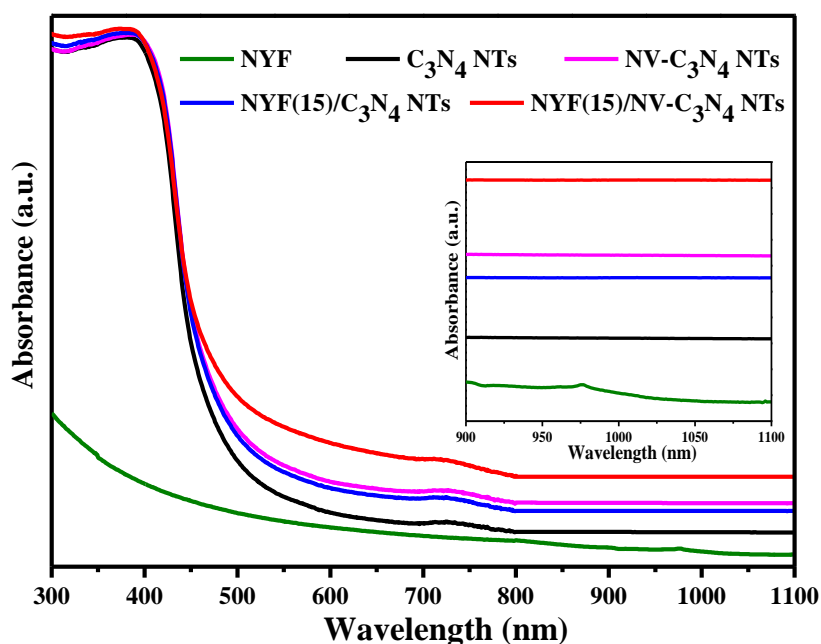


Figure 6.7 UV-vis DRS of the various samples studied in this work.

To explore the adsorption ability of nitrogen gas on the supporting materials, a necessary prerequisite for the photocatalytic reaction, the nitrogen adsorption-desorption isotherms were investigated as shown in Figure 6.8b. The isotherms of  $C_3N_4$  NTs with and without NVs are identified as Type IV isotherms with H3 hysteresis loops regardless of their differences in NVs incorporation, implying the mesoporosity of the materials [37]. Determined by the Brunauer-Emmett-Teller (BET) function, the specific surface areas of  $C_3N_4$  NTs and NV- $C_3N_4$  NTs are 36.4 and 44.3, respectively. The  $N_2$  adsorption amount of  $C_3N_4$  NTs and NV- $C_3N_4$  NTs at  $P/P_0 = 1.0$  is 5.3 and 6.9  $cm^3 g^{-1}$ , respectively, indicating that NV- $C_3N_4$  NTs improves the  $N_2$  physical adsorption ability of the catalyst by 1.3 times, thus further confirming the existence of NVs inside the nanotubes.

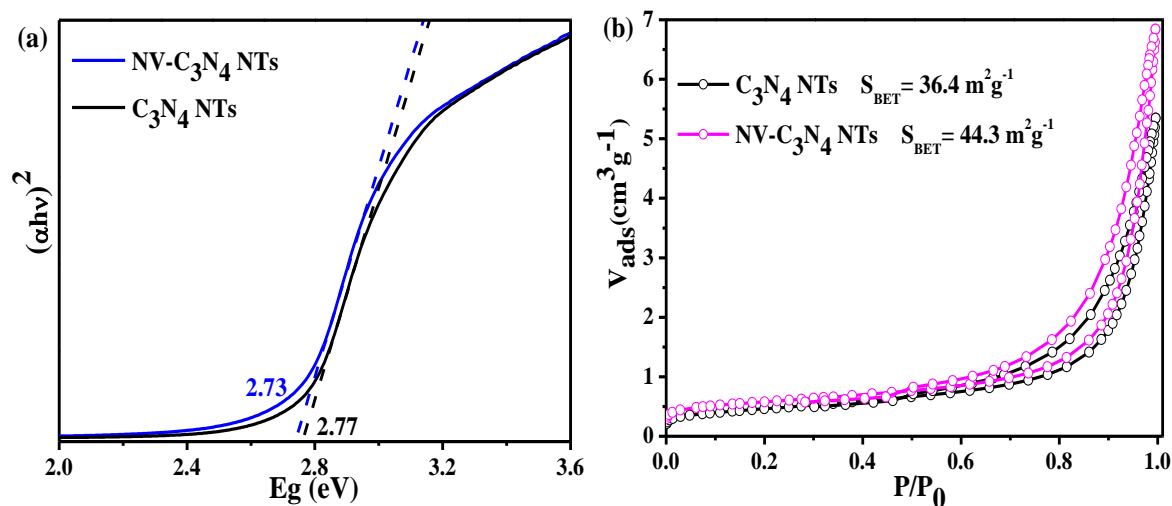


Figure 6.8 Kubelka-Munk plots (a), nitrogen adsorption-desorption isotherms and surface area (b) of the bare  $C_3N_4$  NTs and NV- $C_3N_4$  NTs.

XPS was used to investigate the chemical binding and valence-band position of samples studied in this work. All the signals of elemental C, N, O, Na, Y, F, Yb and Tm elements were detected by the XPS spectra (Figure 6.9a-b and Table 6.1) indicating hybrid structure of NYF(15)/NV- $C_3N_4$  NTs, which is consistent with the SEM-EDX results. The C/N atomic ratio of NV- $C_3N_4$  NT is 0.92, which is higher than that of  $C_3N_4$  NTs (0.76), indicating that the nitrogen is deficient in the NV- $C_3N_4$  NT framework. The high-resolution XPS spectra of N 1s for bare  $C_3N_4$  NTs, NV- $C_3N_4$  NTs, NYF(15)/ $C_3N_4$  NTs and NYF(15)/NV- $C_3N_4$  NTs are shown in Figure 6.5a. The N 1s spectra of  $C_3N_4$  NTs can be deconvoluted into three peaks centered at ca. 398.8, 400.1 and 401.2 eV, respectively, assigned to the two-coordinated N atoms ( $N_{2c}$ ), three-coordinated N atoms ( $N_{3c}$ ) and  $NH_x$  groups in the skeleton of g- $C_3N_4$  [38]. Comparing the peak area ratio of the  $N_{NH_x}$  to the  $N_{3c}$  peak, it decreases from 0.73 for  $C_3N_4$  NTs to 0.61 for NV- $C_3N_4$  NTs, indicating that the loss of N atoms occurs at terminal  $NH_x$  species because of their unsaturated coordination [34, 39]. As a consequence of the formation of NVs, the N 1s spectra of NV- $C_3N_4$  NTs present a negative shift compared that of  $C_3N_4$  NTs. Compared with the spectra of NYF(15)/ $C_3N_4$  NTs, obviously, there are three peaks shifted to a lower bonding energy in NYF(15)/NV- $C_3N_4$  NTs as well.

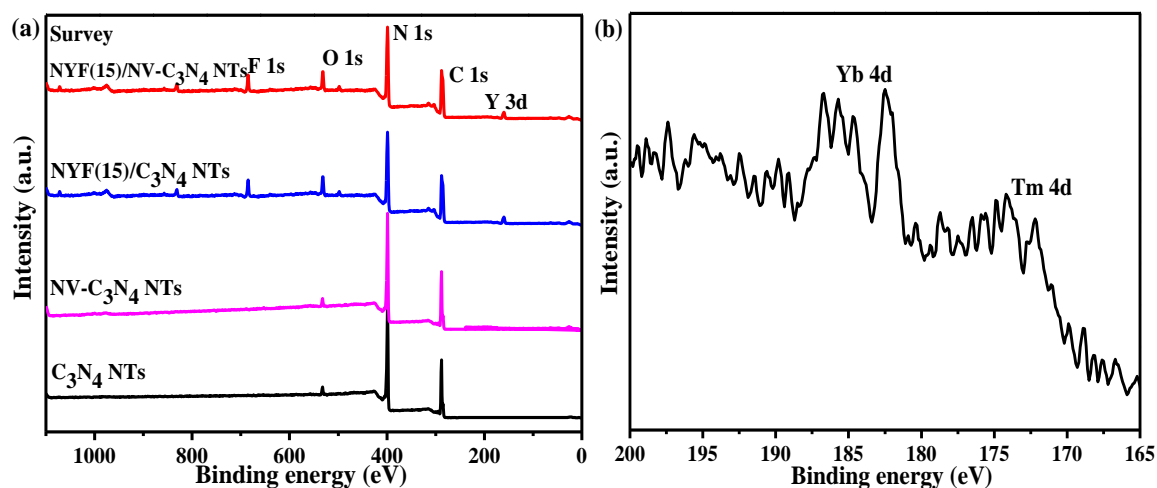


Figure 6.9 XPS wide-scan spectra of  $C_3N_4$  NTs, NV- $C_3N_4$  NTs, NYF(15)/ $C_3N_4$  NTs and NYF(15)/NV- $C_3N_4$  NTs (a); high-resolution Yb 4d and Tm 4d s XPS spectra of NYF(15)/NV- $C_3N_4$  NTs (b).

Table 6.1 Atomic ratios of different elements in XPS analysis.

Name	$C_3N_4$ NTs Atomic %	NV- $C_3N_4$ NTs Atomic %	NYF(15)/ $C_3N_4$ NTs Atomic %	NYF(15)/NV- $C_3N_4$ NTs Atomic %
C 1s	42.41	46.87	41.16	54.70
O 1s	1.90	2.41	1.83	1.20
N 1s	55.69	50.72	51.64	38.41
Na 1s	/	/	0.75	0.79
Y 3d	/	/	0.88	0.96
F 1s	/	/	3.70	3.90
Tm 4d	/	/	0.01	0.01
Yb 4d	/	/	0.03	0.02

In the C 1s peaks two doublets fit the raw peaks very well. For  $C_3N_4$  NTs, it can be deconvoluted into two peaks with binding energies of ca. 288.2 eV and 284.7 eV, corresponding to C-N-C and C-C coordination, respectively (Figure A10, Appendix) [39]. In addition, after the incorporation of NVs the atomic ratio of C-N-C to C-C groups increases from 2.5 to 3.9, which proves the disappearance of the  $NH_x$  groups, thereby further confirming the generation of NVs in  $C_3N_4$  NTs. The high resolution of F 1s XPS spectra from Figure 6.5b



can be deconvoluted into two peaks. As to NYF(15)/C<sub>3</sub>N<sub>4</sub> NTs, 685.5 and 684.8 eV can be ascribed to the F atoms in the NYF NPs and the F-C bond, respectively [11, 40]. The F 1s peaks of NYF(15)/NV-C<sub>3</sub>N<sub>4</sub> NTs were shifted toward higher binding energy region at 685.7 eV and 685.0 eV compared to that of NYF(15)/C<sub>3</sub>N<sub>4</sub> NTs, which suggests that the NVs may bring a strong interaction between NYF NPs and the underlying C<sub>3</sub>N<sub>4</sub> support, thus being beneficial for heterojunction formation and further promoting energy transfer between the two nanomaterials.

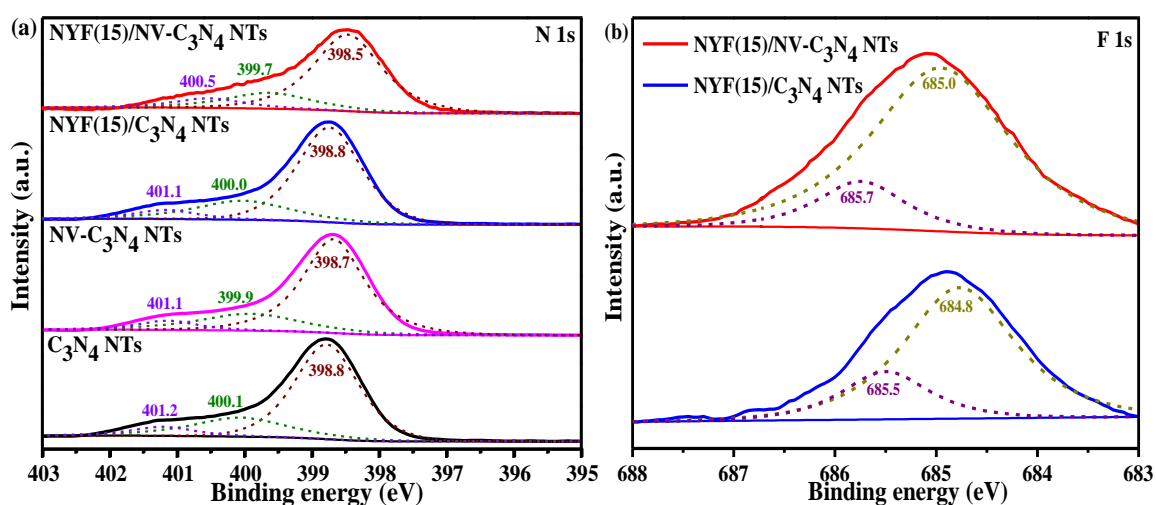


Figure 6.10 High-resolution XPS analysis of N 1s for the catalysts studied in this work (a); and F 1s spectrum of NYF(15)/C<sub>3</sub>N<sub>4</sub> NTs and NYF(15)/NV-C<sub>3</sub>N<sub>4</sub> NTs (b).

The steady-state photoluminescence spectra of the catalysts studied in this work were recorded using a 980 nm laser at 2 W as the excitation light source. As shown in Figure 6.11a, no emission intensity was detected on bare C<sub>3</sub>N<sub>4</sub> NT and NV-C<sub>3</sub>N<sub>4</sub> NT catalysts. The NYF NPs emit intense upconversion emission with the peaks centered at 343 nm (3.62 eV), 360 nm (3.44 eV), 450 nm (2.73 eV), 475 nm (2.61 eV) and 644 nm (1.93 eV), deriving from the radioactive  $^1\text{I}_6 \rightarrow ^3\text{F}_4$ ,  $^1\text{D}_2 \rightarrow ^3\text{H}_6$ ,  $^1\text{D}_2 \rightarrow ^3\text{F}_4$ ,  $^1\text{G}_4 \rightarrow ^3\text{H}_6$  and  $^1\text{G}_4 \rightarrow ^3\text{F}_4$  transitions of Tm ions, respectively [41]. These peaks in the UV and visible regions match well with the absorption edge of the C<sub>3</sub>N<sub>4</sub> NT support. After the attachment with C<sub>3</sub>N<sub>4</sub> NTs or NV-C<sub>3</sub>N<sub>4</sub> NTs, the UC luminescence

signals were quenched; and NYF(15)/NV-C<sub>3</sub>N<sub>4</sub> NTs exhibit much lower intensities than NYF(15)/C<sub>3</sub>N<sub>4</sub> NTs. Thus, the energy of the excited state of Tm<sup>3+</sup> transferred directly to the supporting material and the highest energy transfer efficiencies were achieved in the NYF(15)/NV-C<sub>3</sub>N<sub>4</sub> NT catalyst, which is attributed to the unique nanostructure and stronger interaction within the heterojunction. In addition, from the confocal images of NYF(15)/NV-C<sub>3</sub>N<sub>4</sub> NTs (Figure 6.12), a cumulative image of strong blue and red luminescence was simultaneously detected from the nanocomposites, which further confirms the steady-state PL results and that the NYF NPs were well distributed.

Figure 6.11b displays the PL spectra of the catalysts under an excitation of 360 nm wavelength from a Xenon lamp. The emission peaks of all the samples centered at around 450 nm, which is due to the band-band PL phenomenon with the energy of the light equal to the band-gap energy of the supporting material C<sub>3</sub>N<sub>4</sub> NTs. The intensity of NYF(15)/C<sub>3</sub>N<sub>4</sub> NTs is lower than that of C<sub>3</sub>N<sub>4</sub> NTs, indicating that the heterojunction can improve photogenerated charge separation. The PL intensity of NV-C<sub>3</sub>N<sub>4</sub> NTs is much less than that of C<sub>3</sub>N<sub>4</sub> NTs, suggesting that the NV-C<sub>3</sub>N<sub>4</sub> NTs possesses a high photogenerated charge separation rate. This is probably because the tube-like structure of C<sub>3</sub>N<sub>4</sub> with NVs can create new surface traps for charges, thus hindering the recombination of the electron-hole pairs. Notably, the lowest intensity is observed in the NYF(15)/NV-C<sub>3</sub>N<sub>4</sub> NT catalyst, which is attributed to a synergistic effect from the NYF NPs and NVs. Thus the NYF(15)/NV-C<sub>3</sub>N<sub>4</sub> NTs prepared are effective for charge-carrier separation, showing the potential for higher photocatalytic activity than the other samples.

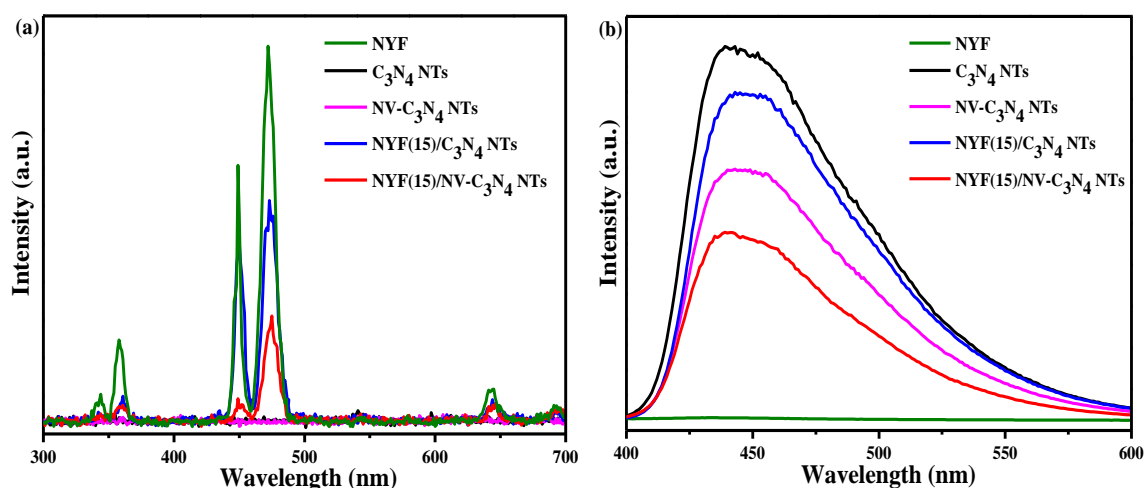


Figure 6.11 PL spectra under 980 nm laser excitation (a) and 360 nm wavelength excitation from Xenon lamp (b).

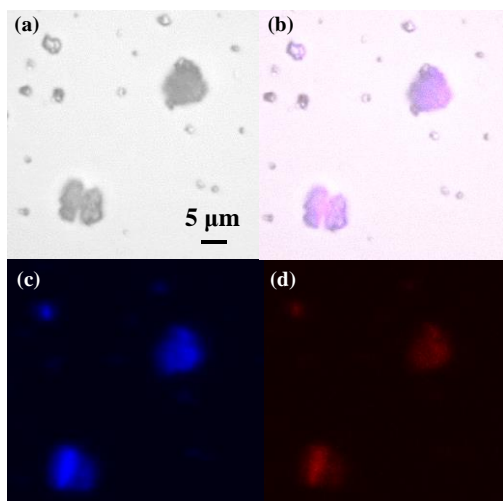


Figure 6.12 Confocal upconversion image of NYF(15)/NV-C<sub>3</sub>N<sub>4</sub> NTs ( $\lambda_{\text{ex}} = 980 \text{ nm}$ ).

To identify the role of NVs play in the photocatalytic activities of the new kind of upconversion photocatalysts, the lifetimes of the nanocatalysts were measured using a 980 nm pulsed laser. Figure 6.13a shows the fluorescence decay curves at 455 nm for the five samples. The average average lifetimes of 115, 0, 0, 140 and 136  $\mu\text{s}$  were obtained for NYF NPs, C<sub>3</sub>N<sub>4</sub> NTs, NV-C<sub>3</sub>N<sub>4</sub> NTs, NYFG(15)/C<sub>3</sub>N<sub>4</sub> NTs and NYF(15)/NV-C<sub>3</sub>N<sub>4</sub> NTs, respectively. The prolongation of the fluorescence lifetime of the heterojunctions in comparison with that of the bare NYF NPs indicates that the energy migration between the heterojunctions is affected by the

decreased surface quenching effect of NYF NPs. It means that  $C_3N_4$  NTs might act as protecting layer for many NYF NPs encased inside the nanotubes [42]. On the other hand, in Figure 6.13b, as for the emitted 475 nm light, the lifetimes of NYFG(15)/ $C_3N_4$  NTs (430  $\mu$ s) was decreased compared to the bare NYF NPs (485  $\mu$ s), whereas NYFG(15)/ $C_3N_4$  NTs exhibited a great improvement to 550  $\mu$ s. The shortening of the fluorescence lifetime of the nanocomposites indicates that the energy migration between  $^1G_4 \rightarrow ^3H_6$  and  $C_3N_4$  NTs is a fluorescence resonance energy transfer (FRET) process rather than a radiation-reabsorption process [43]. One possible reason to explain the energy transfer pathway between  $^1G_4$  level to NV- $C_3N_4$  NTs is that the existence of abundant NVs plays a great role in the surface quenching effect. The great decrease of the surface quenching effect of NYF NPs resulted in longer lifetimes of the  $^1G_4$  level in the heterojunction. Long lifetimes usually mean high efficient upconversion luminescence, therefore, this kind of energy transfer indirectly contributes to the highly enhanced AQE of NYF(15)/NV- $C_3N_4$  NTs. Herein, the PL intensities and the lifetimes correlate well with the photocatalytic performance.

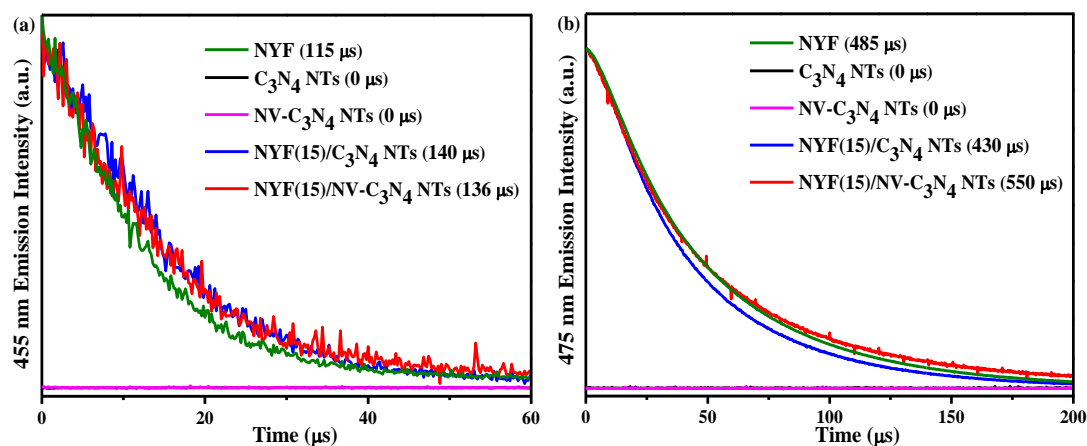


Figure 6.13 The time-resolved fluorescence emission decay curves at 475 nm (a) and 455 nm (b) of the studied catalysts.

Figure 6.14 shows the photocurrent responses of NYF(15)/ $C_3N_4$  NTs and NYF(15)/NV- $C_3N_4$  NTs under  $N_2$  or Ar atmosphere with the NIR laser turned on and off. NYF(15)/NV- $C_3N_4$  NTs

exhibit higher photocurrent density than NYF(15)/C<sub>3</sub>N<sub>4</sub> NTs under Ar atmosphere because of the faster separation of the photogenerated electrons and holes. No obvious difference between the transient photocurrent generated on the NYF(15)/C<sub>3</sub>N<sub>4</sub> NTs under both atmospheres was detected, indicating that the interfacial electron transfer of NYF(15)/C<sub>3</sub>N<sub>4</sub> NTs was not disturbed by the surrounding N<sub>2</sub> gas. Notably, the photocurrent density of NYF(15)/NV-C<sub>3</sub>N<sub>4</sub> NTs under the N<sub>2</sub> atmosphere was lower than that under the Ar atmosphere, suggesting the competition for the trapped electrons between the N<sub>2</sub> gas and the electrode. The results demonstrate that NIR illumination can be harvested by UCNPs-decorated C<sub>3</sub>N<sub>4</sub> NTs, and the photogenerated electrons that arrived on the surface of C<sub>3</sub>N<sub>4</sub> NTs were trapped by the NVs then immediately transferred to the absorbed N<sub>2</sub>. A similar photocurrent response phenomenon was reported by Li [24] and Ma et al [44].

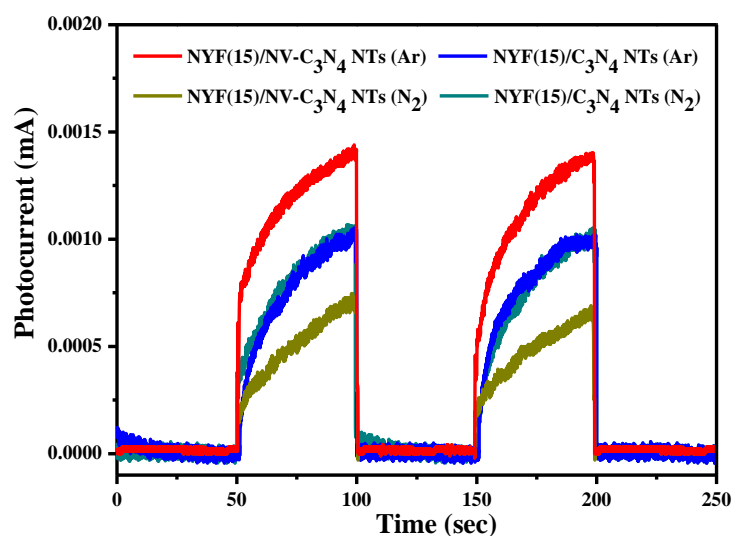


Figure 6.14 Transient photocurrent responses of NYF(15)/C<sub>3</sub>N<sub>4</sub> NTs and NYF(15)/NV-C<sub>3</sub>N<sub>4</sub> NTs under N<sub>2</sub> or Ar atmosphere.

### 6.3.3 Interpretation of charge transfer and reaction pathways

Based on the above results, the possible NIR responsive photofixation process over NYF(15)/NV-C<sub>3</sub>N<sub>4</sub> NTs is illustrated in Figure 6.15. NYF NPs are loaded on the inner and

outer surface of C<sub>3</sub>N<sub>4</sub> NTs with abundant NVs. N<sub>2</sub> molecules are chemisorbed on the NVs of the catalysts. Upon 980 nm irradiation, the Yb<sup>3+</sup> ions in the UC systems are excited. Then the sensitiser Yb<sup>3+</sup> ions transfer their photon energy to the activator Tm<sup>3+</sup> ions multiple times, following by populating several distinct levels of Tm<sup>3+</sup> ions. Besides, the NVs in the protecting layer of C<sub>3</sub>N<sub>4</sub> NTs promote the populating process. After that the NVs incorporated C<sub>3</sub>N<sub>4</sub> NTs are excited by these high levels from Tm<sup>3+</sup> ions via FRET processes as verified in the PL characterisation. Thus, NV-C<sub>3</sub>N<sub>4</sub> NTs are activated simultaneously to produce electron-hole pairs. The excited electrons immediately transfer from the valence band (VB) to the conduction band (CB) of the semiconductors. Subsequently, the electrons arriving on the CB are trapped by the NVs-induced defect states, suppressing the direct recombination of charge carriers. Subsequently, the trapped electrons of the semiconductors react with the N<sub>2</sub> adsorbed on the surfaces, mostly by the NVs, to generate NH<sub>3</sub>. Whereas the holes in the VB are consumed through the oxidation of ethanol to CH<sub>3</sub>CHO and C<sub>2</sub>H<sub>5</sub>OC<sub>2</sub>H<sub>5</sub> spontaneously [45]. The overall reaction equations are summarised as follows:



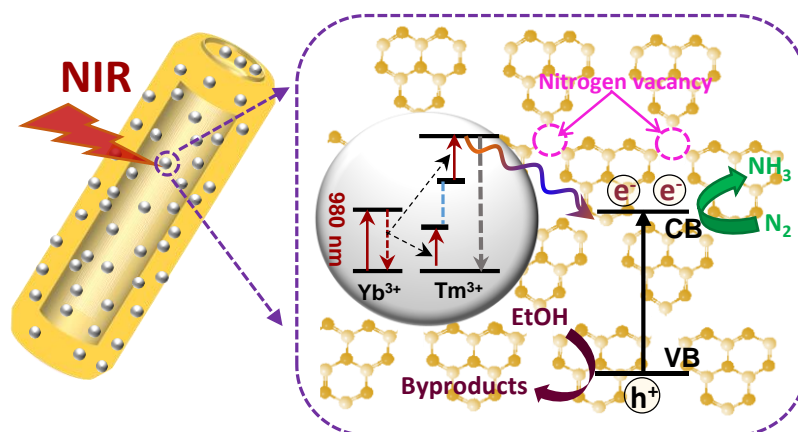


Figure 6.15 Illustrated mechanism of NIR-activated photofixation process on NYF(15)/NV- $C_3N_4$  NTs.

## 6.4 Conclusion

A promising NIR-induced approach to facilitate ammonia production in ambient conditions was realized over NYF NP supported  $C_3N_4$  NTs with NVs. NYF NPs with a size of about 20 nm were homogeneously dispersed on the inner and outer of the nanotubes. At a NYF NP loading of 15 wt.%, the nanocomposite exhibits the highest activity with an ammonia synthesis rate of  $0.80 \text{ mmol L}^{-1} \text{ g}_{\text{cat}}^{-1}$  (AQE of 0.99 %) under irradiation of 980 nm laser light, and  $5.3 \text{ mmol L}^{-1} \text{ g}_{\text{cat}}^{-1}$  under UV-filtered solar light, about three times as high as for the bare  $C_3N_4$  NTs. The characterization results demonstrate that the NVs not only serve as active sites to adsorb and activate  $N_2$  molecules but also promote interfacial energy transfer within the catalysts. Steady-state and dynamic PL analysis confirmed that assembly with NYFs makes NV- $C_3N_4$  NTs NIR-light responsible via the FRET process, owing to the ingenious energy gap match. Overall, the strategy presents new insights into the design of emerging nanocomposites for efficient utilization of the solar spectrum with diverse applications.

## References

- [1] C. Guo, J. Ran, A. Vasileff, S.-Z. Qiao, *Energy & Environmental Science*, 11 (2017) 45-46.

- [2] A.J. Medford, M.C. Hatzell, *ACS Catalysis*, 7 (2017) 2624-2643.
- [3] A. Banerjee, B.D. Yuhas, E.A. Margulies, Y. Zhang, Y. Shim, M.R. Wasielewski, M.G. Kanatzidis, *Journal of the American Chemical Society*, 137 (2015) 2030-2034.
- [4] S. Sun, Q. An, W. Wang, L. Zhang, J. Liu, W.A. Goddard Iii, *Journal of Materials Chemistry A*, 5 (2017) 201-209.
- [5] G. Schrauzer, T. Guth, *Journal of the American Chemical Society*, 99 (1977) 7189-7193.
- [6] X. Chen, N. Li, Z. Kong, W.-J. Ong, X. Zhao, *Materials Horizons*, 5 (2018) 9-27.
- [7] W. Qin, D. Zhang, D. Zhao, L. Wang, K. Zheng, *Chemical communications*, 46 (2010) 2304-2306.
- [8] T. Oshikiri, K. Ueno, H. Misawa, *Angewandte Chemie*, 53 (2014) 9802-9805.
- [9] J. Zhou, Q. Liu, W. Feng, Y. Sun, F. Li, *Chemical reviews*, 115 (2015) 395-465.
- [10] G. Chen, H. Qiu, P.N. Prasad, X. Chen, *Chemical reviews*, 114 (2014) 5161-5214.
- [11] W. Wang, W. Huang, Y. Ni, C. Lu, Z. Xu, *ACS applied materials & interfaces*, 6 (2014) 340-348.
- [12] G. Chen, T.Y. Ohulchanskyy, R. Kumar, H. Ågren, P.N. Prasad, *ACS nano*, 4 (2010) 3163-3168.
- [13] W.J. Ong, L.L. Tan, Y.H. Ng, S.T. Yong, S.P. Chai, *Chemical reviews*, 116 (2016) 7159-7329.
- [14] Z. Zeng, K. Li, L. Yan, Y. Dai, H. Guo, M. Huo, Y. Guo, *RSC Advance*, 4 (2014) 59513-59518.
- [15] K. Li, Z. Zeng, L. Yan, M. Huo, Y. Guo, S. Luo, X. Luo, *Applied Catalysis B: Environmental*, 187 (2016) 269-280.
- [16] W. Wang, Y. Li, Z. Kang, F. Wang, J.C. Yu, *Applied Catalysis B: Environmental*, 182 (2016) 184-192.



- [17] W.-N. Wang, C.-X. Huang, C.-Y. Zhang, M.-L. Zhao, J. Zhang, H.-J. Chen, Z.-B. Zha, T. Zhao, H.-S. Qian, *Applied Catalysis B: Environmental*, 224 (2018) 854-862.
- [18] M.Z. Huang, B. Yuan, L. Dai, M.L. Fu, *Journal of colloid and interface science*, 460 (2015) 264-272.
- [19] E. Cheng, W. Yin, S. Bai, R. Qiao, Y. Zhong, Z. Li, *Materials Letters*, 146 (2015) 87-90.
- [20] W. Fan, H. Bai, W. Shi, *CrystEngComm*, 16 (2014) 3059.
- [21] C. Li, F. Wang, J. Zhu, J.C. Yu, *Applied Catalysis B: Environmental*, 100 (2010) 433-439.
- [22] W. Wang, W. Huang, Y. Ni, C. Lu, L. Tan, Z. Xu, *Applied Surface Science*, 282 (2013) 832-837.
- [23] M. Chatti, V.N. Adusumalli, S. Ganguli, V. Mahalingam, *Dalton transactions*, 45 (2016) 12384-12392.
- [24] H. Li, J. Shang, Z. Ai, L. Zhang, *Journal of the American Chemical Society*, 137 (2015) 6393-6399.
- [25] S. Hu, X. Chen, Q. Li, Y. Zhao, W. Mao, *Catalysis Science Technology*, 6 (2016) 5884-5890.
- [26] P. Niu, L.C. Yin, Y.Q. Yang, G. Liu, H.M. Cheng, *Advanced materials*, 26 (2014) 8046-8052.
- [27] G. Dong, W. Ho, C. Wang, *Journal of Materials Chemistry A*, 3 (2015) 23435-23441.
- [28] G. Wu, Y. Gao, B. Zheng, *Ceramics International*, 42 (2016) 6985-6992.
- [29] Y. Zhu, A. Marianov, H. Xu, C. Lang, Y. Jiang, *ACS Applied Materials & Interfaces*, 10 (2018) 9468-9477.
- [30] J. Zhao, D. Jin, E.P. Schartner, Y. Lu, Y. Liu, A.V. Zvyagin, L. Zhang, J.M. Dawes, P. Xi, J.A. Piper, E.M. Goldys, T.M. Monro, *Nature nanotechnology*, 8 (2013) 729-734.

- [31] Y. Bai, L. Ye, T. Chen, L. Wang, X. Shi, X. Zhang, D. Chen, *ACS Applied Materials & Interfaces*, 41 (2016) 27661-27668.
- [32] S. Xu, W. Xu, Y. Wang, S. Zhang, Y. Zhu, L. Tao, L. Xia, P. Zhou, H. Song, *Nanoscale*, 6 (2014) 5859-5870.
- [33] P. Niu, G. Liu, H.-M. Cheng, *The Journal of Physical Chemistry C*, 116 (2012) 11013-11018.
- [34] Z. Hong, B. Shen, Y. Chen, B. Lin, B. Gao, *Journal of Materials Chemistry A*, 1 (2013) 11754.
- [35] Y. Zhang, Z. Hong, *Nanoscale*, 5 (2013) 8930-8933.
- [36] G. Boulon, A. Collombet, A. Brenier, M.T. Cohen-Adad, A. Yoshikawa, K. Lebbou, J.-H. Lee, T. Fukuda, *Advanced Functional Materials*, 11 (2001) 263-270.
- [37] K. Li, Z. Zeng, L. Yan, S. Luo, X. Luo, M. Huo, Y. Guo, *Applied Catalysis B: Environmental*, 165 (2015) 428-437.
- [38] Q. Tay, P. Kanhere, C.F. Ng, S. Chen, S. Chakraborty, A.C.H. Huan, T.C. Sum, R. Ahuja, Z. Chen, *Chemistry of Materials*, 27 (2015) 4930-4933.
- [39] J. Ding, W. Xu, H. Wan, D. Yuan, C. Chen, L. Wang, G. Guan, W.-L. Dai, *Applied Catalysis B: Environmental*, 221 (2018) 626-634.
- [40] H.L. Hsu, K.R. Leong, I.J. Teng, M. Halamiccek, J.Y. Juang, S.R. Jian, L. Qian, N.P. Kherani, *Materials*, 7 (2014) 5643-5663.
- [41] N. Liu, W. Qin, G. Qin, T. Jiang, D. Zhao, *Chemical communications*, 47 (2011) 7671-7673.
- [42] D.-X. Xu, Z.-W. Lian, M.-L. Fu, B. Yuan, J.-W. Shi, H.-J. Cui, *Applied Catalysis B: Environmental*, 142-143 (2013) 377-386.
- [43] Y. Tang, W. Di, X. Zhai, R. Yang, W. Qin, *ACS Catalysis*, 3 (2013) 405-412.
- [44] H. Ma, Z. Shi, Q. Li, S. Li, *Journal of Physics and Chemistry of Solids*, 99 (2016) 51-58.

[45] W. Zhao, J. Zhang, X. Zhu, M. Zhang, J. Tang, M. Tan, Y. Wang, *Applied Catalysis B: Environmental*, 144 (2014) 468-477.

## Chapter 7 Conclusions and future work

### 7.1 Conclusions

The thesis covers extensively the design and fabrication of various  $C_3N_4$  NT-based photocatalysts: bimetallics deposited  $C_3N_4$  NTs (Ag-Cu/ $C_3N_4$  NTs), metal oxide loaded  $C_3N_4$  NTs (CoO/ $C_3N_4$  NTs and  $Co_3O_4$ / $C_3N_4$  NTs), upconversion NPs anchored on  $C_3N_4$  NTs (NYFG/ $C_3N_4$  NTs) and  $C_3N_4$  NTs with abundant NVs (NYF/NV- $C_3N_4$  NTs). These heterojunctions were synthesised by facile methods for harvesting more visible or NIR light and inhibiting photogenerated charge recombination in order to improve the photocatalytic activities in  $H_2$  generation or ammonia synthesis.

An improved water-induced morphological transformation process was applied to prepare bare  $C_3N_4$  NTs, which show uncontrollable sizes but are active in the absence of any co-catalysts. The Ag-Cu bimetallic nanoparticles with a size of about 10 nm were uniformly distributed on the surface of the nanotubes. The nanocomposite Ag-Cu(3)/ $C_3N_4$  NTs (1:1) exhibits the highest  $H_2$  evolution of 246.0  $\mu\text{mol/g/h}$ , which is higher than the monometallic Ag/ $C_3N_4$  NTs, Cu/ $C_3N_4$  NTs, Pt/ $C_3N_4$  NTs and bare  $C_3N_4$  NTs. The improved performance is attributed to the unique tubular nanostructure, more visible light absorption, effective separation of photo-generated carriers and strong metal-support interaction. Furthermore, experimental evidence indicates that the oxidation potentials played a crucial role in photocatalytic process rather than the pH values. TEA can be oxidised to DEA and acetaldehyde by protons/water in the oxygen-free conditions, because of its relatively high oxidation potential, while methanol cannot be easily decomposed by the photogenerated holes.

Controllable  $C_3N_4$  NTs were successfully synthesised by an improved facile calcination process. Tunable heterojunction architectures of  $CoO_x$  NPs were confined on well-arrayed  $C_3N_4$  NTs using the same one-pot method after annealing under vacuum or static air

atmosphere. Treatment under vacuum resulted in the formation of CoO NPs less than 8 nm, whereas Co<sub>3</sub>O<sub>4</sub> nanoparticles from 10 nm to 25 nm were aggregated under static air atmosphere. CoO/C<sub>3</sub>N<sub>4</sub> NTs with a mass ratio of 7 % exceeds photocatalytic H<sub>2</sub> generation than Co<sub>3</sub>O<sub>4</sub>/C<sub>3</sub>N<sub>4</sub> NTs, bare C<sub>3</sub>N<sub>4</sub> NTs, CoO and Co<sub>3</sub>O<sub>4</sub> under visible light irradiation. This attributes to their unique well-arrayed nanotubes, uniformly distributed finer nanoparticles, the longer life time of excited electrons and the synergetic effect. Comparative studies reveal that the as-prepared CoO/C<sub>3</sub>N<sub>4</sub> NT and Co<sub>3</sub>O<sub>4</sub>/C<sub>3</sub>N<sub>4</sub> NT heterojunctions are identified as Type II and Type I heterojunction, respectively. The electron transfer pathways were evidenced by Kelvin probe force microscopy. This research presents a new strategy to tune Type I and Type II heterojunction architectures.

Further extending the absorption beyond visible light, NIR responsive NaYF<sub>4</sub>:20% Yb,0.5% Tm,2.5% Gd NPs decorated C<sub>3</sub>N<sub>4</sub> NTs were prepared by a facile method. NYFG/C<sub>3</sub>N<sub>4</sub> NT heterojunction with a loading amount of 15 wt. % exhibits the highest hydrogen generation with the achieved AQE of 0.80% under 980 nm laser irradiation and the yield was 618.3  $\mu\text{mol/g}$ , about 1.4 times as high as that of the bare C<sub>3</sub>N<sub>4</sub> NTs under simulated sunlight irradiation. Moreover, the nanocomposite is highly stable after four cycling runs under NIR light. Except for the small nanoparticle size and good distribution of NYFG NPs, the high upconversion intensity attributed to Gd<sup>3+</sup> ions and the stronger interaction between the heterojunction played a crucial role as well. The steady state and fluorescence spectra indicated that the energy migration between NYFG NPs and C<sub>3</sub>N<sub>4</sub> NTs was a fluorescence resonance energy transfer (FRET) process, which was dominated by the surface quenching effect as well. This study provides an effective strategy to make use of low energy photons in C<sub>3</sub>N<sub>4</sub> NT photocatalysis, offering a pathway to significantly improve its photocatalytic performance.

Apart from the H<sub>2</sub> production activities, a promising photoinduced approach to facilitate ammonia synthesis in ambient conditions was realised over NYF NPs decorated C<sub>3</sub>N<sub>4</sub> NTs

containing nitrogen vacancies. The NYF(15)/NV-C<sub>3</sub>N<sub>4</sub> NTs exhibit superior activities with the ammonia synthesis rate of 0.80 mmol L<sup>-1</sup> g<sub>cat</sub><sup>-1</sup> (AQE of 0.99 %) under 980 nm laser light; and 5.3 mmol L<sup>-1</sup> g<sub>cat</sub><sup>-1</sup> under UV-filtered solar light. It is about three times higher than the bare C<sub>3</sub>N<sub>4</sub> NTs. We have demonstrated that the NVs not only serve as active sites to absorb and activate N<sub>2</sub> molecules but also promote interfacial energy transfer within the catalysts. The assembled NYFs make NV-C<sub>3</sub>N<sub>4</sub> NTs excitable by NIR light via FRET process, owing to the ingenious energy gap match.

## 7.2 Future work

This thesis presents the exploration of C<sub>3</sub>N<sub>4</sub> NT-based hybrid nanocomposites and their application in photocatalytic H<sub>2</sub> generation and ammonia synthesis. The breakthroughs in the field of C<sub>3</sub>N<sub>4</sub> NT-based catalysts have undoubtedly witnessed the improved photocatalytic activities. In spite of the promising results shown here, related studies are still in progress and further developments are prominently required.

In bimetallic C<sub>3</sub>N<sub>4</sub> NT catalysts, the current research focuses mainly on how the composition of the Ag-Cu bimetallic NPs influences photocatalytic performance. Bimetallic NPs exhibit various architectures including crown-jewel, hollow, core-shell, porous, alloyed structure and heterostructure, which play an important role in the photocatalytic activities of the catalysts [1]. Thus, the exploration of the relationship between the photocatalytic activities and the structural characteristics in the Ag-Cu bimetallic system is highly desirable. Also, surface segregation is an important phenomenon for bimetallic nanomaterials. In this case, in situ microscopy techniques are required to understand the structure-property correlation at the atomic level.

C<sub>3</sub>N<sub>4</sub> NTs exhibits an energy band gap of around 2.7 eV, corresponding to a 459 nm light threshold, showing that it has a limited visible light absorption range. In addition to the narrow

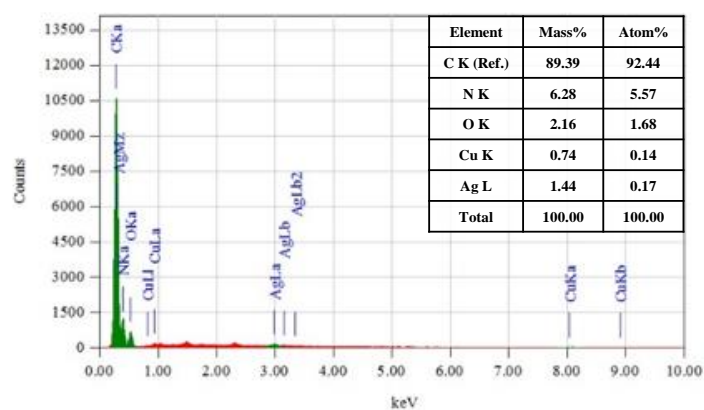
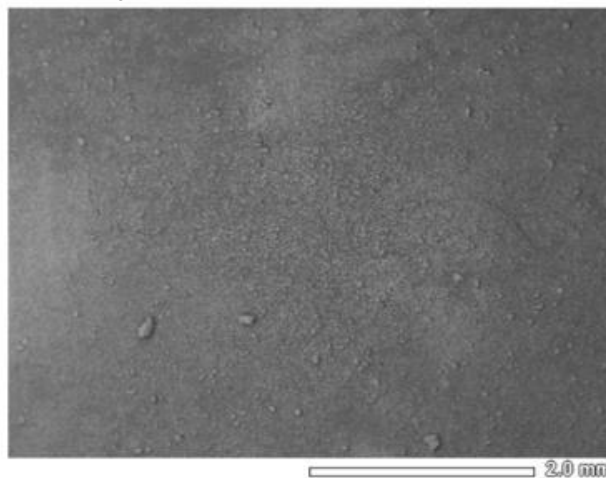
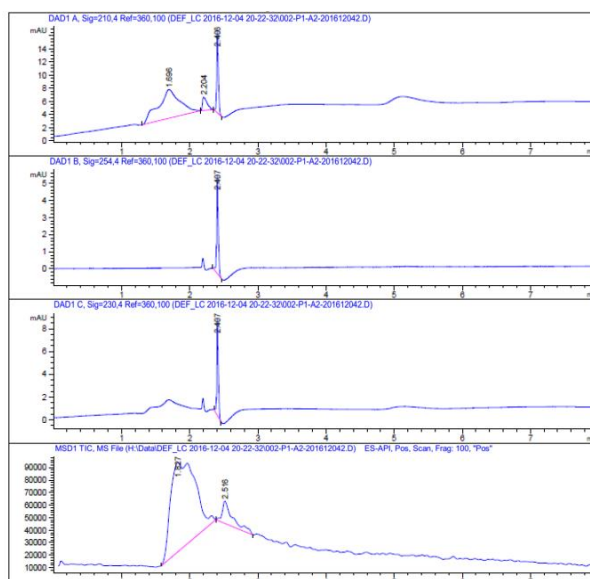
band semiconductors cobalt oxides, many other strategies without metal-containing are of great potential to expand the visible light response to above 460 nm. For example, co-doping cheap elements like B and P into  $C_3N_4$  extends the light absorbance from 460 nm to 550 nm [2]. Simple copolymerisation with organic monomers like barbituric acid is able to extend visible region up to about 750 nm [3].

For the UCNP decorated catalysts, the light absorption in NIR region is limited in the range of 900-1000 nm, the region of 800-900 nm with more photon energies has not been absorbed. Therefore, neodymium ( $Nd^{3+}$ ) ions as the sensitizer at around 800 nm can be introduced in the UCNPs in order to effectively utilise NIR region [4]. Besides, the laser-induced heating effect is expected to be minimised. Furthermore, this work still suffers from the relatively low efficiency, which is far from the industrial requirement. Also, the development of materials with magnetic properties for an easy separation is highly desired.

## References

- [1] X. Liu, D. Wang, Y. Li, *Nano Today*, 7 (2012) 448-466.
- [2] F. Raziq, Y. Qu, M. Humayun, A. Zada, H. Yu, L. Jing, *Applied Catalysis B: Environmental*, 201 (2017) 486-494.
- [3] J. Zhang, X. Chen, K. Takanabe, K. Maeda, K. Domen, J.D. Epping, X. Fu, M. Antonietti, X. Wang, *Angewandte Chemie*, 49 (2010) 441-444.
- [4] Y. Wang, G. Liu, L. Sun, J. Xiao, J. Zhou, C. Yan, *ACS nano*, 7 (2013) 7200-7206.

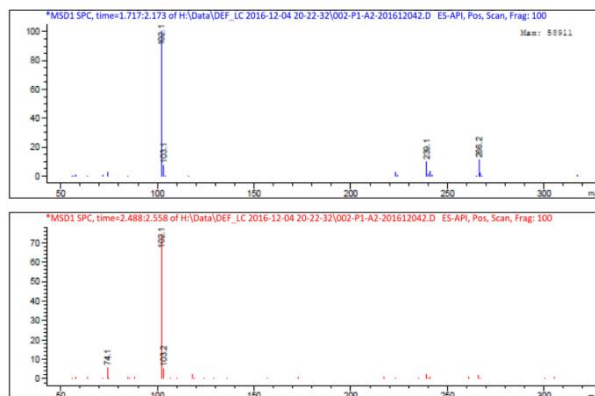
## Appendix

Ag-Cu(3)/C<sub>3</sub>N<sub>4</sub> NTs (1:1)A 1 SEM-EDX spectrum of Ag-Cu(3)/C<sub>3</sub>N<sub>4</sub> NTs (1:1).

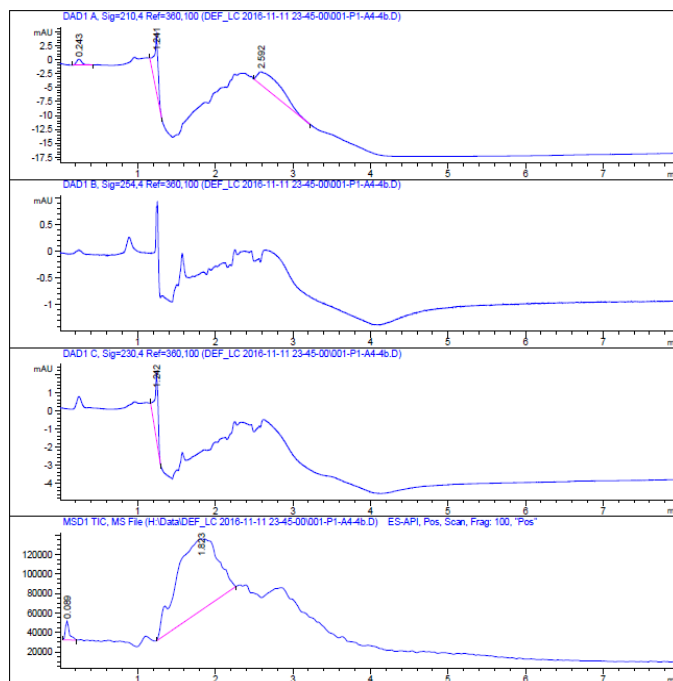


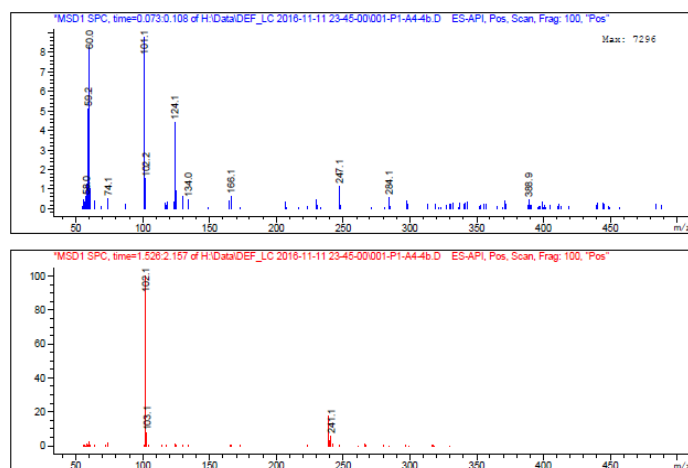
MS Signal: MSD1 TIC, MS File, ES-API, Pos, Scan, Frag: 100, "Pos"  
Spectra averaged over upper half of peaks.  
Noise Cutoff: 1000 counts.  
Reportable Ion Abundance: > 10%.

Retention Time (MS)	MS Area	Mol. Weight or Ion
1.827	1761125	266.20 I 102.10 I
2.516	189898	102.10 I

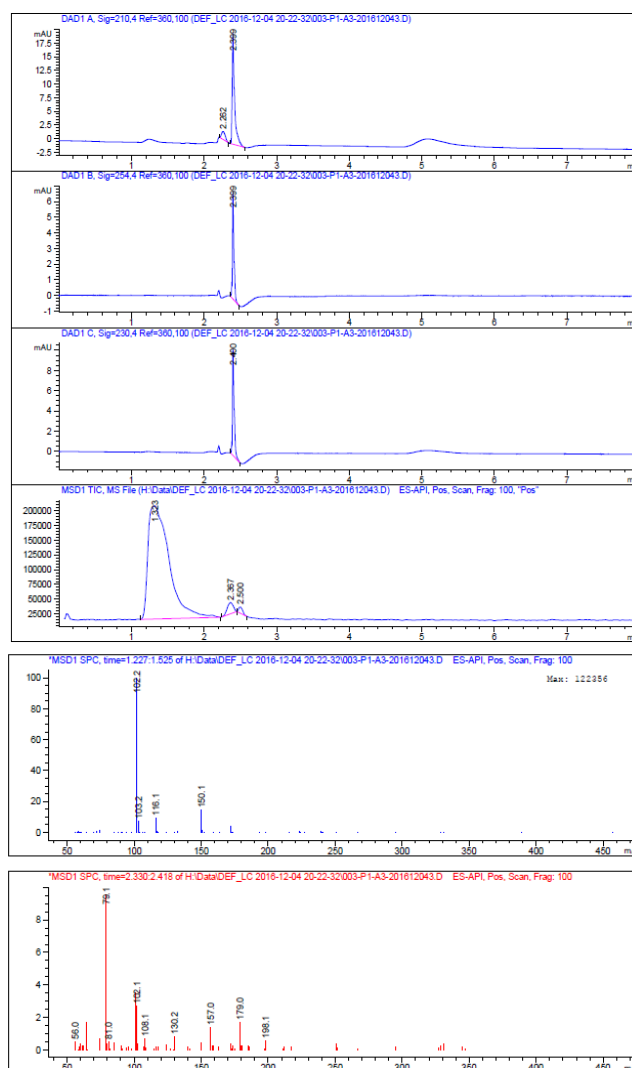


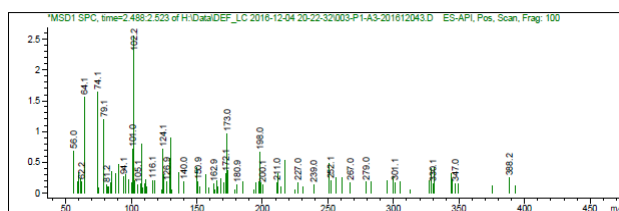
A 2 LC/MS chromatographic profiles of the peak fraction from 3.0 - 3.8 min in 180 min TEA sample (74.1 and 102.1 mass are indexed to DEA and TEA respectively).



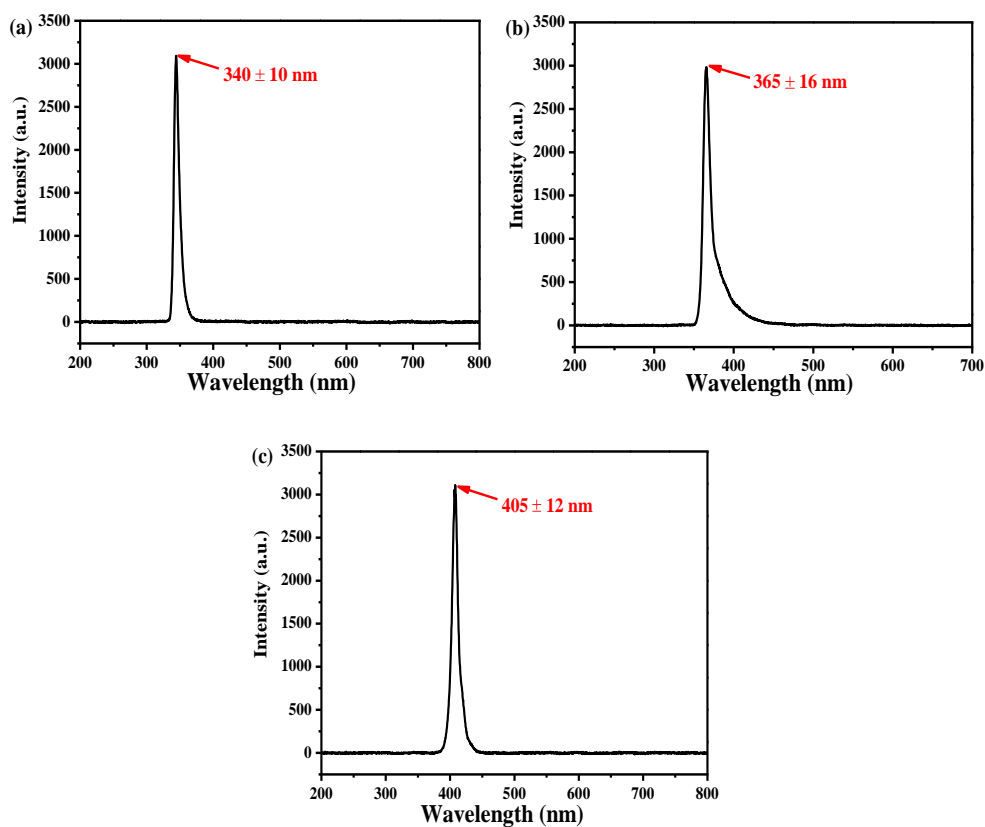


A 3 LC/MS chromatographic profiles of the peak fraction from 4.5 - 4.7 min in 180 min TEOA sample (60.0 mass is assigned to glycolaldehyde although TEA component is still detected because of too large injection amount from last TEA sample).

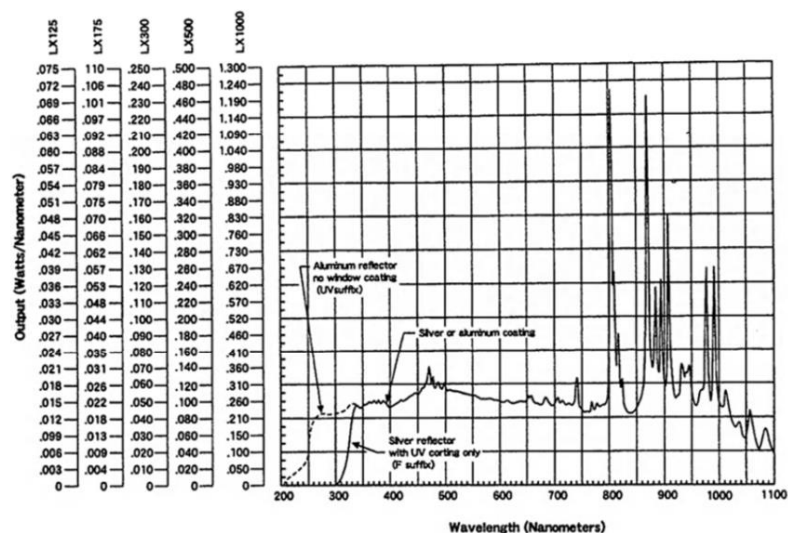




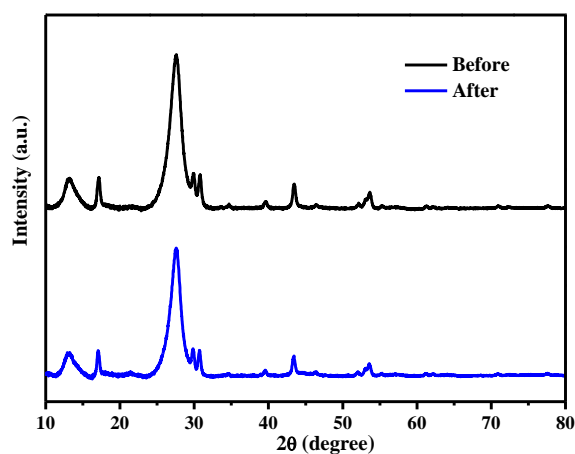
A 4 LC/MS chromatographic profiles of the peak fraction from 8.6 - 12.0 min in 180 min TEOA sample (105.1 and 150.1 mass can match well with DEOA and TEOA respectively although TEA component is still detected because of too large injection amount from last TEA sample).



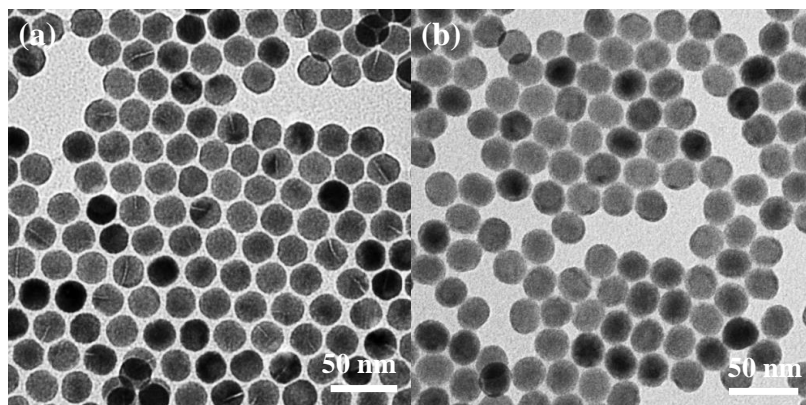
A 5 The transmittance and intensities of 340 nm (a), 365 nm (b) and 405 nm (c) monochromatic light.



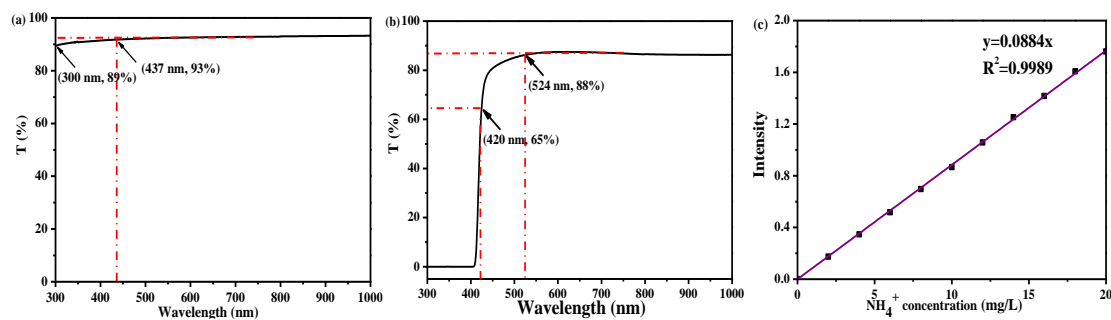
A 6 Spectral distribution of Xenon lamp at the current of 20 A (LX 300, from Hidesada Toriyama, Inc.).



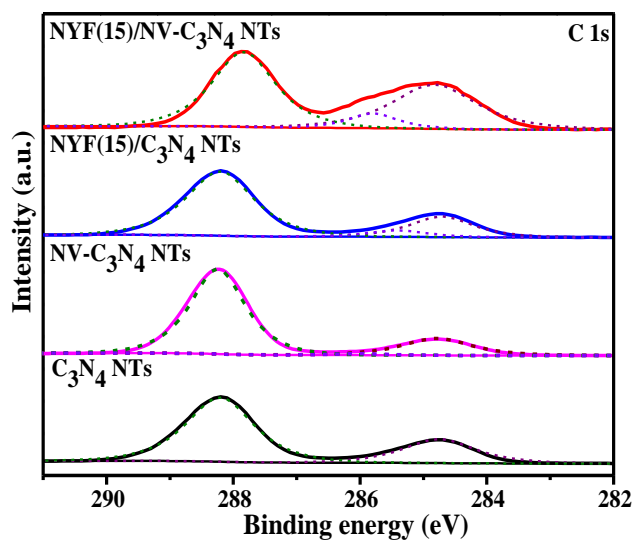
A 7 XRD patterns of NYFG(15)/C<sub>3</sub>N<sub>4</sub> NTs before and after reaction.



A 8 TEM images of NYFG NPs (a) and NYF NPs (b).



A 9 Spectral distribution of Xenon lamp at the current of 20 A (LX 300) (a), transmittance properties of the reactor (Beijing China Education Au-light co., Ltd) (b) and the  $> 420$  nm filter (c), the standard curve measured by indophenol blue method (d).



A 10 High-resolution C 1s XPS spectra of the various catalysts.